Università Politecnica delle Marche
Corso di Dottorato di Ricerca in Ingegneria Civile, Ambientale, Edile e Architettura
Curriculum in Ingegneria Civile, Ambientale, Edile e Architettura
XVIII edition - new series

Dynamic testing for the characterisation of bituminous interlayers

PhD Dissertation of:

Davide Ragni

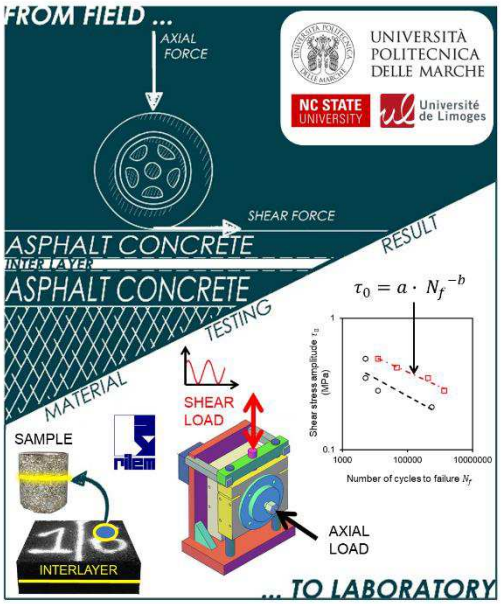

Advisor: **Prof. Francesco Canestrari**

Co-Advisor: **Prof. Andrea Graziani**

Curriculum Supervisor: **Prof. Francesco Fatone**

Università Politecnica delle Marche
Corso di Dottorato di Ricerca in Ingegneria Civile, Ambientale, Edile e Architettura
Curriculum in Ingegneria Civile, Ambientale, Edile e Architettura
XVIII edition - new series

Dynamic testing for the characterisation of bituminous interlayers

PhD Dissertation of:

Davide Ragni

Advisor:

Prof. Francesco Canestrari

Co-Advisor:

Prof. Andrea Graziani

Curriculum Supervisor:

Prof. Francesco Fatone

XVIII edition - new series

Università Politecnica delle Marche
Dipartimento di Ingegneria Civile, Edile e Architettura
Via Brecce Bianche — 60131 - Ancona, Italy

To my family

"…It does not matter how slowly you go

so long as you do not stop…"

Confucius

"…The only way to do great work is to love what you do…"

Steve Jobs

Acknowledgements

First, I would like to express my deepest appreciation to my Advisor, Professor Francesco Canestrari, and Co-Advisor, Professor Andrea Graziani, for being invaluable reference points for my research work. Without their support, this research could not have been possible.

A special mention to Professor Christophe Petit for all the invaluable support given me during my stay in France. It was a unique occasion to grow up as a researcher and to work with interesting and brilliant people. And thanks to him, I realised one of my dreams: flying.

A grateful thank to Professor Y. Richard Kim for all the invaluable support given me during my stay in the US. It was extraordinary cooperation and unrepeatable occasion to meet new, interesting and motivating people. One name above all is Nithin Sudarsanan, a young researcher and friend of great value, who has always been present and very supportive for my research and beyond.

A heartfelt thank is dedicated to the entire research group of the department ICEA-Infrastructure area (professors, researchers, PhD students and technicians) for all their help.

Other fundamental people have made my PhD years an unrepayable experience and deserve a special mention.

My sincere appreciation goes to Arianna Stimilli for being an inspiration and a role model to pursue. A remarkable researcher and, especially, an even more marvellous person. And a true and irreplaceable friend. Always patient, always ready to listen to my questions and complaints. I will always be grateful to her.

Endless thanks go to my colleagues and friends Giorgia Mazzoni, Chiara Mignini, Emiliano Prosperi and Simone Raschia for always encouraging me to move forward during this journey. Thank for understanding me and cheering me to be able to meet the deadlines. If I am less procrastinating today (i.e., no longer a "Cunctator"), it is thanks to them.

Special thoughts go to Cristian De Angelis, Daniele Ragni, Martina Cingolani, Claudia Castaldo, Hedi Bennouri, and Fernando do Couto Rosa Almeida for having been close to me during these years. Their closeness and friendship give me the balance I need. No words can express my affection for them.

Finally, I am deeply grateful to my family for their continuous love, inspiration and support in all my endeavours. I am the way I am thanks to them.

Ancona, 11th February 2020

Abstract

The traffic loading on pavement structures includes both vertical and horizontal stresses (normal and tangent to the pavement surface). The latter become critical in regions that are prone to frequent braking, cornering or on steep grades. Since bituminous pavement is a multilayer structure, the existence of a poor interlayer bonding between bituminous layers could adversely affect the pavement performance and serviceability. Hence, a proper evaluation of the interlayer bonding has the utmost importance in pavement performance. The evaluation of interlayer bonding in bituminous pavements is typically carried out by measuring the interlayer shear strength (ISS) at failure using static laboratory tests. A significant improvement of the current testing approach is the development of dynamic testing devices, which could simulate the field conditions more realistically since the traffic loads applied to the pavement are dynamic. In this context, this PhD thesis describes the experimental activities carried out at Università Politecnica delle Marche, North Carolina State University and University of Limoges within the Task Group 3 "Pavement multilayer system" of the RILEM TC 272-PIM. The activities focused on the design and development of a new testing device for performing dynamic interlayer bond testing at Università Politecnica delle Marche along with carrying out dynamic bond testing using other existing devices. The interlayer behaviour has been investigated through both direct shear and torque tests on double-layered specimens extracted from laboratory compacted slabs prepared using a single bituminous mixture. The stimulating results presented in this thesis, reported both in terms of stiffness and cumulative damage, showed that dynamic bond testing can successfully be used to evaluate the bituminous interlayer performance and can provide a noticeable help for defining the service life of the pavement sections realistically compared to the static bond tests.

Sommario

Il carico di traffico trasferito sulle pavimentazioni stradali include sia sollecitazioni verticali che orizzontali. Queste ultime diventano particolarmente critiche nelle zone soggette a frequenti frenate, in curva o con pendenze elevate. Poiché la pavimentazione stradale è una struttura multistrato, l'esistenza di uno scarso collegamento all'interfaccia tra gli strati bituminosi potrebbe influire negativamente sulle prestazioni e funzionalità della pavimentazione. Pertanto, una corretta valutazione del grado di collegamento tra gli strati è di fondamentale importanza. Finora, tale valutazione viene effettuata misurando la resistenza a taglio dell'interfaccia utilizzando prove di laboratorio statiche. Un miglioramento significativo dell'attuale approccio di prova è lo sviluppo di dispositivi dinamici, che potrebbero simulare in modo più realistico le condizioni in sito. La presente Tesi di dottorato descrive le attività sperimentali svolte presso l'Università Politecnica delle Marche, la North Carolina State University e l'University of Limoges nell'ambito del Task Group 3 "Pavement multilayer system" del RILEM TC 272-PIM. Le attività si sono concentrate sulla progettazione e lo sviluppo di un nuovo dispositivo di prova per l'esecuzione di prove dinamiche all'interfaccia presso l'Università Politecnica delle Marche e sull'esecuzione di prove dinamiche con altri dispositivi esistenti. Il comportamento a taglio delle interfacce è stato studiato sia con prove di taglio diretto che di torsione su campioni carotati da lastre bistrato compattate in laboratorio e preparate con un'unica miscela bituminosa. I risultati presentati in questa tesi, sia in termini di rigidità che di danno cumulativo, hanno dimostrato che le prove di taglio dinamico possono essere utilizzate con successo per valutare le prestazioni delle interfacce bituminose e fornire un notevole aiuto per definire la vita utile delle pavimentazioni in modo più realistico rispetto alle prove di taglio statico.

Contents

List of Figures

List of Tables

0

Introduction

Chapter 1

Background and research description

The development of smart, green and integrated transport is one of the currently societal challenges. Specifically, this challenge aims the boost the competitiveness of the transport industries and achieve a transport system that is resource-efficient, climate-and-environmentally friendly, safe and seamless for the benefit of all citizens, the economy and society.

Moreover, in the current economic situation, National Road Authorities are under increasing pressure to build and maintain their road network with reducing budgets. It is therefore essential that the maximum use is made of innovation, both in the roads sector and transferred from other sectors to assist in the management of the network.

In the field of bituminous materials and pavements, many innovative technologies are under development in laboratories around the world. Since more than 30 years, a relevant part of these innovations has been developed within the framework of RILEM, the International Union of Laboratories and Experts in Construction Materials, Systems and Structures.

Bituminous pavements are composed of several layers with different materials. The mechanical behaviour of the whole multilayer structure depends not only on the material properties of each layer but also on the properties of the interlayer bonding between the layers. In fact, the interlayer between two layers should guarantee an adequate and durable bond in order to be able to transfer stresses induced by the traffic loads through the layers. In the case of interlayer debonding, this stress transfer is not possible, and the multilayer structure does not act as a composite system anymore. Debonding seriously affects pavement performance and could lead to premature failure even though the properties of the single layers, in terms of stiffness modulus, permanent deformation resistance and fatigue properties, are appropriate. In this sense, the performance of the pavement structures is directly influenced by the interlayer bonding conditions between layers. Hence, the correct evaluation of the properties of bituminous interlayers is a very important issue in pavement engineering.

Several test devices have been proposed to experimentally evaluate the behaviour of bituminous interlayers. To date, interlayer bonding in bituminous pavements is usually assessed by measuring the interlayer shear strength (ISS) of double-layered specimens using static test working with monotonic load/displacement application. Static laboratory tests have developed and standardised (European Pre-Standard prEN 12697 Bituminous mixture – Test methods for hot mix asphalt – Part 48: Interlayer bonding). It worth to underline that these static test devices lead to failure of the specimen following stress paths very different from those occurring in an actual pavement. In fact, the repetitive loading applied by vehicles is

considerably lower than the interlayer resistance at the first application measured by a monotonic test.

For this reason, a significant improvement of the current testing approach is the development of dynamic bond testing devices, which better simulate the actual traffic loads. The dynamic/cyclic approach should lead to more reliable performance parameters and help to understand the true bonding at the interlayer in terms of dynamic shear stiffness for better predicting the overall bearing capacity of multilayer pavements. Moreover, also the fatigue resistance at the interlayer could be investigated to start giving a term of comparison with classic fatigue approaches based on tensile stress/strain.

Given this background, the main goal of this PhD thesis was to develop a methodology for the experimental characterisation of the dynamic shear performance of bituminous interlayers. This objective was tackled by the design and construction of new testing equipment able to test bituminous mixtures. The new testing device, then called Cyclic-ASTRA, was designed and constructed in the framework of the strategic research project "Advanced dynamic characterisation of interfaces in multilayer structural systems" coordinated by Prof. Andrea Graziani, Associate Professor in Road, Railway and Airport Engineering at the Department of Civil and Building Engineering and Architecture (DICEA) of Università Politecnica delle Marche.

Moreover, this PhD project was developed in the framework of the Task Group 3 (TG 3), "Pavement multilayer systems" of RILEM Technical Committee (TC) "Phase and Inter-phase behaviour of bituminous Materials" (PIM) coordinated by Università Politecnica delle Marche and in particular by Prof. Francesco Canestrari, Full Professor in Road, Railway and Airport Engineering at the Department of Civil and Building Engineering and Architecture (DICEA) of Università Politecnica delle Marche. The activity of TG3 focused on performance assessment of multilayer bituminous pavements at the structural level. In particular, an advanced experimental methodology based on dynamic shear testing analysis of multilayer structural systems was studied. To this aim, TC 272-PIM/TG3 decided to organise an interlaboratory test aimed at comparing different existing or prototype equipment currently employed to obtain the dynamic shear characterisation of multilayer bituminous systems. It is worth to underline that the project is still ongoing.

Most of the research activities described in this PhD thesis were carried out in the Department of Civil and Building Engineering and Architecture of Università Politecnica delle Marche. Part of the research activities were also carried out in cooperation with the Department of Civil, Construction, and Environmental Engineering of North Carolina State University (Raleigh, USA) and the Laboratoire de Génie Civil, Diagnostic et Durabilité (GC2D) of University of Limoges (Egletons, France) which provided their own equipment and testing protocols to perform dynamic bond tests. The main objectives and activities are briefly summarised in the following section.

1.1 Outline of the dissertation

To achieve the objectives above-mentioned, the research activities have been planned and structured as shown in the scheme of Figure 1.1.

Prior to performing the experimental activities, an extensive literature review was conducted, especially focused on dynamic testing devices and procedure. It allowed assessing the current state-of-the-art on the main existing equipment developed to perform dynamic interlayer bond testing in order to improve the current state of knowledge and give the possibilities for further extend research. Subsequently, the new testing device for performing dynamic bond testing was designed, constructed and checked at Università Politecnica delle Marche. Afterwards, the interlaboratory test on "Dynamic Interlayer Shear Testing" promoted by Task Group 3 "Pavement Multilayer System" of RILEM Technical Committee 272-PIM "Phase and Inter-phase behaviour of bituminous Materials" is presented. Finally, experimental laboratory activities were carried out within the RILEM interlaboratory test by performing dynamic tests using three different devices (Cyclic-ASTRA, Cyclic-MAST, shear-torque fatigue test) respectively at Università Politecnica delle Marche (UNIVPM), at North Carolina State University (NCSU) and at University of Limoges (UNILIM). Additional experimentation was carried out at the University of Limoges with the aim to perform cyclic tests on reinforced specimens cored from a trial section.

This PhD dissertation is composed of several chapters, whose contents deal with the topics above-mentioned.

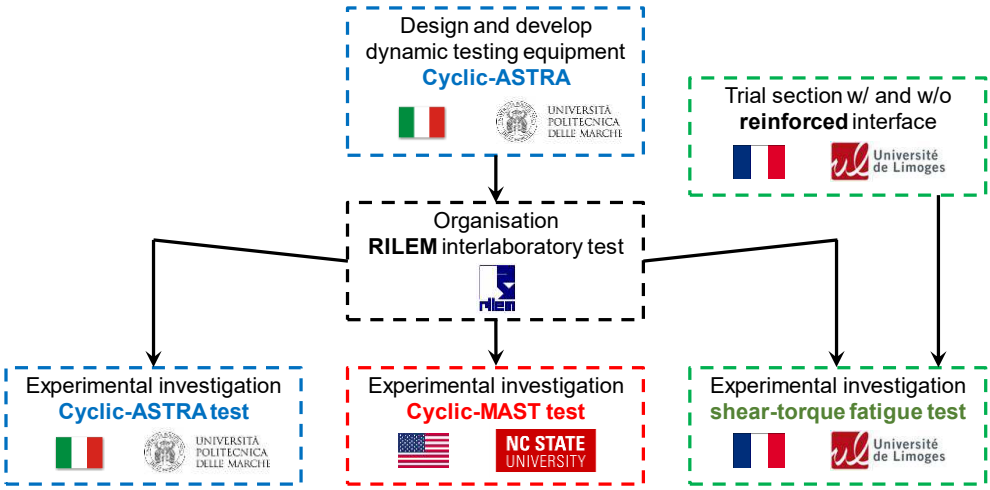

Figure 1.1. Research program flowchart.

Problem statement

Chapter 2

Literature review

2.1 Bituminous pavement

Road pavement is a complex system because involves multiple layers of different materials that are subjected to repetitive or fluctuating irregular traffic loads as well as environmental condition variations. The traffic loads on the road pavement include both vertical stresses (normal to the pavement surface), and horizontal stresses (tangent to the pavement surface).

A traditional distinction, which is becoming scarcely used in modern times, divides road pavements into flexible and rigid; the essential difference between the two types lies in the way in which they distribute the load on the laying surface. In rigid pavements, due to the high modulus of elasticity of the constituent material, the majority of the stresses are supported by the pavement itself, which in this case is composed of cement concrete or reinforced concrete slabs; for this type of pavement, small variations in the bearing capacity on the laying surface have little influence on the structural behaviour and the state of stress. On the contrary, a flexible pavement, generally consisting of a series of layers of increasing quality towards the surface layer, ensures the distribution of the load to the laying surface through the stratified system rather than absorbing the stresses through bending efforts. Using simple words, a flexible pavement can be defined as a pavement comprising of a mixture of aggregates and bitumen, heated and mixed properly and then laid and compacted on a granular layer. The introduction of a cement-treated base course, which has fairly high stiffness, between the layers of a flexible pavement can result in an overall behaviour which, in a sense, is close to that of a rigid pavement; such pavement is defined as semi-rigid. Figure 2.1 presents an example of the load distribution expected for the rigid and flexible pavement. The rigid pavement usually used in airfield constructions, in industrial areas, or in road pavements subjected to particularly heavy load traffic. Flexible pavements are the most commonly adopted and in the following sections will be referred to only this type of road pavement.

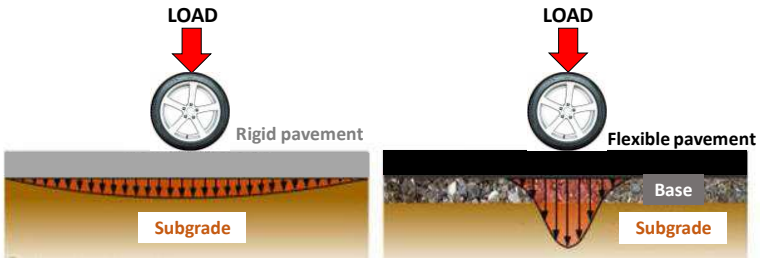

Figure 2.1. Scheme of rigid (left) and flexible (right) pavement.

The flexible pavement (Figure 2.2) is usually composed of the following layers:

- wearing course;
- binder course;
- base course;
- subbase course;
- subgrade course.

The wearing and the binder courses are composed of a mixture of various selected aggregates bound together with bituminous binders. The wearing course has a higher bitumen content and smaller thickness compared to the binder course. These layers are directly subjected to the vertical and horizontal loads, permanently transferred by traffic, and the abrasive action of vehicle tires. The layer in contact with traffic loads must provide specific characteristics such as friction, smoothness, noise control, rut resistance and drainage. The base course serves as the principal structural component of the flexible pavement and distributes the imposed load to the subbase course. The base layer is usually composed of hot mix asphalt, either with plain bitumen or with modified bitumen. Subbase course has the primary function of structural support. The material requirements for the subbase are not as strict as those for the base course since the subbase is subjected to lower load stresses. The subgrade is the most superficial layer of the soil and has the function of absorbing and distributing the loads, avoiding their concentration in a single point, which is the primary cause of potential local subsidence and cracking.

Normally, materials and thicknesses of flexible pavement layers are selected by the road management agencies taking into account the economic availability, the traffic loads and composition, service life and climatic conditions that the pavement undergoes during its service life. The design depends also on adequate knowledge of material properties (aggregate and bituminous) and interlayer characteristics. Despite the availability of numerous studies on bituminous pavements, there is still a lack of sufficient knowledge about the interlayer mechanical performances.

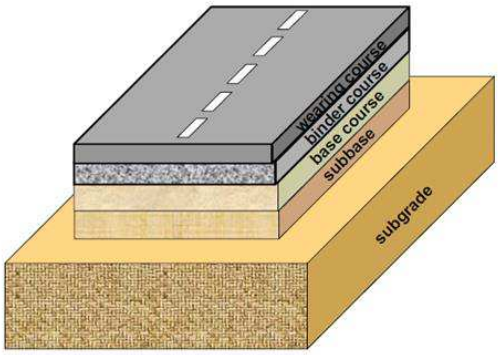

Figure 2.2. Scheme of the flexible pavement layers.

2.2 Interlayer bonding

2.2.1 Importance of a good interlayer bonding

The interlayer bonding is generated by the interlocking of the aggregate particles at the interface, the friction between the surfaces of the two bituminous layers and the adhesion between the asphalt binder of the two layers. The role of the interlayer bonding is to prevent relative movements between the layers in contact allowing the transfer normal and horizontal stress from the surface to the lower layers of the pavement. The importance of the interlayer bonding has increased significantly in recent years due to the increased loads on roads.

Nowadays, it is widely recognised that interlayer bonding conditions between bituminous layers directly influence the overall pavement performance. Indeed, a proper interlayer bonding is fundamental for transferring normal and shear stresses throughout bituminous layers, providing to the pavement structure the intended load-bearing capacity. On the contrary, in the case of poor bonding, the loads cannot be transferred throw the layers because the pavement can no act as a monolithic structure, and this fact causes a high concentration of load stress on the upper layers (Figure 2.3).

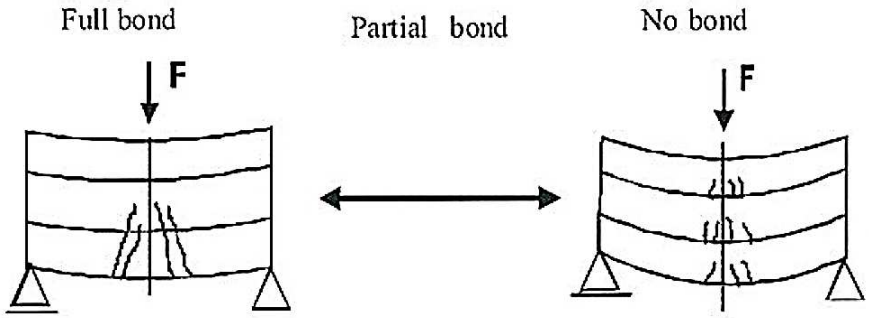

Figure 2.3. Redistribution of stresses in a multilayer system due to the loss of bonding between the layers (Raab et al., 2009).

Poor bonding between layers has a negative effect on pavement performance especially in braking and turning areas or in steep grades, i.e., in areas where there are high shear stresses (Romanoschi and Metcalf, 2001). The existence of poor interlayer bonding between the upper layers may lead to several distresses, such as slippage cracking, delamination and fatigue cracking (Al Nageim and Al Hakim, 1999; Mohammad et al., 2009; Tozzo et al., 2014a; Uzan et al., 1978) which, in turn, may result in premature pavement failure. Poor interlayer bonding could reduce pavement life to as low as 40% (Romanoschi and Metcalf, 2001). A brief description of these bituminous pavement distress type induced by poor bonding is given below.

Slippage cracking is defined as cracking that resembles crescent shapes in the direction of traffic (Figure 2.4). It is produced when braking or turning wheels cause the pavement surface to slide or deform. This distress is a visible indicator of inadequate bonding between wearing and binder layers in bituminous pavements where high horizontal stresses occur. Delamination is an area of pavement surface missing, typically one layer thick (i.e., the thickness of the wearing course), due to the loss of adhesion between the wearing and underlying layers (Figure 2.5). Delamination can propagate more quickly if the water is forced along the interface between two layers by hydrostatic pressures imposed by traffic loads. Fatigue cracking is considered one of the major causes of failure for flexible pavements (Figure 2.6). Fatigue failure is defined as a failure resulting from the repetitive action of traffic loads. But the debonding or loss of bond strength between two bituminous layers may provoke early fatigue cracking reducing the fatigue life of the pavement since the loss of structural integrity accelerate the propagation of cracking (Shahin et al., 1986; Willis and Timm, 2006). West et al. (2005) proved that a 10% decrease in bond strength could result in a 50% reduction in fatigue life. Other study showed that the fatigue life for a fully debonded pavement could decrease drastically and could prompt the need for repairs such as full-depth patches or complete reconstruction (Romanoschi and Metcalf, 2001).

A diagnose of a debonding failure is evident in the case of slippage failure or delamination, but in the case of fatigue cracking, it is not so clear since the cracks generated by a debonding effect could be indistinguishable from other forms of surface cracking generated by other causes (i.e., top-down cracking, bottom-up cracking).

Since the service life of multilayer bituminous pavement strongly depends on the interlayer performance, a correct understanding of the interlayer bonding is necessary to prevent any bond-related problems.

Figure 2.4. Slippage cracking.

Figure 2.5. Delamination.

Figure 2.6. Fatigue cracking.

2.2.2 Theoretical and modelling investigation on interlayer bonding

Computer-based analysis tools are useful to estimate the stresses and strains of road pavement and predict pavement distresses. Under traffic loading, the road pavement is subjected to a complex stress path. Figure 2.7 shows the distribution of vertical and shear stresses along the pavement depth direction. Unlike vertical stresses, the maximum shear stress value is not at the pavement surface. Using finite element (FE) analysis, Su et al. (2008) showed that shear stress peaks are at around 60 mm below the surface. Analogously, Zou et al. (2013) found out that the maximum shear stress values are between 40 mm and 60 mm below the surface. The values of normal and shear stresses decrease gradually with increasing depth. In particular, the shear stress decreases faster than the vertical stress as the depth increases (Powrie et al., 2007) and, therefore, the ratio of shear stress to the vertical stress decreases

with increasing depth. Along the traffic direction in a straight section, during a loading cycle, the vertical stress increases from zero to a peak value and then decreases to zero (Cho et al., 2017a). Whereas, in general, the shear stress changes not only in magnitude but also reverses in direction at the same time, leading to the rotation of principal stress axes (Diakhaté et al., 2006; Ishikawa et al., 2011; Liu and Hao, 2011; Tang et al., 2015). The maximum shear stress can be found at the outer tire edges and the level of shear stress depends mainly on surface layer thickness (i.e., a high level of shear stress is generated for very thin layers) (Akhtarhusein et al., 2004; D'Andrea and Tozzo, 2016; Petit et al., 2009). In correspondence to the shear stress peak, the shear stress value is about equal to the vertical stress (Romanoschi and Metcalf, 2001). D'Andrea and Tozzo (2016) showed that shear stress equals or exceeds the normal stress at about 2 cm beyond the wheel edge. However, stress and deformation conditions change during braking or acceleration of vehicles or in cornering sections. For instance, the level of shear stress is 100% more in a curved road section than in a straight section (Petit et al., 2009). Wang et al. (2018), using BISAR software, showed that the maximum shear stress is located at the front tire during vehicle braking. Contrarily, Cho et al. (2017a), using LVECD software, found out that both maximum normal stress and shear stress occur at the centre of the tire under the braking condition (Figure 2.8).

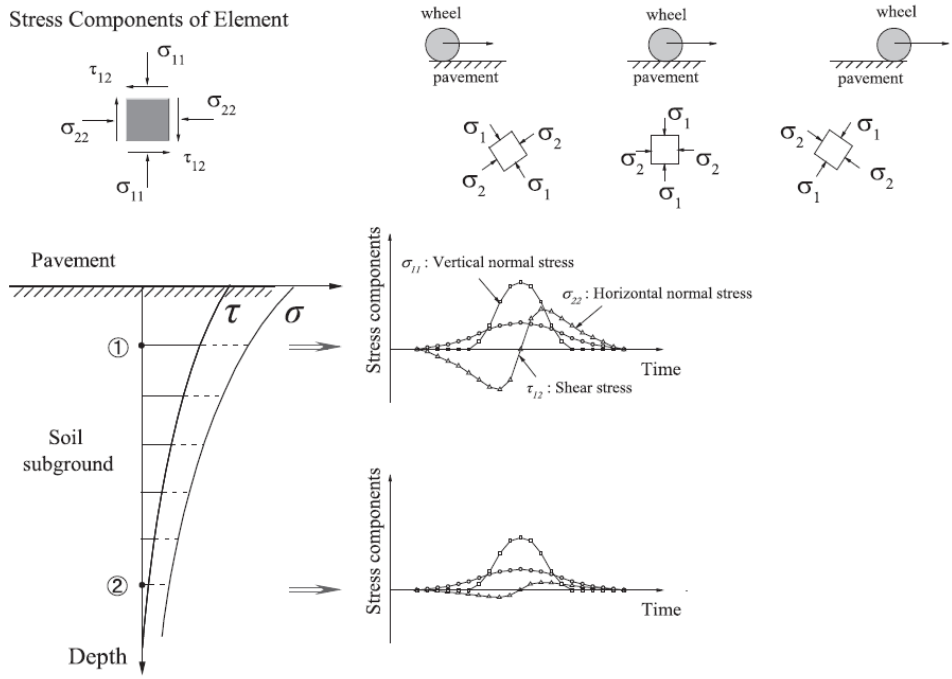

Figure 2.7. Stress components induced by traffic loading (Wu et al., 2017).

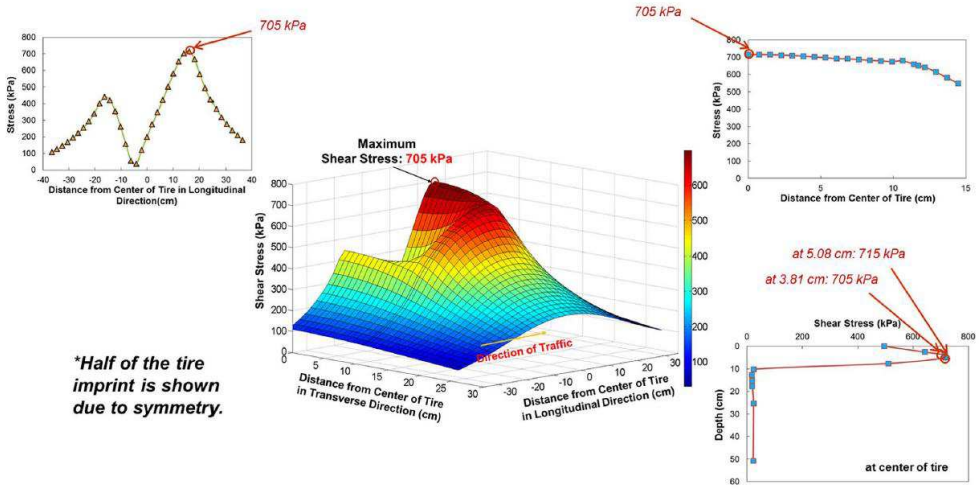

Figure 2.8. Shear stress distribution in 3D space for thin pavement during braking condition (Cho et al., 2017a).

It should be pointed out that an accurate stress field simulation is very difficult if not impossible since the situations really experienced in-situ is quite variegated and imponderable (Romanoschi and Metcalf, 2001). In the literature, many investigations are based on linear elastic multilayer models that assume loads acting only in vertical direction on the pavement surface (Al Hakim et al., 2000; Al Hakim, 2002; Al Nageim et al., 1996; Al Nageim and Al Hakim, 1999; Brown and Brunton, 1984; Khweir and Fordyce, 2003; Romanoschi and Metcalf, 2003; Uzan et al., 1978). But since the traffic loads on road pavement include both vertical loads (normal to the pavement surface) and shear loads (tangent to the pavement surface), some modelling efforts were carried out adding horizontal loads to normal loads on the pavement surface. These studies showed that the simultaneous application of normal and horizontal loads generate a stress-strain condition more severe in the pavement (Hachiya and Sato, 1997; Romanoschi and Metcalf, 2001; Romanoschi and Metcalf, 2002; Shahin et al., 1987).

In terms of strain distribution, Romanoschi and Metcalf (2001; 2002) stated that when horizontal load act on the top of the pavement structure, the strains, originated in correspondence of the surface, control the pavement life reducing its service period.

In terms of stress distribution, Hachiya and Sato (1997) showed that the shear stress at the uppermost interface becomes larger if horizontal surface forces are considered, increasing its value when the magnitude of horizontal loads increases. Moreover, it has been shown that an increase in layer thickness reduces the interlayer shear stress also since the interface has been moved down.

However, it should be pointed out that multilayer elastic analysis may result in erroneous pavement response calculation and performance prediction. In fact, it is unable to capture and predict several important pavements response and distresses (i.e., top-down cracking and permanent deformation) (Ali et al., 2008; Elseifi et al., 2006; Liao and Sargand, 2010; Wang and Al-Qadi, 2009). Nowadays, the use of three-dimensional (3-D) viscoelastic finite element (FE) pavement model allows to better simulate the behaviour of a real pavement system at the interface. Since they allow to characterise the bituminous pavements as viscoelastic materials and allow to consider dynamic traffic loads. In this regard, Hu et al. (2017) simulated dynamic wheel loading conducted three case scenarios (accelerating, steady rolling, and braking traffic) on the pavement using ABAQUS three-dimensional finite element (3-D FE) modelling (Figure 2.9a). They found out that the maximum shear stress occurs during tire braking, as would be theoretically expected (Figure 2.9b), as well as during turning (e.g., tire inclination angle from 0° to 10°). This suggests that intersections and stop-go sections with braking and stopping vehicles are more subjected to shear stresses. Thus, these areas should be designed with more attention to the shear strength characterisation. The same considerations can be carried out in the landing and braking areas of airports (White, 2016). Using a mechanistic analysis, Horak et al. (2009) showed that shear stress during a severe aircraft braking event can be up to 68% of the vertical stress.

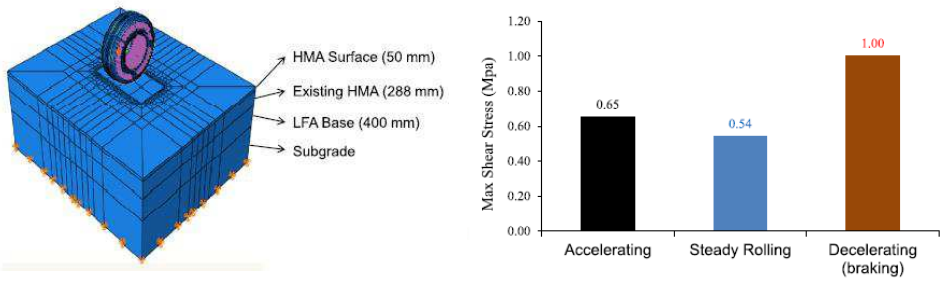

(a) (b)

Figure 2.9. (a) Pavement ABAQUS model and (b) maximum shear stresses for accelerating, steady rolling, and decelerating (Hu et al., 2017).

To understand the role of the interlayer bonding in a multilayer bituminous system, several computational analysis methods have been carried out. The study conducted by Romain (1968) was, perhaps, one of the first examples of evaluation of the interlayer bonding effect in a bituminous pavement. In order to show the effect of bonding on stresses, strains and deflections, Romain considered full bonded and fully slipped interfaces. Figure 2.10 shows the four-layer structure adopted by Romain (1968) as shown by Uzan et al. (1978). They showed that tensile strain increases at the bottom of the layer close to the interface with poor bonding.

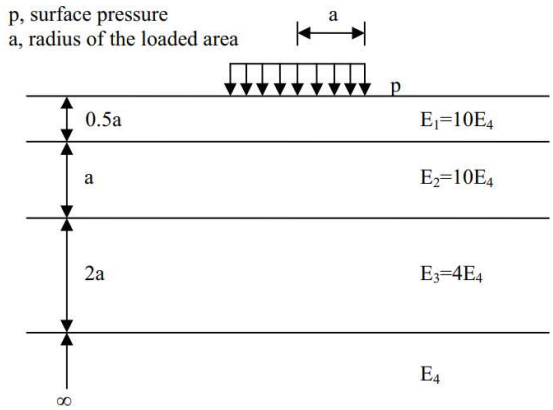

Figure 2.10. Scheme of the four-layer pavement studied by Romain (Uzan et al., 1978).

Ten years later, Uzan et al. (1978) proposed a similar study using a four-layer structure model loaded with a uniform pressure distribution p of radius a (Figure 2.11). The interlayer mechanical behaviour was modelled using the assumption that the interface can be described by elastic theory and considered as a thin material with shear modulus G and thickness h. The interlayer shear stress τ, generated by traffic loads, causes a relative shear displacement $\Delta\xi$ between the two layers. The relationship is expressed as follow:

$$\tau = G \cdot \frac{\Delta\xi}{h} = G \cdot \gamma \tag{2.1}$$

where γ represents the shear strain of the thin interface material. From Eq. (2.1), it is possible to obtain Goodman's constitutive law that describes the interface behaviour in multilayer elastic systems, as follows:

$$\tau = K \cdot \Delta\xi \tag{2.2}$$

where K (equal to G/h) represents the shear stiffness expressed in MPa/mm or kPa/mm.

The parameter K was assumed to be a characteristic value to measure the level of interlayer bonding. Uzan et al. (1978) studied different K-values for the uppermost interface (from $K = 0 \rightarrow$ perfectly smooth, to $K = \infty \rightarrow$ perfectly rough) of a three-layer system on soft subbase. They found that the most considerable change in stress and strain values at the bottom of the upper layer occurred when K varied between 1 and 10^2 MPa/mm. Moreover, they showed that when the K-value increases, the strain approaches the value computed for a perfectly rough interface. This increase in K-value, and thus in interlayer bonding, produces a decrease in the tensile strain at the bottom of each layer and an inversion in the strain sign at the top of the layers (Figure 2.12). When the full-bond between all the pavement layers is assured, the maximum tensile strain is located at the bottom of the pavement. On the contrary,

if one or more interfaces are not completely bonded, as usually happens, high tensile strains rise at the slipping interfaces. At the end, when complete debonding is achieved, the slippage at the interface raises until the layers act independently. For modelling purposes, Al Hakim (2002) identified two limiting values for K, where K below 10^{-2} MPa/mm represents the perfect slippage condition (complete debonding), and K above 10^{2} MPa/mm indicates perfect bonding.

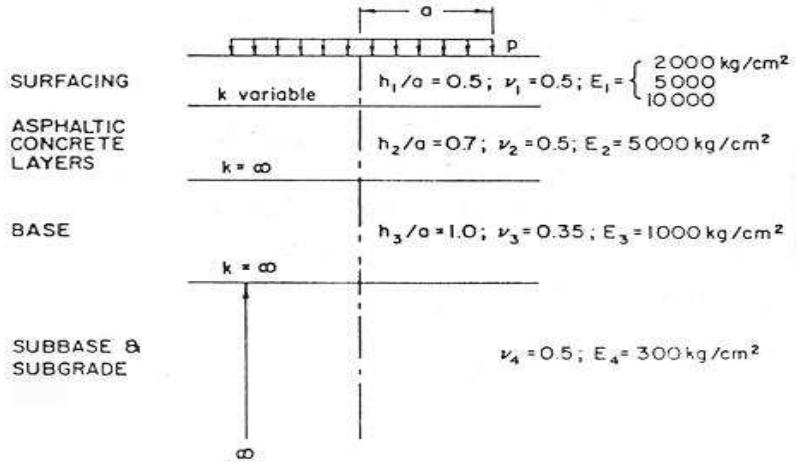

Figure 2.11. Scheme of the pavement studied by Uzan et al. (1978).

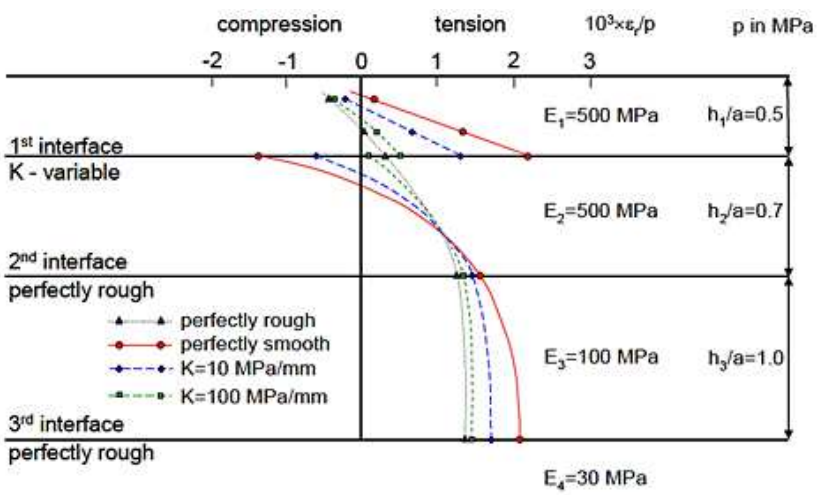

Figure 2.12. Distribution of strain vs depth (Uzan et al., 1978).

Successively, many studies showed that pavement service life decreases when a certain level of debonding occurs at the uppermost interface, both with (Hachiya and Sato, 1997; Jaskula and Rys, 2017; Romanoschi and Metcalf, 2001; Shahin et al., 1987) and without (Al Nageim and Al Hakim, 1999; Brown and Brunton, 1984; Khweir and Fordyce, 2003; Kruntcheva et al., 2005; Shahin et al., 1987) horizontal loads.

Also using 3-D FE models (i.e., viscoelastic layered medium and a moving load), recent studies showed that if the interlayer bonding is inadequate, the strains throughout the pavement may increase significantly and, therefore, negatively impact the pavement service life (Chun et al., 2015; Chupin et al., 2010; Hu and Walubita, 2011; Li et al., 2017; You et al., 2018). As regards stress distribution, Wang and Al-Qadi (2010) showed that debonding between layers significantly increases shear stresses inducing to premature failure.

Based on the literature review, flexible pavements are usually considered as an elastic multilayer and most of the pavement models assume two extreme interlayer conditions: full-bond (i.e., no sliding) or no-bond (i.e., sliding or no friction). It is worth noting that these two conditions are not realistic in the field since there is neither complete slipping between the layers nor is the interlayer shear strength close to the bond strength of the adjacent materials. According to Kim et al. (2011), the interlayer bonding conditions of real pavements appear to be at an intermediate level between full-bond and no-bond condition, that is partial-bond. That is, the interlayer bonding is actually partial-bond and depends on the interlocking strength.

While significant efforts have been carried out on this subject, the real understanding of the interlayer stress time history induced by traffic loading in road pavements is not properly captured. To date, most of the flexible pavement design methods still consider full bonded conditions at the interface between layers and the interlayer bonding is not modelled as a failure mechanism (Diakhaté et al., 2011). It is imperative to incorporate the interlayer bonding failure into pavement design methods for improved accuracy.

2.2.3 Factors affecting interlayer bonding

It is well known that interlayer bonding is related to a large number of factors, such as:

- type of materials (e.g., mixture type, binder type, aggregate texture);
- construction characteristics (e.g., tack-coat, compaction/voids, contamination, reinforcement);
- loading/environmental aspects (e.g., traffic speed, temperature, ageing process).

All these factors should be taken into account during the design process. The following is an overview of the influence of these factors on the interlayer bonding.

Type of materials

One of the most influential factors is the type of materials used for pavement construction. Several studies showed that a correct mix design is crucial to achieving a good interlocking at the interface (Canestrari et al., 2005; Jaskula and Rys, 2017; Mohammad et al., 2011; Raab and Partl, 2004; Raab et al., 2012; Sholar, 2004; West et al., 2005). Also, the type of bitumen of the wearing course can affect the interlayer bonding (Nicholas, 1979; Peattie, 1979).

Several studies showed that also surface roughness and texture are influential factors (Ktari et al., 2016a; Ktari et al., 2017). It was demonstrated that a higher strength is obtained for milled surface (Canestrari et al., 2005; Leng et al., 2009; Mohammad et al., 2008; Recasens et al., 2005; Recasens et al., 2006; Santagata et al., 2009; Tashman et al., 2008). Other studies showed that different conditions of lower layer surface roughness affect interlayer shear resistance (Buchanan and Woods, 2004; Sholar, 2004; West et al., 2005).

Construction characteristics

Several investigations (Carr, 2001; Collop and Thom, 2002; Mirò Recasens et al., 2003; Partl and Raab, 1999; Partl and Raab, 2004) showed that the interlayer shear strength of the uppermost interface is strongly influenced by the air void content of the wearing course. In fact, a well compacted upper bituminous layer leads to higher maximum interlayer shear strength. Santagata et al. (2008) argued that a high air void content (8–9%) leads to having a weak interface, but also with a low air void content (such as 4%) is hard to achieve an adequate interlock between the two layers in contact. As regards the base course, some works (Kennedy, 1978; Peattie, 1979) showed that if the base course is composed of specific type of materials (i.e., wet-mix macadam or dry-bound granular material), laid under particular conditions (i.e., inappropriate moisture content), the pavement structure is more subjected to slippage cracking. The low compaction of the lower layers of the pavement can lead to a low stiffness of the layers themselves. This occurrence could generate a weak zone at the interlayer, that gradually results in a material degradation easily vulnerable to water damage that speeds up the loss of cohesion and thus loss of other material (Al Hakim et al., 2000; Jaskula and Rys, 2017; Khweir and Fordyce, 2003; Nicholas, 1979; Peattie, 1979; Sudyka et al., 2018).

The individual bituminous layers of the flexible pavement are usually connected through a tack coat. Tack coat can include straight run bitumen or bitumen emulsion. Bitumen emulsion can be manufactured from conventional or polymer modified bitumen. The tack coat application increases the interlayer bond strength between two layers since promoting the adhesion between the layers in contact (Canestrari and Santagata, 2005; Jaskula, 2014; Tayebali et al., 2004; West et al., 2005). But, Mohammad et al. (2005) showed that the tack coat increases the interlayer bonding strength at 25 °C but the tack coat had no effect or even negative effect on the bond strength at 55 °C. Besides, the application of modified emulsion significantly increases the interlayer bonding strength compared to a tack coat of unmodified

emulsion (Augustin, 1997; Canestrari et al., 2005; Hachiya and Sato, 1997; Mirò Recasens et al., 2003; Mirò Recasens et al., 2005; Rabiot and Morizur, 1996; Struthers and Richardson, 2002) and non-tack-coated interfaces (Augustin, 1997; Canestrari et al., 2005; Struthers and Richardson, 2002). It should be also underlined that the tack coat application rate influences the level of bond strength that could be achieved. A high rate could weaker bond, thus the application rate to apply has to be optimised in order to achieve the optimum bond strength (Buchanan and Woods, 2004; Jaskula and Rys, 2017; Kruntcheva et al., 2006; Leng et al., 2008a; Uzan et al., 1978; West et al, 2005). For instance, the British standard BS 594-2 (2002) provide a tack coat application rate as a function of the bitumen content of the asphalt layers for both new construction and existing pavement. Mohammad et al. (2011) found that the influence of tack coat type and application rate became more relevant in thin pavements and less dominant in thick pavement structures. Bitumen emulsion curing time is another factor that should be taken into consideration (Chen and Huang, 2010; Destrée et al., 2016; Hachiya and Sato, 1997; Hasiba, 2012).

It should be borne in mind that the surface conditions of the underlying layer are also very important because they influence the interface bonding strength. Presence of water and dirt on the existing surface generally resulted in lower shear strength. Thus, it is recommended to apply tack coat on a clean, dry and well-compacted underlying layer.

Several studies showed that the introduction of geosynthetic at the interface usually reduces the interlayer shear resistance (Canestrari et al., 2006; Ferrotti et al., 2011; Pasquini et al., 2013; Ragni et al., 2020).

Nowadays, many researchers are still studying in the laboratory as the application rate of the tack coat affects pavement performance. The issue related to laboratory study is that the various conditions occurring in-situ are difficult to take in concern (humidity rain, wind, contaminated of the interface). Besides, Jaskula (2014) found out that interlayer bond strength between bituminous layers also depends on the laboratory compaction technique, as well as the compaction effort. The highest bond strengths were obtained for gyratory compaction and the lowest ones for compaction with a static roller.

Loading/environmental aspects

Laboratory studies that varied the normal pressure applied to a sample (Uzan et al., 1978; West et al., 2005) have all concluded that as normal pressure increases the interlayer bond strength increases. This implies that although a heavier load is more likely to produce higher horizontal stresses making slippage failure more likely, it is also likely to provide higher normal stress, which increases resistance to slippage failure.

As it is well known, the temperature is also an important influence parameter. The increased or decreased temperature would change the characteristic of asphalt concrete as well as interlayer bonding. Laboratory studies (Canestrari and Santagata, 2005; Deysarkar and Tandon, 2005; Leng et al., 2009; Sholar, 2004; West et al., 2005) showed that increasing the temperature leads to decrease on the interlayer shear strength for any interface treatment

(with or without tack-coat). This indicates that the interlayer failure is more critical at high temperatures. Interlayer bond strength at low temperature is also critical. Tschegg et al. (1995) and Mirò Recasens et al. (2005) showed that low temperatures (below 0 °C) leads to, also in presence of tack-coat, lower interlayer resistance. Mirò Recasens et al. (2005) supposed that this interlayer bonding behaviour could depend on the Fraass brittle point of the emulsion bitumen. Canestrari and Santagata (2005) found out that the effectiveness of tack-coats becomes negligible below 10 °C.

Raab and Partl (2009) studied the long-term performance of bonding properties of binder, base and subbase layers of asphalt pavements. They found out ageing could have a positive effect on the bonding properties.

2.3 Methods for measuring the interlayer bonding level

Despite the importance of interlayer bonding condition, the pavement design methods currently lack a standardised approach internationally recognised to characterise interlayers. One of the main reasons is that the laboratory characterisation of bituminous interlayers is a challenging issue because of the difficulty of establishing loading conditions that can simulate field behaviour (Figure 2.13).

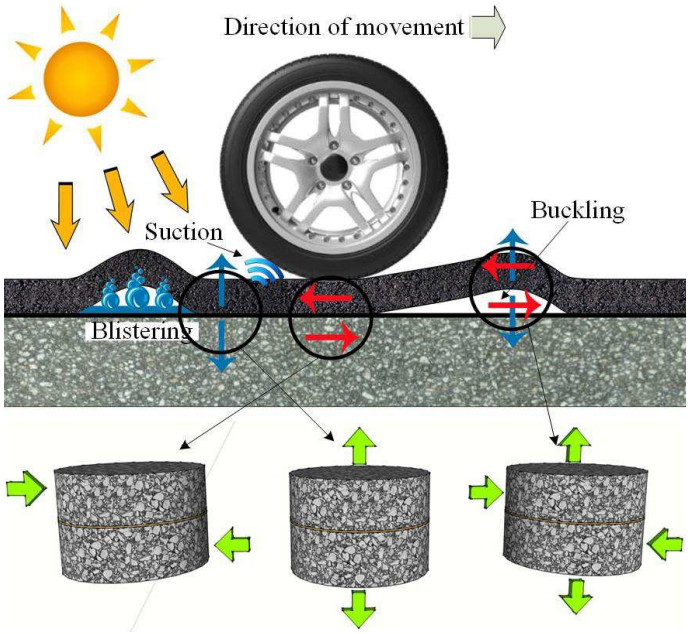

Figure 2.13. Mechanisms of interlayer bonding failure (Sudarsanan et al., 2015).

During years, many countries have developed methods and equipment for testing the interlayer bond of bituminous layers (Canestrari et al., 2013; Petit et al., 2018a). Due to this testing variety, it has been proved that the measurement of interlayer bonding also depends on testing method and device. Testing devices for the measurement of interlayer bonding can be categorised into two main groups:

- static bond testing;
- dynamic/cyclic bond testing.

The main difference between these testing devices is the modality of the application of load/displacement.

2.3.1 Static bond testing

So far, static bond testing devices have been largely used to analyse the interlayer properties. Static bond testing consists of the monotonic application of a load, or displacement, between two pavement layers until failure and measuring the resulting resistance. The most used testing configurations are torque test, tensile test, wedge splitting test, and direct shear test (Figure 2.14) (Canestrari et al., 2013; Petit et al., 2018a). Testing configurations simulate the mode of bond failure in a certain area (e.g., failure due to tensile stresses, in case of blisters, or failure due to shear stresses). Among these testing configurations, shear testing devices are the most popular test configuration for laboratory assessment of bonding condition. Tensile and wedge splitting configuration will not be discussed in detail in the following.

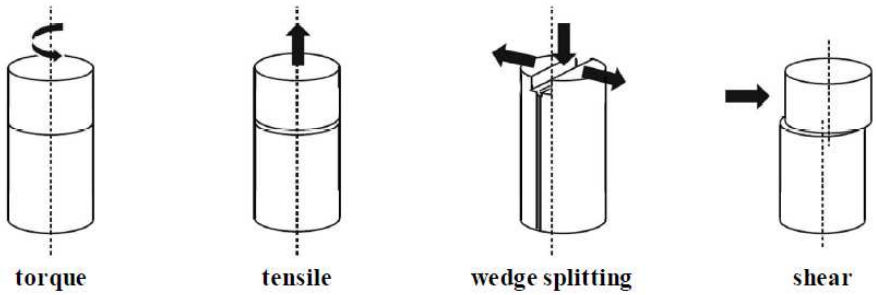

Figure 2.14. Working scheme of different test methods for the interlayer bonding measurement (Canestrari et al., 2013).

The shear testing devices are inspired by shear testing (e.g., shear box) that is used in soil mechanics. Moreover, some shear devices also allow the application of normal stress on the interface plane, in order to better simulate traffic loading. Usually, the shear test consists in the application of a shear displacement rate across the interface of a double-layered specimen and monitor the resulting shear force. While the torque test consists in the

application of a torque on the top of the double-layered specimen, that is glued or clamped to a firm base, which generates a twisting failure mechanism at the interface. The torque is applied until failure, and the measured maximum torque moment at failure is recorded. The torque test was originally developed in Sweden for the in-situ assessment of bond conditions and has been adopted in the UK to measure interface properties between the thin surfacing and the lower layer material (British Board of Agreement, 2004; Walsh and Williams, 2001). The main issue of the torque test configuration is that the failure occurs not necessarily at the interface of the double-layered specimen (Canestrari et al., 2013). Both test configurations are usually carried out on both 100-, 150- and 200-mm diameter specimens (depending on the test device).

However, it should be underlined that the static procedure entails substantial simplification of the real pavement behaviour since the traffic loads applied to the pavement are dynamic in nature. One of the main concerns with using static bond devices is if they lead to the measurement of reliable performance parameters. Using direct shear testing, the interlayer performance is typically expressed in terms of the interlayer shear strength (ISS), which is the maximum value of shear strength in a shear-displacement curve (Figure 2.15). Although the ISS is not representative of typical in-situ traffic loading conditions, it generally provides a reliable quality assessment of interlayer bonding and is commonly adopted because of its simplicity and the relatively short testing procedure (Chang et al., 2014; Rahman et al., 2017). Some technical standards report the minimum values required for ISS (e.g., 0.68 MPa between base and binder courses and 0.85 MPa between binder and wearing courses) (Pasetto et al., 2019). Obviously, the limits of ISS fixed by the technical specifications are more restrictive for the superficial layers (i.e., binder and wearing) because superficially the shear stresses are higher. However, the ISS can only be used for quality control purposes (i.e., to control the right construction) as it does not provide any information on bonding deterioration during the pavement lifespan (Raab et al., 2017).

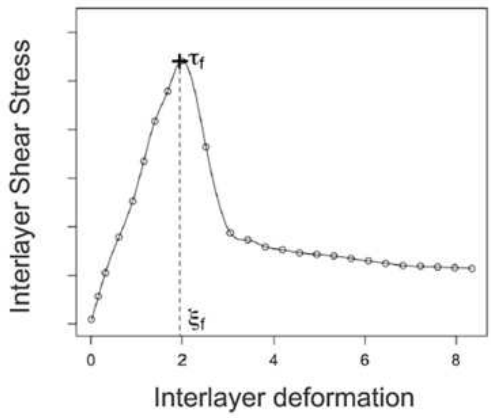

Figure 2.15. Load – deformation curve for the shear test.

2.3.2 Dynamic (cyclic) bond testing

Dynamic (cyclic) bond testing is an innovative testing approach which better simulates the loading conditions induced by the traffic. Dynamic bond testing consists of the repetitive application of a load, or displacement, between two pavement layers. Since the loads applied to the pavement surface are dynamic and the application of repetitive vehicular loading induces progressively fatigue damage and/or accumulation of permanent deformations in correspondence of bituminous pavement interlayers, dynamic (cyclic) bond testing should lead to a more realistic prediction of pavement performance. However, this disagrees with some studies that believe that the effects of interface characteristics could be assessed more accurately by static testing than by dynamic testing (Al-Qadi et al., 2008; Leng et al., 2008b). In the following, this type of test will be called dynamic bond testing or cyclic bond testing indistinctly, because the term "dynamic" is used to counterpoint it to the static test and the term "cyclic" is used to indicate that the test is based on the repetition of a load/displacement in the testing time.

Recently, technological progress has allowed the development of several cyclic interlayer bond testing devices to assess the interlayer bonding behaviour. Each laboratory optimised its own cyclic testing device and method. They differ in terms of design, loading method (stress- or strain-controlled), loading frequency, testing temperature and normal load application. These devices allow the characterisation of the interlayer response both in terms of stiffness (small strain amplitude) and resistance to repeated loading (fatigue, permanent strain accumulation). It should be noted that laboratory simulation of the shear stress at the interface is very complex and, also due to the recent development of these devices, some aspects (e.g., testing parameters) have not yet been clarified and analysed in depth.

A drawback of the cyclic testing device is that it is generally more sophisticated, and the tests are time-consuming and require a considerable computational effort to manage results. However, an important aspect that should be taken into account is that the performance parameters derived from cyclic interlayer shear testing can be appropriately used for pavement design or modelling purposes. Therefore, although this approach seems to be very effective in characterising the real mechanism experienced in-situ, so far very few bond test devices have been used in cyclic conditions. Due to the complexity of installation and configuration, as compared with monotonic modalities, very few shear testing machines have been used in a dynamic mode. A wide overview of the existing cyclic testing devices and procedure are presented below.

At the Virginia Tech, Donovan et al. (2000) developed the Virginia Shear Fatigue test to measure the number of loading cycles necessary to lead to a failure at the interface (Figure 2.16). The Virginia Shear Fatigue device is composed of two independent parts, each with a chamber. The specimen is clamped by the two chambers. A load cell and linear variable differential transformers (LVDTs) continuously measure the applied vertical stress and deflection during the testing. Tests were carried out in a displacement control mode until the failure of composite cylindrical specimens (concrete, geocomposite, hot mix asphalt). A

deflection of 0.40 mm was applied to the specimen in the form of a 0.10 s half-sine wave, followed by a rest period of 0.9 s. Fatigue failure was identified when the slope between the applied shear load and the logarithm of the number of cycles reaches zero.

The Dynamic Shear Box was developed at the University of Nottingham (Brown et al., 2001; Carr, 2001; Kruntcheva et al., 2006). This device is a direct shear box used to test double-layered slabs (320×200×120 mm^3) under cyclic shear loads combined with a constant normal load (Figure 2.17). Kruntcheva et al. (2001) stated that the disadvantage of this device is the non-uniform shear stress distribution at the interface. Brown et al. (2001) applied 1000 loading cycles (2 Hz frequency) on several specimens for each imposed stress level. The load increase occurred in successive steps until the specimen ruptured. The vertical stress was kept constant and equal to 200 kPa throughout the test and at each stage of the test, the interlayer stiffness was determined by measuring the shear strain, using displacement transducers. The results showed that the deformation does not increase linearly with the shear stress applied, i.e., the shear stiffness varies with the stress level.

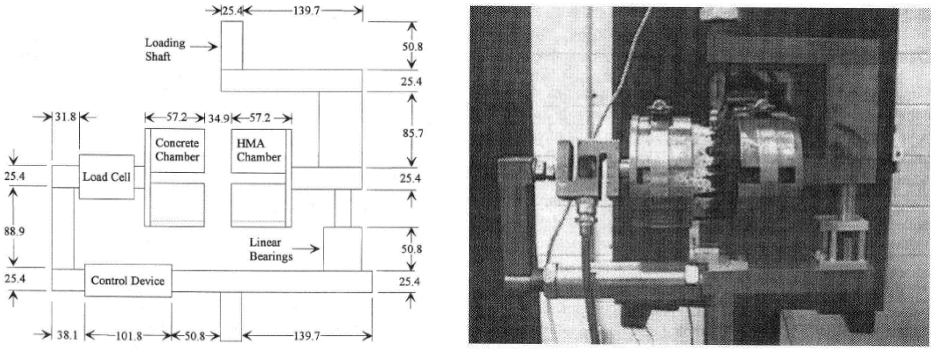

(a) (b)

Figure 2.16. Virginia Shear Fatigue device: (a) schematic view and (b) picture.

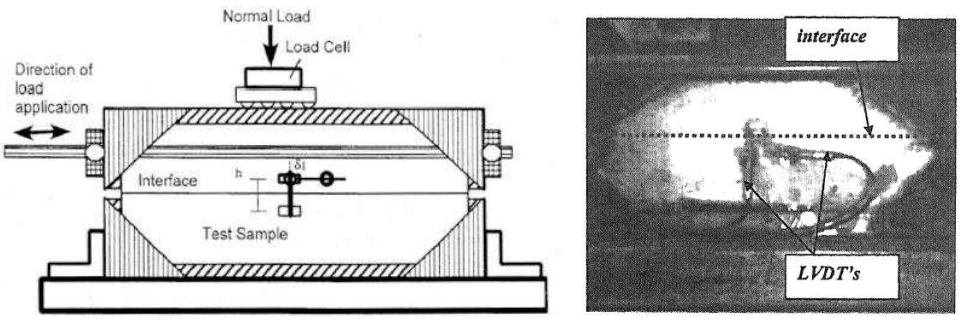

(a) (b)

Figure 2.17. Dynamic Shear Box device: (a) working scheme and (b) position of LVDTs.

Romanoschi and Metcalf (2001) proposed a Shear Fatigue Tester (Figure 2.18) where the longitudinal axis of the specimen forms an angle of 25.5° with the vertical direction, in order to have the shear stress proportional to the normal stress and equal to half of its value. Specimens were tested applying a haversine load (vertical to the loading machine) with a frequency of 5 H at a room temperature of 25 °C. Elastic and permanent displacements at the interface in normal and tangential directions and minimum vertical forces were recorded for each cycle. The tested specimens did not show a failure, not even for a high number of cycles. The fatigue tests were stopped when the permanent shear displacement at the interface was equal to 6 mm or when it was considered that the number of cycles corresponding to permanent deformation of 6 mm could be extrapolated. The fatigue tests indicated a linear increase of the permanent shear displacement with the number of cycles. The number of cycles that produces an increase of permanent deformation of 1 mm was assumed to be a valuable parameter for a comparative evaluation of the fatigue properties of the asphalt-to-asphalt interfaces.

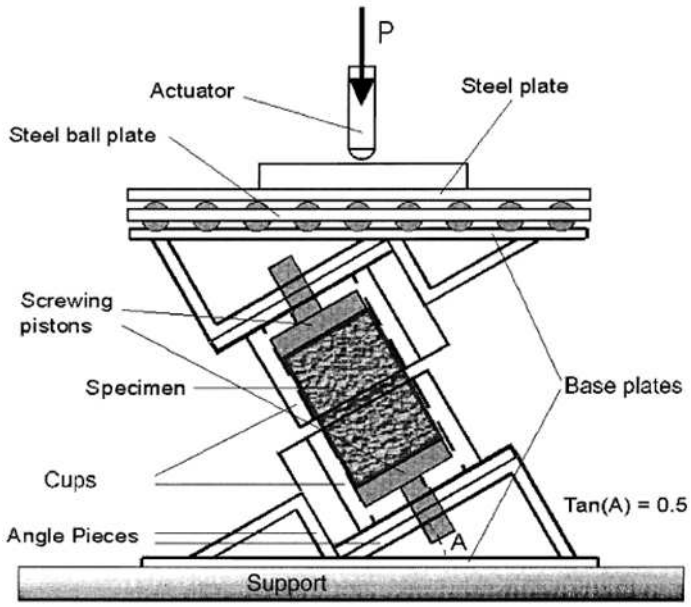

Figure 2.18. Working scheme of Shear Fatigue Tester.

Bognacki et al. (2007) investigated some asphalt pavement slippage failures that occurred at Newark International Airport by testing cores with the Superpave Shear Tester (SST) since a dynamic pulse-load test better simulate the pavement/airfield loading conditions. The SST is able to apply cyclic loads in both the vertical and shear directions to the specimen, simultaneously. In that study, tests were carried out using the Constant Stress

Ratio mode to potentially allow the change in sample height when a failed interface lets the top and bottom lifts to slide over the top of each other. A pulse load of 0.5 s followed by a rest period of 1 s was applied cyclically to the specimen with a stress ratio of 1.25 (vertical stress = 18.75 psi; horizontal stress = 15 psi). Tests were conducted at a temperature of 38 °C (100 °F). The tests were analysed by plotting the shear and axial permanent strains as a function of the number of cycles. The fatigue failure was identified with the sudden change in both the shear and vertical strains evolution.

At the University of Limoges, a Modified Compact Shearing (MCS) device was developed to study the shear fatigue behaviour of different asphalt mixtures and tack coat materials (Diakhaté et al., 2006). The machine was used on prismatic specimens (70×30×100 mm^3), formed by three parts, obtained by gluing back to back two samples of the same couple of layers. Fatigue tests were performed at 1 Hz and 5 °C applying a repetitive displacement, which generates an alternative cyclic shearing load the interface. Because of the low rigidity of the test frame, a new device named Double Shear Test (DST) was developed by Diakhaté et al. (2011) to measure the number of loading cycles required to cause failure at the interface (Figures 2.19 and 2.20). The DST device allows the application of a sinusoidal force on a prismatic specimen including two interfaces. Fatigue testing was carried out at one frequency (10 Hz) and two temperatures (10 °C and 20 °C), and the 50% reduction of the initial value of interlayer shear stiffness was employed as a failure criterion. Boudabbous et al. (2013) used the DST device, in both force and displacement control mode, on specimens with notches at the interface. To analyse the fatigue process, in addition to the conventional approach, the dissipated energy approach was used. Results showed that the change of dissipated energy in each loading cycle could be used as a damage indicator for both damage and failure.

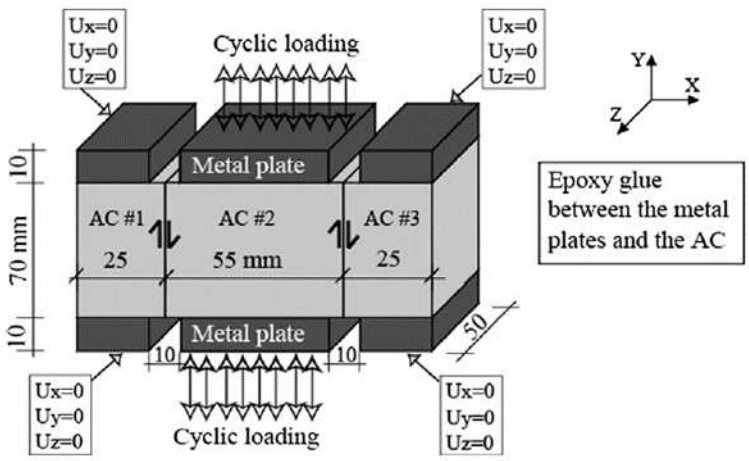

Figure 2.19. Schematic diagram of the Double Shear Test (DST) device.

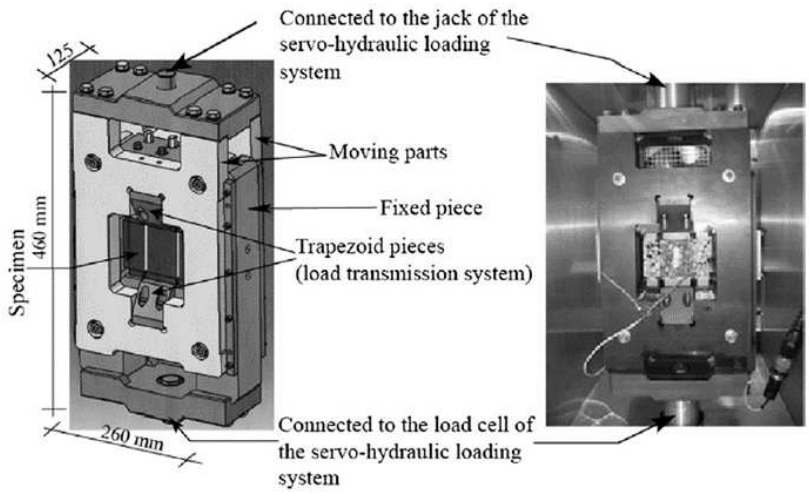

Figure 2.20. Schematic presentation and picture of the Double Shear Test (DST) device.

At the Technical University of Dresden (Germany), Ascher and Wellner (2007) and, subsequently Wellner and Hristov (2015), modified the Leutner shear test (Leutner, 1979) to perform cyclic shear testing. The Cyclic Testing of the Interlayer Bond (CTIB) was designed to apply cyclic shear force in the vertical direction and static normal force in the horizontal to asphalt concrete specimens (Figure 2.21). The specimen was placed and fixed into two jowls (Figure 2.21a) separated by a gap of 1 mm. The sinusoidal shear cyclic loading was applied to one layer of the specimen by the hydraulic cylinder of the servo-hydraulic testing machine. Cyclic shear tests were performed at different temperatures (from −10 °C to 50 °C), normal stresses (from 0 MPa to 0.9 MPa) and frequencies (from 1 Hz to 10 Hz) in the position-controlled mode. The main intent of these studies was to determine the shear stiffness at the interface at different temperatures and normal stresses under sinusoidal repeated shear loading conditions at varying frequencies. In recent studies (Hristov et al., 2016; Hristov, 2018), a master function for the shear stiffness G_s has been developed using the same testing protocol and CTIB device. A similar device (Dynamic shear bond testing) is also present at Empa (Swiss Federal Laboratories for Materials Science and Technology) in Switzerland (Raab et al., 2017).

At the Technical University of Braunschweig (Germany), using an analogous device (Cyclic Shear Test device), Isailović et al. (2017) prepared double-layered cylindrical specimens with and without tack coat application and conducted interface shear fatigue tests at a fixed frequency of 10 Hz and different temperatures (from −10 °C to 50 °C) and normal stresses (from 0 MPa to 0.50 MPa). Interlayer shear stiffness, phase angle and dissipated energy were calculated for each test, and the 50% reduction of the interface stiffness was employed as a failure criterion to build a shear fatigue function.

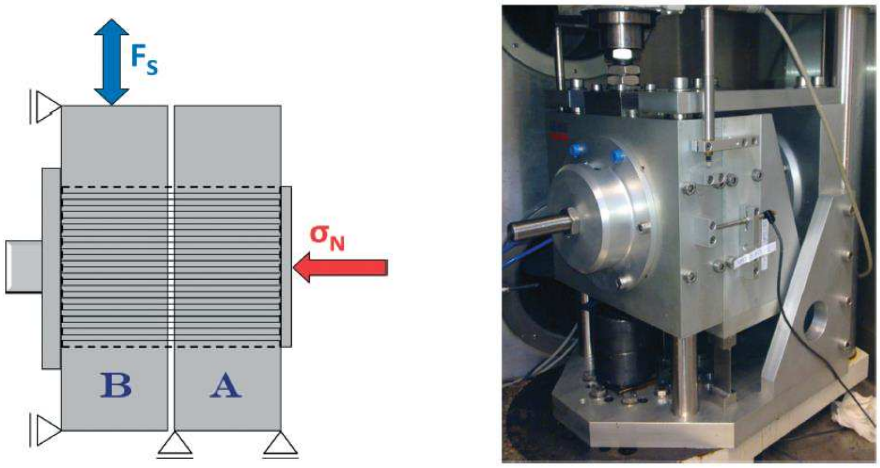

(a) (b)

Figure 2.21. CTIB device: (a) schematic representation and (b) picture of the device.

At the University of Nottingham, Collop et al. (2011) developed a laboratory-based Automatic Torque Bond test able to apply static or repeated interface loadings on double-layered cylindrical specimens of 100 mm nominal diameter (Figure 2.22). Cyclic torque tests were performed at two temperatures (20 and 30 °C) and at a frequency of 2 Hz in a stress (torque) controlled mode. The fatigue failure was defined as the number of cycles that corresponds to a 50% reduction in the normalised shear reaction modulus. Results showed a higher fatigue life of the specimens at 20 °C compared to that at 30 °C.

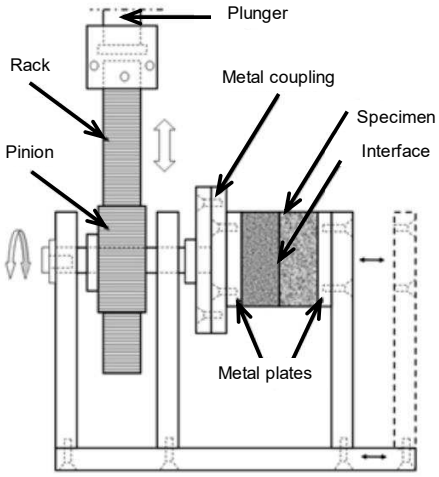

Figure 2.22. Schematic diagram of the Automatic Torque Bond test.

Two dynamic devices were developed at the Sapienza University of Rome (D'Andrea et al., 2013; D'Andrea and Tozzo, 2016; Tozzo et al., 2014a; Tozzo et al., 2014b). In the devices, named Sapienza Inclined Shear Test Machine (SISTM) and Sapienza Horizontal Shear Test Machine (SHSTM), the shear and the normal load act together on the specimen during the test. The SISTM and SHSTM are presented in Figures 2.23 and 2.24, respectively. In the SISTM, the cylindrical specimen is clamped in two half moulds, with 100 mm interior diameter. The moulds are welded on steel plates, and the inclination of these, from two horizontal plates which were hinged, is fixed with bolts and nuts at the beginning of the test series. The inclination can be varied from 0° to 45° on the horizontal plane. There is a fixed 10 mm gap between the two half moulds. The device is equipped with LVDT to measure the interface displacements, and with a ball bearing plate, to allow the lower attachment to move freely in the horizontal direction. Whereas, in the SHSTM, the sample is held horizontally in two collars. Only one collar is supported by a link; the other is free to move vertically due to a low friction guide placed on the backside of the specimen. The interface must be placed with an edge of 5mm from both sides of the collars. The loading machine applies a vertical load on the unrestricted half specimen, while a piston connected with a pneumatic compressor provides the horizontal load. The data acquisition system records the shear load and the interface displacements measured by an LVDT. For both devices, tests are usually performed applying a haversine load with a rest period at a temperature of 20 °C. The 50% reduction of the interlayer shear stiffness and the load repetitions corresponding to the interface detachment are usually employed as a failure criterion.

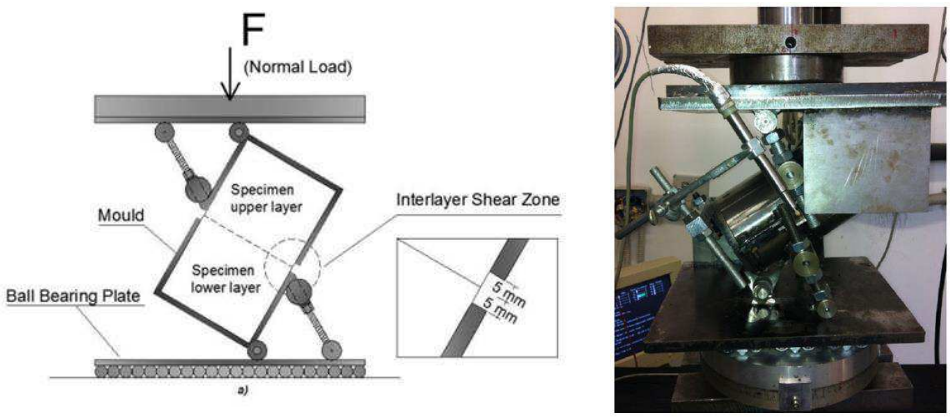

(a) (b)

Figure 2.23. SISTM: a) working scheme and b) device.

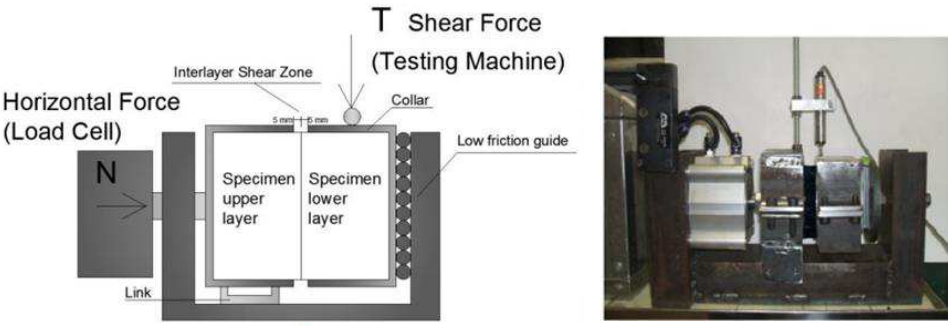

(a) (b)

Figure 2.24. SHSTM: a) working scheme and b) device.

In China, Li and Yu (2014) presented a test apparatus to perform shear fatigue test on the specimens an angle of 45° by a universal test machine (UTM), which can automatically record the load bar displacement and force for each cycle of the load application action (Figure 2.25). Fatigue tests were performed in stress-controlled mode at a frequency of 10 Hz with a sine form, and a temperature of 25 °C on multilayer deck pavement specimens.

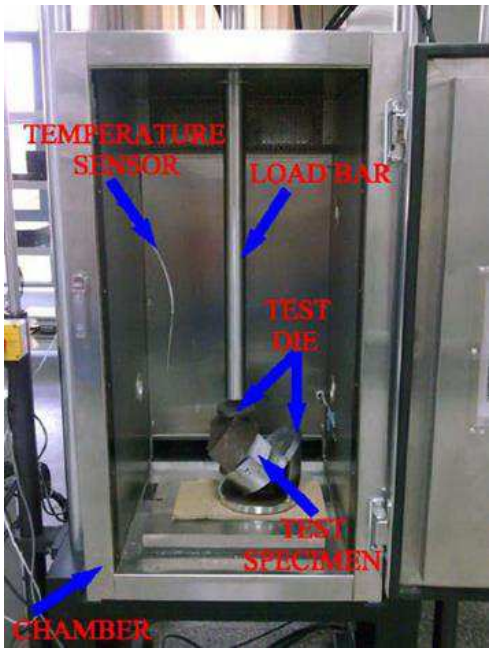

Figure 2.25. Configuration of Shear Fatigue Test apparatus.

At the Changsha University of Science and Technology (China), Li et al. (2014) developed a test apparatus (Interlaminar Shear Fatigue Tester) in which both horizontal stress and vertical compressive stress are considered (Figure 2.26). The test apparatus consists of a loading system (Material Testing System-810), briquetting, supporting block and supporting platform. The briquetting and supporting block are inclined by an angle of 26°34' to simulate the shear state of pavement structure in the case of a vehicle under braking. The test apparatus was used to evaluate interlaminar shear fatigue of asphalt overlay on the rigid pavement. Shear fatigue tests were performed in stress-controlled mode at a frequency of 10 Hz with a semi-sine form, and a temperature of 41 °C. The shear fatigue life was based on the crack initiation/propagation at the interface, which results in a sudden decrease in the modulus.

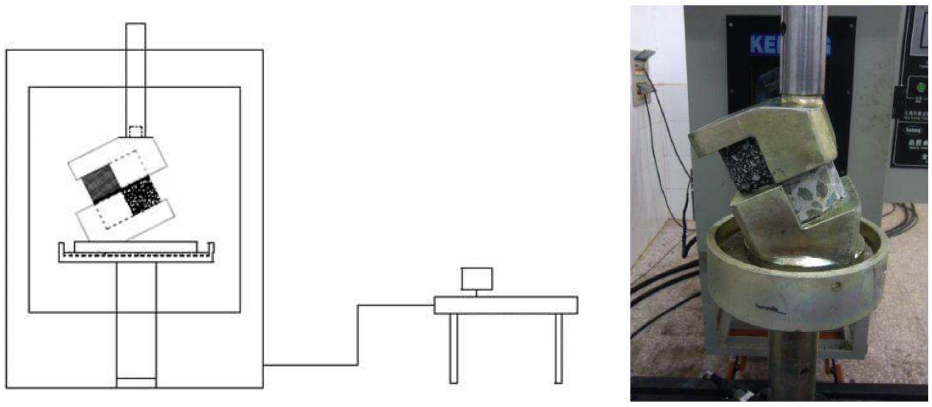

(a) (b)

Figure 2.26. Interlaminar Shear Fatigue Tester: (a) schematic diagram and (b) picture.

In Poland, Zofka et al. (2014; 2015) designed and developed the Advanced Shear Tester (AST) shown in Figure 2.27. The AST is composed of two parts (stationary holder and moving collar) separated by an adjustable gap (from 5 mm to 12 mm). The AST allows the application of bi-directional shear loading on 150-mm diameter specimens. The shear load is measured by a load cell, whereas the shear displacement can be measured using the LVDT sensor. Moreover, a confinement load can be applied by means of a system of sandwich plates connected by four die springs. Zofka et al. (2015) introduced the concept of constant normal load (CNL) and constant normal stiffness (CNS) in their study. The authors clarified that, although the CNL condition is more realistic of the two conditions, as the normal stress remains relatively constant during the shearing process, the CNS condition is more appropriate as a test condition, as the normal stress changes considerably during the shearing process. It is worth noting that the normal stress is not always constant at the top of the asphalt layer due to moving vehicle loads, especially in the case of heavy vehicles at slow speeds over thin pavement layers. Zofka et al. (2014) performed cyclic shear tests at 35 °C

applying haversine loading (load-controlled) with a frequency of 1 Hz and a rest period of 0.7 s. The loading amplitudes were equal to 60% of the interlayer shear strength obtained with monotonic tests. A confining load of 0.5 kN was also applied to the specimens. The dissipated energy was used as a parameter to analyse the fatigue testing results.

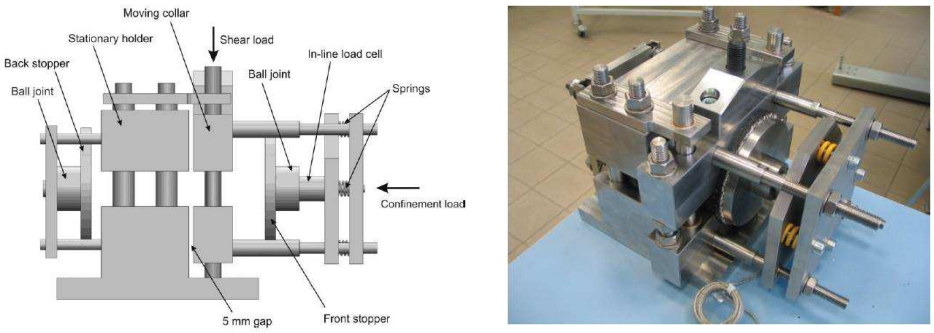

(a) (b)

Figure 2.27. Advanced Shear Tester (AST): (a) schematic view and (b) picture.

At the North Carolina State University (USA), Safavizadeh and Kim (2014) developed the Double Shear Tester (DST). The DST (Figure 2.28) as a work and design concept is very similar to the DST from Diakhaté et al. (2011). In Cho et al. (2017b), the DST was used to perform low strain cyclic shear tests at different temperatures (5, 15, 25, 35 and 45 °C) and frequencies (0.1, 0.5, 1, 5, 10 and 25 Hz) to obtain the interface shear modulus master curves and shift factors for the reinforced asphalt concrete specimens. In addition, the asphalt research team of the NCSU also developed another cyclic bond test by slightly modifying the AST design (Figure 2.27) to remove any friction that may occur between the different components involved in applying normal confining stress while maintaining all the advantages of the AST device. The new device, called Modified Advanced Shear Tester (MAST) and shown in Figure 2.29, is able to investigate the shear properties of uniform asphalt mixtures as well as interlayer interfaces in static or cyclic modality. The MAST has two sides: a fixed side and a movable side. The width of the gap between the two sides is 8 mm. The movable side is free to move vertically, parallel to the interface, as well as horizontally, perpendicular to the interface. In Safavizadeh and Kim (2017), the MAST device was used to perform cyclic tests in load control mode applying sinusoidal alternating loads at 5 Hz and 20 °C on square-shaped specimens. A normal (confining) stress of 207 kPa was also applied to specimens.

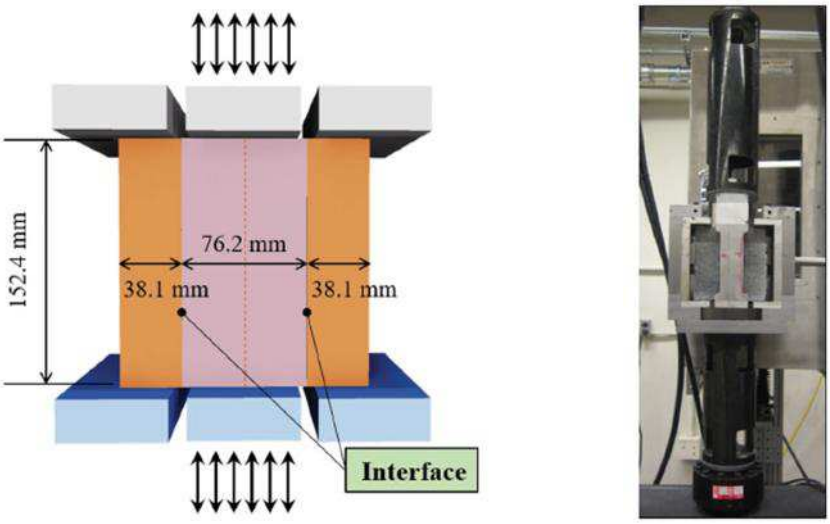

(a) (b)

Figure 2.28. Double Shear Tester (DST): (a) schematic view and (b) picture.

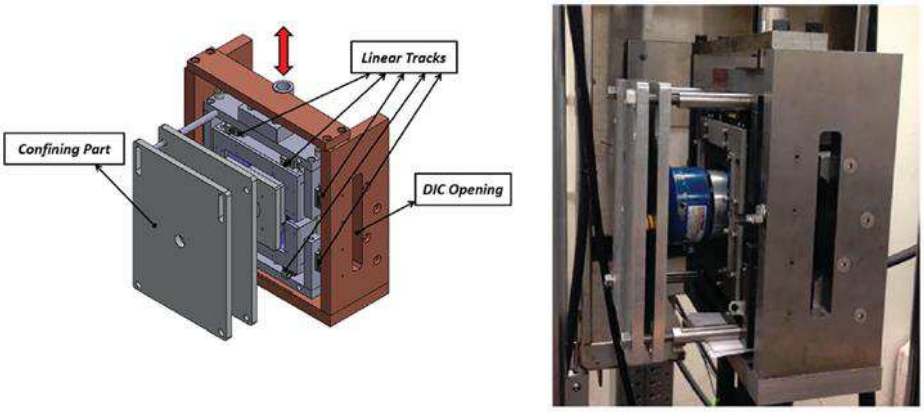

(a) (b)

Figure 2.29. Modified Advanced Shear Tester (MAST): (a) schematic view and (b) picture.

A Direct Shear Fatigue device (Figure 2.30) was developed at the University of Tennessee (USA). This device includes four semi-circular steel rings that are mounted to an MTS machine able to apply shear force in the vertical direction. Song et al. (2016) used this direct shear fatigue device to study the interlayer shear behaviour of systems composed of an open-graded friction course and the underlying layer, with different tack coat application rates. Fatigue tests were performed using sinusoidal stress at 10 Hz and 20 °C. The stress levels were chosen based on the shear strength of the composite specimens, usually, the corresponding stress ratios are approximately 0.3 and 0.6. The 50% reduction of the interlayer shear stiffness and the energy approach were employed as a failure criterion.

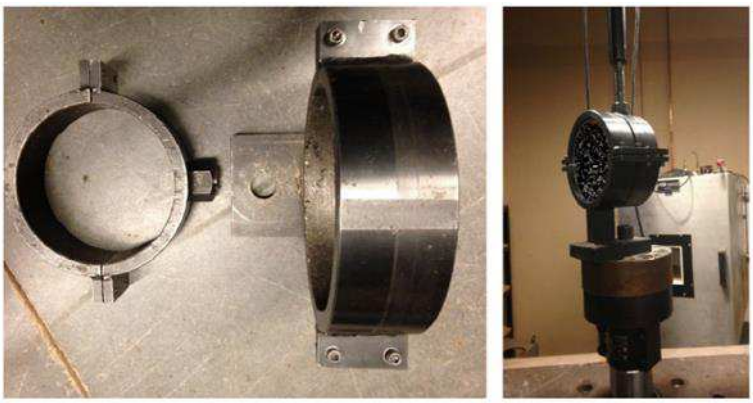

Figure 2.30. Direct Shear Fatigue device set up.

In Poland, Szydlo and Malicki (2016) conducted cyclic shear tests using the Leutner shear test (Leutner, 1979). Fatigue tests were carried out in a controlled stress mode at a frequency of 0.833 Hz with a duration of 0.24 s at a temperature of 20 °C. The dissipated energy was used to analyse the test results.

Recently, the new equipment 2T3C Hollow Cylinder Apparatus (2T3C HCA) was developed at the University of Lyon/ENTPE (France) to characterise interface performances. The 2T3C HCA (Figure 2.31) can apply independently torsion and tension/compression on hollow cylinder specimen (120 mm height, 175 mm external diameter and 125 mm internal diameter) in a monotonic or cyclic mode. Tests can be carried out in displacement- or load/couple-controlled mode. Two pairs of non-contact sensors are used to measure the global displacement between the top and the bottom of the specimen. 3D Digital Image Correlation (3D-DIC) is used to obtain local three-dimensional displacements on the surface of the specimen. To investigate the linear viscoelastic behaviour of bituminous materials, Attia et al. (2018) performed two types of tests (axial test and rotation test) using sinusoidal loadings at a small strain amplitude. Each type of test was performed at two amplitudes of displacement and four frequencies (0.01, 0.03, 0.1 and 0.3 Hz) with five cycles for each

frequency. The testing temperature was set at 20 °C. The complex modulus of the two layers, the complex interface shear modulus and Poisson's ratio were calculated to analyse the results.

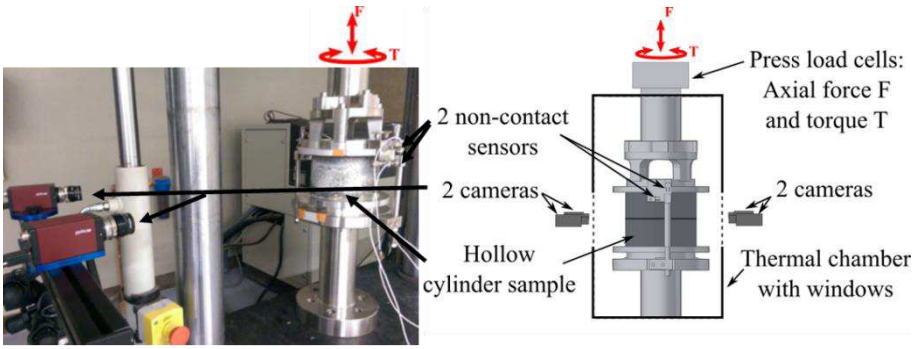

Figure 2.31. 2T3C Hollow Cylinder Apparatus.

The summary of the examined devices is shown in Table 2.1 to provide a better understanding of the variation of testing methods and conditions. Although most likely this is not a completed list, it certainly presents the state-of-the-art of dynamic (cyclic) bond testing for bituminous interlayers. The review showed that cyclic testing equipment is mostly used to evaluate fatigue resistance of double-layered specimens and the shear configuration is the most adopted. Most of these tests apply cyclic shear load parallel to the interface and compressive static normal load perpendicular to the interface. While devices adopting an inclined configuration apply both a shear load and a normal load at the interface cyclically. Since the greater part of the devices statically simulates normal load, it should be highlighted that normal stresses are not constant in the field and they vary during the loading process in the base of the loading conditions. One can also observe that there is no common understanding of the relevant test conditions. In particular, the selection of proper testing temperature is an important decision because bituminous material is very sensitive to temperature and time, in any case, it must be appropriate to situations that occur in-situ. Moreover, there is no univocal consensus on the testing mode (stress or strain-controlled), the loading application (sinusoidal or haversine, with or without a rest period, with or without normal load) and the applied loading amplitude (either stress or strain) to be adopted. This is due to the fact that various loading conditions can be experienced at the interface. In certain positions, those loadings are oriented in the same direction for all the time of the wheel passage, in other positions, they assume opposite orientations during the loading cycle. Consequently, it comes as no surprise that no method or testing procedure was established and internationally accepted for standardisation. However, it is worth saying that the chosen control mode and testing temperature can have a big impact on test results. Hence, to obtain comparable and no contradictory results among different testing devices, standardisation is needed.

Table 2.1. List of dynamic bond testing devices.

Device name	Config.	Type	Temperature (°C)	Control mode	Frequency (Hz)	Rest period	Normal load
Virginia Shear Fatigue device	shear	fatigue	not specified	haversine displ.	10	yes (0.9 s)	yes
Dynamic Shear Box	shear	fatigue	not specified	sinusoidal stress	2	no	yes (200 kPa)
Shear Fatigue Tester	shear	fatigue	25	haversine force	5	no	yes
Superpave Shear Tester	shear	fatigue	38	haversine stress	2	yes (1 s)	yes (103 kPa)
Double Shear Test device	shear	fatigue	10, 20	sinusoidal force	10	no	no
Cyclic Testing of the Interlayer Bond	shear	stiffness	-10, 10, 30, 50	sinusoidal displ.	0.1, 0.3, 1, 3, 10	no	yes (0.0, 0.3, 0.6, 0.9 MPa)
Dynamic Shear Bond Testing device	shear	stiffness	-10, 10, 30, 50	sinusoidal displ.	0.1, 1, 5, 10	no	yes (0.0, 0.3, 0.6, 0.9 MPa)
Cyclic Shear Test device	shear	fatigue	-10, 10, 20, 30, 50	sinusoidal displ.	10	no	yes (0.0, 0.25, 0.5 MPa)
Automatic Torque Bond test	torque	fatigue	20, 30	sinusoidal torque	2	no	no
Sapienza Horizontal Shear Test Machine	shear	fatigue	20	haversine stress	1	yes (0.1, 0.9 s)	yes (0 – 0.3 MPa)
Sapienza Inclined Shear Test Machine	shear	fatigue	20	haversine stress	1, 2, 5	yes (0.95 s, 0.45 s, 0.15 s)	yes
Shear Fatigue Test device	shear	fatigue	25	sinusoidal stress	10	no	yes
Interlaminar Shear Fatigue Tester	shear	fatigue	41	sinusoidal stress	10	no	yes
Advanced Shear Tester	shear	fatigue	35	haversine stress	1	yes (0.7 s)	yes (0.5 kN)
Modified Advanced Shear Tester	shear	fatigue	20	sinusoidal force	5	no	yes (207 kPa)
Double Shear Tester	shear	stiffness	5, 15, 25, 35, 45	sinusoidal strain	0.1, 0.5, 1, 5, 10, 25	no	no
Direct Shear Fatigue device	shear	fatigue	20	sinusoidal stress	10	no	no
Fatigue Leutner Shear Test	shear	fatigue	20	haversine stress	0.8333	yes (0.24 s)	no
2T3C Hollow Cylinder Apparatus	torque	stiffness	20	sinusoidal displ.	0.01, 0.03, 0.1, 0.3	no	no

Chapter 3.

New dynamic testing equipment

3.1 Introduction

This section describes in detail the design and construction of the new testing device, called Cyclic-ASTRA, for performing cyclic interface testing of bituminous interlayers as well as the methodologies adopted for the tests. This working phase was divided into several tasks:

I. concept development;
II. prototype construction;
III. prototype checking;
IV. prototype modification;
V. final device.

The various stages of conception and construction of the new device are described below in the various paragraphs. Finally, the final version of the new device is presented and described.

3.2 Concept development

The design of the Cyclic-ASTRA device was based on the available information collecting on existing dynamic interlayer shear testing, the previous research carried out using static laboratory devices (ASTRA, Leutner) as well as the draft European Standard prEN 12697-48. Figures 3.1 and 3.2 show the concept scheme of the Cyclic-ASTRA consisting of two half-boxes (T and N) separated by an adjustable gap. A cylindrical specimen (S) with a nominal diameter of 100 mm and a variable height is placed a horizontal position. The specimen is composed of two layers (i.e., double-layered specimen), separated by an interface (plane π in Figure 3.2). The specimen can be taken either directly from the field or produced in the laboratory. The half-box (T) moves on two vertical guides (V), fixed to a base (L) and allows the application of a vertical load, parallel to the interface, which gives rise to the shear force.

The half-box (N) can slide horizontally (perpendicular to the interface) along a low friction precision guide, also fixed to the base (L). The device also allows applying a prefixed horizontal load (perpendicular to the interface), by means of a pneumatic actuator (A). For contrast, on one side the vertical contrast element of the base is used, on the other a closing element (C) to be installed on the T-box. The horizontal load is transmitted to the opposing bases of the specimens by means of circular plates and spherical joints.

The base (L) is stiffened by means of two triangular elements (F). The two vertical guides (V) are connected through a horizontal beam, which is linked to the base (L) by means of 2 plates (H) (the horizontal beam O and the plates H have the purpose to stiffen the base). The horizontal element (O) is drilled to allow the vertical load to be applied to the half-box (T), through the cylindrical punch (P). The specimen is placed into the two half-boxes with the interface π is positioned exactly at the centre of the gap between the two half-boxes. The connection of the specimen to the half-boxes is carried out with a system of centring pins.

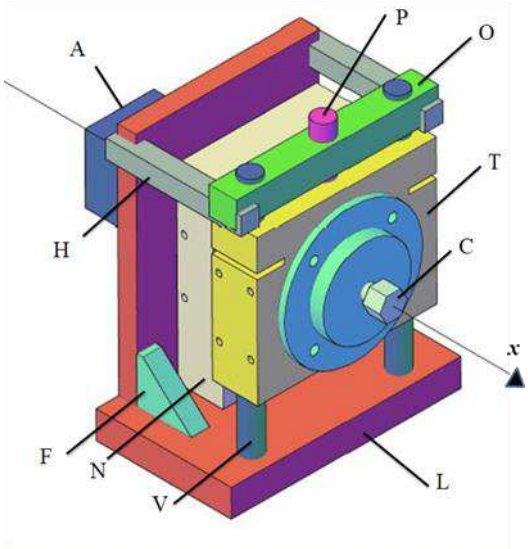

Figure 3.1. Concept scheme of the Cyclic-ASTRA device: assembled view.

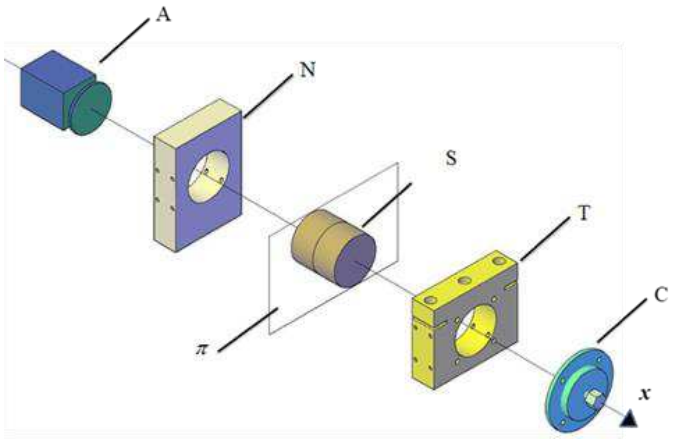

Figure 3.2. Concept scheme of the Cyclic-ASTRA device: exploded view.

3.3 Prototype construction

The final design of the equipment, including drawings and materials selection, and its construction were awarded to an external contractor.

The prototype built (Figure 3.3) was similar to the concept scheme. The specimen is installed in two half-boxes (A and B) with a 97 mm interior diameter, separated by an unconfined interlayer shear zone of 10 mm. The specimen interface must be placed in the middle, leaving 5 mm from the edge of each half-box.

The prototype was suitable for use with the testing frame available at Università Politecnica delle Marche (UNIVPM), which is located inside a climate chamber with temperature control. A servo-pneumatic testing machine applies the shear load (parallel to the interface) on one half-box (B) while the other half (A) can slide horizontally thanks by a low friction guide. The normal load (perpendicular to the interface) is added by a pneumatic actuator, which applies force to the specimen by means of a closing plate (in Figure 3.3, the closing plate is not shown). The prototype was not yet equipped with LVDT for the interface displacement measurement.

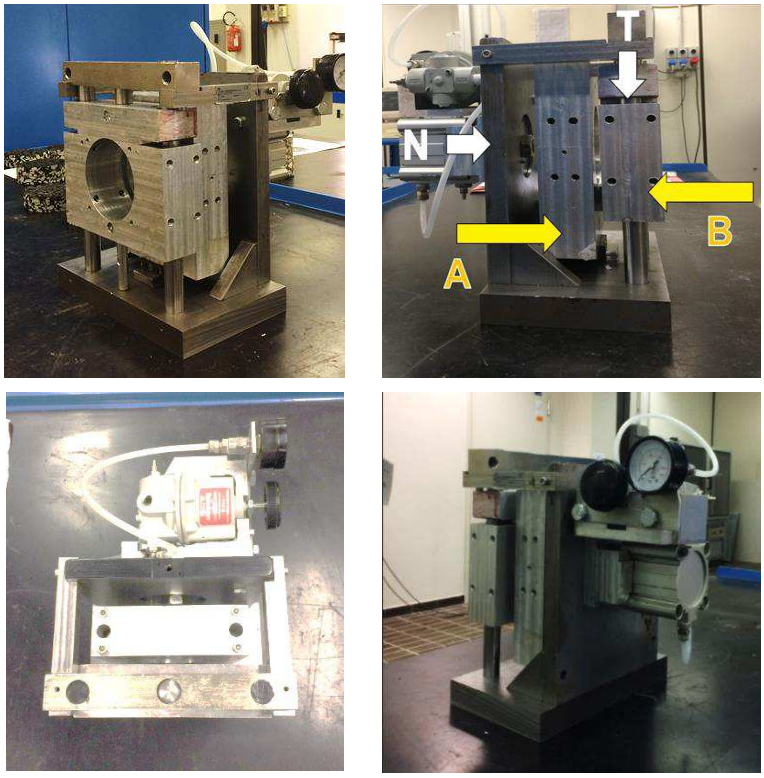

Figure 3.3. Prototype view.

3.4 Prototype checking and modification

In order to verify the prototype in terms of its physical design as well as collected data, an experimental study was conducted. In particular, the first tests were performed on a traditional device called Leutner shear test (Leutner, 1979) (Figure 3.4) to calibrate the testing parameters, i.e., temperature, frequency, load, transducers. The Cyclic-Leutner device was installed into a servo-pneumatic testing frame, equipped with a climate chamber (Figure 3.5).

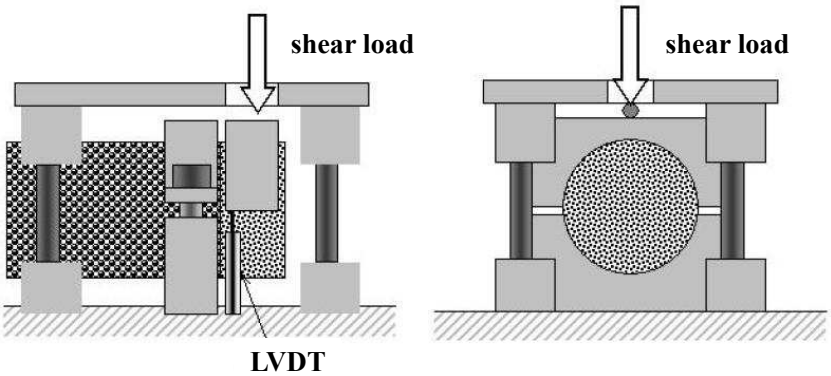

Figure 3.4. Leutner shear device.

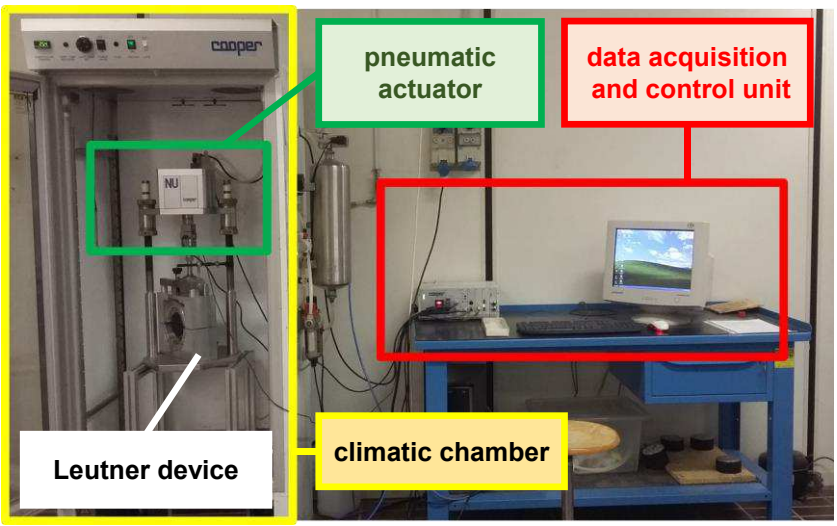

Figure 3.5. Cyclic-Leutner test.

The shear fatigue tests were performed using a haversine cyclic stress loading mode without a rest period. This loading condition is commonly used to simulate certain pavement areas particularly affected by the debonding effect where shear loading is always in the same direction (e.g., braking and curved road sections). The choice of the test mode has fallen back on load-controlled mode because it should represent the field conditions more closely. Besides, at this stage, shear fatigue tests can be conducted only using haversine loading due to the load frame controller that cannot reverse the shear stress sign. Moreover, it is worth pointing out the fact that the tests performed in controlled stress are usually shorter than those under controlled displacement, particularly at low loading levels. Three stress levels of 0.14, 0.29 and 0.7 MPa were used based on the shear strength of the composite specimens and the corresponding stress ratios were approximately 0.2, 0.35 and 0.85. Tests were performed at frequencies of 0.5, 1 and 5 Hz and temperatures of 10 and 20 °C.

The selection of proper test temperatures is an important decision because bituminous material is very sensitive to temperature. To capture the failure behaviour as well as to compute the relative displacements at the layer interface a linear variable differential transformer (LVDT) was used. For each cycle, the load and the interface displacement were recorded. The tests were conducted on double-layered cylindrical specimens prepared in the laboratory. As indicated by the European Pre-Standard prEN 12697-48, a useful parameter for the characterisation of the interface and to detect the collected data is the shear bond stiffness or interlayer shear stiffness (K) evaluated as follows:

$$K = \frac{\tau_0}{u_0} \tag{3.1}$$

It represents the value achieved, cycle after cycle, by the ratio between the amplitude of applied shear stress (τ_0) and the corresponding interface displacement (u_0). It is remembered that the amplitude of applied shear stress (τ_0) is calculated as follows:

$$\tau_0 = \frac{F_0}{A_{eff}} \tag{3.2}$$

where F_0 is the amplitude of the shear force and A_{eff} is the effective cross-sectional area of the specimen.

The typical trend of the interlayer shear stiffness K as recorded in the tests is shown in Figure 3.6. According to the results, since the applied mean shear loading is not zero, repeated load application causes a continuing accumulation of plastic deformation at the interface (i.e., there is a creeping displacement at the interface). Therefore, the shear behaviour of the interface is driven by its viscoelastic and plastic properties. A typical result of the test on a logarithmic chart is shown in Figure 3.7. Moreover, with the increasing of the applied cyclic load level, the number of cycles that the interface can support decrease consistently. For the maximum load (0.7 MPa) the specimen bears a number of cycles of 130. Thus, during the test, the interlayer shear stiffness is decreasing while damage and displacement at the interface are increasing; only the applied shear stresses remain constant.

In synthesis, achieved values are very close to the available literature values which confirms that data collected during the experiment are reasonable.

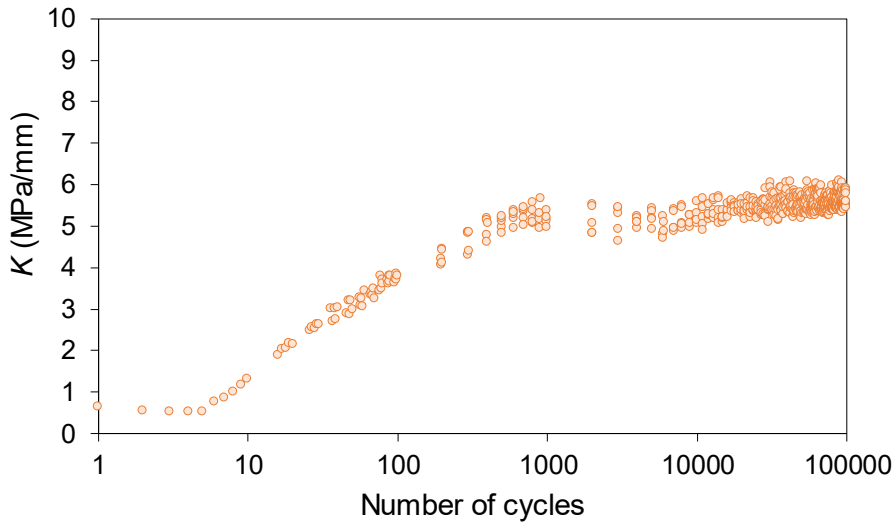

Figure 3.6. Evolution of *K* during the test at 20 °C, 5 Hz and 0.14 MPa.

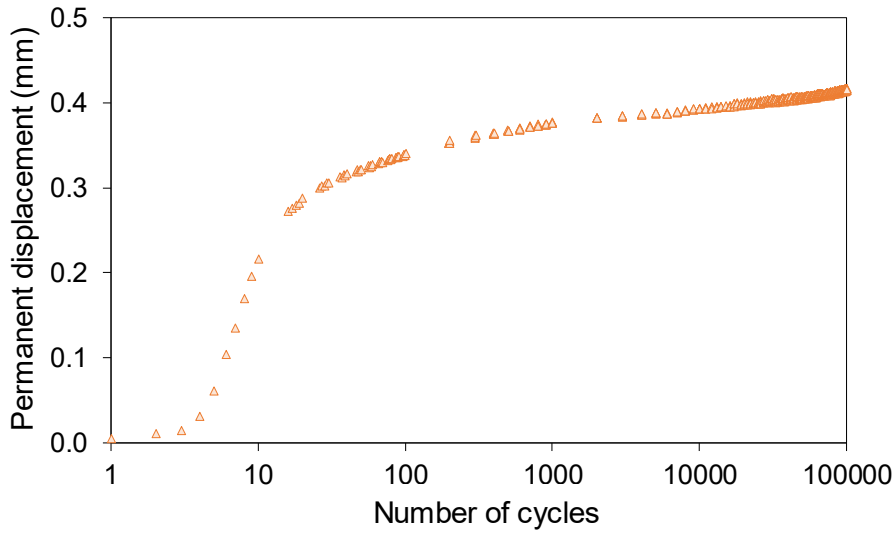

Figure 3.7. Evolution of displacement during the test at 20 °C, 5 Hz and 0.14 MPa.

Based on the results obtained on the cyclic version of the Leutner shear tests, the following conclusions were drawn:

- for the measurement of the applied shear force it is necessary a suitable load cell currently supplied with the pneumatic press available at the Università Politecnica delle Marche;
- for the measurement of the relative displacement of the half-boxes, parallel to the interface, LVDT-type transducers with a full-scale between 1 mm to 5 mm were found to be suitable;
- for the measurement of the relative displacement of the half-boxes, perpendicular to the interface, LVDT-type transducers with a full-scale between 1 mm to 5 mm were found to be suitable.

The developed shear fatigue testing method was performed also on the prototype. Testing was conducted at the same testing conditions on the cyclic-Leutner tests, without normal confinement, to allow a direct comparison of the two devices, and also because the closing element was not suitable. Results in terms of stiffness and fatigue responses were found to be reasonably similar to those obtained in previous tests. In Figure 3.8 a test output of the prototype is presented.

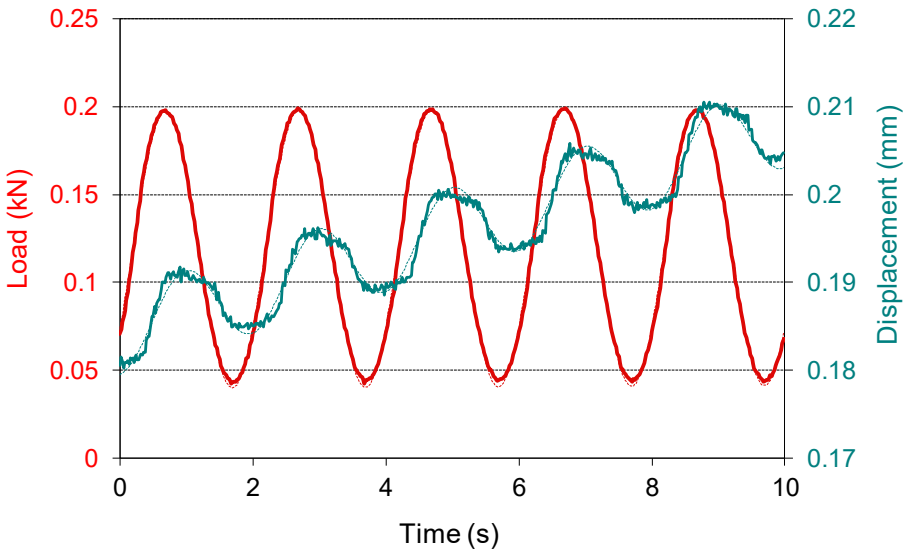

Figure 3.8. Test output of the prototype.

On the basis of the above-mentioned results, the following prototype modifications were needed:

- adding a removable system for adjusting the vertical position of the half-box B to allow perfect alignment of the two half-boxes;
- stiffening of the device to prevent unnecessary movements and vibrations during the execution of the test;
- steel rings for fastening/gluing the specimen with an internal diameter D = 95 mm and a D = 101.5 mm;
- creation of external support for aligning and gluing the steel rings to the specimen;
- improving the closing element;
- equip the device with LVDT for the interface displacement measurements and set up the data acquisition system.

3.5 Dynamic testing equipment: Cyclic-ASTRA

Based on the results presented in the previous section, the prototype was modified. The new device was called Cyclic-ASTRA to highlight the strict relationship with previous research developed at Università Politecnica delle Marche since 1992. Such research led to the development of the ASTRA (Ancona Shear Testing Research and Analysis) which is a static shear testing device (Figure 3.9)

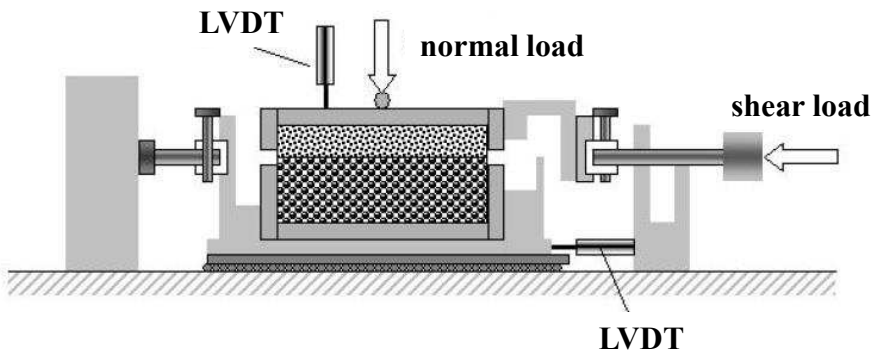

Figure 3.9. ASTRA device.

The Cyclic-ASTRA device is shown in Figure 3.10a. It consists of two half-boxes (T and N) separated by an adjustable gap. The half-box T moves on two vertical guides (V), fixed to a base (L) and allows the application of a vertical load, parallel to the interface. The half-box (N) can slide horizontally (perpendicular to the interface) along a low friction precision guide, also fixed to the base (L). The device also allows applying a prefixed

horizontal load (perpendicular to the interface), by means of a pneumatic actuator (A). The horizontal load is static because a dynamic application would lead to higher complexity of the test frame. The base (L) is stiffened by means of two triangular elements (F). The two vertical guides are connected through a horizontal plate (H), which is linked to the base (L), the plate H has the purpose to stiffen the base.

The main difference compared to the scheme concept and the prototype is that the specimen is connected to the two half-boxes by two cylindrical adapters glued or fixed to the specimen. These adapters (steel rings) have an internal diameter D = 95 mm and an external diameter D = 101.5 mm. The connection of the adapters to the half-boxes is carried out with a system of centring pins. Figure 3.10b shows Cyclic-ASTRA installed in a servo-pneumatic testing machine. The control system allows the application of several loading profiles.

The device is also equipped with a removable system for adjusting the vertical position of the half-box T to allow perfect alignment of the two half-boxes and external support for aligning and gluing the steel rings to the specimen.

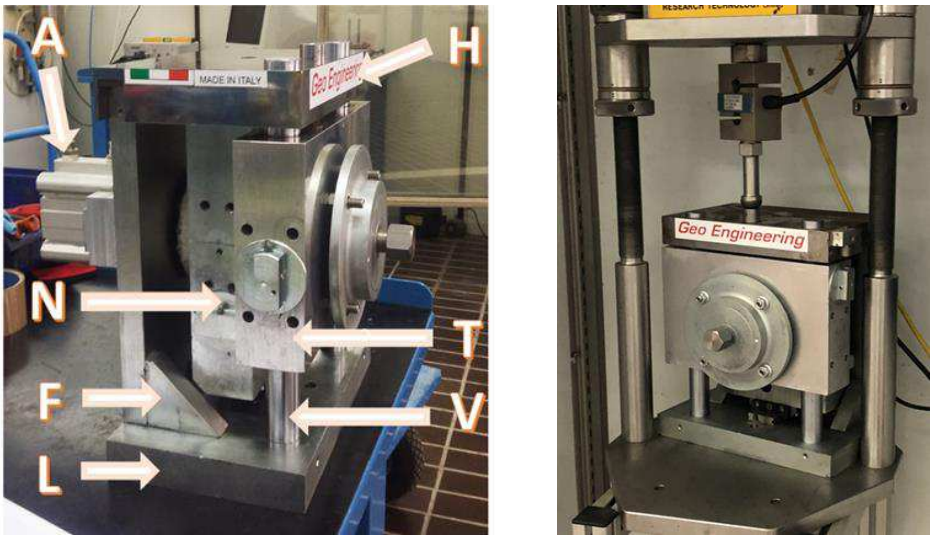

(a) (b)

Figure 3.10. Cyclic-ASTRA device.

Chapter 4.

RILEM interlaboratory test

4.1 General overview

This project thesis was also developed in the framework of the RILEM Technical Committee 272-PIM "Phase and Inter-phase behaviour of bituminous Materials", which organised an interlaboratory test aimed at comparing different prototype equipment currently employed to obtain the dynamic shear characterisation of multilayer bituminous systems.

This chapter describes the objectives and participating laboratories at the RILEM interlaboratory test on "Dynamic Interlayer Shear testing" as well as the experimental activities carried out at Università Politecnica delle Marche consisting in the organisation of the interlaboratory test, the preparation of the double-layered slab samples to be tested by the participating laboratories.

4.2 Background of RILEM interlaboratory test

The interlayer behaviour should be investigated through an innovative experimental methodology based on the dynamic shear testing analysis. Compared to the quasi-static laboratory tools, currently used to analyse the interface shear properties mainly expressed in terms of interlayer shear strength, it is generally recognised that the dynamic shear testing approach will lead to more reliable performance parameters, strictly linked to the field behaviour of pavements under traffic loading.

In this sense, it would be helpful to understand the true bonding at the interface in terms of dynamic shear stiffness for better predicting the overall bearing capacity of multilayer pavements. Moreover, the fatigue resistance at the interface should be investigated to start giving a term of comparison with classic fatigue approaches based on tensile stress/strain. This latter aspect is fundamental to establish, for a given pavement structure, which is predominant between bottom-up cracking and slippage failure.

For the abovementioned reasons, the TC 272-PIM/TG3 promoted an interlaboratory test on "Dynamic Interlayer Shear Testing" involving international research centres provided of the proper experimental equipment. Within the RILEM interlaboratory test, different cyclic bond testing devices were used to characterise a single interlayer system, with the aim of identifying appropriate testing protocols and meaningful parameters.

The interlaboratory test was organised into three phases. The first phase was carried out at the Università Politecnica delle Marche during which the double-layered slab samples (having the same composition and volumetric properties) were prepared in the laboratory and then shipped to each participating laboratory to be tested. During the second phase, the

participating laboratories performed tests using different cyclic shear testing methodologies as well as analysed and interpreted the test results. Instead, the third phase was dedicated to collect results of dynamic test devices and to compare the adopted test conditions (i.e., temperature, normal stress, shear strain/stress amplitude and frequency of application) in order to define the more appropriate testing protocols and meaningful parameters for the dynamic characterisation of bituminous interlayers.

4.3 Participating laboratories

Nine laboratories from six countries (5 in Europe and 1 in the United State of America) have participated in the interlaboratory test. The list of participating laboratories is presented in Table 4.1 and Figure 4.1.

Table 4.1. Participating laboratories ed equipment.

Participating institution (laboratory) name	Country	Device name
Università Politecnica delle Marche (UNIVPM)	Italy	Cyclic-Ancona Shear Testing Research and Analysis (Cyclic-ASTRA)
University of Lyon/ENTPE	France	2T3C Hollow Cylinder Apparatus (2T3C HCA)
Gdansk University of Technology (GUT)	Poland	Dynamic Leutner device
North Carolina State University (NCSU)	United State of America	Modified Advanced Shear Tester (MAST)
University of Minho (UMinho)	Portugal	Dynamic Interlayer Shear Testing (DIST)
University of Limoges (UNILIM)	France	Shear-torque fatigue test device
Swiss Federal Laboratories for Materials Science and Technology (Empa)	Switzerland	Cyclic Compressed Shear Bond (CCSB)
University of Bologna (UNIBO)	Italy	Repeated Impulse Leutner (RIL)
Roads and Bridges Research Institute (IBDiM)	Poland	Advanced Shear Tester (AST)

Figure 4.1. Participating laboratories.

4.4 RILEM interlaboratory test: slab sample

4.4.1 Asphalt concrete

The double-layered slabs for the RILEM interlaboratory test were prepared in the laboratory at the Università Politecnica delle Marche (UNIVPM). The same asphalt concrete (AC) mixture was used for the lower and the upper layers. It was a typical Italian dense graded mix for surface courses (AC 12.5 surf) containing basalt coarse aggregate, limestone fine aggregate and filler. The binder was a Styrene-Butadiene-Styrene (SBS) polymer modified bitumen classified as PMB 45/80-65 (EN 12591) and dosed at 5.5% by aggregate mass. Figure 4.2 shows the grading curve of aggregates and the reference envelope of Italian specifications. Table 4.2 reports the apparent particle density (EN 1097-6) of the aggregates. The main characteristics of the SBS polymer modified binder are reported in Table 4.3. This material was produced in a mixing plant, sampled and transferred to the laboratory (i.e., it was reheated once, prior to the compaction without additional ageing process).

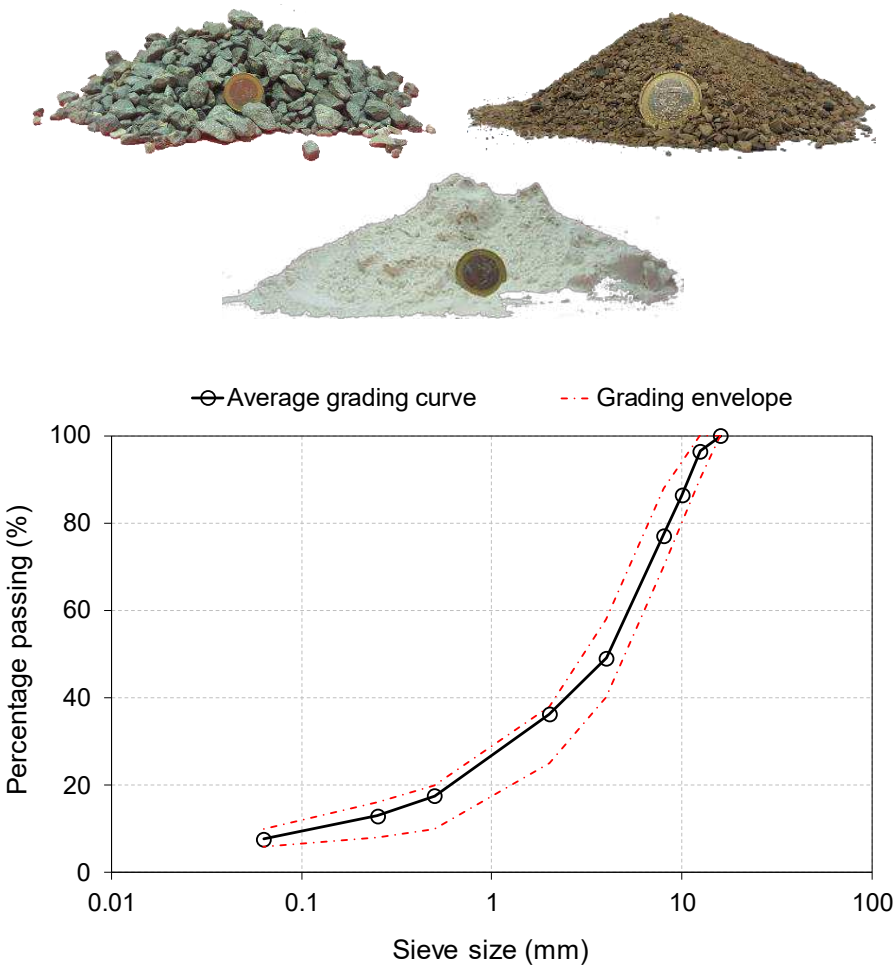

Figure 4.2. Grading curve of aggregates.

Table 4.2. Aggregates characterisation.

Aggregate type	Apparent particle density (g/cm^3)
Course	2.720
Fine	2.709
Filler	2.650

Table 4.3. Basic characteristics of the SBS polymer modified binder.

Characteristics	Standard	Unit	Value
SBS polymer content by weight	-	%	4.75-5.25
Penetration (25°C; 100 g; 5s)	EN 1426	0.1 mm	45-80
Ring and Ball softening point	EN 1427	°C	65
Elastic recovery (25 °C; 5 cm/min)	EN 13398	%	80
Dynamic viscosity @ 135 °C	EN 12595	Pa·s	0.4
RTFOT at 163 °C			
Mass loss	EN 12607-1	%	0.5
Penetration	EN 1426	0.1 mm	60
Ring and Ball softening point	EN 1427	°C	8

4.4.2 Slabs preparation and properties

The double-layered square slabs were compacted in the laboratory in a stainless-steel mould (Figure 4.3) by means of a roller compactor according to EN 12697-33. Roller compactor (Figures 4.4 and 4.5) is a pneumatic device used for compacting bituminous mixture by simulating in-situ compaction in the laboratory. Slabs manufactured with roller compactor have dimensions 305×305 mm^2 with the possibility to obtain thicknesses between 40 and 100 mm. The final thickness of the slab can be fixed using two knurled nuts (Figure 4.6a). The volume of the mould is cross-sectional area multiplied by the height of the material, therefore, by compacting a certain mass, the slab density can be easily found. During the cycle, four different pressure levels can be applied (Figure 4.6b). The first pressure can vary between 0 and 2.5 bar and simulates the compaction effect of the paver. Whereas, the other three pressures range between 0 and 1 bar and represent the compaction performed in-situ by rollers. For each pressure, the number of roll passages can be fixed between 0 and 100. Setting the number of cycles equal to zero, the roller compactor skips the corresponding pressure.

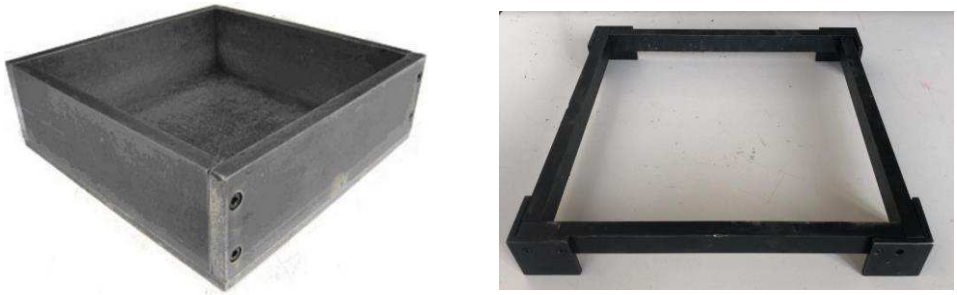

Figure 4.3. Roller compactor mould for the preparation of the bituminous slabs (left) with the collar for the containment of the not yet compacted material (right).

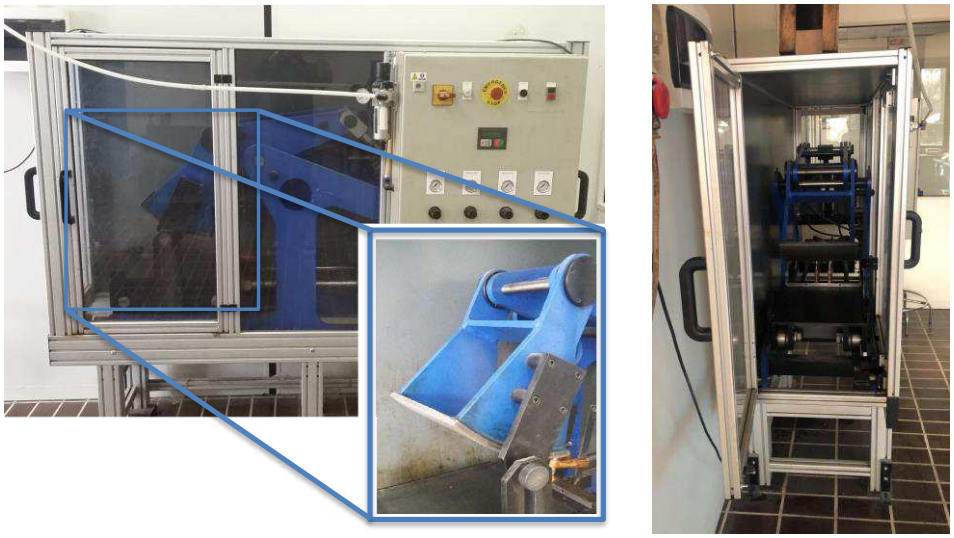

Figure 4.4. Roller compactor.

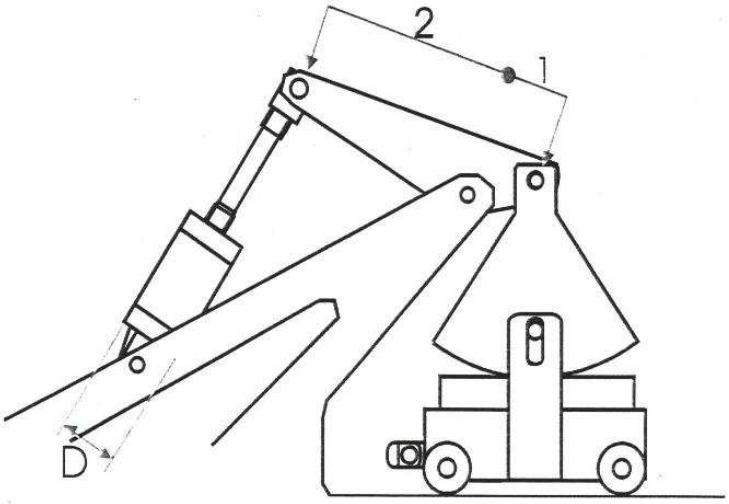

Figure 4.5. Roller compactor working scheme.

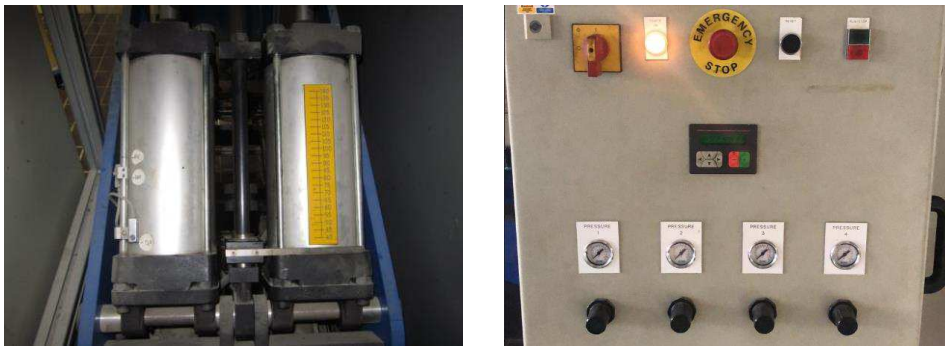

(a) (b)

Figure 4.6. (a) Guide for adjusting the height of the slabs and (b) panel control.

For the RILEM interlaboratory test, the lower layer of each slab was compacted at the temperature of 150 °C until reaching a target thickness of 60 mm. Then, after cooling at room temperature for 3 h, the upper layer was compacted at the same temperature reaching a target thickness of 40 mm. A tack coat or reinforcement was not applied at the interface in order to study the failure mechanism in the simplest condition. The slab was demoulded after cooling at room temperature for one day. The compaction direction was marked on each slab, in order to perform the shear tests in the same direction. A total of 19 double-layered slabs were prepared with a final geometry of 305×305×100 mm^3 (Figures 4.7 and 4.8). An identification number (from 1 to 19) was also marked on each slab.

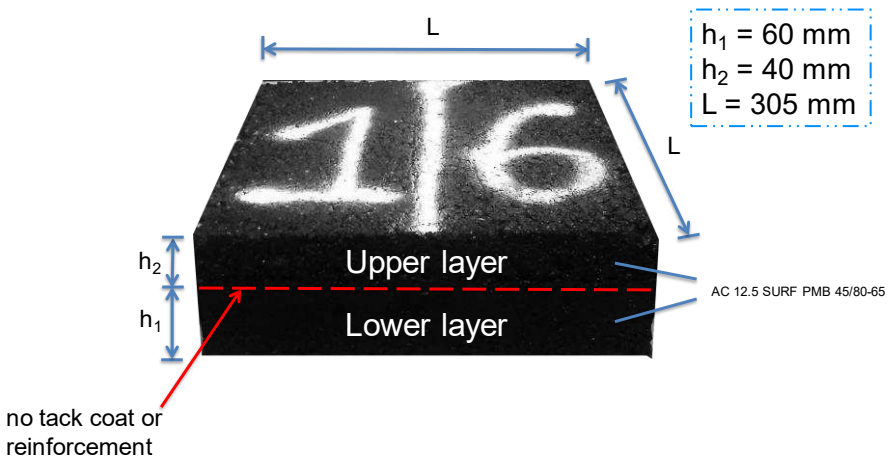

Figure 4.7. Double-layered slab geometry.

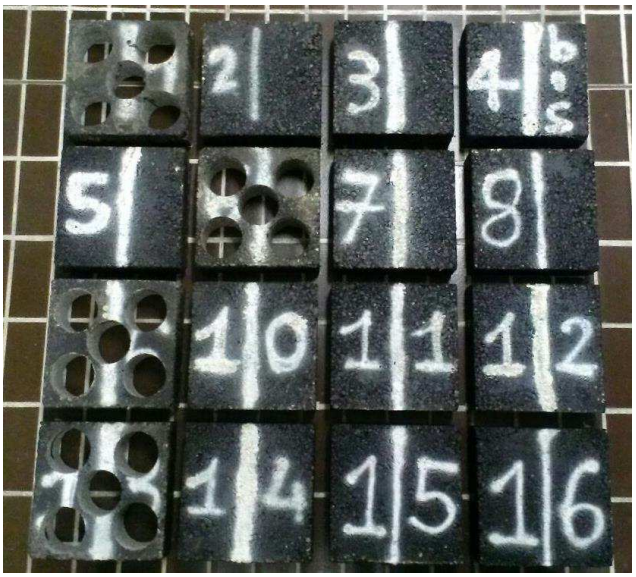

Figure 4.8. RILEM double-layered slabs (three slabs are missing in the image).

To monitor the production quality, 4 out of 19 slabs produced in total were used. From each double-layered slab, five cylindrical specimens with a diameter of 95 mm were cored (Figure 4.9), to measure thickness and air voids content. The maximum density of the mixture was measured according to EN 12697-5 (clause C). The bulk density of all specimens was measured according to EN 12697-6 (clause D – by dimensions). For each slab, the bulk density of one specimen was also measured according to EN 12697-6 (clause C – sealed specimens). The average thickness and air void content of the slabs are summarised in Table 4.4.

Figure 4.9. Cored double-layered cylindrical specimens.

Table 4.4. Properties of the slabs.

Slab	Thickness		Air voids *Sealed specimens*	Air voids *By dimensions*	
(#)	Avg (mm)	Std. Dev.	(%)	Avg (%)	Std. Dev.
1	100.6	1.4	4.3	5.2	1.1
6	103.8	0.5	5.7	7.0	0.7
9	99.5	0.6	3.1	7.0	0.7
13	100.4	2.0	3.0	4.5	1.0

Of the remaining 15 double-layered slabs, 10 slabs were packed and shipped to the various participating laboratories (Table 4.5 and Figure 4.10), while 5 slabs were tested at the Università Politecnica delle Marche (UNIVPM).

Table 4.5. Slabs tested by the participating laboratories.

Slab (#)	Participating institution (laboratory) name	Country
14, 16, 17, 18, 19	Università Politecnica delle Marche (UNIVPM)	Italy
10	University of Lyon/ENTPE	France
3	Gdansk University of Technology (GUT)	Poland
12, 15	North Carolina State University (NCSU)	United State of America
8	University of Minho (UMinho)	Portugal
5, 7	University of Limoges (UNILIM)	France
11	Swiss Federal Laboratories for Materials Science and Technology (Empa)	Switzerland
2	University of Bologna (UNIBO)	Italy
4	Roads and Bridges Research Institute (IBDiM)	Poland

Figure 4.10. Slab packing.

Chapter 5.

Experimental investigation with Cyclic-ASTRA

5.1 Introduction

This chapter contains the materials, the testing program, the discussion and the interpretation of the results obtained in the experimental investigation carried out in the Department of Civil and Building Engineering and Architecture at the Università Politecnica delle Marche. Specimens were cored from the double-layered slabs prepared for the RILEM interlaboratory test described in the previous chapter. In this study, additional slabs were prepared with a tack-coat application at the interface for comparison purpose. Once cored, specimens were tested by means of the new Cyclic-Ancona Shear Testing Research and Analysis (ASTRA) device as well as with the ASTRA (static) and Leutner (static and cyclic) devices. The reported results include the ISS of the double-layered slab samples measured with the ASTRA and Leutner devices. Moreover, the results of the cyclic Leutner device were presented along with the preliminary outcomes obtained with the new Cyclic-ASTRA device, both in terms of stiffness and cumulative damage.

5.2 Materials and sample preparation

Five double-layered slabs (coded as 14, 16, 17, 18 and 19) of the set of slabs prepared for the RILEM interlaboratory test (chapter 4) were used in this study. The double-layered slabs ($305\times305\times100$ mm^3) were prepared in the laboratory using, for both layers, the same type of asphalt concrete. No tack coat or reinforcement was applied at the interface. From each double-layered slab, five cylindrical specimens with a diameter of 95 mm were cored as shown in Figure 5.1.

In addition, the specimens cored from the slabs used to monitor the production quality (slabs coded as 1, 6, 9 and 13) described in chapter 4 were tested.

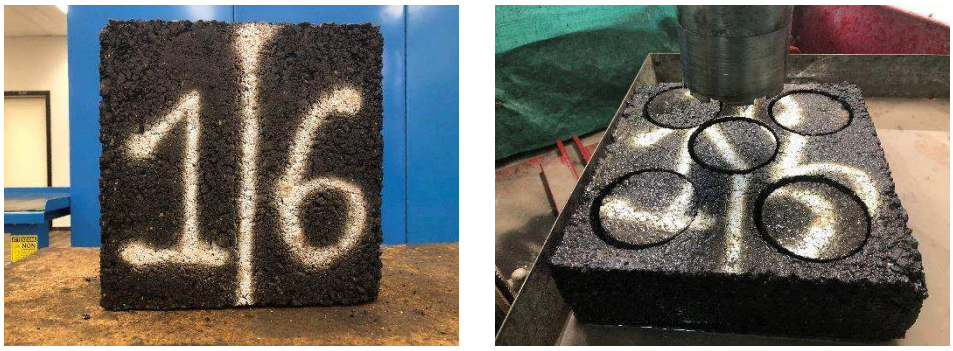

(a) (b)

Figure 5.1. Slab (a) before and (b) after the coring procedure.

Besides the slabs prepared for the RILEM interlaboratory tests, for this study two additional slabs (coded as 20 and 21) were produced with the same composition and volumetric properties, but with the application of a tack coat at the interface. Hence, after that the lower layer was compacted with a thickness of 60 mm, it was for 3 h at room temperature for cooling. Then, an SBS polymer modified bitumen (3.8% of SBS by bitumen weight) was applied manually on the surface of the lower layer with a dosage of 0.70 kg/m^2 (Figure 5.2a). The main characteristics of the tack coat are reported in Table 5.1. Lastly, the upper layer of the slab was compacted with a thickness of 40 mm. Also, for these slabs, five cylindrical specimens (95-mm diameter) were cored from each slab. Each cored specimen was marked by an identification code (ID) defining the number of the slab and the coring position into the slab (according to Figure 5.2b); for example, 14_3 represents the specimen cored in the slab 14 in the position 3.

In this study, the two different interface configurations were considered in order to verify if the used devices (in particular the new cyclic testing device) are able to distinguish their different mechanical performance.

To check the specimen-to-specimen variability, measurements of thickness, bulk densities and air voids content were performed on each specimen. The bulk density of all specimens was measured according to EN 12697-6 (clause B – saturated surface dry SSD and clause D – by dimensions). The average thickness and air void content (according to EN 12697-8) of the cored specimens are summarised in Table 5.2. The 95-mm diameter cored specimens showed an air void content of 3 to 7%. The specimen cored from slabs 1, 6, 9, and 13 were not reported in Table 5.2, because their characteristics are described in Table 4.4.

(a) (b)

Figure 5.2. (a) Tack coat application; (b) specimen code according to the coring position.

Table 5.1. Main properties of the tack coat.

Characteristics	Standard	Unit	Value
SBS polymer content by weight	-	%	3.8
Penetration (25°C; 100 g; 5s)	EN 1426	0.1 mm	54
Ring and Ball softening point	EN 1427	°C	71
Elastic recovery (25 °C; 5 cm/min)	EN 13398	%	89
Dynamic viscosity @ 135 °C	EN 12595	Pa·s	1.24
RTFOT at 163 °C			
Mass loss	EN 12607-1	%	0.05
Penetration	EN 1426	0.1 mm	27
Ring and Ball softening point	EN 1427	°C	77

Table 5.2. Main properties of the specimens.

Specimen ID	Diameter (mm)	Thick. (mm)	Mass (g)	Bulk density SSD (g/cm^3)	Air voids SSD (%)	Bulk density By dimens. (g/cm^3)	Air voids By dimensions (%)
14.1	94.35	98.90	1605.10	2392.66	4.11	2321.30	6.97
14.2	94.25	99.08	1623.30	2416.90	3.13	2348.45	5.88
14.3	94.25	103.20	1701.80	2424.13	2.84	2363.61	5.27
14.4	94.40	103.80	1712.00	2427.56	2.71	2356.53	5.55
14.5	94.10	100.18	1651.40	2419.72	3.02	2370.41	5.00
16.1	94.10	99.85	1691.90	2419.36	3.04	2436.45	2.35
16.2	94.35	101.73	1670.90	2404.15	3.64	2349.36	5.84
16.3	94.10	100.25	1650.70	2422.97	2.89	2367.63	5.11
16.4	93.75	102.35	1635.20	2404.11	3.65	2314.46	7.24
16.5	93.85	102.38	1681.60	2421.64	2.94	2374.49	4.83
17.1	94.70	98.99	1622.80	2396.64	3.95	2327.53	6.72
17.2	94.58	100.11	1623.30	2405.20	3.60	2308.17	7.49
17.3	95.15	102.86	1709.80	2427.46	2.71	2337.66	6.31
17.4	95.08	102.79	1693.10	2410.95	3.37	2320.17	7.01
17.5	94.80	99.50	1646.00	2401.90	3.73	2343.69	6.07
18.1	94.48	99.31	1644.60	2414.90	3.21	2362.29	5.32
18.2	94.30	99.01	1644.10	2417.72	3.10	2377.52	4.71
18.3	94.93	101.74	1695.80	2435.64	2.38	2355.28	5.60
18.4	94.43	101.25	1678.40	2420.96	2.97	2367.21	5.13
18.5	94.38	99.93	1662.40	2425.48	2.79	2378.25	4.68
19.1	94.45	98.96	1644.50	2412.63	3.31	2371.75	4.94
19.2	94.60	98.73	1629.40	2399.64	3.83	2348.16	5.89
19.3	95.00	101.73	1698.20	2425.48	2.79	2355.18	5.61
19.4	94.43	101.33	1688.70	2422.86	2.89	2379.97	4.61
19.5	94.60	99.76	1659.60	2419.14	3.04	2366.81	5.14
20.1	94.30	99.49	1646.60	2343.91	6.06	2369.77	5.02
20.2	94.70	102.55	1697.40	2358.09	5.49	2349.95	5.82
20.3	94.38	102.00	1687.40	2374.44	4.84	2364.91	5.22
20.4	94.45	99.25	1643.30	2343.75	6.07	2363.16	5.29
20.5	94.45	100.68	1663.30	2361.48	5.35	2358.06	5.49
21.1	94.13	99.74	1642.50	2425.73	2.78	2366.72	5.14
21.2	94.45	99.64	1635.40	2423.13	2.88	2342.65	6.11
21.3	94.55	103.03	1712.00	2430.59	2.59	2366.73	5.14
21.4	94.60	103.98	1720.90	2450.54	1.79	2354.80	5.62
21.5	94.70	100.95	1665.60	2430.50	2.59	2342.47	6.12

5.3 Testing device and program

5.3.1 ASTRA test

The ASTRA (Ancona Shear Testing Research and Analysis) device was designed and developed at the Università Politecnica delle Marche (Canestrari et al., 2005). ASTRA is a direct shear box, similar to the device commonly used in soil mechanics and is compliant with the Italian Standard UNI/TS 11214 and the European Pre-Standard prEN 12697-48.
The general scheme of the ASTRA device is shown in Figure 5.3. A cylindrical specimen is installed in two half-boxes separated by an unconfined interlayer shear zone (the gap width between the two half-boxes is usually 10 mm). Two steel adaptors, one for each half-box, with a square outer section and a cylindrical cavity, lock cylindrical specimens to be subjected to the direct shear test (Figure 5.4). These elements are connected to the half-boxes by means of special concealed screws. Besides, for each diameter, a series of shims are available to adapt the specimens also in height (Figure 5.4).

During the test, a constant horizontal displacement rate of 2.5 mm/min speed, parallel to the interface plane, is applied to the lower half-box and the force transmitted to the upper half-box is measured by a load cell. At the same time, two linear variable displacement transducers (LVDTs) measure the shear and normal displacement of the specimen. During the test, the shear stress at the interface τ, calculated as the ratio between the shear force and the specimen cross-sectional area, is reported as a function of time. Hence, the interlayer shear strength (ISS) is obtained as the maximum shear stress τ_f. A constant vertical load, perpendicular to the interface plane, can also be applied during the test through a system of weights and levels. Applying different normal loads, it is possible to obtain the peak envelope and the friction envelope (Canestrari et al., 2015). The whole apparatus is located inside a climatic chamber with temperature and relative humidity control.

In this study, ASTRA tests were carried out at a temperature of 20 °C without applying a normal load, in order to compare the results with those obtained with the Leutner test.

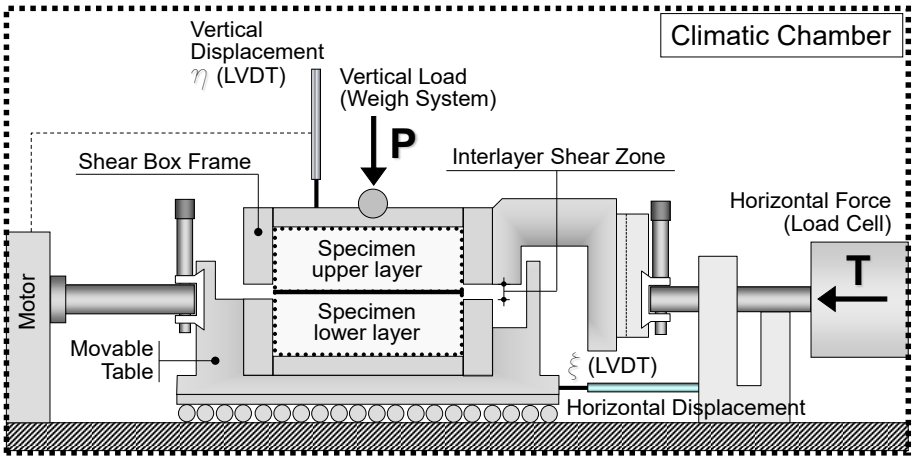

Figure 5.3. Scheme concept of ASTRA device.

(a) (b)

Figure 5.4. (a) Half-boxes, steel adaptors and shims; (b) specimen inside the half-boxes.

5.3.2 Leutner test

Shear tests were performed also with the Leutner equipment (Figure 5.5), that is and is compliant with the European Pre-Standard prEN 12697-48. The Leutner device (Leutner, 1979) is used to measure the ISS on specimens with a nominal diameter of 100 mm or 150 mm, without applying a normal load. The device was installed into a servo-mechanic press frame able to apply displacement rates up to 50 mm/min (Figure 5.6a). The apparatus was not located inside a climatic chamber.

Figure 5.6b shows the scheme of the Leutner equipment, which is divided into two parts. The lower part is connected to the loading plate of the press that moves upward, whereas the upper part is positioned in contrast with the loading frame. An interface gap of

about 5 mm is left between the two parts. To highlight how the shear load is applied to the specimen, a section of the Leutner equipment, normal to the shear plane, is shown in Figure 5.6c. The specimen can be ideally divided into three sections. In correspondence of section A, the specimen is fixed to the lower part of the Leutner equipment through a screw that is manually locked to ensure adequate contact. In correspondence of section B, the lower part of the specimen is in contact only with the lower part of the equipment, whereas its upper part is unconfined. In correspondence of section C, the lower part of the specimen is unconfined whereas on the top it is in contact with the upper part of the Leutner equipment.

An external transducer (LVDT) was added to compute the relative displacement between the lower and the upper part of the Leutner device. For each test, the device returns a dataset where the displacement of the loading plate, the load measured by the load cell and the deformation measured by the LVDT, are reported as a function of time. As shown in Figure 5.7, the measured displacement increases linearly during the test because of the imposed constant displacement rate (nominal test speed). Load and deformation show an initial flat phase which is due to an adjustment of the specimen inside the Leutner device. Afterwards, both load and deformation start to increase contemporaneously, indicating that the measured load is due to the relative displacement imposed to the specimen on opposite sides of the interface (upper and lower layers).

The applied load could also cause a small rotation of the specimen that, together with the compliance of the testing apparatus (Leutner equipment and press), explains the difference between displacement (applied by the press) and deformation (read by the transducers), as shown in Figure 5.7.

In this study, Leutner tests were carried out at a temperature of 20 °C applying a constant shear displacement rate of 2.5 mm/min (the same as in the ASTRA test) across the interface of the double-layered specimen.

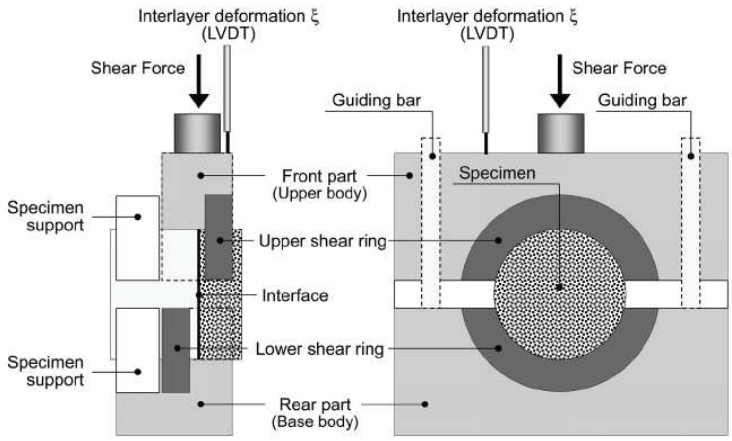

Figure 5.5. Scheme concept of Leutner device.

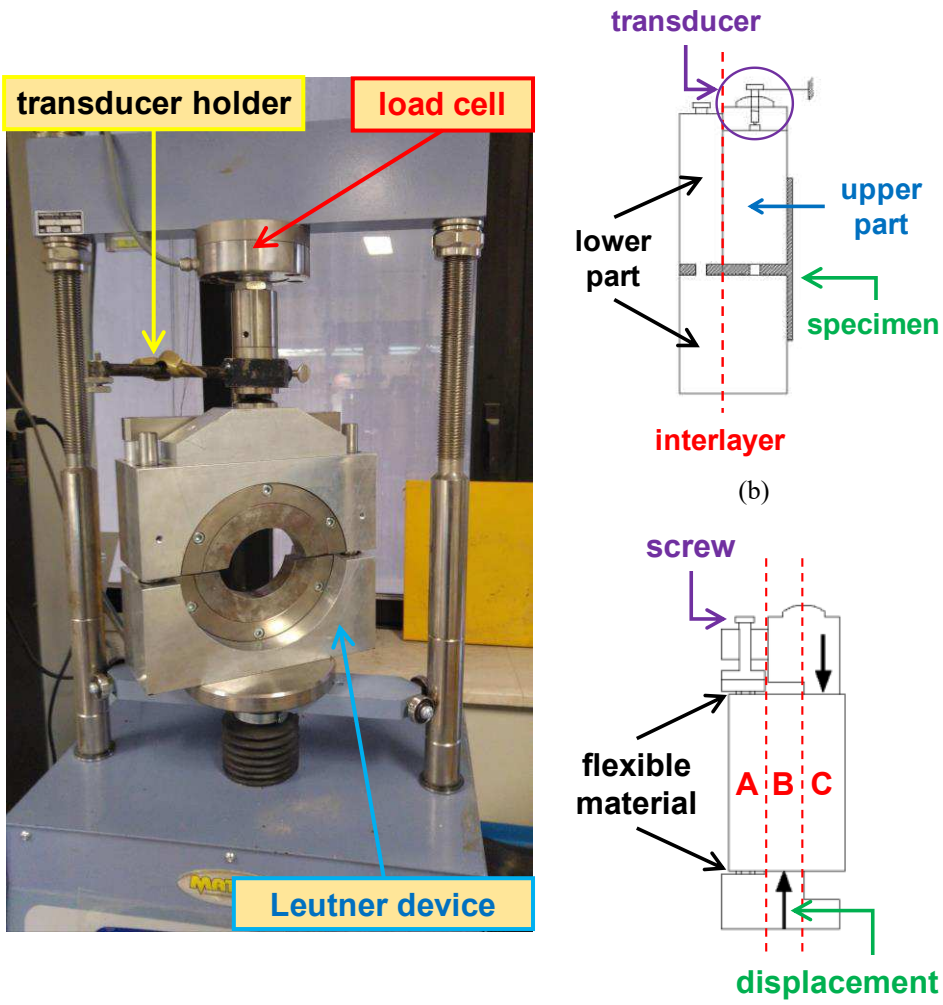

(a) (b) (c)

Figure 5.6. Leutner shear device: (a) inside the loading frame; (b) scheme of the side view; (c) scheme of cross-section normal to the shear plane.

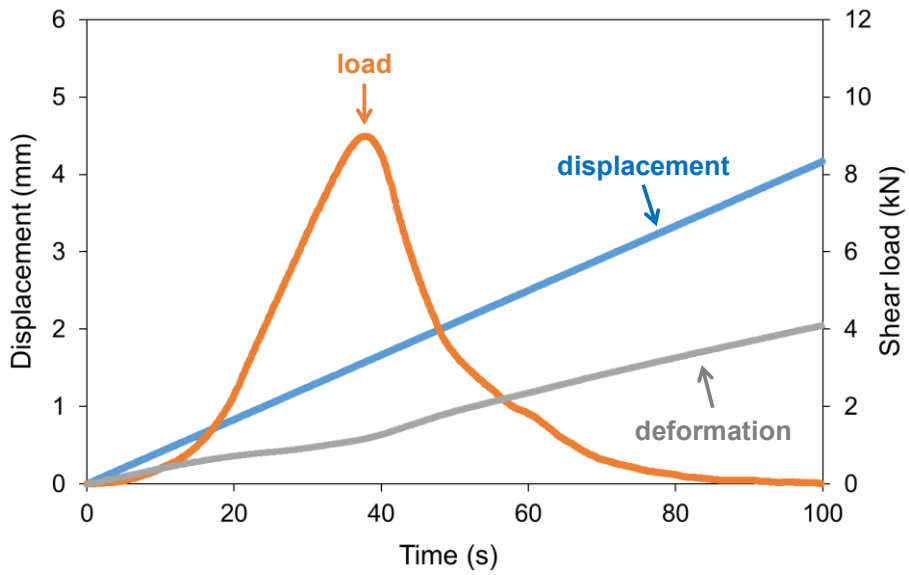

Figure 5.7. Leutner test result for the single specimen.

In addition to the static tests, cyclic-Leutner tests were also performed by installing the Leutner device into a servo-pneumatic testing frame, equipped with a climate chamber (Figure 5.8a). The cyclic tests were performed applying a sinusoidal (haversine) cyclic stress load, at a frequency of 5 Hz and temperature of 20 °C. Four stress amplitudes were used, based on the average ISS of the double-layered specimens measured with the static test. The ratio between the applied amplitudes and the measured ISS were 0.22, 0.29 and 0.37. An LVDT was used in order to measure the shear displacement parallel the layer interface. For each cycle, the load and the interface displacement were recorded with a sampling frequency of 50 Hz.

5.3.3 Cyclic-ASTRA test

Key aspects and detail of this new cyclic shear testing are reported in chapter 3. As shown in Figure 5.8b, the Cyclic-ASTRA device was installed into a servo-pneumatic testing frame, equipped with a climate chamber (the same of cyclic-Leutner).

In this study, Cyclic-ASTRA shear tests were carried out at 10 °C and 20 °C. The gap between the two shear boxes was set a 10 mm. A sinusoidal (haversine) cyclic load was applied with a frequency of 5 Hz and without the application of a normal load. Four stress amplitudes were used, based on the average ISS of the double-layered specimens measured with the static test. The ratio between the applied amplitudes and the measured ISS were 0.29, 0.37, 0.44 and 0.51. Two LVDTs were used in order to measure the shear displacement

parallel the layer interface. For each cycle, the data acquisition system recorded the shear load and the relative interface displacement.

(a) (b)

Figure 5.8. (a) Cyclic-Leutner test and (b) Cyclic-ASTRA test.

5.3.4 Experimental program

In short, the experimental program of this investigation is summarised in Table 5.3 and Figure 5.9. For each test configuration, specimens were conditioned for at least 3 hours in a climatic chamber. For simplicity, the specimens obtained from slabs prepared for the RILEM interlaboratory tests, i.e., without tack coat (slabs 1, 6, 9, 13, 14, 16, 17, 18, and 19), are identified as “UN”, whereas the specimens obtained from slabs with tack coat (slabs 20 and 21) are identified as “TC”.

ASTRA tests were carried out only on UN specimens, whereas Leutner, Cyclic-Leutner and Cyclic-ASTRA shear tests were carried out on UN and TC specimens. As shown in Table 5.3 and Figure 5.9, a total of 16 specimens were tested with ASTRA, 8 specimens with Leutner, 7 specimens with Cyclic-Leutner and 20 specimens with Cyclic-ASTRA. 4 UN specimens (i.e., 1.1, 2.4, 9.5, 13.5) were not tested since they were sealed with wax to measure the bulk density of the slabs.

Table 5.3. Experimental program.

Static test		Cyclic test	
Leutner	ASTRA	Cyclic-Leutner	Cyclic-ASTRA
v = 2.5 mm/min		Frequency = 5 Hz	
deformation controlled		haversine load controlled	
σ_v = 0.0 MPa			
T = 20 °C		T = 20 °C	T = 10 & 20 °C
8 tests (UN & TC)	16 tests (UN)	7 tests (UN & TC)	20 tests (UN & TC)

Figure 5.9. Experimental program.

5.4 Result and analysis

5.4.1 Static test

Figure 5.10 shows the results of ASTRA and Leutner (static) tests, in terms of average ISS along with the error bars, for UN and TC specimens. The Leutner test leads to a higher ISS value (1.11 MPa) compared with the ASTRA test (0.80 MPa).

Figure 5.10 also shows that the presence of tack coat (TC) at the interface leads to higher ISS (1.33 MPa) than the corresponding system without tack coat (UN). This confirms that, in general, the proper dosage of tack coat improves the ISS by increasing the adhesion between the two asphalt layers (Augustin, 1997; Canestrari et al., 2005). Moreover, less scattered results were observed for the TC interface. Figure 5.11 depicts the specimens at the end of the ASTRA test and Leutner test. All the specimens presented a failure at the interface.

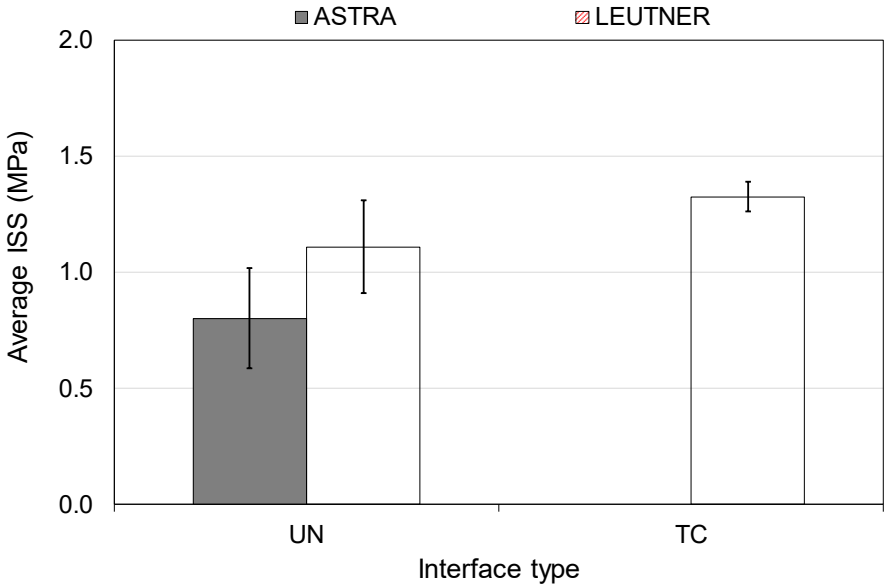

Figure 5.10. Average interlayer shear strength (ISS) from two static shear tests (error bars represent the standard deviation).

Figure 5.11. Specimens after ASTRA test and Leutner test.

5.4.2 Cyclic-Leutner test

Figure 5.12 shows the evolution until the failure of the permanent displacement at the layer interface as a function of the number of cycles. It is possible to notice that these curves do not display the typical three stages of a fatigue test result (Di Benedetto et al., 2013). In particular, the application of the haversine load caused the accumulation of permanent deformation with an increasing rate. Moreover, in general, with the increasing of the applied cyclic load level, the number of cycles to failure decreases. When considering the same number of cycles and applied shear load, specimens with tack coat (TC) show a greater deformation compared to specimens without tack coat (UN), especially for higher imposed shear loads.

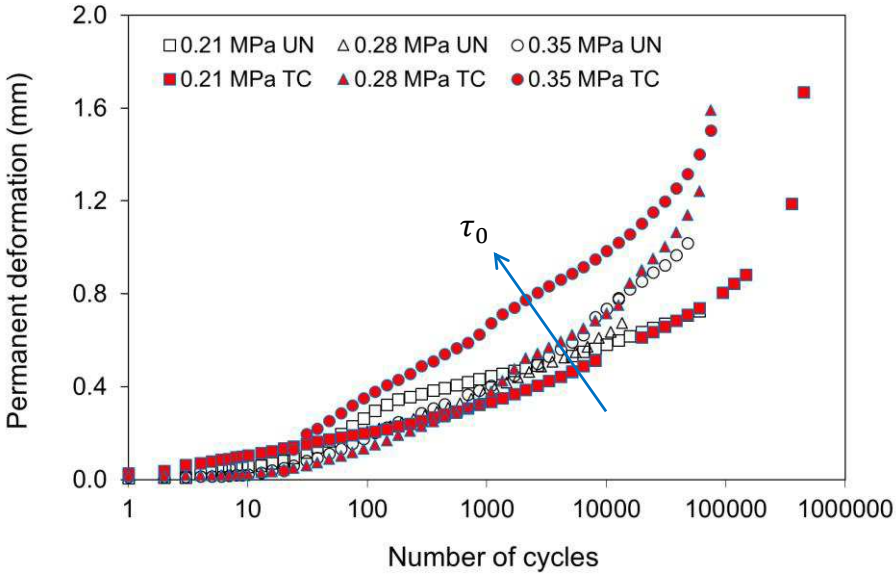

Figure 5.12. Displacement at the layer interface during the Cyclic-Leutner test.

Figure 5.13 shows the applied shear stress amplitude versus the number of cycles to failure (detachment between the two layers of the specimen). These preliminary results show high variability. In particular, tests carried out at the higher stress amplitude (0.35 MPa) resulted in unexpected high values of cycles to failure for both UN and TC interfaces (circled in green in Figure 5.13). This result can be explained considering the cyclic Leutner device is not able to provide an effective clamping of the specimen. Thus, for the higher stress levels, the specimen moved during the test, and therefore the shear stress was not applied exactly on the interface. This resulted in a higher number of cycles to failure. However, when considering the same applied shear load, the specimens with tack coat (TC) show a higher strength compared to specimens without tack coat (UN) obtaining similar results to that of the static Leutner. These findings are in agreement with Diakhaté et al. (2011).

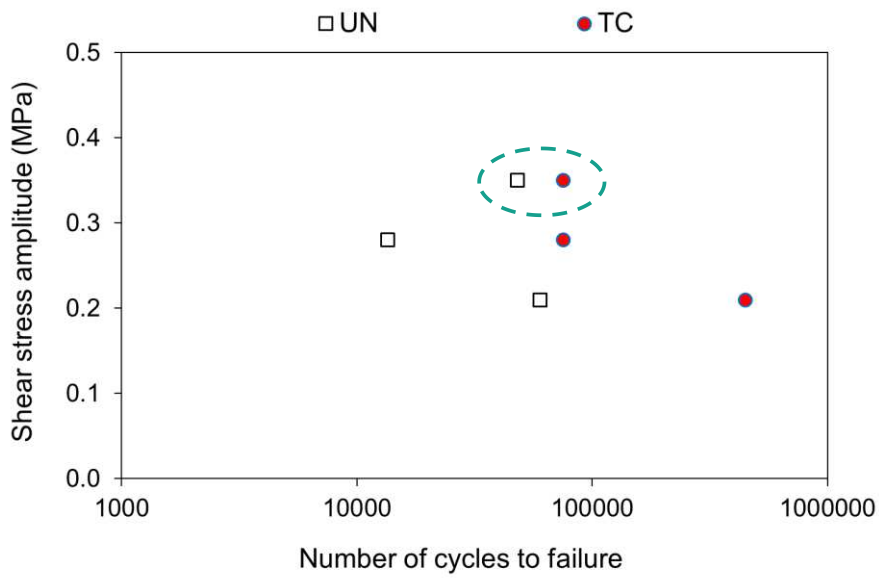

Figure 5.13. Interlayer shear fatigue curves obtained from Cyclic-Leutner test (T = 20 °C).

5.4.3 Cyclic-ASTRA test

Figure 5.14 shows an example of the measurements carried out with the Cyclic-ASTRA device. In particular, the shear load and interlayer relative displacement time histories are reported.

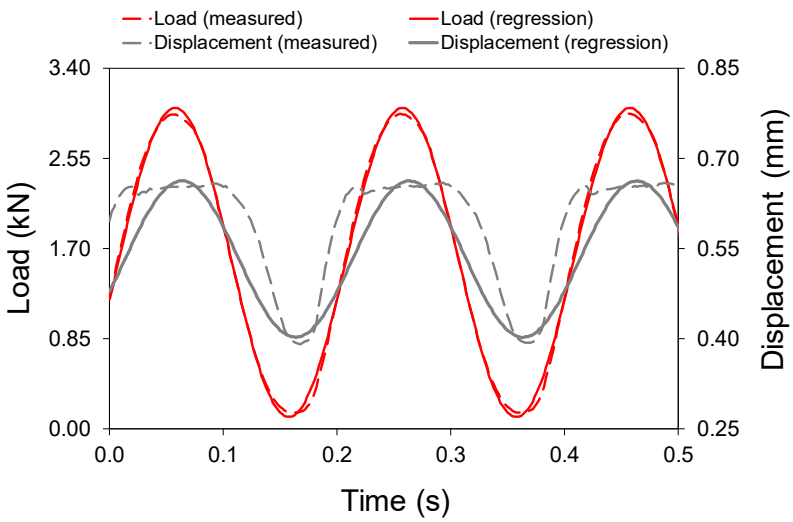

Figure 5.14. Shear load and deformation measured with the Cyclic-ASTRA testing device.

The interlayer shear stiffness (K) can be defined as follows:

$$K = \frac{\tau_0}{u_0} \tag{5.1}$$

where τ_0 is the amplitude of applied shear stress and u_0 is the amplitude of the relative displacement at the interface. K values after 1000 cycles of UN specimens are shown in Table 5.4. As can be observed, K decreases with increasing testing temperature and, in general, with decreasing shear stress amplitude.

Table 5.4. Interlayer shear stiffness (K) values.

Temperature (°C)	Shear stress amplitude (MPa)	K (MPa/mm)
10	0.28	2.27
	0.35	2.79
	0.42	2.80
	0.49	3.09
20	0.21	1.94
	0.28	1.35
	0.35	2.06
	0.49	2.50

Figure 5.15 shows the evolution until the failure of the permanent displacement at the layer interface as a function of the number of cycles. It can be noted that the permanent interface displacement increases with the increasing number of cycles as a consequence of the interlayer deformation. Contrary to the results of the Cyclic-Leutner tests, this curve shows the typical three stages of a fatigue test result, consisting of a rapid increase of displacement at the beginning of the test, followed by a quasi-stationary displacement increment, and then a rapid increment of displacement at the end of the test (complete separation of the two layers) (Di Benedetto et al., 2013). The improved output of the Cyclic-ASTRA device can be explained with the increased precision of the measurements and the lower compliance of the testing equipment. Moreover, the Cyclic-ASTRA device allows displacements perpendicularly to the shear plane during interface shear tests. This is imperative in order to avoid additional normal stress due to the inhibition of dilatancy. In the case of Leutner test, this effect may lead to an overestimation (Canestrari et al., 2018) of mechanical properties (e.g., ISS, number of cycles to failure).

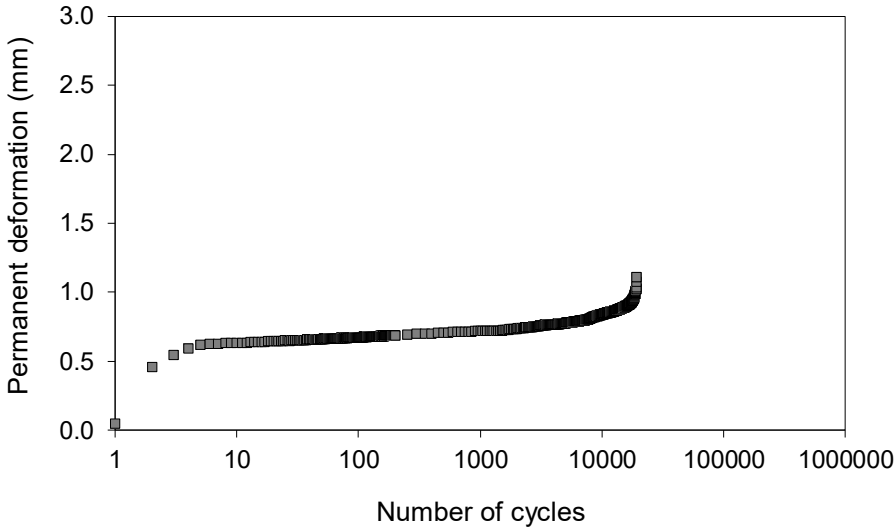

Figure 5.15. Displacement at the layer interface during the Cyclic-ASTRA test at 10 °C, 5 Hz and 0.42 MPa.

As an example, Figure 5.16 shows the effect of the temperature and the loading amplitude on the evolution of permanent displacement at the layer interface for UN specimens during Cyclic-ASTRA. Considering the same temperature (10 °C), the permanent deformation rate increases with increasing applied shear load. Considering the same applied shear load (0.42 MPa), the permanent deformation rate increases with increasing temperature, this is due to temperature-dependent bituminous interlayer material. Thus, cyclic shear tests showed the best interlayer shear fatigue performance at the testing temperature of 10°C.

As an example, Figure 5.17 shows the effect of interface type (presence or absence of tack coat) on the evolution of permanent displacement at the layer interface during Cyclic-ASTRA at 20 °C. It is possible to observe that specimens with tack coat (TC) show a greater deformation compared to specimens without tack coat (UN). This is in agreement with Cyclic-Leutner test results and Diakhaté et al. (2011).

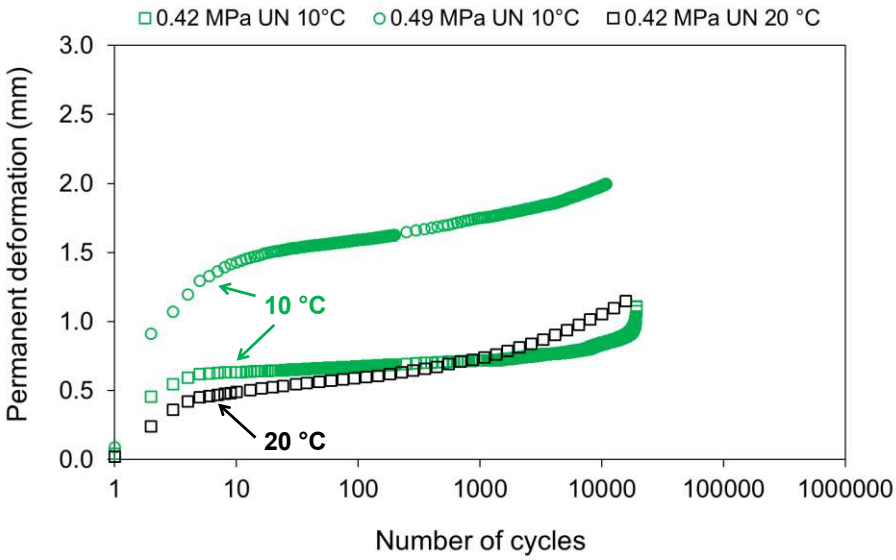

Figure 5.16. Effect of temperature and loading amplitude on the displacement at the layer interface during the Cyclic-ASTRA test.

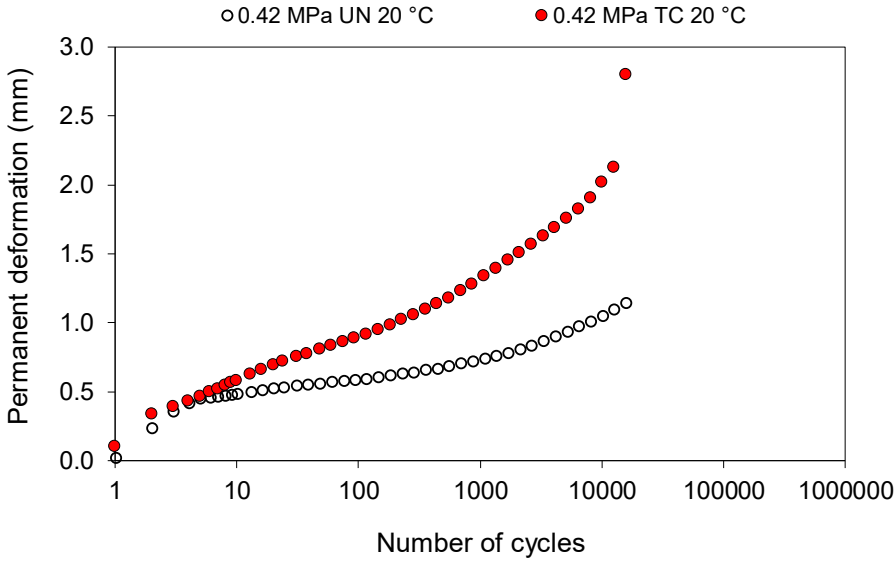

Figure 5.17. Effect of interface type on the displacement at the layer interface during the Cyclic-ASTRA test at 20 °C, 5 Hz and 0.42 MPa.

Figure 5.18 shows the applied shear stress amplitude versus the number of cycles to failure (considered as the number of cycles that cause the detachment between the two layers of the specimen) for UN specimens at 10 °C and 20 °C. Also, the characteristic interlayer shear fatigue curves were drawn in the figure based on the following equation:

$$\tau_0 = a \cdot N_{50}{}^{-b} \tag{5.2}$$

where a and b are the regression coefficients. The specimens cored at the centre of the slabs were not considered in the regression line since they showed out-of-trend behaviour.

From Figure 5.18, it can be noted that decreasing the applied shear stress, the number of cycles to failure increases. Besides, the specimens show a higher shear fatigue resistance at 10 °C compared to specimens at 20 °C. It is possible to observe that parameter a is sensible to the temperature (i.e., a increases decreasing the temperature), whereas b remains constant and close to -0.1. Moreover, the coefficients of determination (R^2) is higher at 10 °C since scattered results were obtained for specimens at 20 °C. However, either way, the results showed an acceptable correlation, although it is well known that fatigue test results have usually a significant dispersion.

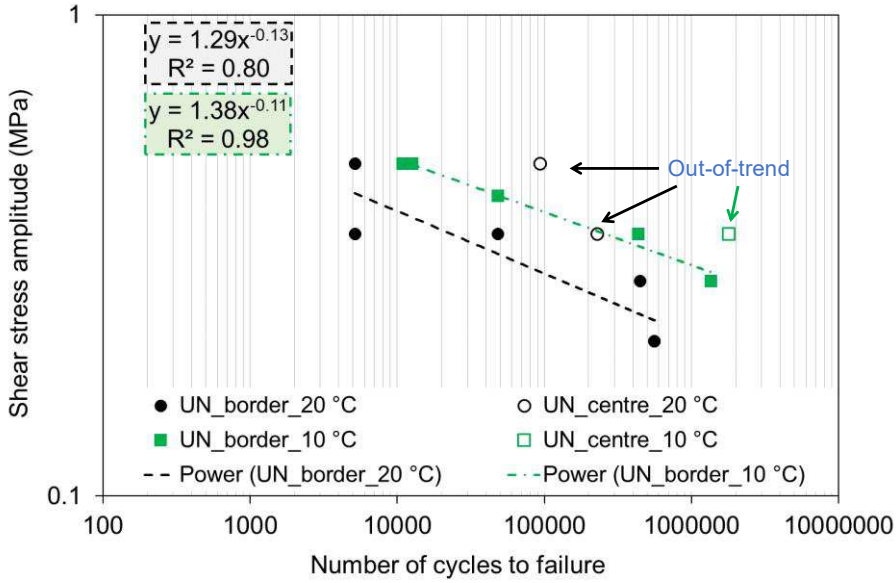

Figure 5.18. Interlayer shear fatigue curves of UN specimens obtained from Cyclic-ASTRA test (T = 10 °C and 20 °C).

Figure 5.19 shows the applied shear stress amplitude versus the number of cycles to failure (considered as the number of cycles that cause the detachment between the two layers of the specimen) for UN and TC specimens at 20 °C and the respective characteristic interlayer shear fatigue curves. The specimens cored at the centre of the slabs were not considered in the regression line since they showed out-of-trend behaviour. From Figure 5.19, it can be noted that, considering the same shear load amplitude, the number of cycles to failure increases in presence of tack coat (TC). Thus, the specimens with tack coat (TC) show a higher shear fatigue resistance compared to specimens without tack coat (UN) obtaining similar results to that of the Cyclic-Leutner. The coefficients of determination (R^2) is higher for TC specimens even if the tests conducted on the TC specimens are lower than the UN specimens.

Moreover, it was noticed that specimens cored at the centre of the slabs showed a better interlocking between the two layers in contact (Figure 5.20).

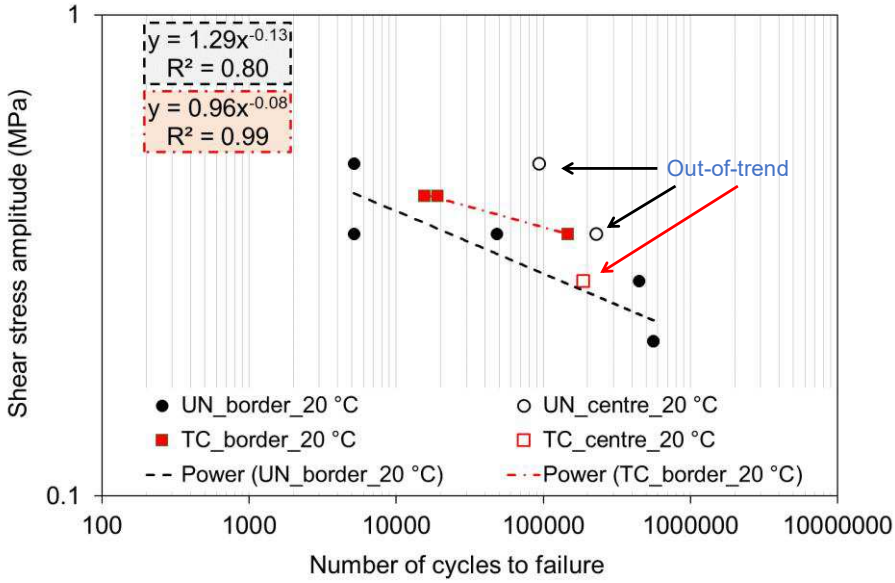

Figure 5.19. Interlayer shear fatigue curves of UN and TC specimens obtained from Cyclic-ASTRA test (T = 20 °C).

Figure 5.20. Failure mechanisms of the specimens cored at the centre (left) and border (right) of the slab.

5.5 Conclusions

This chapter summarises the experimental activities carried out at Università Politecnica delle Marche (UNIVPM) to identify an appropriate testing procedure for the dynamic characterisation of interface properties (stiffness, fatigue) in bituminous pavements and verify the effectiveness of the new dynamic testing device (Cyclic-ASTRA). To this end, an extended testing program was carried out in order to assess the interlayer shear properties by means of static and cyclic tests and to perform tests with a new cyclic testing device within the RILEM TC 272-PIM framework. Based on the test results, the following main conclusions can be drawn:

- The static test showed that, in the same testing conditions (speed and temperature), the ASTRA device measured lower ISS values with respect to the Leutner device. As regards Leutner test, ISS with the application of tack coat are better than those for specimens without tack coat.
- Cyclic tests allow characterising the interlayer properties, in terms of stiffness and resistance to repeated loading (cumulative damage). In particular, cyclic tests simulate the repetitive load of moving vehicles in order to measure the number of shear load cycles that is required to cause failure at the interface. The results obtained performing the Cyclic-Leutner test and the Cyclic-ASTRA test showed that the presence of the tack coat at the interface provides a significant increase of the resistance to repeated shear loading. This finding is in agreement with the results of static Leutner tests.
- The preliminary results of the new Cyclic-ASTRA device are promising due to increased precision of the measurements, lower compliance of the testing equipment and possibility to allow dilatancy movements perpendicular to the interface, as well as the application of normal stress at the interface. The measured interlayer shear stiffness decreases as the testing temperature is increased.
- To improve the Cyclic-ASTRA device and its testing procedure, further experimental investigations are needed conducting cyclic tests using both field cores and laboratory-fabricated specimens composed of various types of interlayer systems.
- During the Cyclic-ASTRA test, the cored specimens in the centre of the double-layered slabs showed a dissimilar behaviour compared to the other specimens, indicating a lack of homogeneity in the mechanical properties at the interface between the centre and border of the slab.

Chapter 6.

Experimental investigation with Cyclic-MAST

6.1 Introduction

In the framework of the RILEM interlaboratory test (chapter 4), this chapter describes the research activities entirely carried out in the Department of Civil, Construction, and Environmental Engineering at North Carolina State University (Raleigh, USA) under the supervision of Professor Y. Richard Kim and Dr Nithin Sudarsanan. The double-layered asphalt concrete slab samples, prepared at the laboratory of the Università Politecnica delle Marche, were shipped to the North Carolina State University (NCSU), Raleigh, USA. The cylindrical specimens for carrying out cyclic shear tests using Modified Advanced Shear Tester (MAST) were cored from these slabs at NCSU's pavement laboratory. The following paragraphs present the MAST device and describe the test methodology. Subsequently, the findings of the outcomes during the experimental investigation are discussed.

6.2 Specimen preparation

Two double-layered slab samples with tag numbers 12 and 15 among the 19 RILEM slab samples set (described in chapter 4) were used in this study. The current NCSU laboratory procedure for MAST specimen extraction from the slab samples recommends coring the specimens at least an inch (25 mm) away from the edge of the slab in order to eradicate the effect of air void gradient. This practice allows the user to obtain uniform and consistent test specimens. Thereby, four cylindrical specimens were cored from each slab with a nominal diameter of 100 mm (Figure 6.1). After that, a manually operated saw was used to cut the specimens to a height of 80 mm (Figure 6.2) to obtain the final MAST specimen. Each cored specimen was marked by a unique identification code (ID) defining the slab number and the core's position within the slab (Figure 6.1); for example, 12_1 represents the specimen cored in slab 12 in the position 1.

Air voids of all MAST specimens were measured prior to testing. Two methods were employed to measure the air voids of each specimen (1) Dimension method (EN 12697-06, clause D) and (2) CoreLok method (AASHTO T 331). The two methods differ in the measuring technique used for quantifying the bulk specific gravity. The former method dries the wet specimen after sawing by keeping it in a well-aerated rack for 24 hours before weighing as well as makes use of the physically measured specimen dimensions to calculate its volume, thereby the bulk specific gravity. While the latter method dries the specimen

using a CoreDry unit that expedites and completes the drying procedure within 30 minutes (Figure 6.3). In addition, the CoreLok method measure the specimen volume using Archimedes principles and utilises a vacuum-sealing device composed of an automatic vacuum chamber (shown in Figure 6.4a) with a specially designed, puncture-resistant plastic bag, which tightly conforms to the sides of the specimen (shown in Figure 6.4b) and prevents water from infiltrating into the specimen during the submergence in water. After obtaining the bulk specific gravity of cored specimens, the air voids of specimens were computed. Table 6.1 provides the final properties of the specimens. The specimens presented an average air void content of 3.8±0.8%.

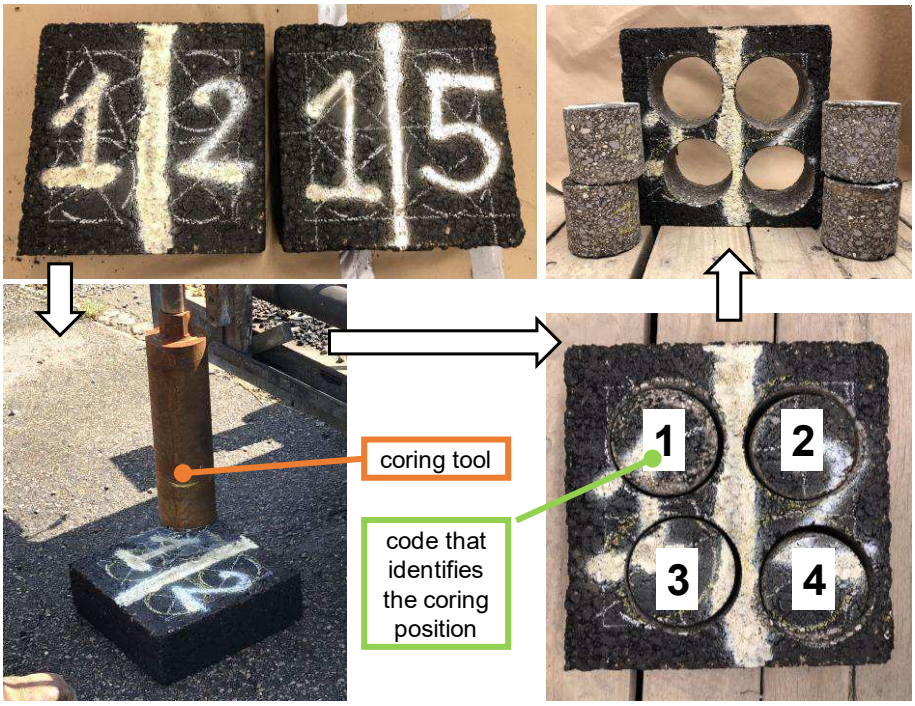

Figure 6.1. Coring procedure.

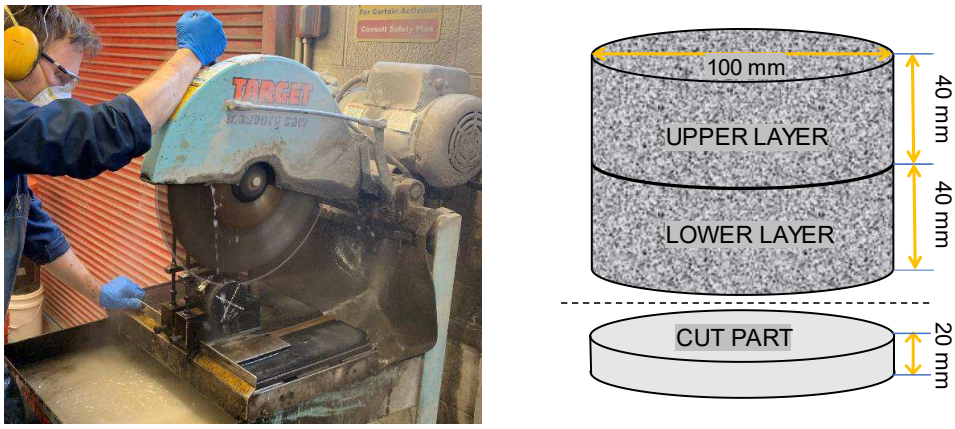

(a) (b)

Figure 6.2. (a) Cutting procedure and (b) scheme of specimen cutting.

(a) (b)

Figure 6.3. (a) CoreDry device and (b) specimen inside the CoreDry device.

(a) (b)

Figure 6.4. (a) CoreLok device and (b) sealed specimen.

Table 6.1. Final properties of the specimens.

Specimen ID	Bulk specific gravity (g/cm^3)		Air voids (%)	
	By dimensions	*CoreLok method*	*By dimensions*	*CoreLok method*
12.1	2.39	2.37	4.4	5.2
12.2	2.40	2.42	3.6	3.1
12.3	2.41	2.41	3.4	3.3
12.4	2.39	2.42	4.1	3.1
15.1	2.39	2.39	4.0	4.3
15.2	2.38	2.38	4.5	4.8
15.3	2.42	2.42	3.2	3.2
15.4	2.41	2.42	3.5	3.2

6.3 Testing device and program

6.3.1 Modified Advanced Shear Tester (MAST)

MAST device was designed and developed at NCSU to investigate the interface shear strength properties of double-layered AC specimens. It has the capability to test specimen with different geometries, such as cylindrical specimens with 101.6 mm diameter and square-shaped specimens with dimensions 152.4 mm by 101.6 mm. Figure 6.5 presents the schematics of the MAST device. This device can perform both static as well as cyclic shear tests under different environmental conditions (e.g., load- or displacement-controlled mode at various temperatures) at various confining pressures.

The MAST device is composed of a fixed side platen and a movable side platen separated by a shear gap of 8 mm. The movable side platen is free to move vertically (parallel to the interface) as well as horizontally (perpendicular to the interface). This unconstrained movement is provided by employing some linear tracks with ball bearings. The pavement response study shows that the normal stress changes considerably in the top bituminous layers under moving vehicle loadings during the shear loading process. Henceforth, the MAST is designed for the user to apply a normal confining load to the specimen by means of a bolt and spring system. The confinement system is based on the normal load application concept previously utilised in the design of the advanced shear tester (AST) developed by Zofka et al. (2015). The four springs system also permits the specimen interlayer to dilate or contract during the test while maintaining the constant normal stiffness (CNS) condition. Based on the laboratory experience and field observations, Zofka et al. (2015) showed that CNS conditions mimic the realistically stress-states observed by bituminous pavement structures.

The initial step in placing the MAST specimen to the loading jig was to glue the specimen to the steel shoes using DEVCON steel putty (Figures 6.6 and 6.7). Every steel shoe has grooves to provide sufficient bond between the shoes and the specimen. Extreme care was taken to clean the shoes before each glue application to prevent failure at the glued area. A special guiding jig was employed to ensure proper alignment of the specimen during gluing, thus minimising any eccentricity that might occur during the test. Once the specimen was properly glued into the shoes, it was allowed to cure for 24 hours. Further, the specimen in the shoes was mounted to the MAST device through a system of screws (Figure 6.8).

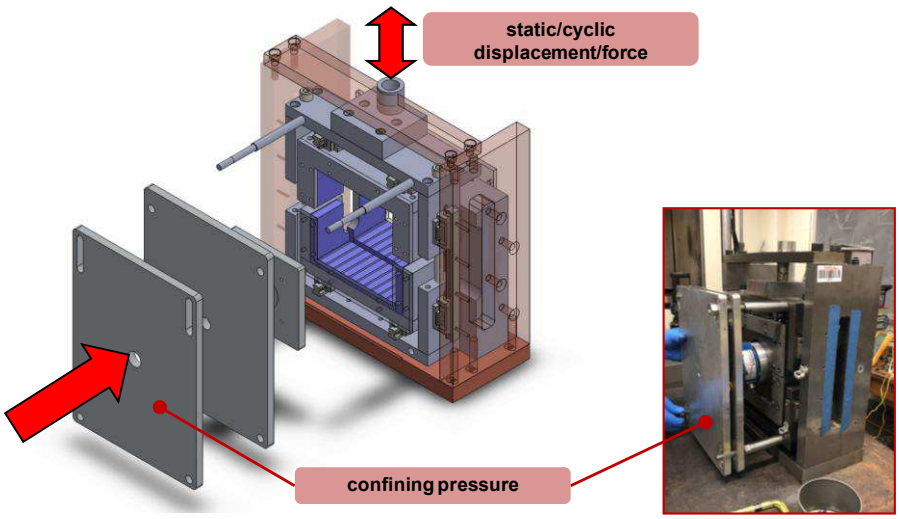

Figure 6.5. MAST device.

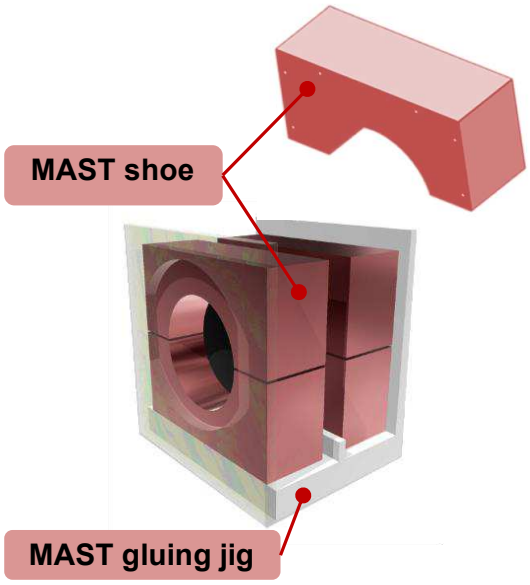

Figure 6.6. MAST shoe and gluing jig.

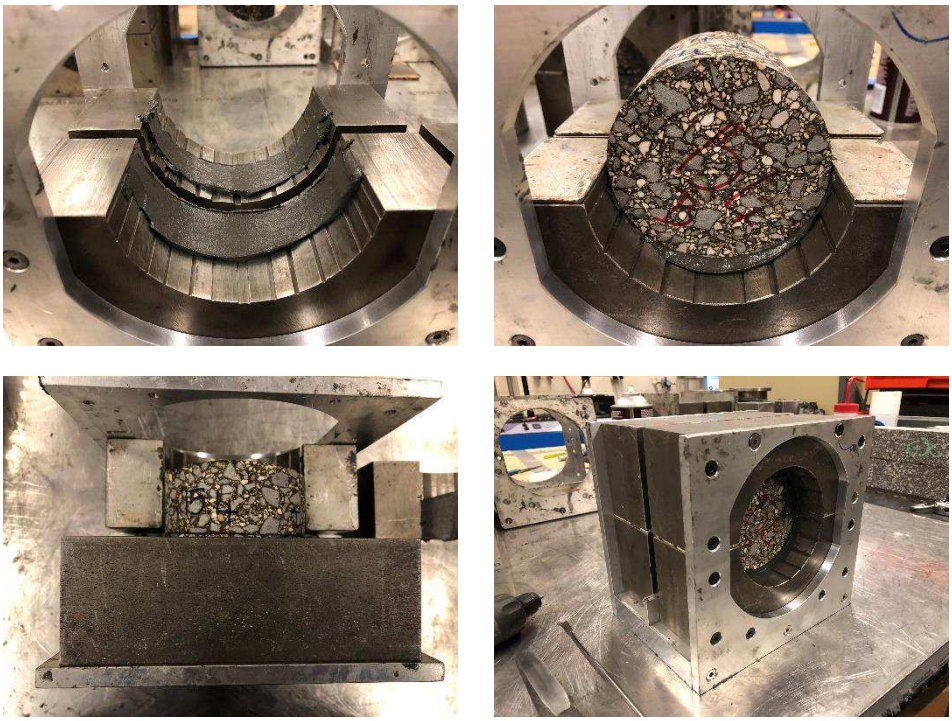

Figure 6.7. Gluing procedure of MAST specimen.

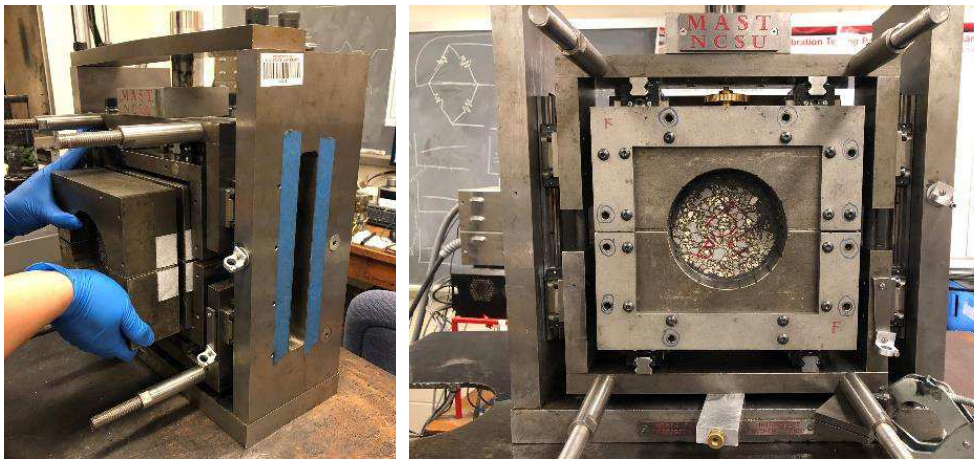

(a) (b)

Figure 6.8. (a) Loading specimen into the MAST and (b) specimen mounted into the MAST setup.

6.3.2 Digital image correlation (DIC) technique

In this study, digital image correlation (DIC) technique was used to measure the on-specimen displacements at the interface instead of conventional LVDTs due to the expected rocking action of the specimen during the test and the lack of proper mounting facilities for LVDT in the test setup. DIC is a noncontact technique based on the concept of optical flow, proposed by Gibson (1950), combined with automated photo-matching developed in the 1970s for photogrammetry (Andrawes and Butterfield, 1973; Butterfield et al., 1970). In the recent past, DIC method has been utilised in asphalt concrete testing to study the mechanisms of cracking and debonding (Buttlar, 2014; Chehab et al., 2007; Kim and Wen, 2002; Safavizadeh and Kim, 2017).

The DIC technique comprises capturing a sequence of images of the sample at regular intervals during the testing. Then, the post-processing image software compares and detects the difference between the location of pixel points between consecutive images taken during the test. These differences are interpreted in the image space (in pixels) are translated to object space (in mm or inches depending on the unit of calibration scale) as deformations or movements of the sample at a specific time while the image was captured.

The MAST device has been designed to capture images of the sample surface (or shoe) near the interface through an opening provided in the testing frame (Figure 6.9). The DIC technique tracks the movement of image pixels in the side by side images. In order to make smooth and distinct tracking of pixels for the analysis software, a uniformly sized speckled pattern should be marked or glued onto the specimen surface. In this study, four speckled papers were attached to steel shoes (Figure 6.9). Each speckle paper is a white paper piece with black paint sprayed over to form fine dots. Figure 6.9 also presents the basic concept used in the DIC analysis. The key aspects and details of the DIC analysis can be found in Safavizadeh and Kim (2017).

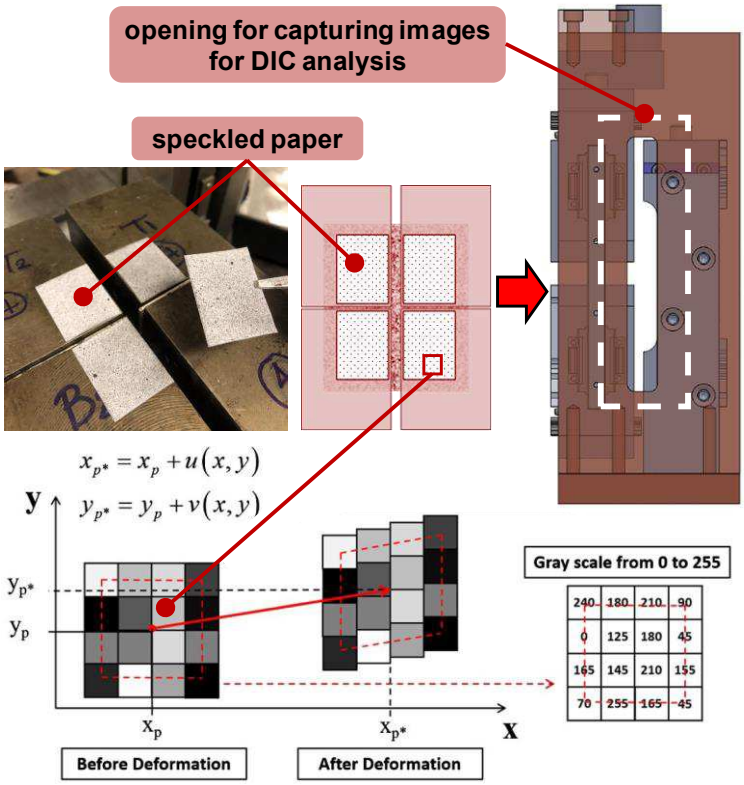

Figure 6.9. Speckled paper and DIC matching process (Safavizadeh and Kim, 2017).

The DIC setup (Figure 6.10) includes a 5-megapixel camera along with a 35–75 mm f:3.3–4.5 manual focus lens to capture images. The two dual-fibre optical gooseneck lights were used to provide consistent, cool and sufficient lighting on the specimen surface. An adjustable tripod stand with built-in bubble levels was used to level the camera and place it at an approximate distance of 75 cm from the specimen and at the same height and lateral position as the specimens. A relatively high shutter speed of 1.5 ms was used to prevent blurry images. An f-stop of 3.3, which is a relatively wide lens aperture size, was used to let the maximum possible light to hit the camera sensor. A relatively low gain setting close to -3 db was used to prevent unwanted image noise. The DIC camera was connected to a computer that was installed with two commercial available DIC software developed by Correlated Solutions, Inc: Vic-Snap and Vic-2D. Vic-Snap software was used to acquire the images during the test, and also aid in controlling the camera shutter speed, position, and lighting levels. While VIC-2D is a two-dimensional DIC analysis software used to calibrate the scales, analyse the captured images, and calculate the displacements and strains through

the comparison of images using advanced mathematical algorithms. During the current cyclic shear tests, images were taken at a regular time interval of 214-ms. Finally, a MATLAB code was used to elaborate on the displacement at the layer interface.

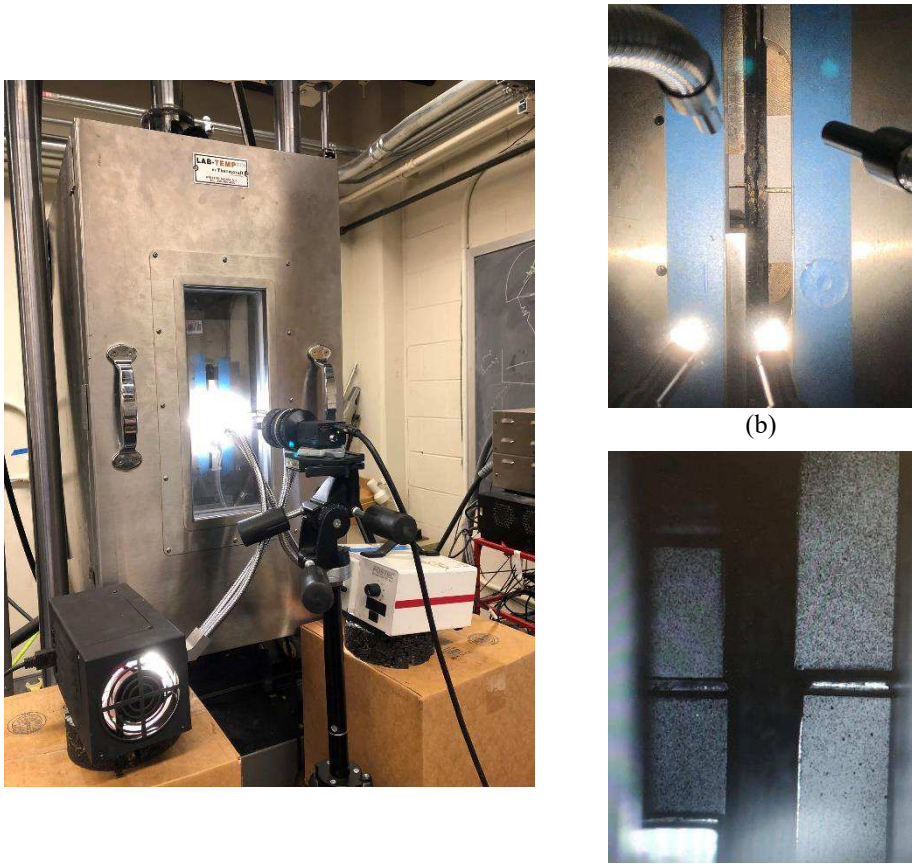

(a) (b) (c)

Figure 6.10. (a) DIC camera and light setup, (b) MAST with DIC lighting, (c) image taken using Vic-Snap.

6.3.3 Cyclic-MAST test

In this study, the MAST device was used to perform cyclic shear tests. A climate chamber, equipped with liquid nitrogen as the coolant and a closed-loop feedback system, was used to control and maintain a constant testing temperature (Figure 6.11). Cyclic shear tests were carried out in haversine displacement control mode applied to the specimens using an MTS servo-hydraulic material testing system with a 100 kN load cell (Figure 6.11). The tests were performed in tension mode until failure of the specimen, but since the tests were carried out

in displacement control mode, it may happen that the specimen does not fail destructively. The tests were carried out at a temperature of 20 °C with a frequency of 5 Hz. A normal (confining) stress was not applied to the specimen. The specimens were kept in the testing climate chamber at 20 °C for at least 3 hours before testing. Actuator displacements and shear loads were acquired using a 16-bit National Instruments data acquisition board and collected using LabVIEW software. DIC analysis was also adopted to track the interface displacement.

Thus, compared to the test protocol used for the Cyclic-ASTRA test, the same type of load (haversine), frequency (5 Hz), testing temperature (20 °C) and absence of normal load were used. The only difference is that the tests were performed in the displacement control mode because it is a safer test mode at the fracture points.

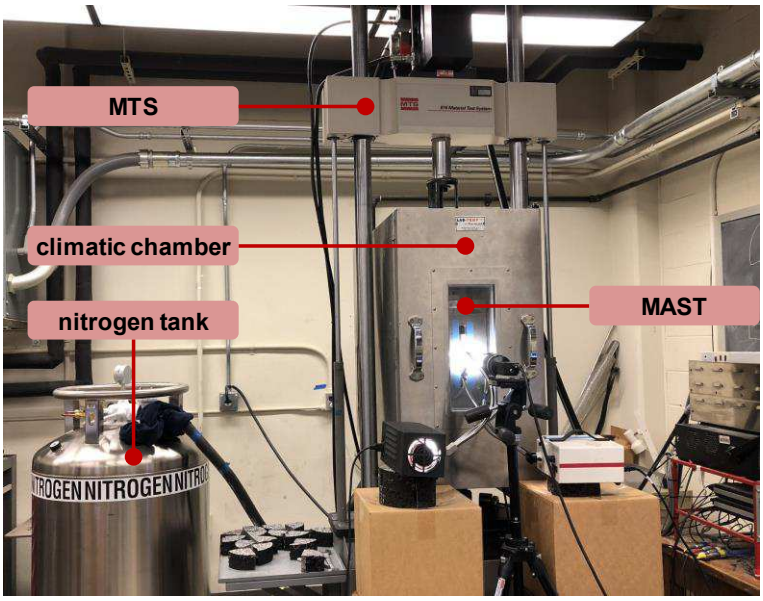

Figure 6.11. MAST installed in the MTS machine.

Figure 6.12 depicts the flowchart of the testing program. The primary step prior to cyclic shear tests is to determine the acceptable displacement amplitudes levels for the cyclic shear test. A displacement amplitude sweep (DAS) test was performed to fix the threshold displacement levels for the cyclic shear test. Subsequently, constant displacement amplitude cyclic (CDAC) tests were carried out to evaluate the shear fatigue resistance. Finally, the fatigue curve was obtained applying a 50% failure criterion ($N_f = N_{50}$) to the test results.

The DAS tests were performed in order to define the actuator displacement level that allows the specimen to fail within reasonable loading cycles during the cyclic shear test. DAS test was designed based on a test duration of 5500 cycles, as such tests are relatively quick to run (less than 20 min). The test protocol consisted of 22 displacement amplitude

steps (from 0.0625 mm to 2.5 mm), each step with 250 cycles and a rest period of 5 seconds between two consecutive loading steps (Figure 6.13). Table 6.2 reports the level of displacement amplitude applied in each loading step. The actuator displacement amplitude of the last loading step was 2.5 mm. The maximum amplitude value of 2.5 mm was chosen as it represents the typical actuator displacement that corresponds to the maximum shear strength during the Static-MAST tests at 20 °C performed by the previous researchers at NCSU on the asphalt concrete specimens. Based on this test results, a particular displacement amplitudes range was selected in such a way to create CDAC test with a spread of numbers of cycles to failure (N_f) in the range of 10^3–10^6 cycles. However, this choice does not consider the unexpected circumstances that can arise during testing.

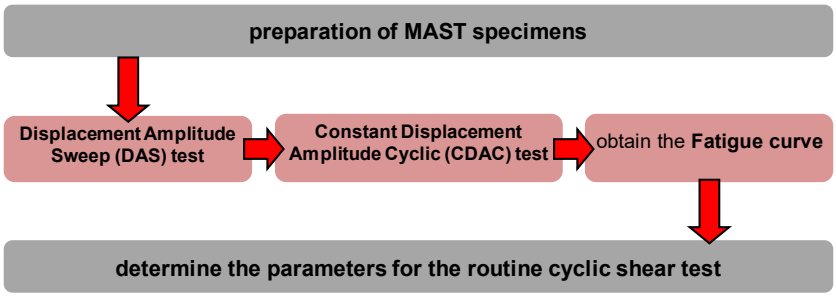

Figure 6.12. Cyclic-MAST test sequence.

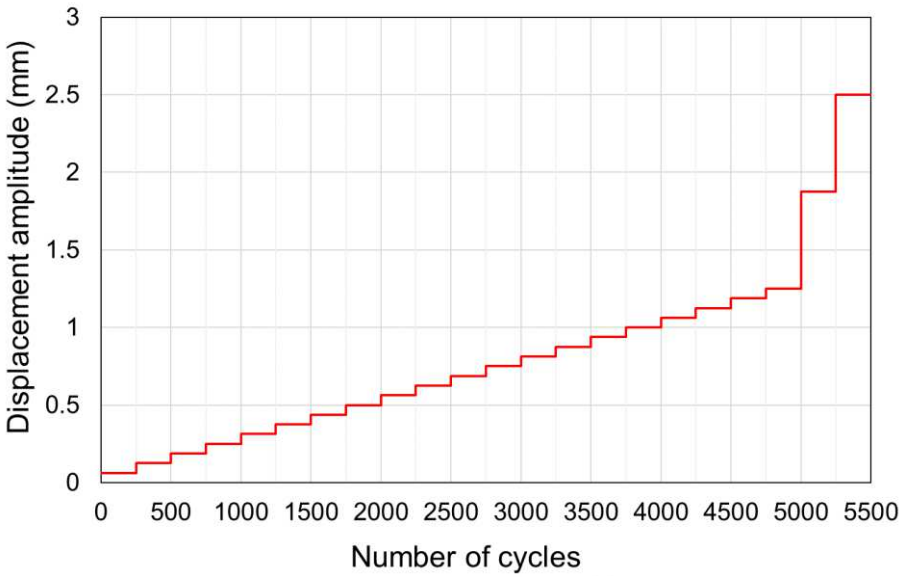

Figure 6.13. Test protocol for DAS test.

Table 6.2. Test protocol for DAS test.

Step (#)	Displacement amplitude u_0 (mm)	Displ. ratio* $u_{0,i}/u_{0,22}$ (-)	N. cycles
1	0.0625	0.03	250
2	0.125	0.05	250
3	0.1875	0.08	250
4	0.25	0.1	250
5	0.3125	0.13	250
6	0.375	0.15	250
7	0.4375	0.18	250
8	0.5	0.2	250
9	0.5625	0.23	250
10	0.625	0.25	250
11	0.6875	0.28	250
12	0.75	0.3	250
13	0.8125	0.33	250
14	0.875	0.35	250
15	0.9375	0.38	250
16	1	0.4	250
17	1.0625	0.43	250
18	1.125	0.45	250
19	1.1875	0.48	250
20	1.25	0.5	250
21	1.875	0.75	250
22	2.5	1	250

*Displacement ratio calculated as the ratio between displacement amplitude at the ith step ($u_{0,i}$) and at the 22nd step ($u_{0,22}$).

The experimental program was based on two DAS tests (one specimen from each slab cored in position 1, see Figure 6.14) and six CDAC tests (three specimens from each slab, see Figure 6.14). The specimens for the CDAC tests were cored from the same position in the two slabs (i.e., #2, #3, #4) and were tested with the same displacement amplitude.

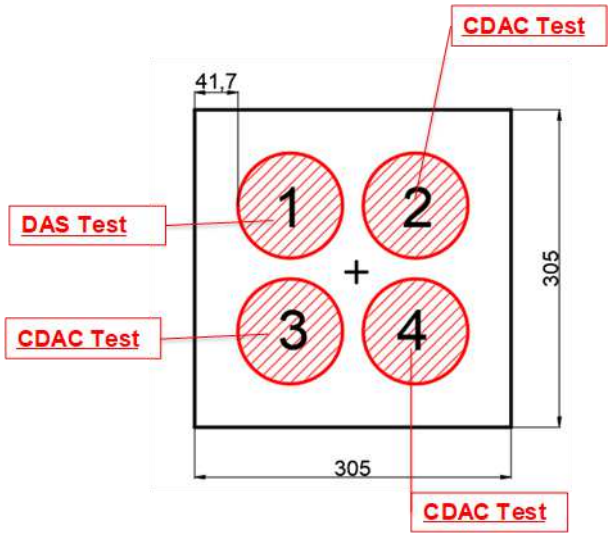

Figure 6.14. Testing scheme based on specimen coring position.

A unique identification code was used for each tested specimen (X.Y_Z) in order to facilitate comparisons among the different tests. X stands for the slab code (i.e., 12 or 15), Y stands for the coring position (from 1 to 4, see Figure 6.14) and Y stands for the type of test performed (A for DAS test, and F for CDAC test). For example, the specimen ID 12.1_A represents the specimen cored from the slab 12 in position 1 tested with a displacement amplitude sweep (DAS) test.

Figure 6.15 presents typical inputs and responses obtained from the cyclic-MAST test. Even though the actuator displacement remains in tension throughout the cyclic test, the stress response includes both tensile and compressive stress levels in the cycle because of the material's viscoelastic nature. Besides, it is noteworthy that DIC analysis was only processed for DAS tests.

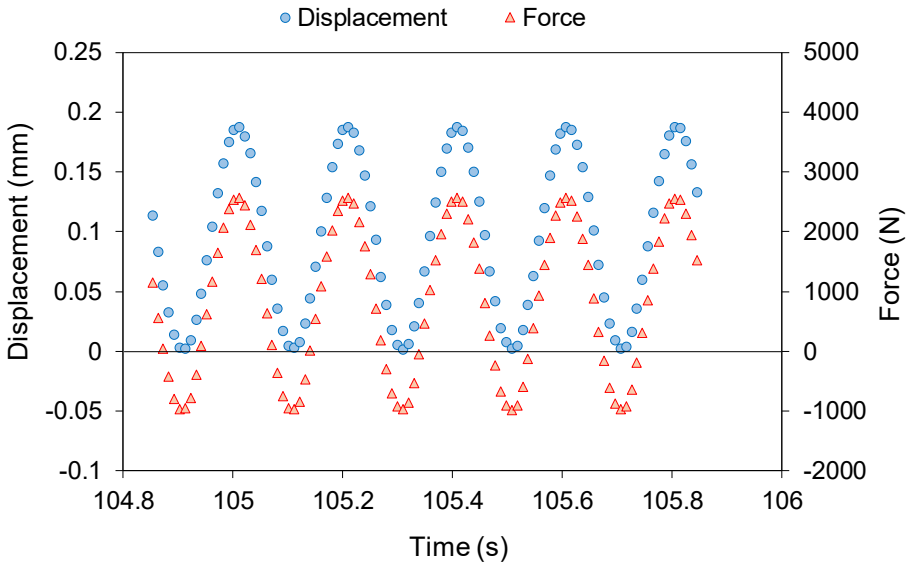

Figure 6.15. Typical input and response for displacement and force versus time.

During the cyclic-MAST, test displacement and force are recorded, the amplitude of the shear stress τ_0 can be calculated from the following equation:

$$\tau_0 = \frac{F_0}{A} \tag{6.1}$$

where F_0 is the amplitude of the force and A is the cross-sectional area of the specimen.

The interlayer shear stiffness (K) can be assumed to be a characteristic value to be used to measure the level of interlayer bonding and can be calculated based on the following equation:

$$K = \frac{\tau_0}{u_0} \tag{6.2}$$

where u_0 is the amplitude of the displacement at the interface.

One of the issues in determining the failure criterion in a displacement-controlled test is the fact that there is no catastrophic failure as the specimen is pushed and pulled at a specific distance. In this study, a conventional failure criterion was used, referring to classical fatigue tests performed on asphalt mixtures. This is expressed as the number of loading cycles to failure ($N_f = N_{50}$), which is equal to the cycle corresponding to a 50% reduction of the initial interlayer shear stiffness (K) as shown in Figure 6.16. The initial K value (K_{in}) is

defined at the loading cycle where defined displacement amplitude was achieved (approximately after 100 loading cycles).

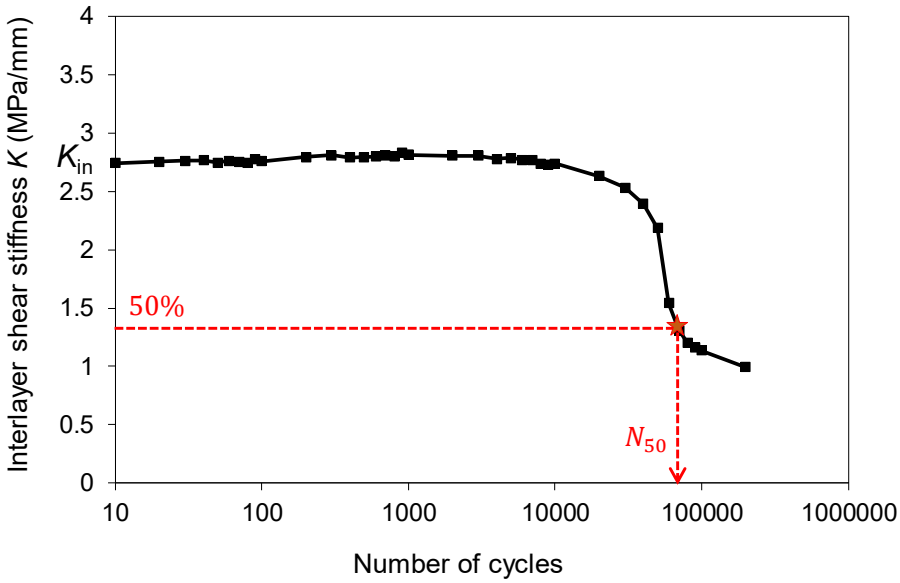

Figure 6.16. Identification of N_{50}.

Based on the fatigue lives of three different displacement amplitudes with two repetitions (6 CDAC tests in total), the characteristic interlayer shear fatigue curves were drawn based on the following equation:

$$u_0 = a \cdot N_{50}{}^{-b} \tag{6.3}$$

where a and b are the regression coefficients.

6.4 Result and analysis

6.4.1 Displacement amplitude sweep (DAS) test

Figures 6.17 and 6.18 present the results of the DAS tests at 20 °C conducted on the specimens 1.1_A and 2.1_A calculated using the actuator displacement. In Figure 6.17, it is possible to observe that the force amplitude required for achieving a specific displacement amplitude increases to a critical value, after which a drop in the force amplitude occurs. Although the displacement amplitude continues to increase, the force amplitude remains at low levels, due to the failure at the interlayer of the specimen. The force amplitude peak is

not the same for the two specimens; the specimen 12.1_A shows higher resistance to displacement amplitude increase. This could be due to the specimen-to-specimen variability or slab compaction variability. In Figure 6.18, it can be observed that increasing displacement amplitudes lead to interlayer shear stiffness (*K*) degradation. Suddenly, an abrupt decrease in *K* occurs.

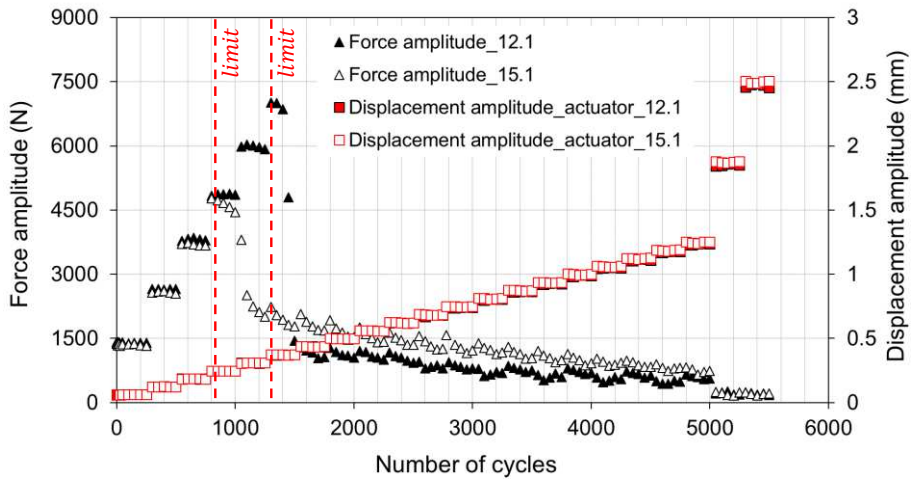

Figure 6.17. Evolution of the force amplitude and actuator displacement amplitude as a function of the number of cycles in the DAS test at 20 °C.

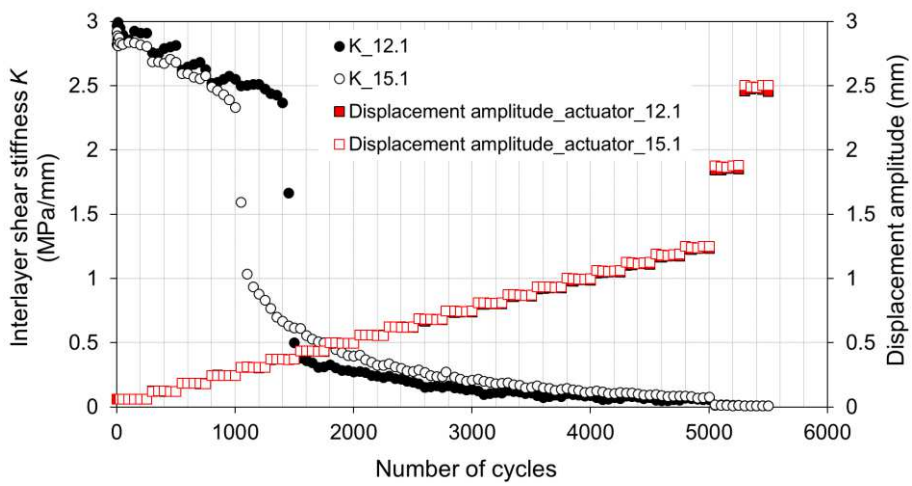

Figure 6.18. Evolution of the interlayer shear stiffness and actuator displacement amplitude as a function of the number of cycles in the DAS test at 20 °C.

Figures 6.19 presents the interlayer shear stiffness (*K*) of the specimens 1.1_A and 2.1_A calculated using the displacement amplitude calculated by the DIC technique instead of actuator displacement. The same observations of Figure 6.18 can be carried out. However, comparing Figures 6.18 and 6.19, it is possible to note that the interlayer shear stiffness (*K*) determined by use of DIC displacement has a higher value than that determined by use of actuator displacement (a higher order of magnitude). This is due to the fact that DIC displacements, that are measured on the specimen, are lower than the actuator displacements due to machine compliance issues (i.e., deformation of certain machine components throughout the loading frame) as shown in Figure 6.20. This observation is in agreement with previous studies (Chehab et al., 2002).

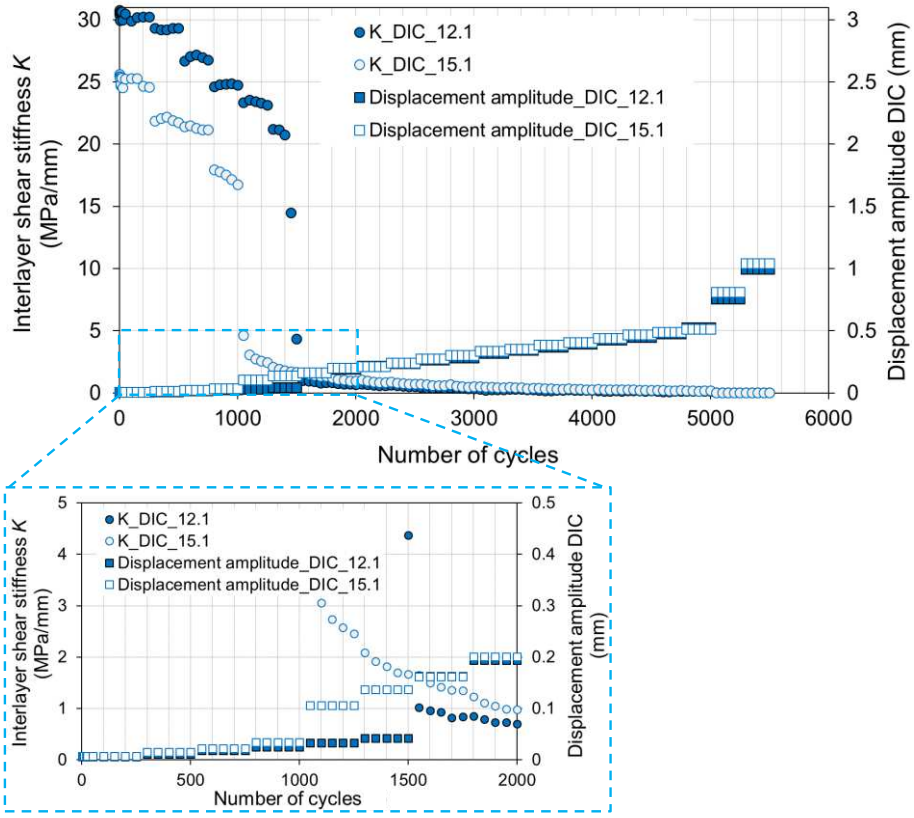

Figure 6.19. Evolution of the interlayer shear stiffness and DIC displacement amplitude as a function of the number of cycles in the DAS test at 20 °C.

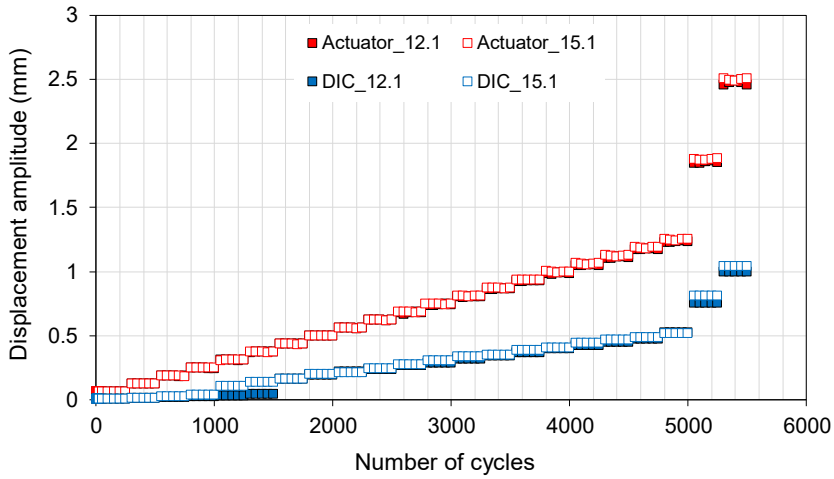

Figure 6.20. Evolution of actuator displacement amplitude and DIC displacement amplitude as a function of the number of cycles in the DAS test at 20 °C.

In Figure 6.17, the displacement amplitude at which a sudden drop in force amplitude occurs can be considered as the upper limit for CDAC tests since selecting that amplitude would lead to short fatigue life. These limits were 0.375 mm and 0.3125 mm for specimen 12.1_A and 15.1_A, respectively (red dashed line in Figures 6.17). The same response can be found while considering the interlayer shear stiffness (K). The maximum displacement amplitude for CDAC tests should be selected below the identified upper limit. Analogously, the lowest displacement amplitude that has been applied by the actuator for the DAS test was (0.0625 mm) selected as the lower limit of the displacement amplitudes range for the CDAC test. Consequently, the following displacement amplitudes were selected for CDAC tests: 0.25 mm, 0.19 mm, and 0.15 mm as shown in Table 6.3.

Table 6.3. Displacement amplitude input for CDAC test.

Specimen ID	Displacement amplitude u_0 (mm)
12.2	0.25
12.3	0.19
12.4	0.15
15.2	0.25
15.3	0.19
15.4	0.15

6.4.2 Constant displacement amplitude cyclic (CDAC) test

Figures 6.21 and 6.22 show the evolution of the interlayer shear stiffness (*K*) for CDAC tests of specimens cored from slab 12 and slab 15, respectively. During the CDAC test, the interlayer stiffness is almost constant with the number of cycles, but a sudden drop occurs after a certain number of cycles. After the drop, the interlayer shear stiffness remains at a very low level.

Another important observation is that an increase in the constant displacement amplitude causes a faster stiffness degradation. As regards Figure 6.22, the result of specimen 15.2_F, tested with a constant amplitude displacement of 0.25 mm, was not reported because the specimen failed immediately after the start of the test (a few numbers of cycles).

Figure 6.23 shows the comparison of interlayer shear stiffness *K* of specimens cored from the two slabs (12 and 15). Looking at the results of the specimens 12.3_F and 15.3_F, that were tested at the same constant displacement amplitude (0.19 mm), it is possible to observe that the general trend is the same, but specimen 12.3_F shows an initial higher *K* and a higher shear fatigue resistance compared to specimen 15.3_F. Since the specimens were cored out of the slabs in the same position and tested at the same displacement amplitude, this difference could be due to the variability of fatigue tests as well as to the variation of the compaction quality in the two slabs. This is consistent with the previous findings for DAS tests. However, it is worth noting that the failure mechanisms of the investigated double-layered specimens occurred perfectly at the interface. An example of a specimen at the end of the test is reported in Figure 6.24.

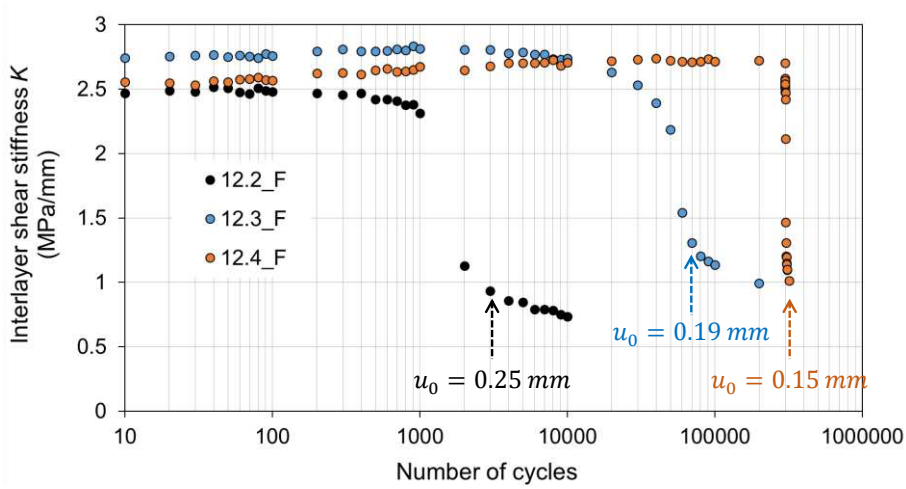

Figure 6.21. Evolution of interlayer shear stiffness as a function of the number of cycles in the CDAC test at 20 °C for specimens cored from slab 12.

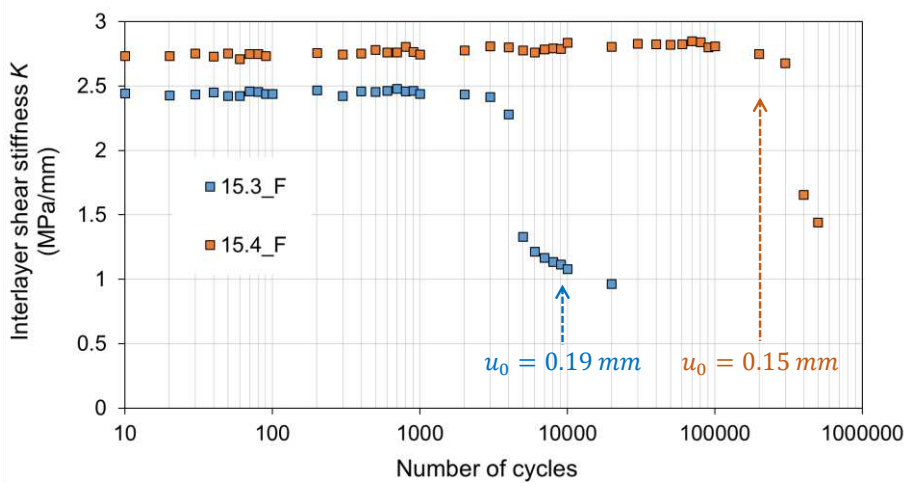

Figure 6.22. Evolution of interlayer shear stiffness as a function of the number of cycles in the CDAC test at 20 °C for specimens cored from slab 15.

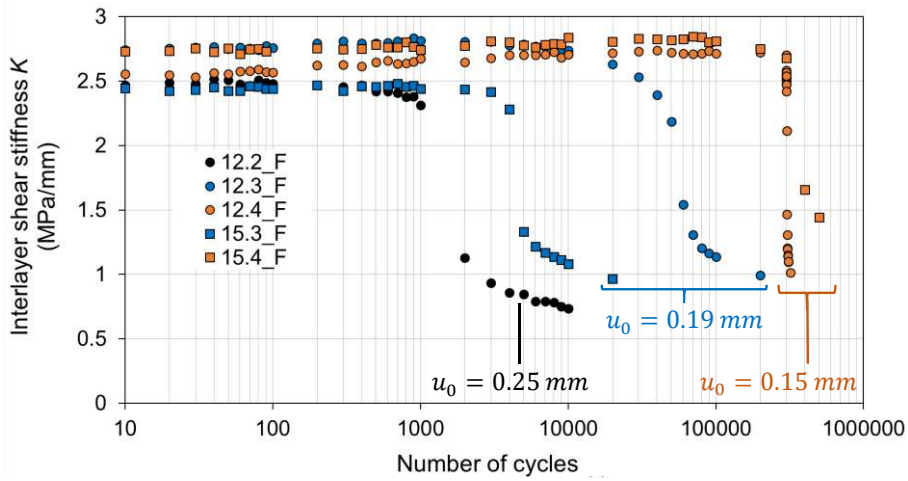

Figure 6.23. Comparison of interlayer shear stiffness as a function of the number of cycles in the CDAC test at 20 °C for specimens cored from slab 12 and slab 15.

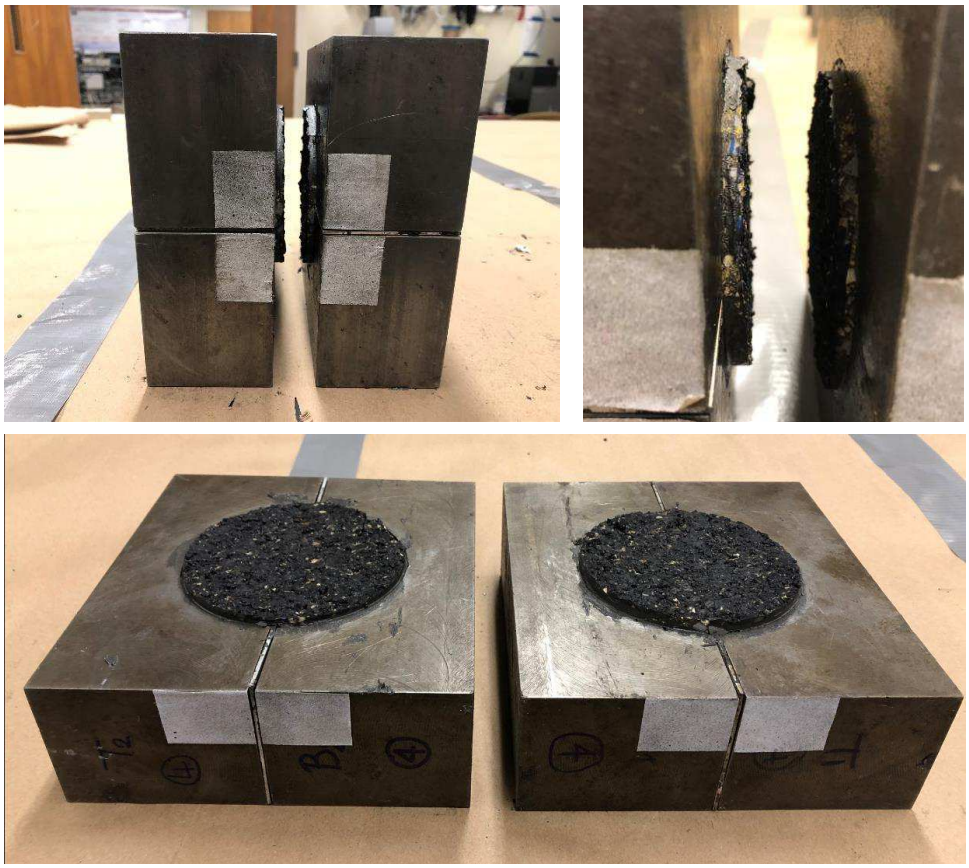

Figure 6.24. Failed specimens after the CDAC test.

Figure 6.25 presents the test results as the input displacement amplitude levels versus the number of cycles to failure (N_{50}) in the log-log scale. A good agreement was found between the measured fatigue lives of the specimens (R^2 = 0.83). However, the not so high value of R^2 is mainly due to the variation that occurred during the fatigue tests as well as the specimen-to-specimen variation. However, it can be seen that fatigue law parameter b (i.e., slope) is in the same range than that of Cycle-ASTRA (stress-controlled) test (b = -0.13).

To reduce the uncertainty of fatigue test results, an improvement of this method could be to conduct fingerprint tests at constant actuator displacement before running the CDAC tests in order to check the specimen-to-specimen variability more precisely. The fingerprint test shall be performed at the same temperature and frequency of CDAC test for 50 or 100 cycles using a displacement amplitude of 0.0625 mm (i.e., the first step of the DAS test, a very low displacement amplitude to remain in the linear viscoelastic range). The same

concept is used for Asphalt Mixture Performance Tester (AMPT) Cyclic Fatigue Test (AASHTO TP 133-19).

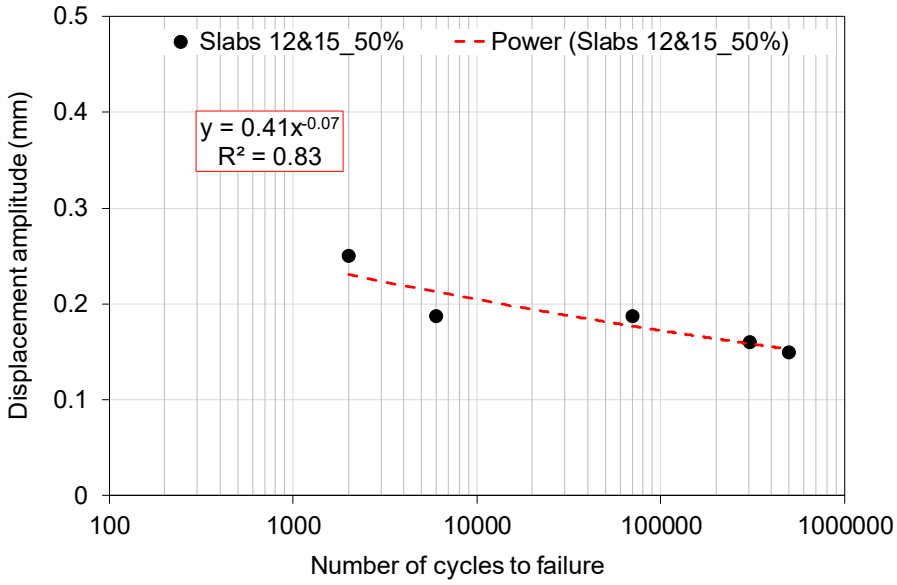

Figure 6.25. Interlayer shear fatigue curve obtained from CDAC tests.

6.5 Conclusions

This study presents the research work carried out at North Carolina State University (USA). MAST device was used to perform cyclic shear tests on 8 cylindrical specimens cored from two double-layered slabs prepared for the RILEM interlaboratory test. A new test protocol is proposed based on the displacement amplitude sweep (DAS) test and constant displacement amplitude cyclic (CDAC) test. Based on the test results, the following main conclusions can be drawn:

- Results showed that cyclic shear tests allow characterising the interlayer damage in terms of interlayer shear stiffness with the number of loading cycles.
- DAS tests allow determining the displacement amplitude level for CDAC tests. The displacement amplitudes should lead to achieving a reasonable test time, that is, to achieve a reasonable number of cycles to failure (10^3-10^6 cycles). Besides, the displacement amplitudes should be selected according to the material under investigation.

- The continuous application of cyclic shear loading in CDAC tests causes a decrease of the interlayer shear stiffness and provokes a failure at the interface of the double-layered specimen.
- CDAC test results were analysed with the traditional approach (50% initial interlayer shear stiffness reduction). A unique interlayer shear fatigue failure curve was identified, but more results are needed to increase the accurateness of the results.

Lastly, Cyclic-MAST test results are promising, but further research is needed to obtain a more exhaustive picture of the governing mechanical properties. In the future, once this test method has been improved, a model based on shear viscoelastic continuum damage (shear-VECD) can be developed and implemented in a three-dimensional finite element program, such as FlexPAVE™ software.

.

Chapter 7.

Experimental investigation with shear-torque fatigue test

7.1 Introduction

Research activities were also carried out at the Laboratoire GC2D of the University of Limoges (UNILIM) under the supervision of Professor Christophe Petit. In particular, the torque testing configuration described in a previous study was adopted (Petit et al., 2018b), but it was used for the first time to assess the interlayer bonding properties follows a new testing procedure. The newly testing method was called shear-torque fatigue test. The experimental investigation at UNILIM is divided into 2 phases:

I. Phase I describes the work carried out in the framework of the RILEM "Dynamic interlaboratory test", which consisted in performing tests on the double-layered slabs prepared at the laboratory of the Università Politecnica delle Marche (chapter 4). Basically, phase I was divided into two subparts: Part A and Part B, which are described in chapter 8 and chapter 9, respectively.
II. Phase II describes the activities that were carried out to assess the effect of geogrid reinforcement on the shear fatigue behaviour of bituminous pavements using the same torque test configuration. This Phase II (called as Part C) is described in chapter 10.

Given this background, this chapter describes the preparation of the RILEM double-layered samples, that were then tested, and the shear-torque fatigue test configuration.

7.2 Specimen preparation

Two double-layered slabs (coded as 5 and 7) of the set of slabs described in chapter 4 were used. For this study, a single-layered slab (coded as 0) was manufactured at Università Politecnica delle Marche, with the same material and volumetric properties of the double-layered slabs used for RILEM interlaboratory test. Five cylindrical specimens, with a nominal diameter of 100 mm, were cored from each slab, as shown in Figure 7.1.

Once cored, the upper and the lower parts of each specimen were sawed (about 10 mm) and, subsequently, trimmed with an abrasive disc circular saw in order to provide a ridge-free surface and to ensure parallel alignment of the edges of the specimen (Figure 7.2).

Each specimen was named by means of an identification code (ID) that indicates the slab, the coring position; for example, A_2 represents the specimen cored in the slab A, in the position #2 (according to Figure 7.1a).

Prior to testing, the bulk specific gravity of each specimen was measured according to EN 12697-06 (clause D – by dimensions). The final properties of the specimens are summarised in Table 7.1 (only one specimen of slab A was used and reported in this table).

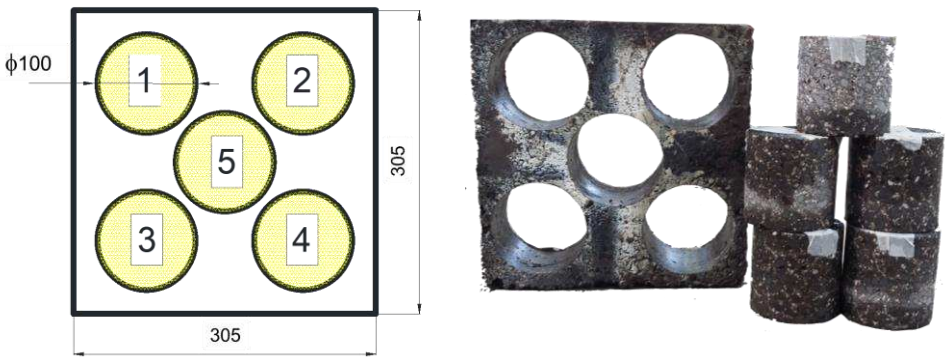

(a) (b)

Figure 7.1. Slab coring procedure: (a) specimen identification and (b) cored cylindrical specimens.

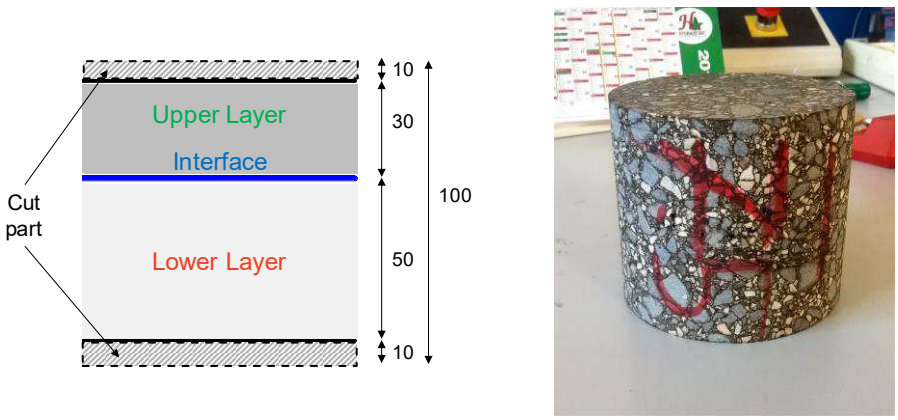

Figure 7.2. Sawed and trimmed cylindrical specimens of slabs 5 and 7.

Table 7.1. Final properties of the specimens.

Slab	Specimen position (#)	Diameter (mm)	Thick. total (H) (mm)	Thick. lower layer (h_1) (mm)	Thick. upper layer (h_2) (mm)	Mass (g)	Bulk density (g/cm^3)
0	2	99.0	74.9	-	-	1395.2	2.42
5	1	99.2	77.5	49.6	27.9	1445.0	2.41
	2	99.4	76.5	47.2	29.3	1436.2	2.42
	3	99.2	72.7	46.9	25.9	1348.0	2.40
	4	99.4	78.0	45.4	32.6	1474.0	2.44
	5	99.3	76.7	47.6	29.1	1436.1	2.42
7	1	99.3	75.8	46.5	29.3	1416.7	2.41
	2	99.3	78.7	50.7	28.0	1461.1	2.40
	3	99.3	82.8	48.2	34.6	1562.1	2.44
	4	99.3	84.2	50.6	33.6	1573.0	2.42
	5	99.2	74.0	46.6	27.4	1391.5	2.43

7.3 Cyclic torque test

The shear-torque configuration was chosen to carry out fatigue tests on double-layered cylindrical specimens. This configuration leads to a non-uniform (i.e., linear) distribution of the shear stress, with the maximum on the outer circumference (Canestrari et al., 2013; Petit et al., 2018a). This fact does not represent a shortcoming considering that also in the direct shear configuration, the shear stress state at the interface is unknown because distortions occur in the material, due to the specimen clamping system as shown in Figure 7.3 (Uzan et al., 1978). Moreover, for both configurations, the comparison of the shear stress state to field conditions is extremely difficult, because the actual shear stress distribution at the interface due to vehicular loading is not uniform as well.

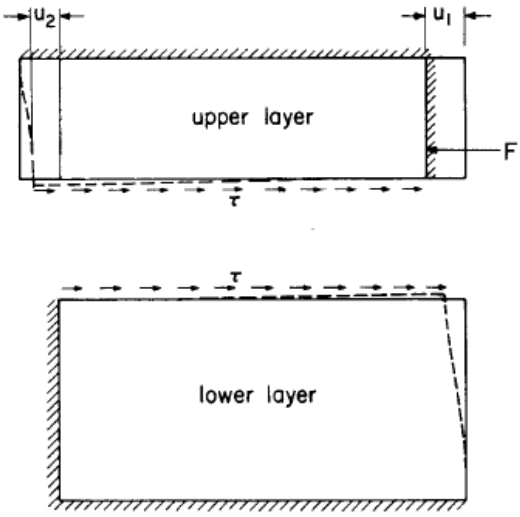

Figure 7.3. Scheme of the sample deformation during shear (Uzan et al., 1978).

7.3.1 Shear-torque fatigue test

Shear-torque fatigue device is available at the Laboratoire GC2D of the University of Limoges. Shear-torque fatigue tests were carried out by means of a material testing system (MTS) device equipped with a temperature-controlled chamber. The MTS device is able to apply a torque of 1000 Nm and an axial load of 100 kN. The fatigue tests were performed at a temperature of 20 °C as normally suggested for static tests (Canestrari et al., 2013; Raab et al., 2009). A sinusoidal torque with a frequency of 10 Hz and an amplitude T_0 was applied to the cylindrical specimens. The alternative cyclic test in controlled torque amplitude is performed considering in the pavement straight wheel passing without braking and acceleration, whereas the frequency of 10 Hz simulates a traffic speed of about 80 km/h on a pavement at a depth of 10–20 cm (Boudabbous et al., 2013). An axial compression load N of 0.05 kN was also applied and kept constant during the whole test. A general view of the working scheme of the shear-torque fatigue test is shown in Figure 7.4. In order to measure the sinusoidal torsional rotation angle, a non-contact angular sensor located on the upper steel plate was used (accuracy of 0.001°) (Figures 7.4 and 7.5).

Before testing, the cylindrical specimen was glued between two stainless-steel platens using an epoxy resin. The bottom platen was rigidly fixed to the load cell and the upper platen was connected to an axial-torsional load actuator. A minimum amount of glue was applied to ensure high torsional stiffness and an optimal adhesion between the specimen and the steel platens. After gluing, the specimen was conditioned for 4 hours at the testing temperature.

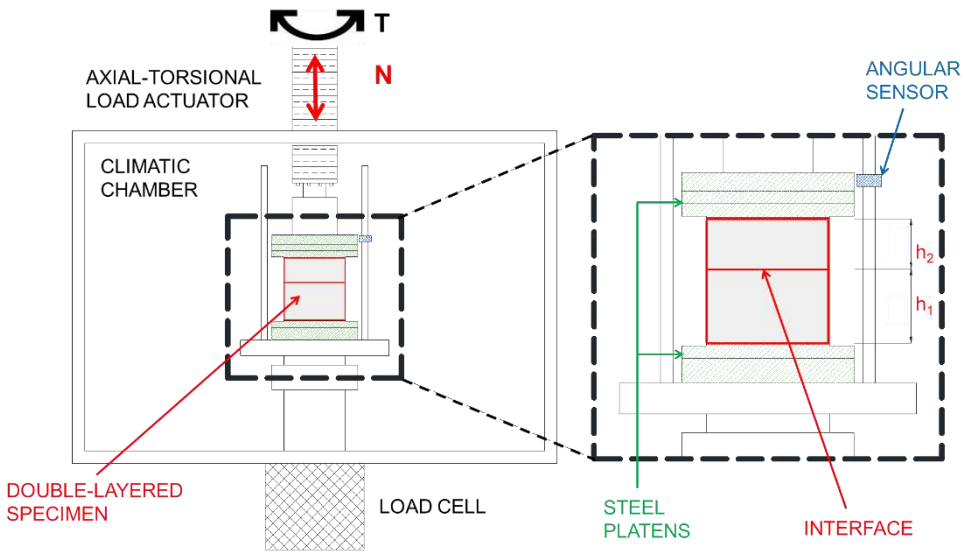

Figure 7.4. Working scheme of shear-torque fatigue test.

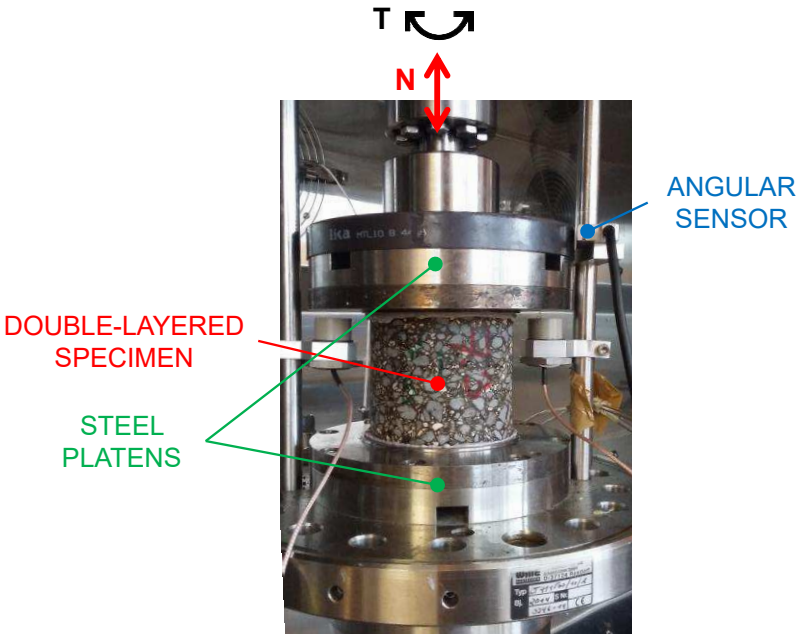

Figure 7.5. Picture of the specimen inside the temperature-controlled chamber.

Figure 7.6a shows the coordinate reference system set for the specimen. The X and Y axes lie in a plane located at the interface of the specimen, whereas the Z-axis is perpendicular to the interface plane. This coordinate reference system will be useful to understand the results presented in chapter 8.

During the test, the cyclic torque test returns a dataset which reports the evolution of torque, axial load, torsional rotation angle and phase angle as a function of the number of cycles. Figure 7.6.b shows a set of recorded data (100 points per cycle) by the load cell and the non-contact angular sensor during cyclic torque tests. The shear-torque fatigue tests were carried out until the physical separation of the upper and the lower layers of the specimen.

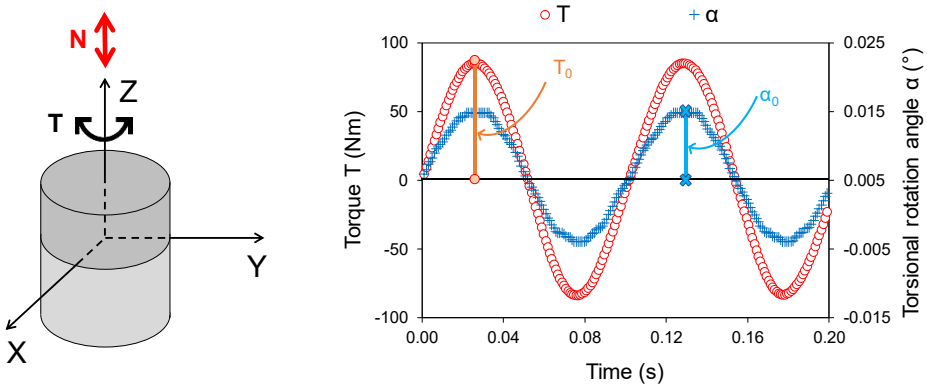

(a) (b)

Figure 7.6. Schematic representation of the test: (a) identification of the coordinate reference system and (b) set of recorded data.

7.3.2 Shear-torque fatigue test analysis

Torque test on a cylindrical specimen generates shear stresses in XY plane equal to zero in the centre and maximum on the outer circumference, as shown in Figure 7.7, where $\delta(t)$ and $\gamma(t)$ are, respectively, the displacement and the shear strain over time. Assuming that the shear stress has a linear variation over the radius of the specimen, the maximum value τ_{max} is expressed by the following equation:

$$\tau_{max} = \frac{2T}{\pi R^3} \tag{7.1}$$

where T is the applied torque and R is the radius of the specimen.

For sinusoidal loading, $\tau_{max}(t)$ is given by the following equation:

$$\tau_{max}(t) = \tau_{max,0}\sin(\omega t) = \frac{2T_0}{\pi R^3}\sin(\omega t) \tag{7.2}$$

where T_0 is the amplitude of the applied torque, ω is the pulsation, equal to $2\pi f$ with f the load frequency, and t is the time.

The applied torque generates a maximum shear strain γ_{max} that can be calculated through the following equation:

$$\gamma_{max} = \frac{\delta_{max}}{H} = \frac{R\alpha_{max}}{H} \tag{7.3}$$

where H is the specimen height and α_{max} is the torsional rotation angle.

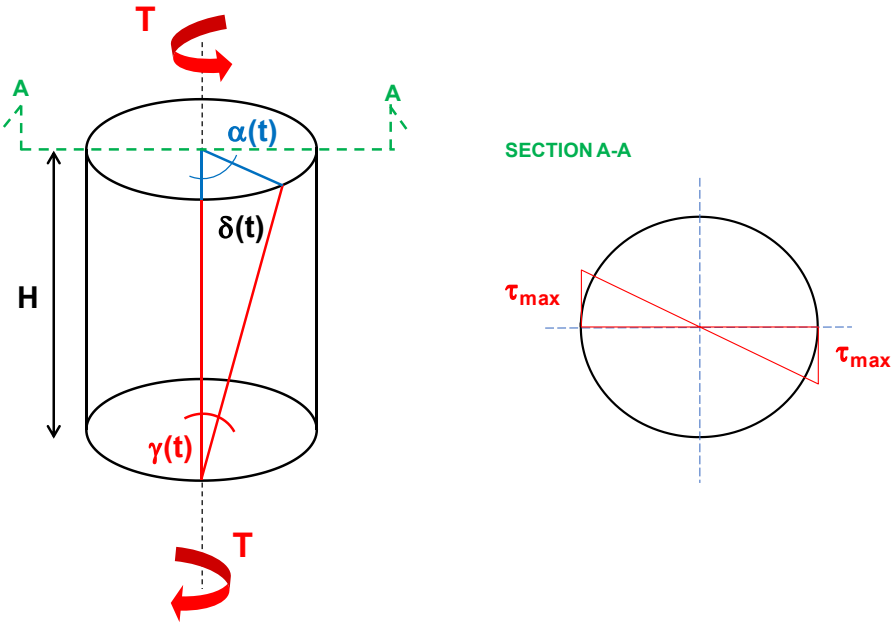

(a) (b)

Figure 7.7. Schematic view of the (a) sample and (b) its section A-A subjected to shear-torque fatigue load.

For sinusoidal loading, $\gamma_{max}(t)$ is given by the following equation:

$$\gamma_{max}(t) = \gamma_{max,0}\sin(\omega t - \varphi) = \frac{R}{H}\alpha_0\ \sin(\omega t - \varphi) \tag{7.4}$$

where α_0 is the amplitude of the torsional rotation angle and φ is the phase angle, which is related to the time lag between stress and strain.

It is well known that the material behaviour can be characterised through its stiffness properties. Specifically, the complex shear modulus G^* for a single layer homogeneous specimen is given by the following equation:

$$G^* = \frac{\tau^*_{max}}{\gamma^*_{max}} = \frac{\tau_{max,0}\exp[\,\mathrm{j}\omega t]}{\gamma_{max,0}\exp[\mathrm{j}(\omega t - \varphi)]} = |G^*|\exp[j\varphi] \tag{7.5}$$

where j is the imaginary unit (defined by $\mathrm{j}^2 = -1$) and $|G^*|$ is the norm of the complex shear modulus.

By substituting Eqs. (7.2) and (7.4) into Eq. (7.5), G^* can be calculated through the following equation:

$$G^* = \frac{H}{I_p}\frac{T_0\exp[\,\mathrm{j}\omega t]}{\alpha_0\exp[\mathrm{j}(\omega t - \varphi)]} \tag{7.6}$$

where $I_p = \frac{\pi R^4}{2}$ is the polar moment of inertia of the circular section.

The change of this equivalent G^* can be used as an indicator of fatigue damage. Figure 7.8 shows a typical example of the evolution of $|G^*|$ as a function of the number of cycles. During a fatigue test, three phases can be identified (Babadopulos et al., 2019; Di Benedetto et al., 2004; Nguyen et al., 2012). The first phase (or adaption phase) consists of a rapid decrease of the complex modulus. This phase is not attributable to fatigue, but it is caused by bulk reversible phenomena (e.g., self-heating, thixotropy). The second phase (or quasi-stationary phase) is associated with a quasi-linear decrease of the complex modulus, during which the initiation and propagation of micro-cracks within the specimen occur. In the third phase (or failure phase), irreversible phenomena (e.g., fatigue damage) start and a rapid decrease of the complex modulus begins. During this phase, macrocracks appear and propagate within the specimen, generating a not homogeneous distribution of stresses and strains. These three phases are not separated by a clear border but by a smooth transition zone.

For double-layered specimens, G^* represents an equivalent complex shear modulus associated with the overall behaviour of the specimen. Hence, in Eq. (7.6) $H = h_1 + h_2$ (Table 7.1). The amplitude of the torsional rotation angle α_0 also deserves some attention. Different from homogeneous specimens, where α_0 is given only by the mixture shear strain, for double-layered specimens α_0 is given by the contribution of the mixture shear strain and the interlayer shear strain. This concept will be deeply discussed in chapter 9.

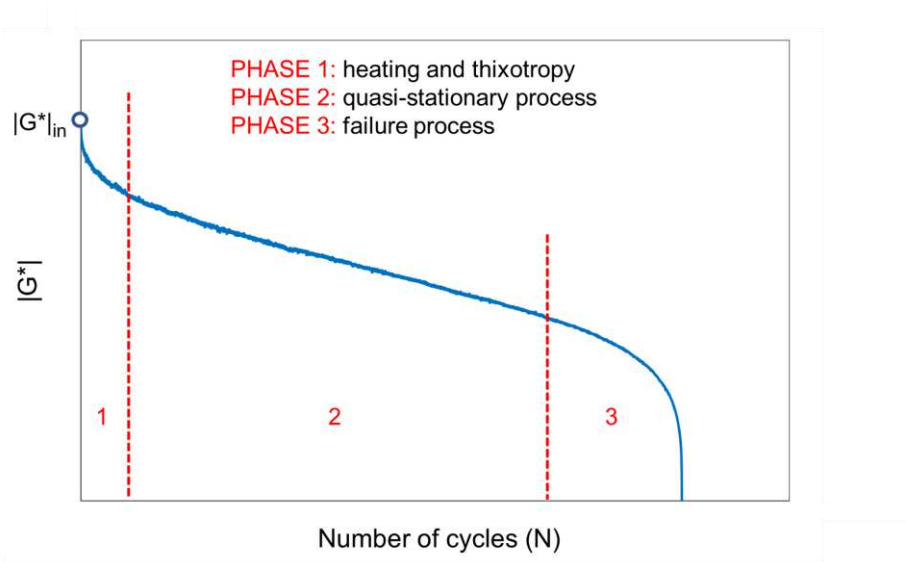

Figure 7.8. Evolution of the norm of the complex shear modulus $|G^*|$ as a function of the number of cycles.

.

Chapter 8.

Experimental investigation with shear-torque fatigue test

Part A

8.1 Introduction

This chapter describes experimental activities carried out at the University of Limoges (UNILIM) during Part A. Since shear-torque fatigue tests were used for the first time to assess the fatigue behaviour of double-layered asphalt specimens during Part A. Shear-torque fatigue tests coupled with acoustic emissions (AE) analysis were used to evaluate the fatigue behaviour of bituminous pavement interlayers. The main objectives of Part A were:

i. to use the AE technique for investigating the damage evolution occurring in double-layered asphalt specimens during shear-torque fatigue tests;
ii. to compare the evolution of stiffness to the accumulation and localisation of the AE events in order to understand the mechanism leading to interface failure;
iii. to improve the interlayer failure criteria based only on stiffness evolution.

8.2 Literature review on acoustic emission

As described in paragraph 2.3.2, the literature review shows that shear fatigue failure of multi-layered asphalt specimens subjected to cyclic loading is currently analysed using the same criteria developed for homogeneous specimens (Di Benedetto et al., 1996; Di Benedetto et al., 2004). The main disadvantage of this approach is that it is not able to highlight if the damage occurs within the asphalt matrix or is localised at the interlayer. In this context, acoustic emission (AE) techniques could be a useful tool to detect interlayer damage. AE events are elastic waves produced by the rapid release of energy from a localised source within a material. These transient waves can be received and recorded by transducers applied on the surface of the specimen (Figure 8.1). Counting the AE events is a common way to assess the damage accumulation inside the material (Figure 8.2).

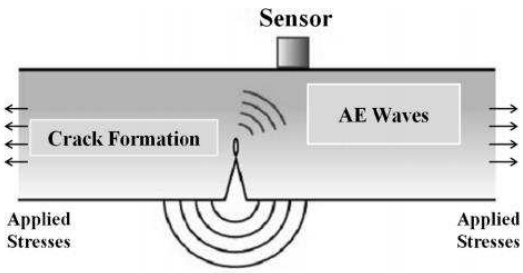

Figure 8.1. Acoustic emission (AE) technique.

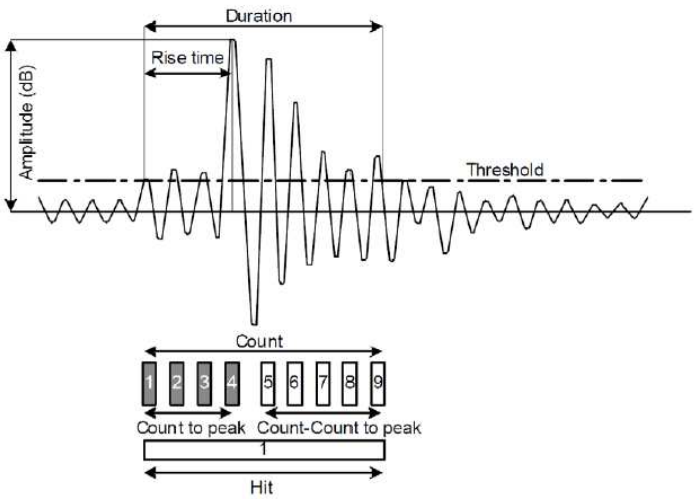

Figure 8.2. Parameters of a typical AE signal (Grosse and Ohtsu, 2008).

AE techniques have been used to monitor damage evolution in composite materials, wood (Brunner et al., 2006; Chen et al., 2006; Lamy et al., 2015) and concrete (Landis, 1999; Maji and Shah, 1988; Prashanth et al., 2019; Shah et al., 2014). However, AE applications aimed at characterising the damage progression in asphalt concrete are relatively limited and mainly focused on low-temperature cracking (Behnia et al., 2018; Nesvijski and Marasteanu, 2006). A first attempt to detect crack initiation and propagation through AE in bituminous mixtures was made by Khosla and Goetz (1979). After performing indirect tensile tests at - 23 °C, the experimental results showed that failure happens when a sharp increase in the cumulative AE events is detected. Hesp et al. (2000) observed that during restrained cooling tests the AE activity detected on polymer-modified asphalt mixture is lower than that of the mixture with plain bitumen. Seo and Kim (2008) found that the peak of AE events in uniaxial tensile cyclic tests approximately coincides with the macro-crack formation, showing a

correlation between AE events and asphalt distresses (Figure 8.3). Li and Marasteanu (2010) used AE measurements to locate the crack propagation in semi-circular bending tests at low temperatures for asphalt mixtures (-6 °C, -18 °C and -30 °C) (Figure 8.4). They found that the number of AE events increased as test temperature decreases. Diakhaté et al. (2012) performed DST tests on notched asphalt concrete specimens without an interface, in order to guide the shear band localisation and generate the crack from the tip of the notch (Figure 8.5a). Results showed that AE measurements are capable of detecting micro-cracking formation induced by shear loading and that the peak of the cumulative number of AE events corresponds to the transition from micro- to macro-cracks. Moreover, the number of accumulated AE events quickly increased when the 70% reduction of the initial shear modulus was reached (Figure 8.5b).

(a)

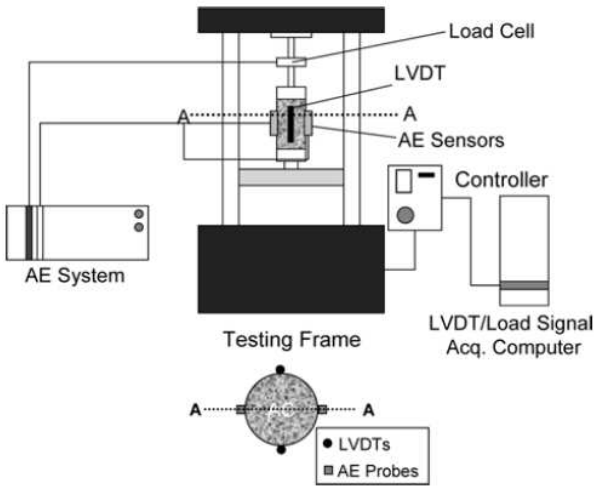

(b)

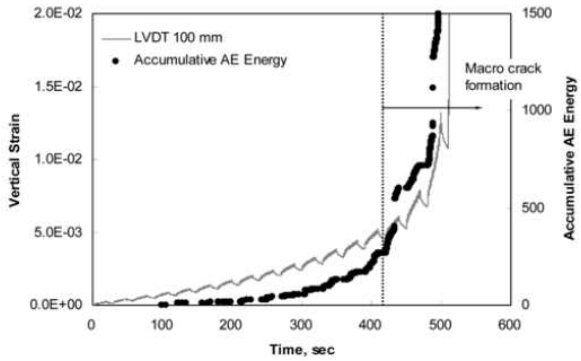

Figure 8.3. (a) Uniaxial tensile cyclic test and AE testing set up; (b) accumulative AE energy and vertical strains versus time (Seo and Kim, 2008).

(a)

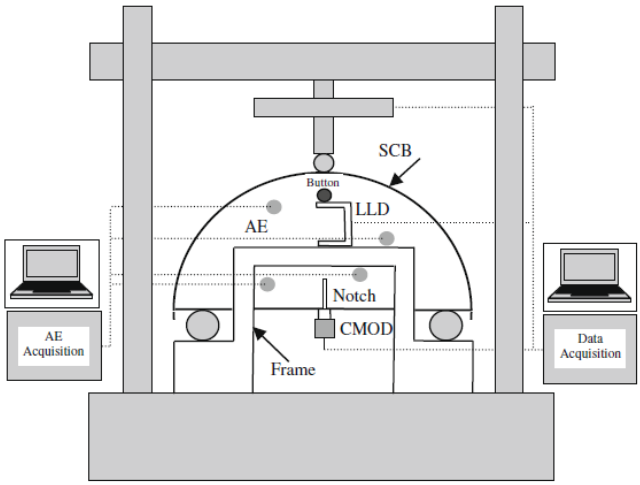

(b)

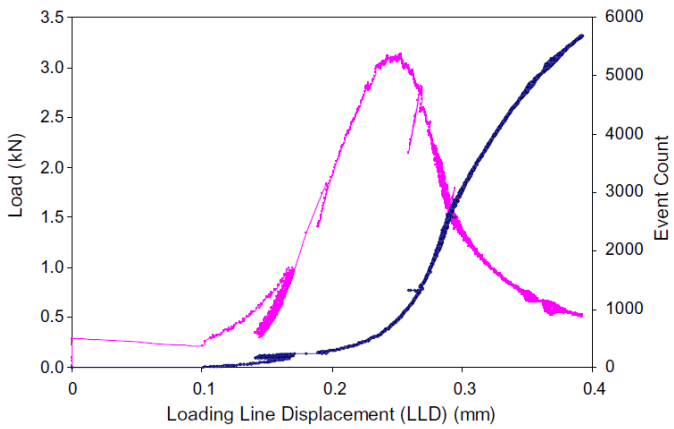

Figure 8.4. (a) Indirect tension strength test and AE testing set up; (b) typical plot for AE event and load with loading line displacement (Li and Marasteanu, 2010).

(a)

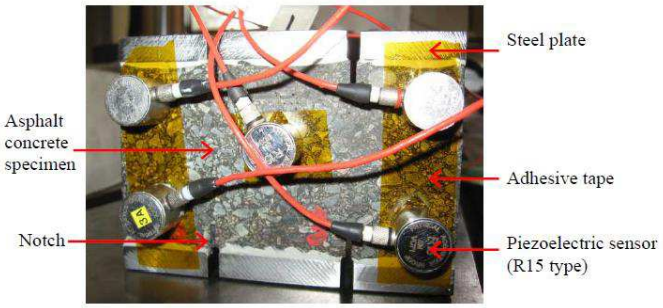

(b)

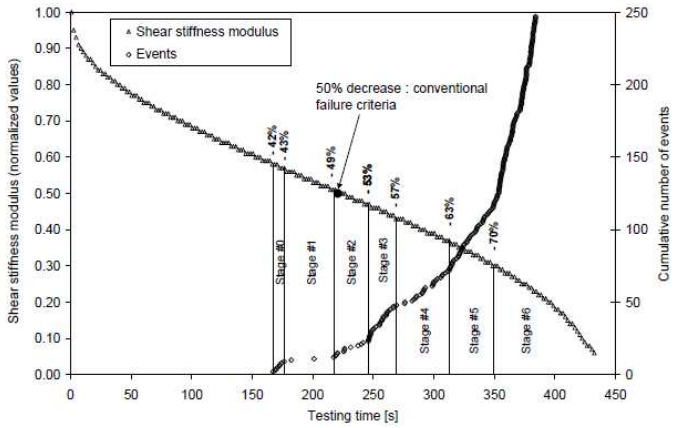

Figure 8.5. (a) Specimen instrumented with AE sensors; (b) evolution in stiffness modulus and number of events during the test (Diakhaté et al., 2012).

8.3 Material and testing methods

8.3.1 Specimens

Two double-layered specimens cored from slab 5 (coded as 5.2 and 5.5) were used for this investigation. Figure 8.6 shows the position of these specimens inside the slab 5. The final properties of the specimen, after coring and cutting, are summarised in Table 8.1. Details of the coring and cutting procedure can be found in chapter 7. It is recalled that slab 5 is part of the set of slabs prepared for the interlaboratory test on "Dynamic Interlayer Shear Testing" organised within RILEM TC 272-PIM/TG3 (chapter 4).

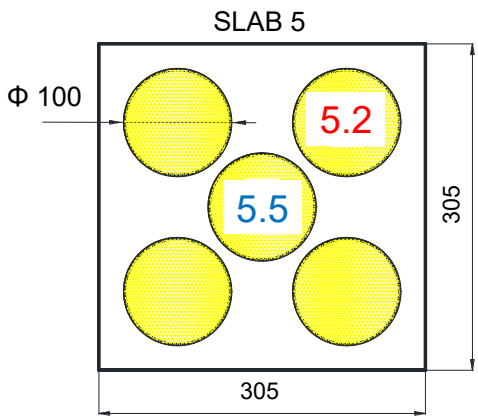

Figure 8.6 Specimen identification.

Table 8.1. Final properties of the specimen 5.2 and specimen 5.5.

Specimen ID	Diameter (mm)	Thickness total (H) (mm)	Thick. lower layer (h_1) (mm)	Thick. upper layer (h_2) (mm)	Mass (g)	Bulk density (g/cm^3)	Air voids (%)
5.2	99.4	76.5	47.2	29.3	1436.2	2.42	3.00
5.5	99.3	76.7	47.6	29.1	1436.1	2.42	3.11

8.3.2 Shear-torque fatigue test

Shear-torque fatigue tests were performed at a temperature of 20 °C as normally suggested for static tests (Canestrari et al., 2013; Petit et al., 2018a). A sinusoidal torque with a frequency of 10 Hz and an amplitude T_0 of 85 Nm and 95 Nm was applied on specimens 5.5 and 5.2, respectively. An axial compression load N of 0.05 kN was also applied and kept

constant during the whole test. Details of the shear-torque fatigue test procedure can be found in chapter 7. The specimen was conditioned at 20 °C for 4 hours and then tested.

8.3.3 Acoustic emission technique

During the fatigue test, AE signals were recorded using a Euro Physical Acoustics (EPA) system. AE signals were detected by eight piezoelectric transducers (miniature sensors Nano30), with an optimum operating frequency range of 125–750 kHz. As shown in Figure 8.7, four transducers were mounted on the upper layer of the specimen (Plane U), whereas four transducers were mounted on the lower layer (Plane L). A silicon grease was applied between the sensors and the specimen in order to enhance the coupling and to reduce the loss of acoustic signal at the transducer-sample interface. AE signals were pre-amplified using four pre-amplifiers (IL40S model) with a 40 dB gain set in order to reduce noise (Figure 8.8). AE signals were sampled at a rate of 20 MHz and filtered with an amplitude threshold of 40 dB. Therefore, a single AE event is defined as an AE signal that exceeds the threshold level, and it can be detected on several sensors (Figure 8.2).

The position where an AE event is generated is not known a priori. The location method is usually based on evaluating the differences of the time of arrival (TOA) of AE waves among the sensors placed on the surface of the specimen. Another important parameter required for the location method is the wave propagation velocity. Detailed information on the adopted AE localisation method are described in Lamy et al. (2015) and Diakhaté et al. (2012).

In this study, the 3D localisation of the AE sources was improved by performing a calibration protocol called pencil lead break (PLB) test. This test consists in simulating an AE event using the fracture of a brittle graphite lead in a prefixed PLB position. This fracture generates an intense acoustic signal, quite similar to a natural AE source that the sensors detect as a strong burst. The PLB test was performed at the end of the shear-torque fatigue test on the fractured surfaces of each specimen considering 13 points as shown in Figure 8.9. Six pencil lead break repetitions were performed in each position.

The calibration results are shown in Figure 8.9b and the data are summarised in Table 8.2. Dispersion in acoustic location was less significant in the centre of the fracture surface (x = 0 mm; y = 0 mm), and more significant closer the transducers.

The wave velocity was experimentally evaluated using the Auto Sensor Test (AST) protocol (Lamy et al., 2015) by artificially generating short-duration and localised impulses, like the breaking of a pencil lead, at known distances from sensors. The average effective AE wave velocity through the AC specimens was measured equal to 3500 m/s.

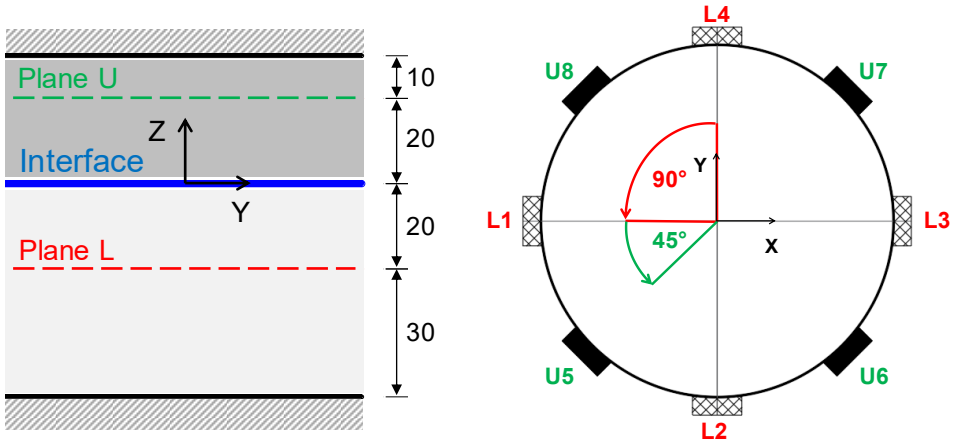

(a) (b)

Figure 8.7. Sections of the cylindrical specimen and piezoelectric transducers location: (a) vertical and (b) horizontal.

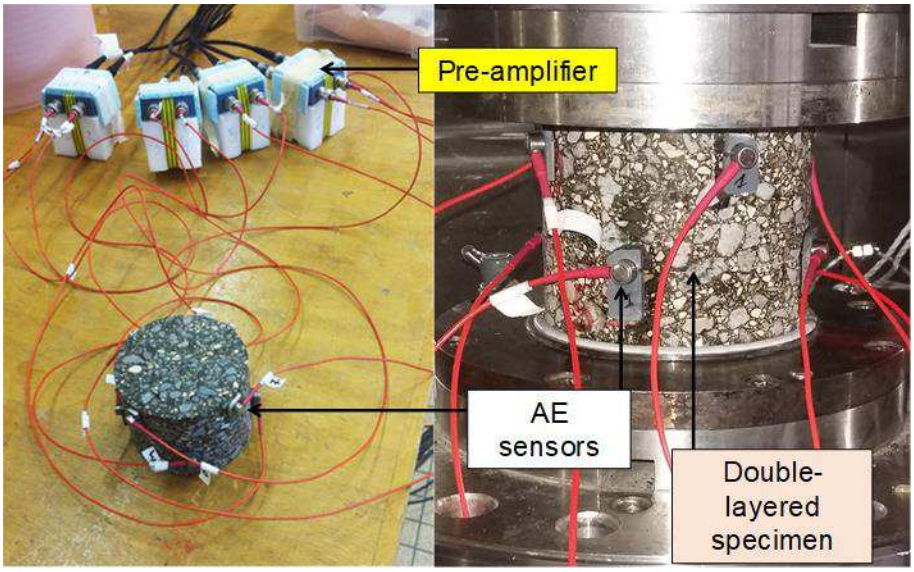

Figure 8.8. AC specimen instrumented with acoustic emission sensors and pre-amplifiers.

(a)

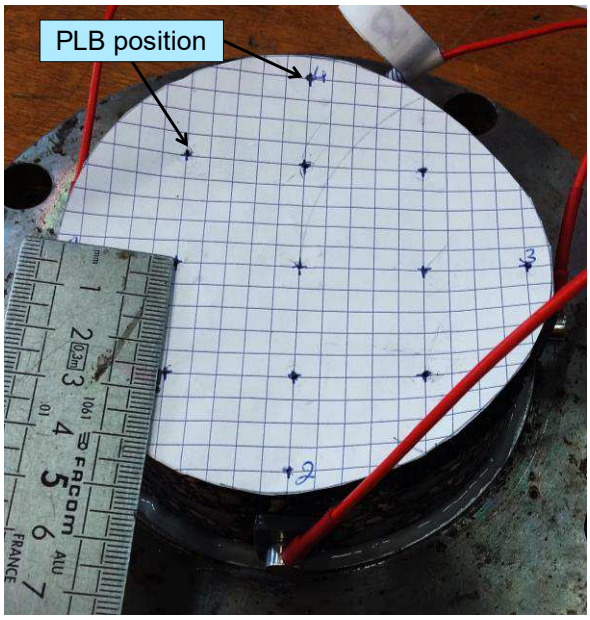

(b)

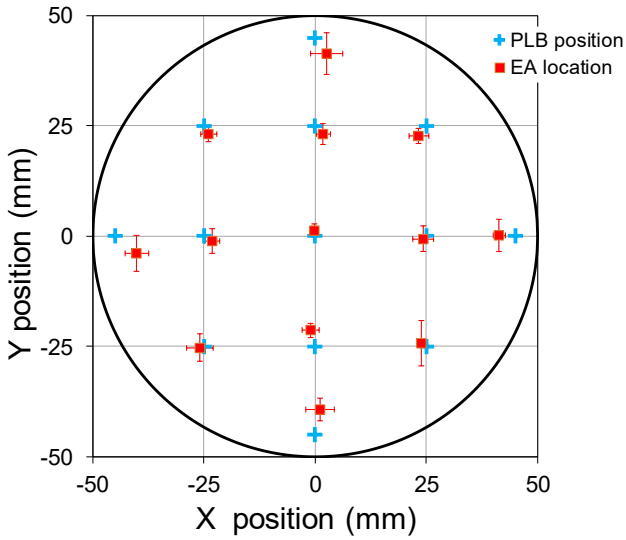

Figure 8.9. Calibration of the AE-location with the PLB test: (a) square mesh of 25 mm overlaid on the fractured surface and (b) PLB test results.

Table 8.2. Average and standard deviation of the AE-locations.

PLB position (mm)		EA location			
		average (mm)		standard deviation (mm)	
X	Y	X	Y	X	Y
0	0	-0.30	1.33	0.74	1.50
0	-25	-0.95	-21.33	1.91	1.68
0	-45	1.15	-39.27	3.19	2.62
0	25	1.80	23.15	1.54	2.29
0	45	2.55	41.44	3.67	4.70
-45	0	-40.14	-3.97	2.68	4.08
-25	0	-23.09	-1.16	1.71	2.80
25	0	24.31	-0.57	2.35	2.82
45	0	41.39	0.29	1.41	3.66
25	25	23.27	22.75	2.25	1.65
-25	25	-23.99	23.25	1.84	1.91
25	-25	23.95	-24.33	1.15	5.18
-25	-25	-26.02	-25.23	2.97	3.09

8.4 Result and discussion

8.4.1 Mechanical analysis

The cyclic torque applied during the test caused the progressive damage of the specimen, leading to a complete separation between the two layers at the end of the test. This mode of failure confirms that the interlayer is a zone of weakness in a double-layered specimen (Santagata et al., 2008).

The damage evolution of the specimen was analysed using the normalised norm of complex shear modulus $|G^*|_n$ given by the following equation:

$$|G^*|_n = \frac{|G^*|_N}{|G^*|_0} \tag{8.1}$$

where $|G^*|_N$ is the norm of the complex shear modulus calculated at any given number of loading cycles (N), and $|G^*|_0$ is the initial norm of the complex shear modulus when the double-layered specimen is still not damaged.

Figure 8.10 shows $|G^*|_n$ as a function of the number of loading cycles for the two tested specimens. As expected, $|G^*|_n$ decreases with the number of loading cycles and the number of loading cycles required to completely fracture the specimen (N_{max}) increases with

decreasing applied torque. Specimen 5.5 failed after 953263 cycles and the evolution of $|G^*|_n$ was similar to that observed for asphalt concrete subjected to cyclic testing, where three typical stages can be normally observed (Babadopulos et al., 2019; Di Benedetto et al., 2004; Nguyen et al., 2012). In the first stage, the complex modulus decreases rapidly, whereas, in the second stage, the complex modulus decreases quasi-linearly. Finally, the third stage is characterised by a quick decrease of complex modulus until the complete failure of the specimen. Specimen 5.2 failed after 61150 cycles and different stages cannot be distinguished. This behaviour can be due to the higher applied torque. However, it is highlighted that specimen 5.2 was cored close to the corner of the slab (Figure 8.6). In this area, the presence of the rigid mould restricts the movement of the aggregates close to the border (boundary effect) during the compaction. This generally results in differences in the internal aggregate structure of the material between the corners and the centre of the slab, and for this reason, the material could present lower mechanical performance (Hunter et al., 2004; Masad et al., 1999).

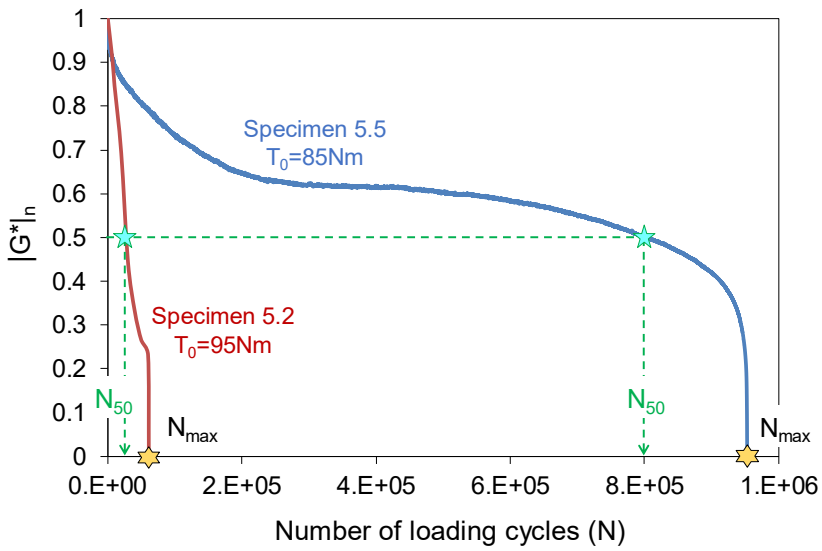

Figure 8.10. Evolution of $|G^*|_n$ in shear-torque fatigue test at 10 Hz and 20 °C and classical fatigue failure criterion.

As explained in paragraph 7.3.2, the mechanical behaviour of asphalt materials under cyclic load is very complex, and, in general, the decrease of $|G^*|_n$ is due to different phenomena (nonlinearity, heating, thixotropy and fatigue) that coexist and cannot be separated directly. In particular, some of these phenomena are reversible such as heating, thixotropy and recoverable nonlinearity (complex modulus dependency on stress/strain amplitude), whereas fatigue is irreversible and corresponds to the true damage. Since the cyclic torque tests were carried out on double-layered specimens, the complexity of the

problem increases. The fatigue life may be estimated by considering various failure criteria, and it is generally defined as the number of loading cycles to failure (N_f). The value N_f is lower than N_{max} and is usually associated with the number of loading cycles at which the initial modulus is reduced by a prefixed percentage (e.g., 50% → $N_f = N_{50}$). As shown in Figure 8.10, by referring to the classical fatigue failure criterion (N_{50}), the fatigue life for specimens 5.5 and 5.2 are of 800000 and 30000 cycles, respectively. This fatigue failure criterion does not provide any information on the localisation of the damage and is not able to distinguish if the damage occurs in the asphalt matrix or is localised at the interlayer.

8.4.2 Acoustic Analysis: 3D AE-localisation

The localisation of the AE event is fundamental to investigate the fracture mechanism evolution. Figures 8.11 and 8.12 show the AE events (each dot represents an individual event recorded inside the specimen) projected onto the X-Z plane and Y-Z plane, respectively for specimens 5.5 and 5.2. The total number of events was higher for specimen 5.2 (about 500) compared to specimen 5.5 (about 170). In both specimens, AE events seem to be mostly located in the interlayer zone, which ultimately became the macro-crack leading to the complete failure of the specimen. Some AE events were located near the bottom and upper steel platens. This effect can be explained by the fact that in these areas the stress state is affected by the confinement effect (Poisson effect) due to the gluing. Besides, a certain number of points are also identified outside the specimen (in correspondence of the steel platens). This could be due to the uncertainties of the localisation method and/or because of echo events that generate position errors. This behaviour was consistent for both specimens and confirms that AE analysis can be used to investigate the development of the damage process of asphalt materials.

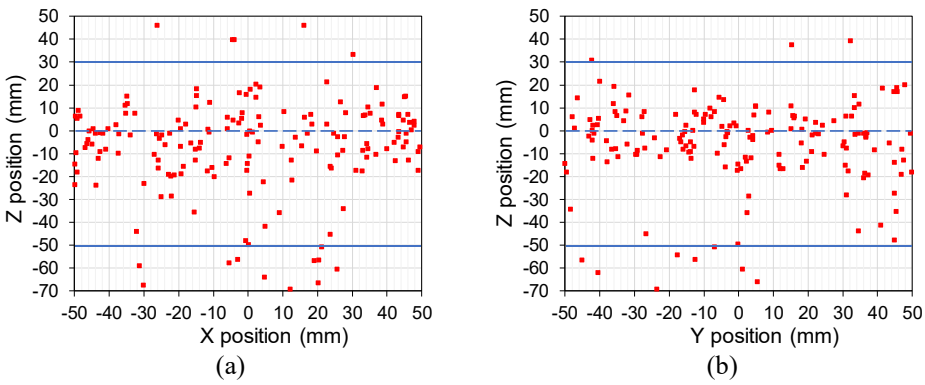

Figure 8.11. Cumulated location of AE events for specimen 5.5: (a) X-Z plane, and (b) Y-Z plane.

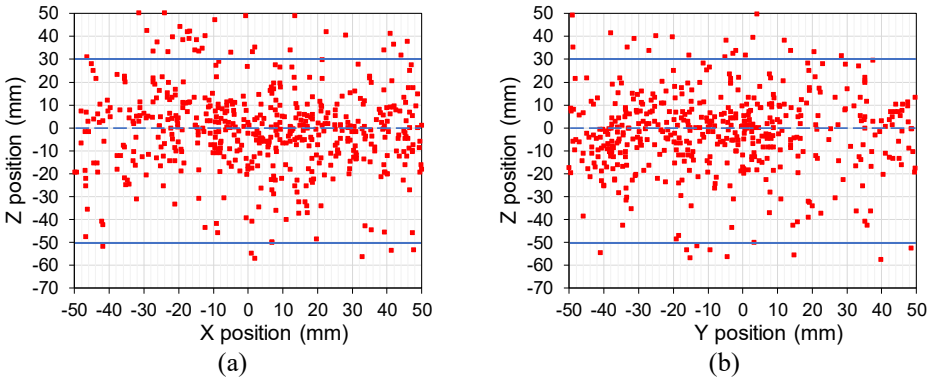

Figure 8.12. Cumulated location of AE events for specimen 5.2: (a) X-Z plane, and (b) Y-Z plane.

In order to better understand the results obtained from the acoustic analysis, a statistical analysis was carried out. Figures 8.13 and 8.14 show the frequency distribution along Z position of the EA events reported in Figures 8.11 and 8.12, respectively. For both specimens, it can be observed that the EA events are mostly concentrated within the range - 7.5 and +7.5 mm (i.e., thickness = 15 mm).

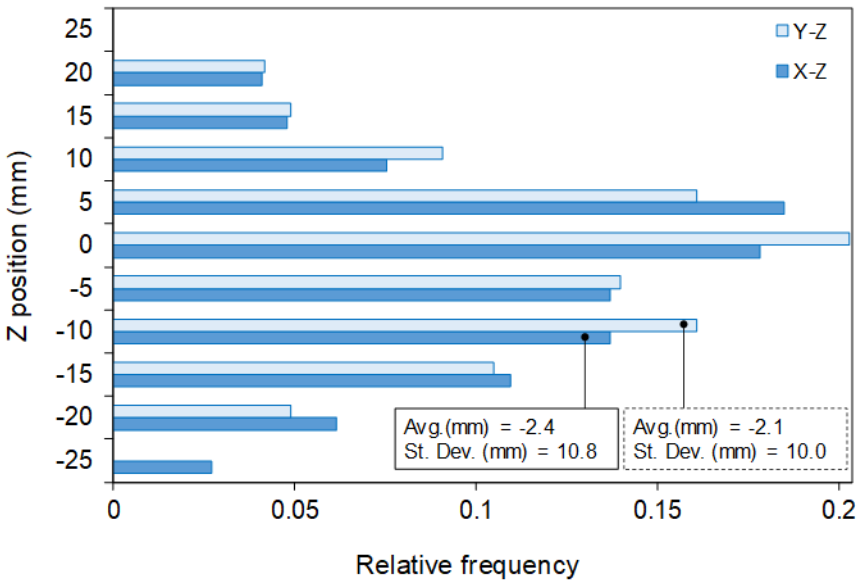

Figure 8.13. EA events frequency distribution along Z position for specimen 5.5.

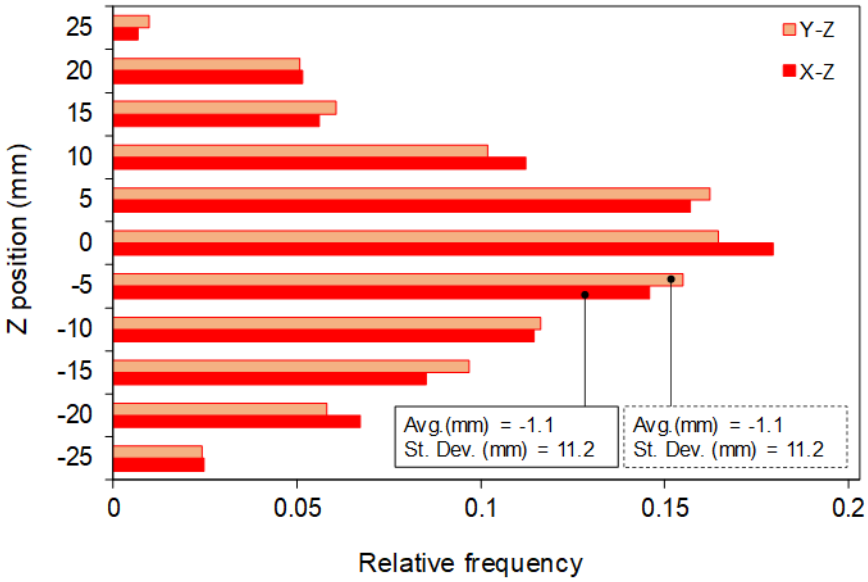

Figure 8.14. EA events frequency distribution along Z position for specimen 5.2.

The statistical distribution of the measurements along the Z position was checked using a normal Quantile-Quantile (Q-Q) plot. Figure 8.15 reports the data for both specimens in the X-Z and Y-Z planes. The points plotted along the equality line, confirming that most of the AE events may be considered normally distributed around the interface. The two tails outside the range -2 and +2 show a possible deviation from normality. These points can be related to the AE events located close to the steel platens which are not part of the same normal distribution. Thus, it is possible to affirm that the damage tends to localise in the interlayer zone, confirming that this is the weakest part of the specimen.

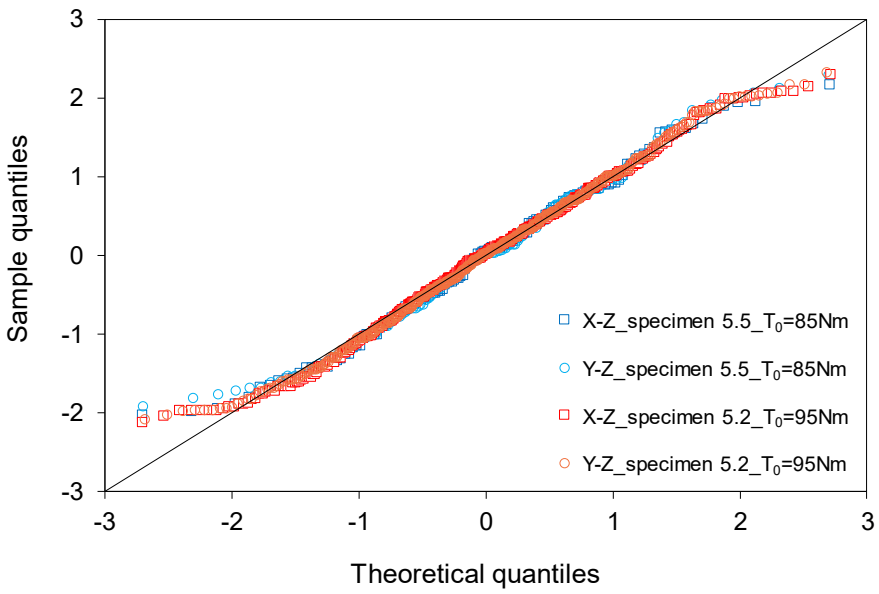

Figure 8.15. Normal Q-Q plot of AE events along Z position for specimen 5.5 and specimen 5.2.

Figure 8.16 presents the AE events on the X-Y plane for specimens 5.5 and 5.2 at the end of the test. The events are classified with the scale of the peak amplitude. It was observed during the tests that only AE events with small amplitudes occurred at the initial stage, and the events with large amplitudes began gradually to occur until reaching the peak at the end of the test. In Figure 8.16, for both specimens, it can be observed that AE events were distributed mostly around the border of the specimen. A certain number of points were also identified outside the specimen. These events could be generated by uncertainties of the localisation method and/or because of echo events as already observed in Figures 8.11 and 8.12. A statistical analysis of the distribution of AE events on the X-Y plane was also carried out. The cross-section of each specimen was divided into four annuluses with the same area and with an outer radius equal to 25, 35.35, 43.3 and 50 mm, respectively. Figure 8.17 shows the density of the EA events (number of events per unit area) reported in Figure 8.16 as a function of the distance from the centre of the specimen ($R = \sqrt{X^2 + Y^2}$). The density was higher close to the circumference of the specimen (i.e., where the maximum shear stress occurs). Moreover, the cross-section of each specimen was also divided into eight sectors formed by angles of 45 degrees each. Figure 8.18 shows the polar frequency distribution of the AE events reported in Figure 8.16. The frequency of the events is not homogeneously distributed on the X-Y plane. These results agree with the previous observations and indicate that the AE events were mostly concentrated in certain areas.

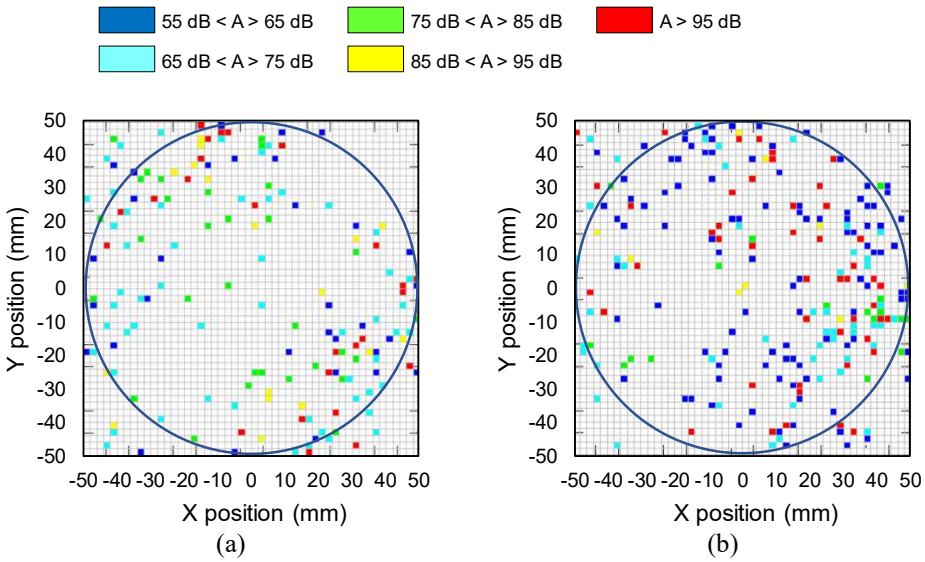

Figure 8.16. Location of AE events on the X-Y plane: (a) specimen 5.5 and (b) specimen 5.2.

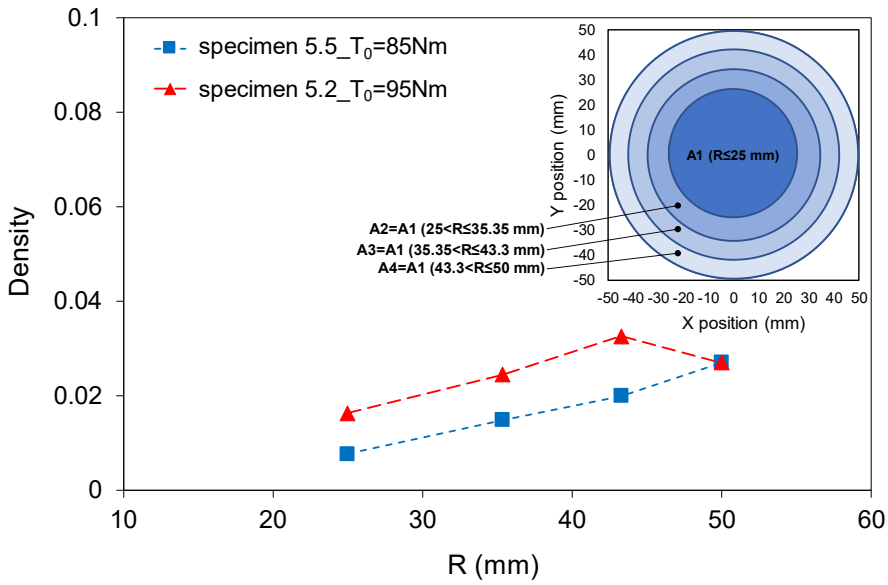

Figure 8.17. EA events density on the X-Y plane as a function of the distance from the centre of the specimen (R) for specimen 5.5 and specimen 5.2.

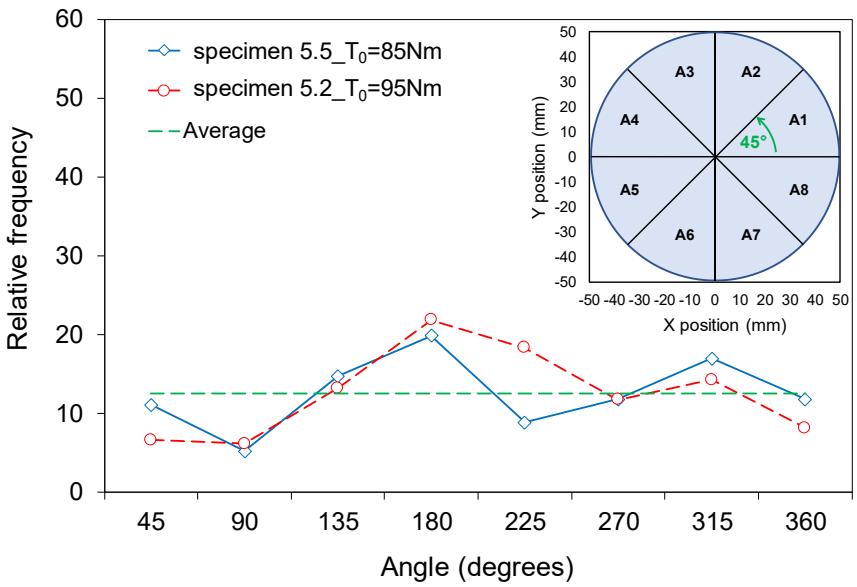

Figure 8.18. EA events polar frequency distribution on the X-Y plane for specimen 5.5 and specimen 5.2.

8.4.3 Comparison between mechanical and AE results

Figures 8.19 and 8.20 show the evolution of the cumulative number of AE events as a function of the number of loading cycles superposed to parameter $|G^*|_n$ for specimen 5.5 and specimen 5.2, respectively. Focusing on the evolution of the cumulative number of AE events, it is possible to identify two phases during the shear-torque fatigue test. A first phase during which the number of AE events increases almost linearly as the number of loading cycles increases. Subsequently, it can be observed a second phase during which the cumulative number rapidly increases as approaching the end of the test. Indeed, it is generally accepted that when the material is undamaged, the acoustic emission activity is almost negligible (Behnia et al., 2018; Chen et al., 2006). The subsequent abrupt rise of AE activity indicates the formation of micro-cracks at the interlayer, as observed before, and occurs after 945000 and 59340 cycles for specimen 5.5 and 5.2, respectively, as shown in Figures 8.19 and 8.20. This sharp increase of AE events, that corresponds to a rapid acceleration to failure, occurs when $|G^*|_n$ reaches approximately 30% for specimen 5.5 and 25% for specimen 5.2 (i.e., when the complex shear modulus decreases by about 70%). Since acoustic activity is generally a sensitive precursor to the failure process (Behnia et al., 2018; Bourchak et al., 2007; Lamy et al., 2015; Landis, 1999; Unnthorsson et al., 2008), these results indicate that a huge part of the decrease is not accompanied by the formation of micro-cracks. These

observations appear to be in strict agreement with those presented in a previous study (Diakhaté et al., 2012).

A possible explanation is that, before the formation of the micro-cracks, the whole double-layered system reacts to the cyclic load. Thereafter, the damage tends to localise at the interlayer. Finally, the formation and propagation of macro-cracks at the interlayer leads to the complete separation of the two layers. Hence, it can be hypothesised that the $|G^*|_n$ evolution is governed by the properties of the double-layered system at the beginning of the test, and progressively in a more pronounced way by the interlayer behaviour until the failure. In this context, it is important to interpret the change in complex modulus during fatigue tests correctly. In fact, the term "damage" is typically referred to any microstructural change within the material that occur during a loading application. Considering that AE activity clearly represents the damage process of the AC specimen, this leads to conclude that asphalt pavement shear-fatigue life could not be estimated properly using the classical failure criterion (N_{50}). In fact, it could be argued that close to the 50% decrease of the parameter $|G^*|_n$, cracks do not begin to develop in the material or grow at undetectable rates. Therefore, it is helpful to develop a better failure criterion capable to evaluate the fatigue life during cyclic shear loading.

As a final remark, acoustic data and analysis can lead to further modelling and seem to be suitable for understanding and describing the failure mechanisms, as well as damage process during shear-fatigue behaviour.

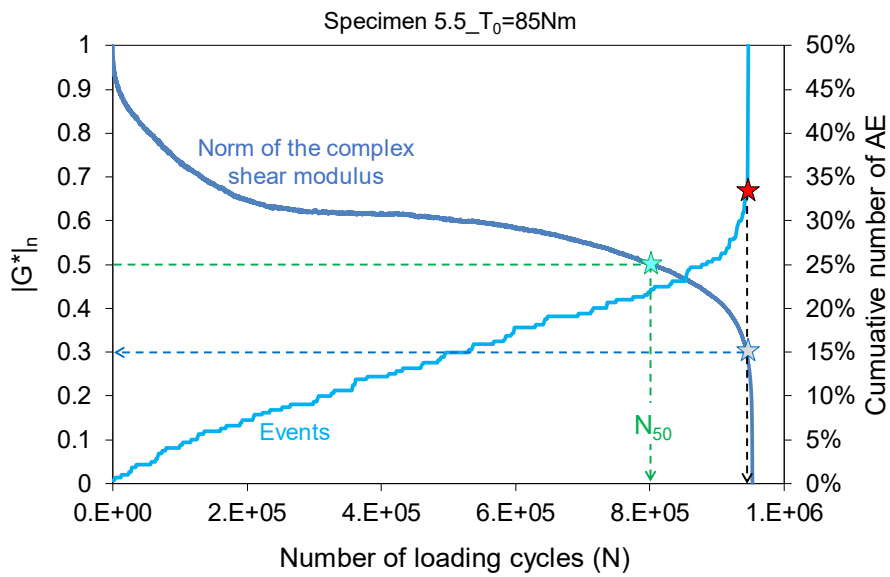

Figure 8.19. Evolution of the cumulative number of AE events and of $|G^*|_n$ during the shear-torque fatigue test for specimen 5.5.

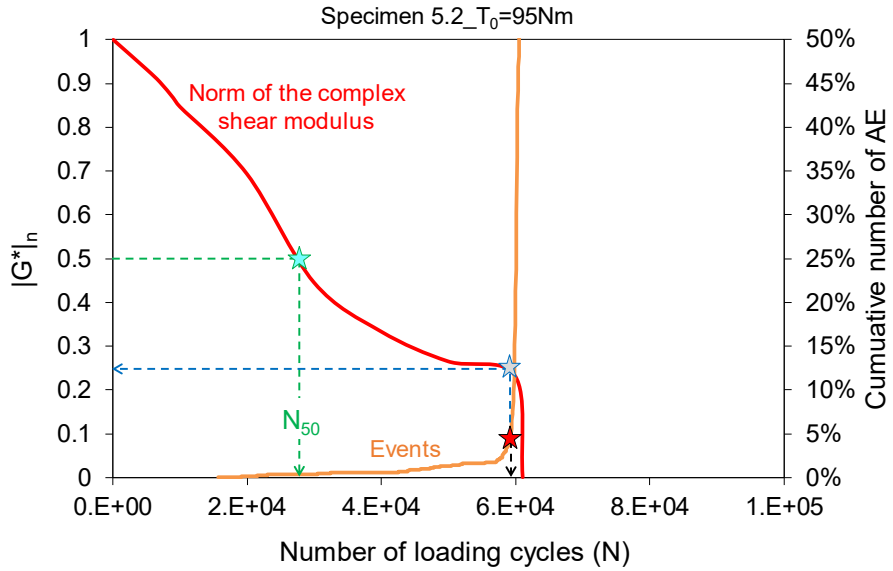

Figure 8.20. Evolution of the cumulative number of AE events and of $|G^*|_n$ during the shear-torque fatigue test for specimen 5.2.

8.5 Conclusions and perspectives

Shear-torque fatigue tests were used for the first time to assess the fatigue behaviour of asphalt pavement interlayers. During the test, an AE technique was used to study the fatigue behaviour of asphalt interlayers. The main goal of this study was not to present the fatigue characterisation of a specific asphalt interlayer, which certainly requires a higher number of specimens, but the optimisation of the measurement AE technique using two virtually identical specimens. The AE analysis included the cumulative number and the localisation of the AE events. From the results, it can be concluded that:

- Shear-torque fatigue loading led to the physical separation of the upper and the lower layers.
- The complex shear modulus $|G^*|$ decreases with the number of cycles as a result of the deterioration of the interlayer mechanical properties.
- The AE analysis shows that the AE events are concentrated in the interlayer zone, where the specimen is weaker and where the failure actually occurs. Besides, the AE events are concentrated in the outermost of the cross-sectional area of the specimen, where the shear stress is higher. This allows concluding that the cracks initiate on the perimeter and proceeds inward.
- Comparing the results of both mechanical and AE analysis, the available data suggest that, despite an important “stiffness” decrease, the AE activity (formation

of cracks) mainly occurs at the final stage of the test. The abrupt rise of AE events starts approximately when the corresponding decrease in the norm of complex modulus is approximately 70–75%. Thus, the results seem to indicate that the classical failure criterion (N_{50}) to predict asphalt pavement fatigue life, as usually proposed in the literature, does not seem to correspond to the critical damage condition of double-layered specimens and should be revised.

Although this work describes a preliminary experimental campaign, its outcome is very important for analysing and interpreting cyclic torque tests in asphalt mixtures. Thanks to the innovative use of AE analysis, the presented results can have an impact on the shear-fatigue characterisation of double-layered asphalt concrete systems, but they should be validated considering more data and different testing conditions.

.

Chapter 9.

Experimental investigation with shear-torque fatigue test

Part B

9.1 Introduction

The results obtained during Part A showed that during shear-torque fatigue tests, the damage (i.e., the highest deformation) is mainly concentrated in the interlayer region of double-layered specimens. Therefore, it can be assumed that, for the most part, the specimen failure is due to the interlayer damage, which could be modelled by using shear-torque fatigue test results. This chapter (Part B) presents the modelling of the behaviour of pavement bituminous interlayers during shear-torque fatigue tests, by including a preliminary validation of the model and a new fatigue failure criterion. To this end, three main phases have been considered as follows:

i. the model of the evolution of the interlayer complex shear modulus is presented;
ii. shear-torque fatigue tests were performed on both single- and double-layered bituminous specimens with the aim of preliminary validate the model;
iii. a new fatigue failure criterion has been proposed to be used in the result elaboration of the shear-torque fatigue tests, allowing the determination of the interlayer shear fatigue curve.

9.2 Modelling of interlayer behaviour during shear-torque fatigue tests

The model of the evolution of the interlayer complex shear modulus was obtained through theoretical consideration involving shear-torque fatigue test results and equations.
As explained in chapter 7, it is well known that Eq. (9.1) can be used for the calculation of the complex shear modulus G^* only when homogeneous systems are considered. While, for double-layered specimens, the presence of the interface increases the complexity of the phenomenon.

$$G^* = \frac{H}{I_p} \frac{T_0 \ \exp[\mathrm{j}\omega t]}{\alpha_0 \ \exp[\mathrm{j}(\omega t - \varphi)]} \tag{9.1}$$

Specifically, when double-layered specimens are tested, G^* can be considered as an apparent modulus that considers the contribution of the two-layer asphalt concrete as well as the interlayer, assumed as a layer at the interface with an appropriate thickness. Hence, the total height of the specimen (H) becomes equal to the sum of the heights of the lower layer (H_1), the upper layer (H_2) and the interlayer (H_i) (Figure 9.1a). Analogously, the amplitude of the torsional rotation angle α_0 comprises the torsional rotation angle of the asphalt mixture of the lower and upper layers plus the torsional rotation angle of the interlayer. Since the fracture usually occurs in correspondence of the interface as shown in Part A (chapter 8), it can be assumed that the shear strain of the interlayer γ_i and the interlayer complex shear modulus G_i^* control the specimen failure. Then, these two parameters are analytically determined to evaluate their evolution during shear-torque fatigue tests on double-layered specimens. In the following formulas, the parameters obtained during the double-layered shear-torque fatigue tests and referred to the overall response of the specimen are named with the subscript "*bulk*", the parameters referred to the two layers in asphalt concrete are named with the subscript "*AC*" and the parameters referred to the interlayer are named with the subscript "*i*". It can be assumed that the general trend of the maximum shear strain γ_{bulk} (i.e., γ_{max}), obtained during the double-layered test and denoted with a black dotted line in Figure 9.1b, can be schematically represented by the contribution of the shear strain of the asphalt concrete γ_{AC} (red dashed lines) and by the contribution of the interlayer shear strain γ_i (blue dashed line).

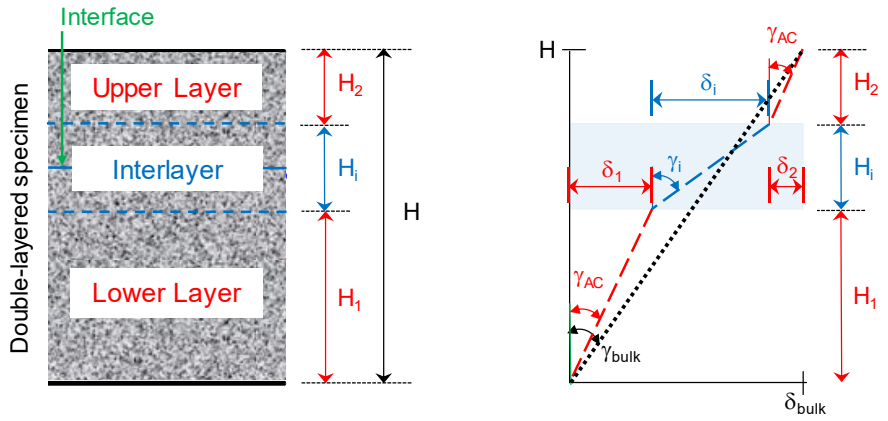

(a) (b)

Figure 9.1. (a) Cross-section of a double-layered specimen and (b) plane representation of the shear strain interpretation.

Based on this assumption, it is possible to separate the different contributions to the shear strain (i.e., bulk, asphalt concrete and interlayer). Indeed, the value of the interlayer shear strain γ_i can be calculated as follows:

$$\gamma_i = \frac{\delta_i}{H_i} \tag{9.2}$$

with the clear meaning of the symbols and where δ_i can be obtained by the following equation:

$$\delta_i = \delta_{bulk} - (\delta_1 + \delta_2) \tag{9.3}$$

Assuming that both layers are prepared with the same asphalt concrete, it can be considered that $\delta_1 = \gamma_{AC} \cdot H_1$ and $\delta_2 = \gamma_{AC} \cdot H_2$, allowing the following equation to be obtained:

$$\delta_i = \delta_{bulk} - \gamma_{AC} \cdot (H_1 + H_2) = \delta_{bulk} - \gamma_{AC} \cdot (H - H_i) \tag{9.4}$$

The shear strain of the asphalt concrete γ_{AC} can be calculated from the norm of the complex shear modulus $|G_{AC}^*|$. Thus, γ_{AC} can be obtained as follows:

$$\gamma_{AC} = \frac{\tau_{max,0}}{|G_{AC}^*|} \tag{9.5}$$

Considering that $\delta_{bulk} = R\alpha_0$, the substitution of Eqs. (9.4) and (9.5) in Eq. (9.2) allows the following equation to be obtained:

$$\gamma_i = \frac{R\alpha_0 - \frac{\tau_{max,0}}{|G_{AC}^*|}(H - H_i)}{H_i} \tag{9.6}$$

Consequently, the interlayer complex shear modulus G_i^* can be expressed using the following equation:

$$G_i^* = \frac{\tau_{max,0}\ \exp[\mathrm{j}\omega t]}{\gamma_i \exp[\mathrm{j}(\omega t - \varphi)]} \tag{9.7}$$

And the norm of the complex shear modulus $|G_i^*|$ can be calculated by the following equation:

$$|G_i^*| = \frac{\tau_{max,0}}{\gamma_i} = \frac{\tau_{max,0} \cdot H_i}{R\alpha_0 - \frac{\tau_{max,0}}{|G_{AC}^*|}(H - H_i)} \tag{9.8}$$

It is worth noting that the determination of the norm of the complex shear modulus of the interlayer $|G_i^*|$ is subjected to the knowledge of the norm of the complex shear modulus of the asphalt concrete $|G_{AC}^*|$ and of the interlayer thickness H_i. The importance of both

parameters ($|G_{AC}^*|$ and H_i) on the application of Eq. (9.8) will be in-depth discussed in the following paragraphs.

9.3 Experimental program

9.3.1 Specimens

In this study, one cylindrical specimen without interface (obtained from slab 0) and ten double-layered specimens (obtained from RILEM slabs 5 and 7 as shown in chapter 7) were tested and analysed. The characteristics of the specimens are reported in Table 7.1 (chapter 7).

9.3.2 Experimental investigation

All the shear-torque fatigue tests were performed according to the procedure described in paragraph 7.3.1. Constant torque amplitudes (T_0) ranging from 70 to 100 Nm were applied during the investigation, according to a preliminary shear-torque fatigue test which showed that these stress levels guarantee a proper number of cycles before failure.

For the preliminary validation of the model, shear-torque fatigue tests were performed on both one specimen of slab 0 (without interface) and one specimen of slab 7 (with interface), applying a torque amplitude T_0 equal to 80 Nm.

Finally, in order to correctly characterise the fatigue interlayer behaviour through the determination of the fatigue curve, the testing program shown in Table 9.1 was carried out. One different level of torque amplitude was applied to each specimen, by stopping the test when the complete fracture of the specimen was obtained (i.e., the separation between the two layers).

Each specimen was named by means of an identification code (ID) that indicates the slab, the coring position (Figure 7.1), and the applied torque amplitude. For example, 7_4_80 represents the test on the specimen cored in slab 7, in the position #4, performed with a torque amplitude equal to 80 Nm.

Table 9.1. Experimental program.

Slab (#)	Specimen position (#)	Temperature (°C)	Frequency (Hz)	Torque amplitude T_0 (Nm)	Specimen ID
5	1	20	10	100	5_1_100
	2			95	5_2_95
	3			85	5_3_85
	5			85	5_5_85
7	1	20	10	70	7_1_70
	2			85	7_2_85
	3			75	7_3_75
	4			80	7_4_80
	5			90	7_5_90

9.4 Preliminary validation of the model

The results obtained by the specimens coded as 0_2_80 (without interface) and 7_4_80 (with interface) were employed in this second phase and the norms of the complex shear modulus $|G^*|$ as a function of the number of loading cycles of these specimens are shown in Figure 9.2. Since the specimens are characterised by an analogous bulk density (about 2.42 g/cm^3) and the same torque amplitude (T_0 = 80 Nm) was applied, Figure 9.2 provides evidence that the presence of the interface represents a weakness zone, leading to early failure compared to the specimen without interface. Indeed, specimen 7_4_80 failed after about 143000 cycles with an evolution of $|G^*|$ showing the three phases of the decay law seen in Figure 7.8, whereas the specimen 0_2_80 did not fail even after 8500000 cycles. Due to the excessive testing time, the 0_2_80 test was stopped when the decrease of the norm of the complex shear modulus was approximately 58%, before reaching the failure condition. For this reason, the first and the second phase of the decay law can be identified, but the third phase cannot be seen.

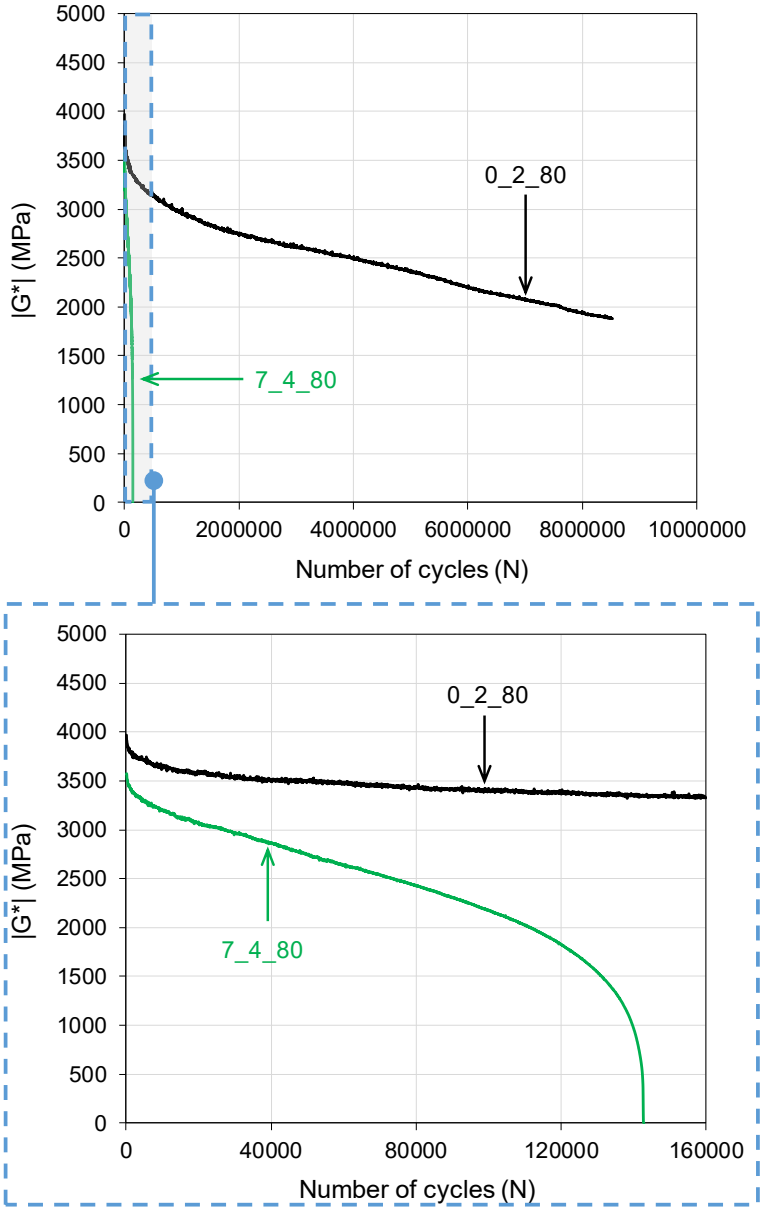

Figure 9.2. Evolution of the complex shear modulus $|G^*|$ for specimens 0_2_80 and 7_4_80$_{bulk}$ during the shear-torque fatigue test.

The remarkable difference just observed between single-layered and double-layered specimen (Figure 9.2) confirms the assumption that the interlayer shear strain γ_i controls the failure of the latter. Thus, the effect of the presence of the interface on the response of double-layered systems under shear-torque fatigue loading was assessed by considering the interlayer complex shear modulus $|G_i^*|$ determined according to Eq. (9.8). However, as above-mentioned, a proper estimation of the norm of the complex shear modulus $|G_{AC}^*|$ and of the interlayer thickness H_i is fundamental for a correct evaluation of $|G_i^*|$. In the following observations, the variation of each of the two parameters was considered separately.

As regards the first parameter, it is necessary to determine if $|G_{AC}^*|$ can be assumed constant during the whole double-layered specimen test or if it must be considered progressively reduced. Indeed, during the test, $|G_{AC}^*|$ decreases due to the specimen damaging and it is important to understand the influence of this reduction on the $|G_i^*|$ determination. To this end, both a constant value and a progressive reduction law of $|G_{AC}^*|$ were considered in Eq. (9.8), by fixing an interlayer thickness of 15 mm, according to the results emerged in Part A (chapter 8).

As far as the constant value law of $|G_{AC}^*|$ is concerned, it can be assumed that during the cyclic test the double-layered specimen initially reacts as a single-layered system, so that the $|G_{AC}^*|$ can be considered equal to the $|G^*|_{bulk}$ of the double-layered specimen C_4_80 in the first loading cycles (i.e., when the specimen is still undamaged), allowing the determination of $|G_i^*|_{const}$ by means of Eq. (9.8).

Diversely, the progressive reduction of $|G_{AC}^*|$ was evaluated through the study of the behaviour of the single-layered specimen 0_2_80. Specifically, Figure 9.2 clearly shows that, during the testing time of the specimen 7_4_80 (about 143000 cycles), also $|G^*|$ of 0_2_80 is subjected to a gradual reduction, leading to consider that also the AC outside the interlayer likely suffers some damage during the 7_4_80 shear-torque fatigue loading. Thus, cycle by cycle, the decay law of $|G^*|$ of 0_2_80 was deduced and used for obtaining the decay law of $|G_{AC}^*|$ of 7_4_80 (named $|G_{AC}^*|_{red}$). This law was introduced into Eq. (9.8), by allowing the calculation of $|G_i^*|_{red}$ of the specimen 7_4_80 in correspondence of each cycle.

Furthermore, in order to allow an easier comparison, the values assumed by $|G_i^*|_{const}$ and $|G_i^*|_{red}$ at the nth cycle were normalised with respect to their initial values. Their plots (7_4_80$_{i\text{-}const}$ and 7_4_80$_{i\text{-}red}$, respectively) as a function of the number of loading cycles are shown in Figure 9.3, as well as the evolution of the normalised moduli of the specimens 0_2_80 and 7_4_80$_{bulk}$ (that indicates the double-layered specimen test results).

The differences observed between 7_4_80$_{i\text{-}const}$ and 7_4_80$_{i\text{-}red}$ in the greatest part of the test are obviously due to the fact that in the calculation of 7_4_80$_{i\text{-}const}$ it is assumed that all the damage is immediately localised at the interface, whereas, for 7_4_80$_{i\text{-}red}$, part of the damage affects also the AC outside the interlayer. However, in the proximity to the end of the test, the two interlayer moduli ($|G_i^*|_{const}$ and $|G_i^*|_{red}$) become very similar and thus, at this stage, the damage at the interface can be considered predominant and consequently, the damage of the AC outside the interface negligible. Therefore, the effect of the reduction

of $|G_{AC}^*|$ plays a minor role in the damage trend of $|G_i^*|$ when the "effective" damage at the interface occurs (as shown in chapter 8). Thus, the assumption of considering no damage in the material outside the interlayer zone can be considered valid without committing significant errors.

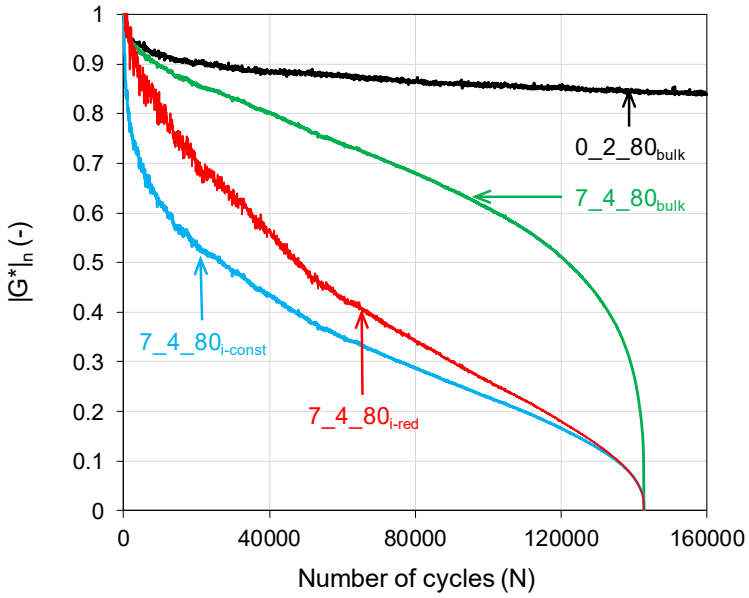

Figure 9.3. Evolution of the normalised complex shear modulus $|G^*|_n$ for specimens 0_2_80 and 7_4_80 during the shear-torque fatigue test.

The second aspect, that should be taken into account, is the selection of the proper value for the interlayer thickness H_i. Santagata et al. (2008) used X-ray Computer Tomography to measure the interlayer and in-layer air void content of double-layered specimens and found out that the interlayer region has approximately 25 mm of thickness. Analogously, Ktari et al. (2016b) utilised the Digital Image Correlation (DIC) technique to determine the interlayer thickness on double-layered specimens. The results showed that, in their study, the interlayer thickness was about 3 mm. Likewise, the results emerged in chapter 8 showed that the thickness of the interlayer can be approximately assumed equal to 15 mm.

In this study, a range of variation from 3 to 21 mm, with a step of 2 mm, was considered for the interlayer thickness H_i, by assuming a constant value for $|G_{AC}^*|$ equal to $|G^*|_{bulk}$ of 7_4_80. Based on what previously stated, Eq. (9.8) was used for the calculation of the interlayer complex shear modulus $|G_i^*|$ of the double-layered specimen 7_4_80.

Figure 9.4 presents $|G_i^*|$ (in blue), obtained with different values of H_i, as a function of the number of loading cycles, as well as the comparison with the corresponding $|G^*|_{bulk}$.

Figure 9.4 clearly shows that $|G_i^*|$ curves are characterised by the typical three phases of fatigue tests. In the beginning, $|G_i^*|$ decreases drastically and then decreases quite steadily until approaching the end of the test, when a sudden reduction of the interlayer modulus occurs. It can be observed that a sudden decrease in the initial value of $|G_i^*|$ occurs for low H_i values (i.e., less than 11 mm), indicating that $|G_i^*|$ is markedly affected by the value of the interlayer thickness H_i. Moreover, it can also be noticed that the higher the H_i value, the closer $|G_i^*|$ to the behaviour of $|G^*|_{bulk}$ (7_4_80$_{bulk}$).

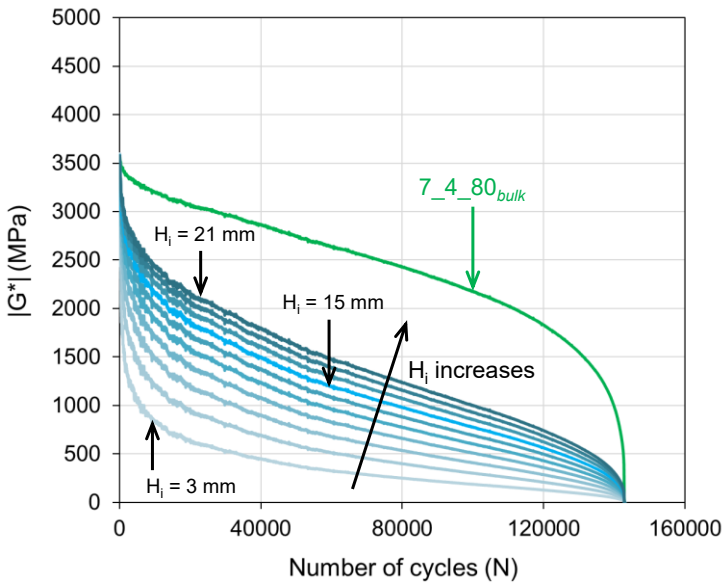

Figure 9.4. Evolution of $|G^*|_{bulk}$ and $|G_i^*|$ for specimen 7_4_80$_{bulk}$ during the shear-torque fatigue test.

Since the applied torque induces a mechanical response within the material in the form of shear strain γ and the increase in the strain is usually due to damage accumulation in the material, it is interesting to evaluate the influence of the interlayer thickness H_i on this parameter. The shear strain of the bulk system γ_{bulk} and the interlayer shear strain γ_i (in blue) of the specimen 7_4_80, calculated for different values of H_i, are reported in Figure 9.5. The shear strain of the bulk system γ_{bulk} shows a two-phase process consisting of an almost constant trend until the proximity of the end of the test when a sharp increase occurs. It is therefore clear that the double-layered asphalt concrete specimen absorbs the shear-torque fatigue loading by producing very low shear deformations for the greatest part of the test duration. On the contrary, by analysing the behaviour of γ_i, it is possible to observe that the shear strain tends to increase with the number of loading cycles and three distinct phases can be identified as in the case of $|G_i^*|$ (Figure 9.4). Moreover, it can be noted that the value of

H_i strongly influences the evolution of γ_i. The higher the value of H_i, the closer γ_i to the behaviour of γ_{bulk}. Specifically, changes in shear strain appear to be more noticeable assuming an interlayer thickness less than 11 mm. These outcomes suggest that H_i appears to be the variable which plays the most important role in the interlayer characterisation. For this reason, further research, focused on the accurate identification of H_i (for example, by utilising digital image correlation technique), can considerably help in the development of a more precise evaluation of the interlayer behaviour. Nevertheless, an interlayer thickness H_i equal to 15 mm was assumed in the following discussion, according to the results emerged in Part A.

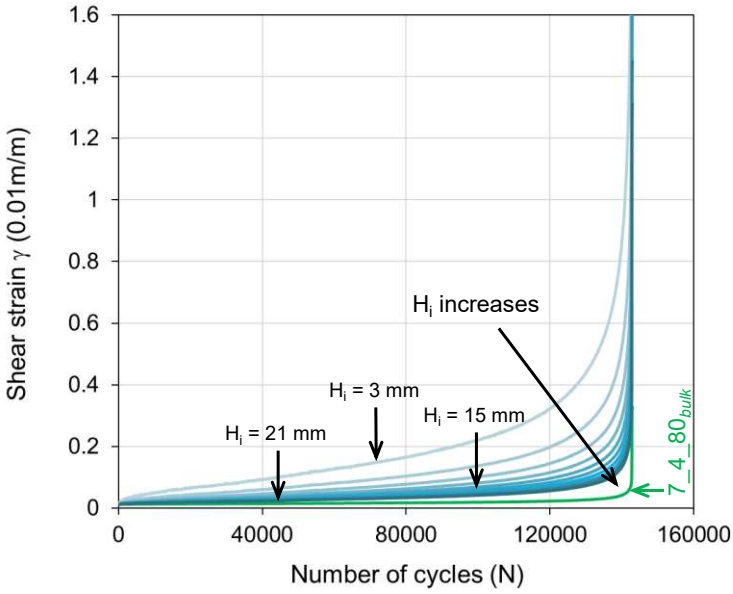

Figure 9.5. Evolution of γ_{bulk} and γ_i for specimen 7_4_80$_{bulk}$ during the shear-torque fatigue test.

9.5 Interlayer shear fatigue law

9.5.1 Fatigue failure criterion

A proper failure criterion should predict the fatigue life of the material and capture the failure of the specimen accurately (i.e., in this case, the formation of macro-cracks at the interlayer). In this regard, the results of Part A (chapter 8) showed that, for shear-torque fatigue tests performed on double-layered specimens, the classical fatigue failure criterion, which defines failure as the point at which the stiffness modulus value reduces to 50% of its initial value,

seems to provide an inaccurate estimation of the number cycle to failure (N_f) since it is not able of quantifying the damage mechanisms that occur within double-layered specimens. In chapter 8, it is suggested that a 70% reduction of $|G^*|_{bulk}$ used as failure criterion seems to better describe the material behaviour under shear-torque fatigue loading.

As an example, Figure 9.6a through Figure 9.6d present the criterion of the 70% reduction of $|G^*|_{bulk}$ applied to four test results in this study. These graphs suggest that the number of cycles to failure (N_f) determined based on this failure criterion correspond to a reduction of the interlayer complex shear modulus $|G_i^*|$ approximately equal to 90%, that is $|G^*|_n = 0.1$. Consequently, rather than to use the 70% reduction of $|G^*|_{bulk}$, the 90% reduction of the initial value of the interlayer complex shear modulus $|G_i^*|$ can be adopted as a failure criterion for shear-torque fatigue test carried out on double-layered asphalt specimens.

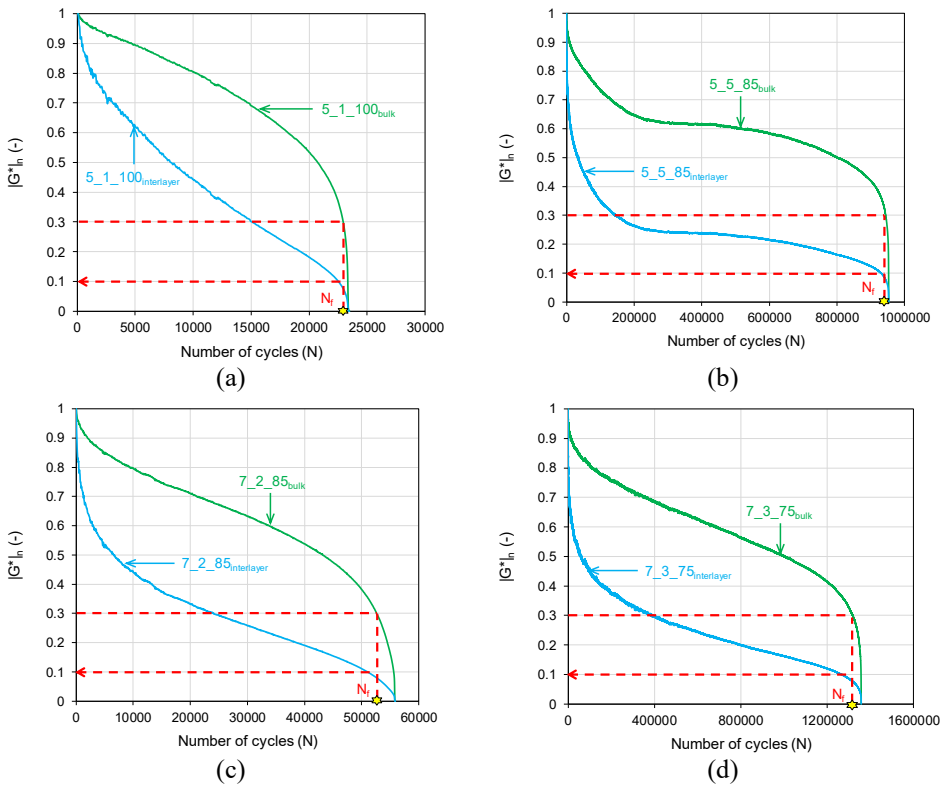

Figure 9.6. Evolution of the normalised complex shear modulus $|G^*|_n$ during the shear-torque fatigue test and fatigue failure criterion: a) 5_1_100; b) 5_5_85; c) 7_2_85; d) 7_3_75.

9.5.2 Fatigue curve

In Figure 9.7, the interlayer shear fatigue curve of the specimens cored from slabs 5 and 7 is plotted in a log-log plane. Such analysis was based on a power-law relationship between the amplitude of the applied shear stress $\tau_{max,0}$ and the number of loading cycles to failure N_f, recorded in correspondence of the 90% reduction of the initial value of $|G_i^*|$, using the following equation:

$$\tau_{max,0} = a \cdot {N_f}^{-b} \tag{9.9}$$

where the parameters a and b are regression coefficients and usually depend on the material and testing temperature. Specifically, b represents the slope of the linear regression which is obtained in a log-log plane. Figure 9.7 shows that as the level of shear stress (i.e., torque) decreases, the shear fatigue life of the bituminous material increases. This is due to the fact that a high shear stress level accelerates the damage accumulation at the interlayer and this result in a faster decrease in $|G_i^*|$ as shown in Figure 9.6. The test performed on the specimen 5_3_85 was discarded and not reported in Figure 9.7 because of premature failure in the specimen. At the end of the test, it was found that the interface was wet. A plausible explanation of such fact is that the specimen was not sufficiently dry as a result of the rectification process, in fact, it is demonstrated that the presence of water at the interface leads to a decrease in the interlayer resistance compared to the dry specimen (Raab and Partl, 2004).

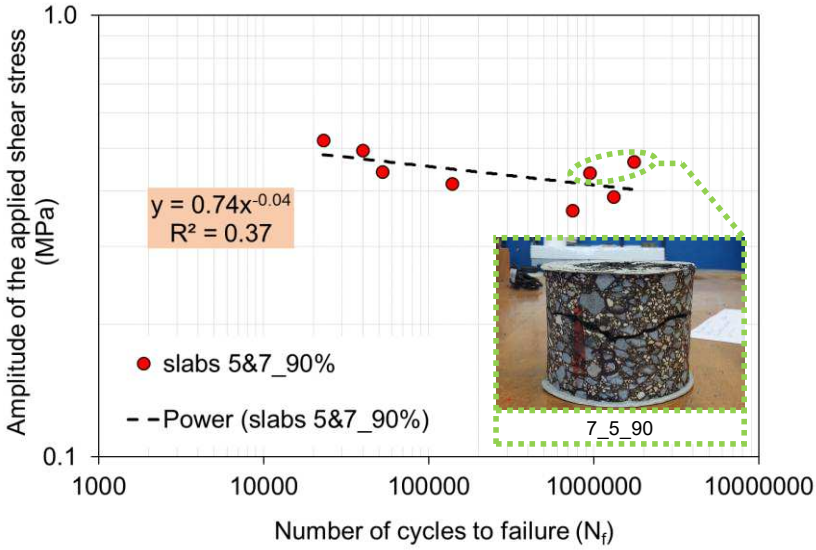

Figure 9.7. Interlayer shear fatigue curve in terms of the amplitude of the applied shear stress as a function of the number of cycles to failure.

In Figure 9.7, it can be noticed that the correlation between the obtained data is not good (R^2 = 0.37) but this can be due to the fact that the two data points circled in green, do not follow the general trend as they provide higher values of N_f for higher values of $\tau_{max,0}$. Looking for the reason for this behaviour, it was observed that, in both cases, the crack pattern at the interface was irregular (see the box in Figure 9.7), contrarily to what happened for all the other specimens, for which the fracture occurred exactly at the interface (Figure 9.8). Moreover, it was noticed that both these specimens (5_5_85 and 7_5_90) were cored at the centre of the slabs (i.e., position #5 of Figure 7.1a), where a better interlocking between the two bituminous layers in contact could be achieved due to the not homogeneous compaction process performed by the roller compactor (i.e., higher compaction energy is expected in the centre of the slab). However, it is worth pointing out that, among the laboratory methods used to fabricate laboratory specimens, the roller compactor provides the best correlation with field cores in terms of both internal aggregate structure and mechanical properties (Airey et al., 2005; Airey and Collop, 2016; Dubois et al., 2010).

Figure 9.8. Failure mechanisms of the specimens at the border of the slab.

In Figure 9.9, the updated interlayer shear fatigue curve, in which the specimens cored in position #5 (empty dots) were not considered, is reported. In this case, the good correlation coefficient (R^2 = 0.85) clearly indicates that the coring position is relevant, at least for shear-torque fatigue tests. This thesis is based on limited data and needs to be verified by further testing. Moreover, it can be seen that fatigue law parameter b is very close to -0.1, hence very similar to that obtained with the Cyclic-ASTRA and Cyclic-MAST tests (i.e., b equal to -0.13 and -0.07, respectively).

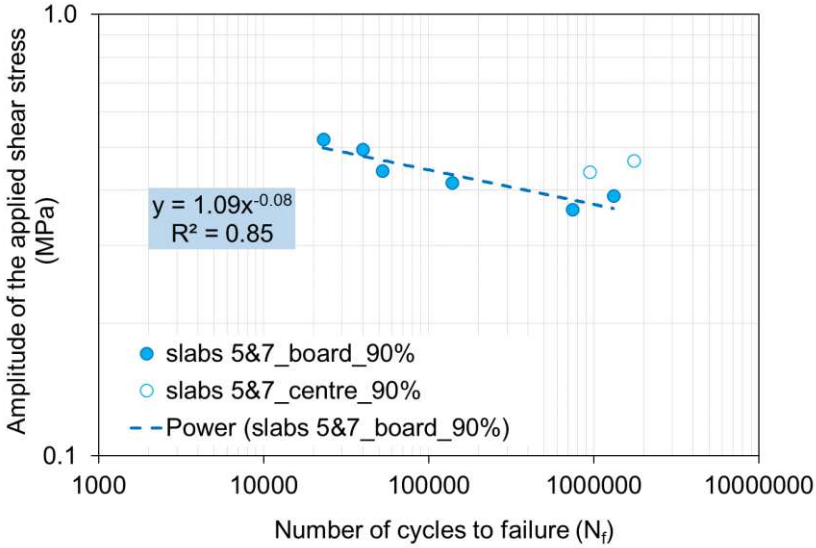

Figure 9.9. Interlayer shear fatigue curve of the border specimens in terms of the amplitude of the applied shear stress as a function of the number of cycles to failure.

It can be concluded that the fatigue process of a double-layered specimen is a complex phenomenon due to a twofold factor: the heterogeneous nature of the bituminous material and the presence of a weakness zone (i.e., interlayer). Besides, other viscoelastic phenomena occur during fatigue tests (e.g., self-heating, thixotropy, non-linearity) but have not been taken into account in this study. However, the adopted approach globally allows assessing the fatigue shear behaviour of double-layered specimens. This shear fatigue interpretation permits a more intrinsic damage evolution corrected from the damage effects that do not occur at the interlayer always assuming that the two phenomena are not coupled. The hypothesis that the non-coupled effect of the damage occurring inside and outside the interlayer can be considered valid when the level of damage increases (i.e., the number of loading cycles increases). It is underlined that the work herein is expected to be a foundational basis for further developments. More experiments are needed to confirm the theoretical assumptions and broaden the materials tested.

9.6 Conclusions

This Part B was focused on the evaluation of the fatigue behaviour of pavement bituminous interlayers subjected to shear-torque fatigue tests. A preliminary experimental investigation was carried out on single- and double-layered specimens (RILEM specimens) performing shear-torque fatigue tests at fixed temperature and frequency (20 °C and 10 Hz) to investigate the influence of the interface on shear-torque fatigue properties. Based on these preliminary finding, a model describing the evolution of the interlayer damage and a new fatigue failure criterion were proposed in order to correctly identify the material behaviour at the interlayer and to overcome the classical damage approach. Based on the results, the following main conclusions can be drawn:

- The presence of the interface constitutes a weakness zone in the double-layered specimen, and therefore, it noticeably influences the shear fatigue performance.
- The norm of the interlayer complex shear modulus $|G_i^*|$, as well as the norm of the complex shear modulus $|G^*|_{bulk}$, decreases as the number of loading cycles increases, indicating to be a good indicator of damage within the interlayer of the specimen.
- The proposed model describes the evolution of the interlayer damage of double-layered specimens under shear-torque fatigue tests through the analysis of the variation of the norm of the interlayer complex shear modulus $|G_i^*|$. Preliminary validation of the model showed that it adequately characterises the evolution of the interlayer properties during cyclic torque loading even if further refinements to the model are needed.
- A new fatigue failure criterion ($|G_i^*|_n = 0.1$ or 90% reduction of the initial value of $|G_i^*|$) was proposed to be used for cyclic torque test since seems to better correspond to the mechanisms of failure that occurred at the interface of double-layered specimens. Results showed a significant increase in shear fatigue life with the decrease in the applied shear stress, denoting to be extremely sensitive to the applied torque level.
- A comparison between specimens cored at the centre and the border of the compacted slab seems to show the existence of a non-uniformity compaction which is reflected in a dissimilar shear fatigue life of the specimens. This result must be confirmed by future experimentation.

Summarising, this study suggests that the proposed testing method and analysis can effectively provide a noticeable help for the understanding of shear-torque fatigue phenomena at the interface of double-layered asphalt concrete specimens. Further efforts should be lavished to confirm the theoretical assumptions and broaden the materials tested to assess the reliability and precision of the model.

Chapter 10.

Experimental investigation with shear-torque fatigue test

Part C

10.1 Introduction

Maintenance and rehabilitation of road pavements are important issues for motorway agencies. In the last forty years, the interlayer reinforcement system has been demonstrated to be as a valid solution to improve performance, to extend service life and thus to reduce maintenance costs of bituminous pavements. The main issue in using this technique is that the presence of an interlayer reinforcement may hinder the full transmission of horizontal shear stress between bituminous layers, reducing the overall efficiency of the pavement system. However, the mechanisms underlying the effectiveness and proper installation of this type of reinforcement system are still not fully understood, and the choice of the most appropriate geosynthetic and its optimal location in the pavement system are mainly based on experience. Then, in addition to the experimental investigation discussed in the previous chapters, another analysis was conducted at the University of Limoges, always under the supervisor of Professor Christophe Petit. The aim was to evaluate the mechanical behaviour of reinforced interfaces in asphalt concrete pavements under cyclic shear loading. For this purpose, an experimental trial pavement section was realised with different types of interfaces (reinforced with geogrids and unreinforced). After that, cores were taken from the trial section to carry out shear-torque fatigue tests. The first part of this chapter presents the state-of-the-art review of the literature related to reinforcement system within bituminous pavements. The second part presents and discusses the realisation of the trial section and shear-torque fatigue torque tests performed on double-layered asphalt concrete specimens with different types of interface cored from field test section. Finally, the first results obtained are described. It is important to underline that the work presented in this chapter represents the first stage of a wider study, hence one should keep in mind that these results should be treated as exploratory, but they provide interesting insights.

10.2 General overview

Nowadays, the intensification of traffic and the increase in axle loads accelerate asphalt pavement degradation generating high-stress values which lead to premature failure

processes and loss of functional characteristics. Moreover, the degradation process of bituminous pavements is accelerated by heavy passing over/near a crack and/or by daily and seasonal temperature changes (Brown et al., 2001; Francken, 2005; Jayawickrama and Lytton, 1987; Kim et al., 1999; Zhou and Scullion, 2003). It is now well accepted that fatigue cracking, reflective cracking, and rutting are the major mechanisms of distress in bituminous pavements. These distresses have been reported in many parts of Europe, the United States and other countries.

The reduced budget for pavement maintenance forces civil engineers to seek effective road maintenance solutions to achieve adequate pavement performance, as well as alternative materials for the design and rehabilitation of bituminous pavement. Usually, the most common rehabilitation technique is the construction of asphalt overlay above the existing cracked pavement (Figure 10.1). Asphalt overlay is a cost-effective method, but this solution is rarely durable because of the propagation of pre-existing cracks through to the new surface generating by traffic loading and temperature variations. Generally, the thicker the overlay, the longer it will last.

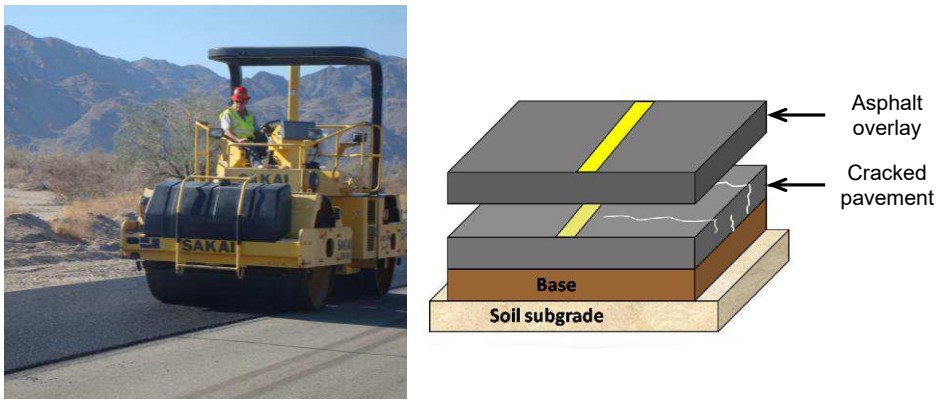

Figure 10.1. Asphalt overlay.

In recent years, maintenance and rehabilitation processes in the road networks are often performed by placing within asphalt layers reinforcement systems in order to prevent or delay the development of cracks (Figure 10.2). In this sense, these systems can significantly increase the maintenance intervals of asphalt pavements resulting in a cost-effective and long-lasting pavement rehabilitation method. It is worth saying that these reinforcement systems can be also used in the construction of new pavement.

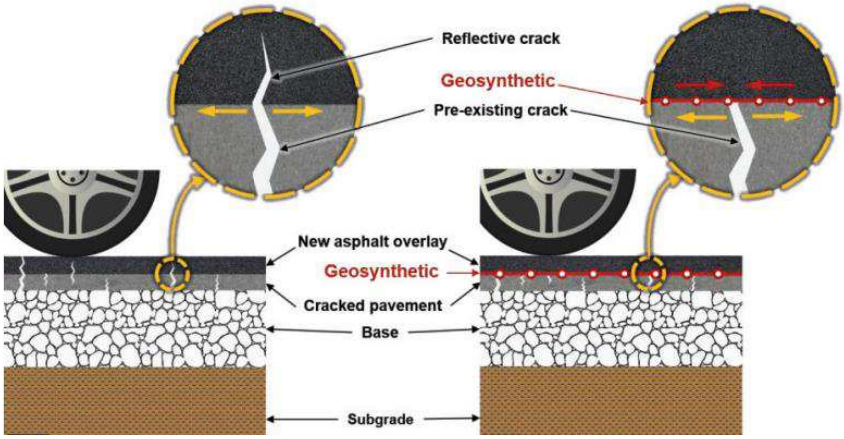

(a) (b)

Figure 10.2. Use of reinforcements in mitigation of reflective cracking in asphalt overlays: a) roadway designed without reinforcements, b) roadway designed with reinforcements (Zornberg, 2017).

Several reinforcement systems from many manufacturers worldwide are available in the market. The types of geosynthetic (Figure 10.3) are divided into four groups: geotextile, geomembrane, geogrid and geocomposite (Button and Lytton, 2007). Geotextiles are permeable products, consisting of polymeric materials produced from crude oil (mainly polypropylene and polyester), but may also contain nylon, other polymers, natural organic material or glass fibres. Geomembranes are waterproof bituminous products, they are generally composed of a three-state system, of which the lower one is formed by bituminous compounds with a self-adhesive lower surface, the central one by a glass fibre grid, the upper one by a bituminous compound with a thermo-adhesive upper surface (adhesion occurs when in contact with the bituminous mixture for temperatures above 120 °C). Geogrids are products with a planar reticular structure and open mesh (range from 5 to 50 mm) resistant to tensile stress (they can also reach tensile strength values of 200 kN/m), composed of synthetic fibres (polyester, polyethene, polypropylene) or glass, carbon connected together. Furthermore, in order to provide good adhesion, some geogrids ribs can be coated with asphalt binder, foil or other materials Due to their high resistance, geogrids are used to perform the reinforcement function where no particular waterproofing function is required. Whereas, geocomposites are products obtained by the combination of two or more geosynthetics (e.g., bituminous membrane and geogrid) and represent a valid solution since such materials join the tensile properties of the geogrids with the stress-relieving and the waterproofing effects of the bituminous membranes (Figure 10.4).

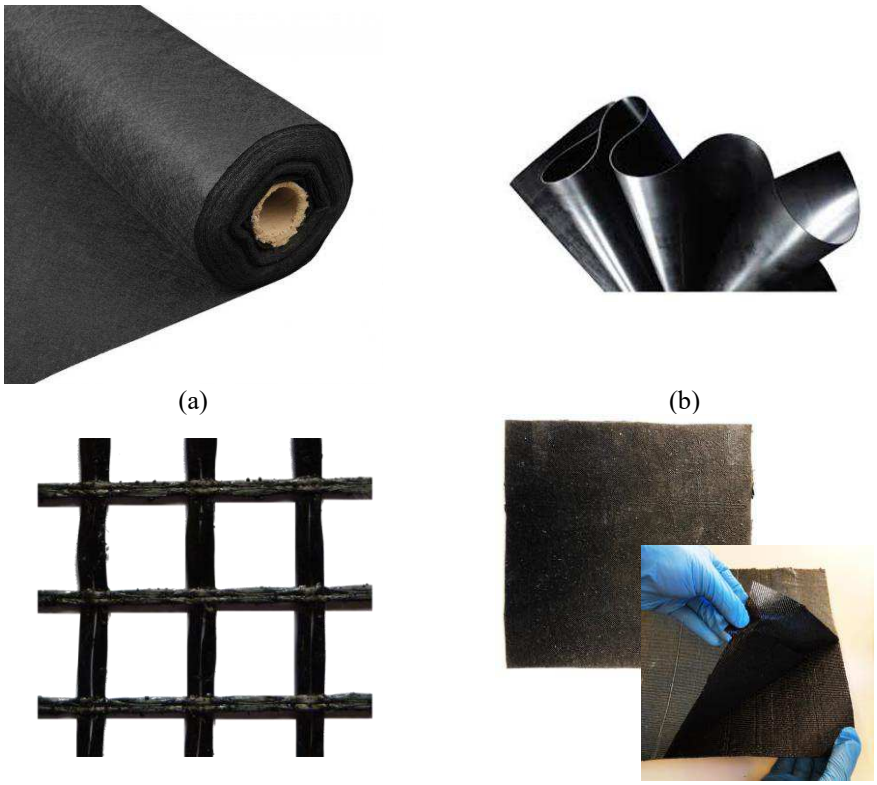

(a) (b)

(c) (d)

Figure 10.3. Different geosynthetics for road pavements: a) geotextile, b) geomembrane, c) geogrid, d) geocomposite.

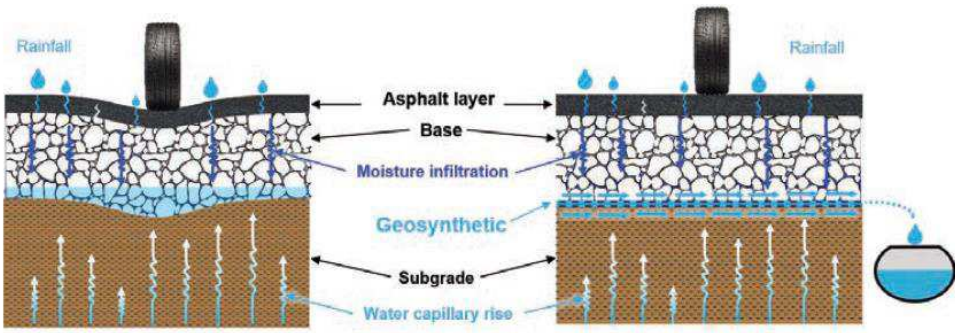

(a) (b)

Figure 10.4. Waterproofing action: a) roadway designed without geocomposite, b) roadway designed with geocomposite (Zornberg, 2017).

The first studies on geosynthetics were carried out in the 1980s (Brown et al., 1985). Many studies have been conducted over the last 40 years in order to investigate the behaviour of reinforced asphalt pavement. Different studies (Austin and Gilchrist, 1996; Brown et al., 2001; Canestrari et al., 2015; Ferrotti et al., 2012; Nejad et al., 2016; Prieto et al., 2007; Ragni et al., 2020; Saride and Kumar, 2017; Shukla and Yin, 2004; Sobhan and Tandon, 2008) showed that geosynthetics can clearly extend the pavement fatigue life, improve resistance to reflection cracking, and increase rutting resistance. Therefore, the extra effort and costs associated with such reinforcement are justified by the longer service life and lower lifecycle costs of the pavement. On the other hand, the presence of a reinforcement inevitably causes a considerable reduction of the interlayer shear resistance at the interface, this phenomenon is known as "debonding effect" (Brown et al., 2001; Caltabiano and Brunton, 1991; Canestrari et al., 2006; Ferrotti et al., 2011; Pasquini et al., 2013; Zamora-Barraza et al., 2010). This debonding effect at the interlayer influences the pavement response in terms of stress-strain distribution (Canestrari et al., 2005; Shukla and Yin, 2004; Sobhan and Tandon, 2008), as shown in chapter 2. Graziani et al. (2014) built a reinforced asphalt pavement instrumented with pressure cells and asphalt strain gauges. In this study, falling weight deflectometer (FWD) tests along with a layered elastic theory (LET) model analysis showed that certain grids cause a noticeable interface slip and this could lead to an increase in the tensile strain measured within the pavement due to debonding phenomena. Therefore, if the interlayer shear resistance excessively decreases due to the presence of the reinforcement, the overall pavement strength would be negatively affected, and slippage would also appear at the pavement surface due to tangential stress produced by vehicular motion.

The most used geosynthetics for pavement applications are geogrids. Brown et al. (2001) found out that when fibreglass geogrids are used as reinforcement at the interface, reinforced specimens provide a service life 1.2-1.8 times higher than those unreinforced (Figure 10.5). Moreover, geogrids are usually more effective as reinforcement system than geotextiles, probably due to the interlocking effect and to the higher stiffness of the grid mesh, according to the results obtained by Zamora-Barraza et al. (2011). In particular, Caltabiano and Brunton (1991) observed that the shear resistance at the interface is reduced by about 20% in the case of specimens with geogrid and about 30% in the case of specimens with geotextile compared to the unreinforced specimen.

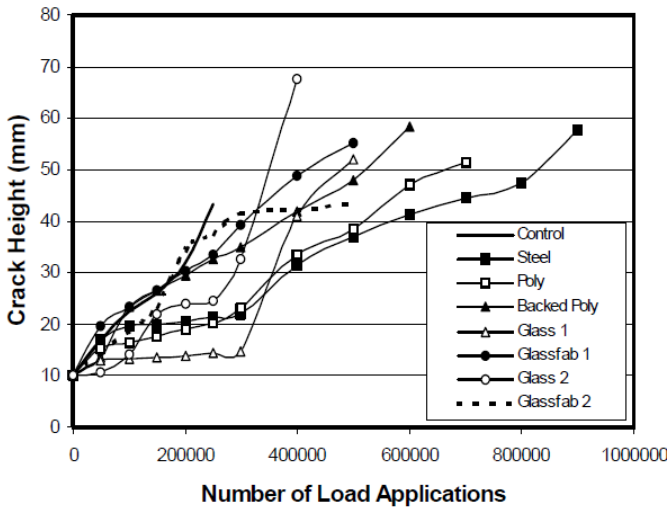

Figure 10.5. Variation of crack height with the number of load cycles (Brown et al., 2001).

The performance of the reinforced system by using geogrids depend on their mesh size, shape and coating, and the position of the geogrid within the bituminous pavement. The influence of these parameters has been thoroughly studied by means of both laboratory and in-situ investigations. In order to obtain a stable reinforced paving system, geogrids should permit mechanical interconnection, i.e., mutual contact, between adjacent bituminous layers through the mesh openings (Brown et al., 1985; Canestrari et al., 2006), in order to assurance a good distribution of stress (Ferrotti et al., 2012; Pasquini et al., 2014; Sobhan and Tandon, 2008). In this regard, the mesh size is one of the most important aspects to consider when assessing the "debonding" effect in the presence of geogrids. Canestrari et al. (2006) have found that a mesh size excessively tiny could inhibit the interconnection between bituminous layers in contact, compromising the shear strength, while a mesh size excessively wide could result in limited mechanical performance, compromising the flexural strength (per unit length). However, it is worth noting that the interlayer properties also depend on the asphalt concrete characteristics, such as aggregate gradation. In this sense, the mesh size should depend on the aggregate gradation and on the depth at which the grid is placed. In addition, the type of material or possible coating of the geogrid must be such as to develop a good degree of adhesion and compatibility between the bituminous mixture and the geogrid. Therefore, the interface reinforced with geogrids should improve the mechanical performance of the multilayer pavements in terms of bending without penalising their shear performance. Otherwise, the application of geogrids at the interface can be ineffective from a technical and economic point of view or even detrimental.

However, to exploit the potential of the reinforcement system as much as possible, particular attention must be paid to the in-situ installation (Figure 10.6). It should be noted that to maximise the effectiveness of the reinforcement installation, the layer on which the reinforcement is applied must be devoid of structural defects (e.g., rutting, depressions) or drainage problems. In fact, numerous installations of these materials have shown that the laying surface must be thoroughly clean, dry and free of other loose material, as the humidity combined with dust, water, snow or ice inhibits the proper adhesion of the reinforcement to the layer underneath. Any deficiencies must be resolved beforehand with special interventions (e.g., crack sealing, patch). To ensure a correct application, the geosynthetic must be perfectly laid on the layer underneath avoiding any possible corrugation and should remain flat during the laying of the upper layer with the paver machine (Bocci et al., 2007; Franken, 2005; Shukla and Yin, 2004; Uijting et al., 2002; Vanelstraete and De Visscher, 2004). Lastly, the application of tack coat, before the application of the reinforcement system, is of fundamental importance, especially for those products which do not have adhesive coatings or pre-bituminous coatings, or which are not inserted into bituminous membranes (Ferrotti et al., 2011). When applying the tack coat, it is essential to pay attention both to its correct dosage, in order to obtain the maximum degree of adhesion, avoiding reflux or sliding, and to its complete "breakage" before the application of the reinforcement system and/or the bituminous layer. Instead, the application of tack coat may adversely affect the interface shear strength for some products (e.g., bituminous membranes) due to the bituminous film which may inhibit the thermo-adhesive lower layer of the membrane (Canestrari et al., 2012; Pasquini et al., 2014). In any case, it is good practice to follow the recommendations of the manufacturers.

Figure 10.6. Application of the reinforcement system on a new (left) or milled (right) surface.

Besides, to fully characterise the reinforced systems, a comprehensive laboratory study should be based on tests able to investigate the performance of the reinforced system against repeated loading (e.g., three-point bending test, four-point bending test) as well as on

tests to determine the interlayer shear resistance, that is, the adhesion of the interlayer system with the upper and the lower layers (e.g., shear test). Laboratory tests usually consider double-layered specimen reinforced with geosynthetic placed at the interface to study the effectiveness of the reinforcement system. However, double-layered reinforced specimens prepared in the laboratory may lead to results that do not occur in-situ due to different compaction between in-situ and laboratory and different reinforcement installation techniques (Ragni et al., 2020). Consequently, the construction of full-scale test pavement is more appropriate for evaluating the effect of reinforcement systems.

Given this background, in order to improve knowledge of pavement reinforcements application, this part of the study focused on the analysis of the interlayer bonding between bituminous pavement layers and reinforcements. The main goal of this study concerned a better understanding of reinforcement systems behaviour and their effects on the interlayer mechanical properties under cyclic loading at the interface. To accomplish the objective of this study, a real-scale trial section characterised by different types of interfaces (reinforced with geogrids and unreinforced) were built. Two reinforced interface conditions were considered for the realisation of the pavement section. An unreinforced reference system was also included for comparison purposes. Shear-torque fatigue tests were performed in-situ cored specimens in order to verify the effectiveness of the reinforcement. To determine the failure of each specimen, different fatigue failure criteria were adopted also to determine the most appropriate fatigue approach.

10.3 Experimental program

10.3.1 Reinforcing materials

Two different geosynthetics (coded as CF and FG) were used as reinforcement in this experimental study. CF geogrid (Figure 10.7a) is characterised by carbon fibre rovings with a square 15 mm pre-coated with bitumen. Whereas, FG geogrid (Figure 10.7b) is characterised by a fibreglass yarns with a square 25 mm mesh in conjunction with a light polyester knitted veil. The basic characteristics of CF and FG geogrids are listed in Table 10.1.

Table 10.1. Characteristics of the geosynthetics.

Geogrid	Material	Grid size (mm)	Tensile modulus (N/mm^2)	Elongation at rupture (%)	Tensile force mesh (kN/m)	Treatment
CF	carbon fibre	15	240000	1.75	200	Bitumen
FG	glass fibre	25	not given	3	100	Uncoated

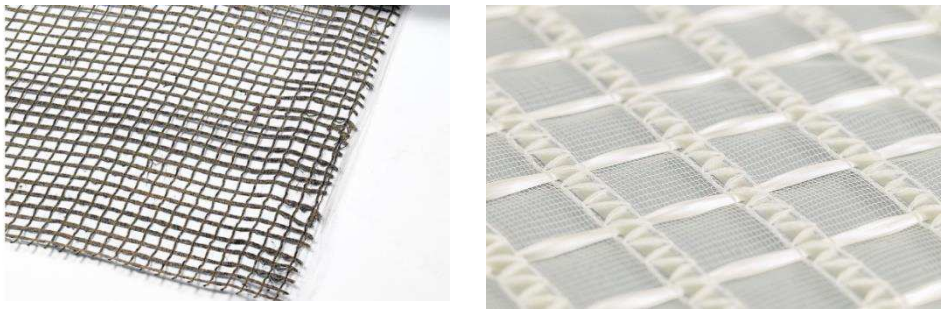

(a) (b)

Figure 10.7. Detail of the installed geosynthetics: (a) carbon fibre geogrid CF and (b) glass fibre geogrid FG.

10.3.2 Trial section

A full-scale trial section was constructed at the Laboratoire GC2D of the University of Limoges (Egletons, France) at the beginning of 2018. This experimental section (8 m long, 3 m wide, and 2 m deep) was built in a pit installed in a building with the possibility to control several conditions (e.g., temperature, humidity) More detailed information is available in Petit et al. (2019). The trial section was characterised by different interfaces as follows:

- unreinforced with a tack-coat interface used as a reference for comparison purposes (coded as UN);
- tack-coat + reinforced with carbon fibre geogrid (coded as CF);
- tack-coat + reinforced with fibre glass geogrid (coded as FG).

Figure 10.8 depicts the dimensions and position of the three different interfaces included in the trial section.

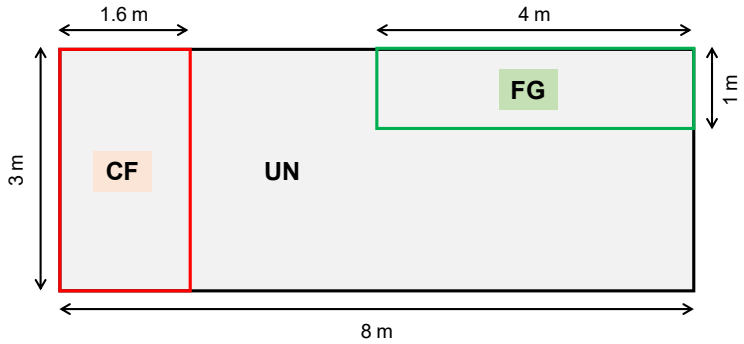

Figure 10.8. Scheme of the trial section.

The main construction activities of the pavement section are summarised below (Figures 10.9-10.11):

- laying on of 20/40 gravel with a thickness of 200 mm on the bottom of the pit;
- realisation of the subgrade course constituted of decomposed granite having a thickness of 1400 mm;
- realisation of the subbase course with untreated gravel of maximum diameter 31.5 mm (Grave Non-Traitée GNT 2 according to NF EN 13285) having a thickness of 300 mm;
- realisation of the base course with asphalt concrete AC 14 base (according to EN 13108-1) having a thickness of 90 mm;
- accurate cleaning and preparation of the surface;
- application of the tack-coat at a rate of 300 g/m^2 of the residual binder;
- hand application of the geogrids (except for the unreinforced section). The geogrids were placed directly on the fresh emulsion right after spreading;
- tack-coat was also applied above the geogrid FG at a rate of 200 g/m^2 of the residual binder;
- once the tack-coat emulsion was fully cured, placement of the wearing course with asphalt concrete AC 10 surf (according to EN 13108-1) having a thickness of 50 mm.

Figure 10.12 shows the cross-section of the full-scale trial section.

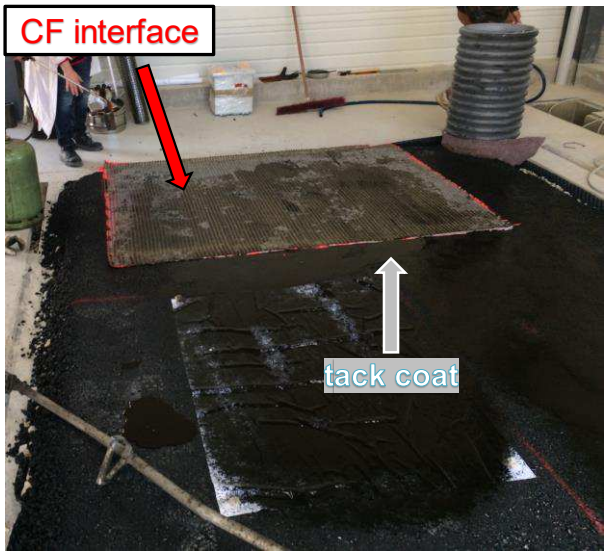

Figure 10.9. Installation of carbon fibre geogrid (CF).

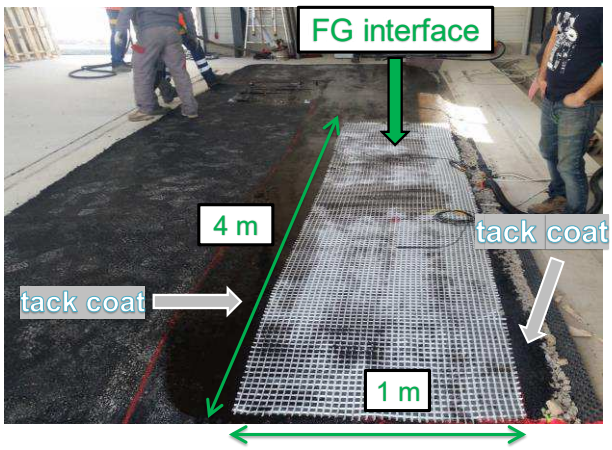

Figure 10.10. Installation of glass fibre geogrid (FG).

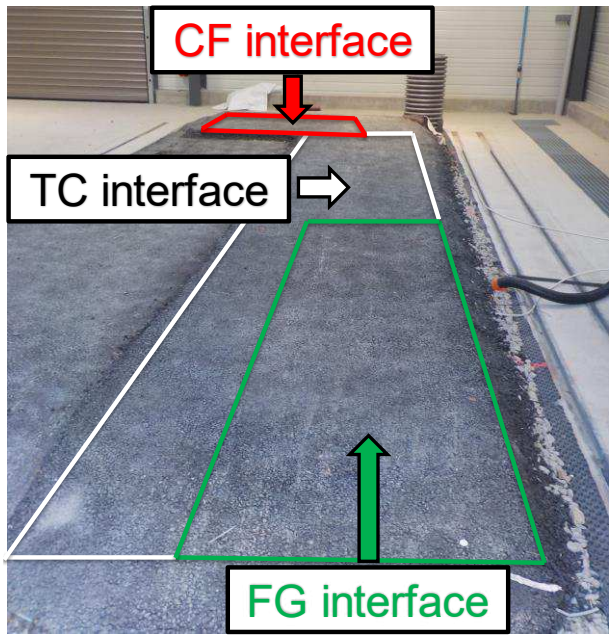

Figure 10.11. Completed full-scale trial section.

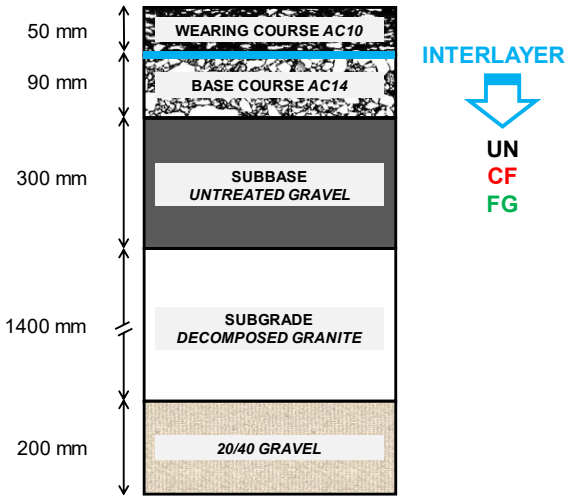

Figure 10.12. Cross-section of the full-scale trial section.

10.3.3 Testing program and procedure

In May 2018, several core samples with a nominal diameter of 100 mm and a thickness of 140 mm were extracted from the experimental pavement section (Figure 10.13). Specifically, 5 samples were cored from the UN section, 4 samples from the CF section and 8 samples from the FG section. Each cored specimen was marked by an identification code (ID) defining its location in the trial section; for example, UN_2 represents the specimen number 2 taken from the unreinforced section (UN).

In the laboratory, each core was sawed in order to obtain a total thickness of about 90 mm (Figure 10.14a). Finally, both specimen sides were polished with a lapping device in order to obtain a perfectly regular and smooth surface (Figure 10.14b). The thickness of the specimens and their bulk densities, measured according to EN 12697-6, are summarised in Table 10.2.

Figure 10.13. Field cored specimens.

(a) (b)

Figure 10.14. Rectification of the specimen: (a) cutting and (b) lapping.

Table 10.2. Final properties of the specimens.

Interface type	Specimen (#)	Diameter (mm)	Thickness total (mm)	Thick. lower layer (mm)	Thick. upper layer (mm)	Mass (g)	Bulk density (g/cm^3)
UN	1	99.3	86.6	45.1	41.5	1491.9	2.23
	2	99.3	88.4	45.4	43.0	1510.9	2.20
	3	99.3	82.3	40.5	41.8	1402.6	2.20
	4	99.2	79.5	41.5	37.9	1336.2	2.18
	5	99.3	83.6	39.4	44.3	1443.0	2.23
CF	1	99.4	88.4	46.1	42.3	1515.2	2.21
	2	99.4	88.7	45.3	43.5	1514.5	2.20
	3	99.5	88.8	45.7	43.1	1513.4	2.19
	4	99.3	88.3	43.0	45.3	1500.8	2.20
FG	1	99.3	90.0	45.7	44.4	1616.5	2.32
	2	99.3	89.1	45.2	43.9	1589.9	2.30
	3	99.3	89.7	44.0	45.7	1584.5	2.28
	4	99.2	88.1	44.0	44.1	1536.8	2.26
	5	99.3	86.2	41.6	44.6	1498.4	2.24
	6	99.2	87.5	45.5	42.2	1498.3	2.21
	7	99.2	89.0	44.9	44.1	1453.5	2.11
	8	99.3	90.7	47.5	43.5	1633.0	2.32

Shear-fatigue torque tests were carried out on the cored cylindrical double-layered specimens to evaluate the influence of the reinforcement on the interlayer fatigue shear performance. Tests were carried out at a temperature of 20 °C and a frequency of 10 Hz for each interface type. For specimens FG, 3 repetitions were also carried at 10 °C always at a frequency of 10 Hz. The temperature was controlled with a climatic chamber, all specimens were conditioned for 3 hours at each temperature before testing. Extreme care was taken when gluing the specimen to the test machine in order to avoid any eccentricity that could affect the test results. The testing program is summarised in Table 10.3. For each interface type, one or two tests were conducted applying different torque levels to obtain a wide enough range of the number of cycles to failure.

Table 10.3. Experimental program.

Interface type	Diameter (mm)	Shear-torque fatigue test replicates (#)	
		20 °C; 10 Hz	10 °C; 10 Hz
UN	100	5	-
CF	100	4	-
FG	100	5	3
Total		14	3

As explained in paragraph 7.3.2, the test consists of measuring the sinusoidal torsional rotation angle (α) when a sinusoidal torque (T) is applied along with a small axial compression load (N) on a cylindrical specimen of asphalt concrete, by means of a servo-hydraulic press. Small axial load amplitude (0.05 kN) was applied to ensure a good alignment of the specimen and steel platens in order to guarantee the homogeneity of the stress states in the specimen. The sinusoidal evolution with time of the two measured values is defined by the following equations:

$$T(t) = T_0 \sin(\omega t) \tag{10.1}$$

$$\alpha(t) = \alpha_0 \sin(\omega t - \varphi) \tag{10.2}$$

where T_0 is the amplitude of the applied torque, ω is the torque pulsation ($\omega = 2\pi f$ with f the load frequency), t is the time, α_0 is the amplitude of the torsional rotation angle, and φ is the phase angle, which is related to the lag between stress and strain.

Considering complex notations where j is the complex number defined by $j^2 = -1$, the measured values can be written as follows:

$$T^*(t) = T_0 \exp[j\omega t] \tag{10.3}$$

$$\alpha^*(t) = \alpha_0 \exp[\mathrm{j}(\omega t - \varphi)] \tag{10.4}$$

Complex shear modulus G^* of materials can then be calculated from cyclic torque tests with the following equation:

$$G^* = \frac{H}{I_p} \frac{T_0 \ \exp[\mathrm{j}\omega t]}{\alpha_0 \ \exp[\mathrm{j}(\omega t - \varphi)]} \tag{10.5}$$

where H is the specimen height, $|G^*|$ is the norm (or absolute value) of the complex shear modulus, and $I_p = \frac{\pi R^4}{2}$ is the polar moment of inertia of the circular section.

The choice of fatigue criterion has paramount importance for the understanding of material behaviour. The fatigue life value (N_f) of the tested specimen is defined as the number of cycles corresponding to the failure point for a given specific criterion. Different approaches for the prediction of fatigue life can be found in the literature. Usually, traditional approach defines failure as the point at which the decrease of the material modulus reaches a certain value. The most classical fatigue criterion ($N_f = N_{50}$) used a threshold value of 50% of the initial modulus values (Shen and Lu, 2011) as shown in Figure 10.15. As an alternative to the traditional approach, Reese (1997) suggested a new failure approach based on the evolution of the phase angle φ taking into account the viscoelastic behaviour of asphalt materials. During cyclic loading, the measured phase angle of asphalt concrete generally shows a steady increase followed by a sudden decrease. The cycle corresponding to this sudden decrease is defined as the number of cycles to failure ($N_f = N_{\varphi max}$) (Figure 10.16). Compared to the traditional approach, this approach seems to have a more theoretical underpinning, as the sudden reduction of the phase angle represents a viscoelastic behaviour modification of the material probably due to the formation of macro-cracks. However, the real mechanism governing the phase angle evolution (e.g., nonlinear viscoelasticity, fatigue cracking) is not yet fully understood.

Fatigue failure criterion that can accurately define the effective failure of the double-layered asphalt concrete during cyclic torque tests has yet to be developed. As shown in chapter 8 (Part A), adopting the acoustic emission (AE) technique to study the fatigue behaviour of bituminous interlayers in cyclic torque test, it was noticed that the damage evolution phase occurs in the specimen when its complex shear modulus decreases by about 70%. According to these results, the 70% decrease of the stiffness initial value can be used as fatigue criterion ($N_f = N_{70}$), as shown in Figure 10.15.

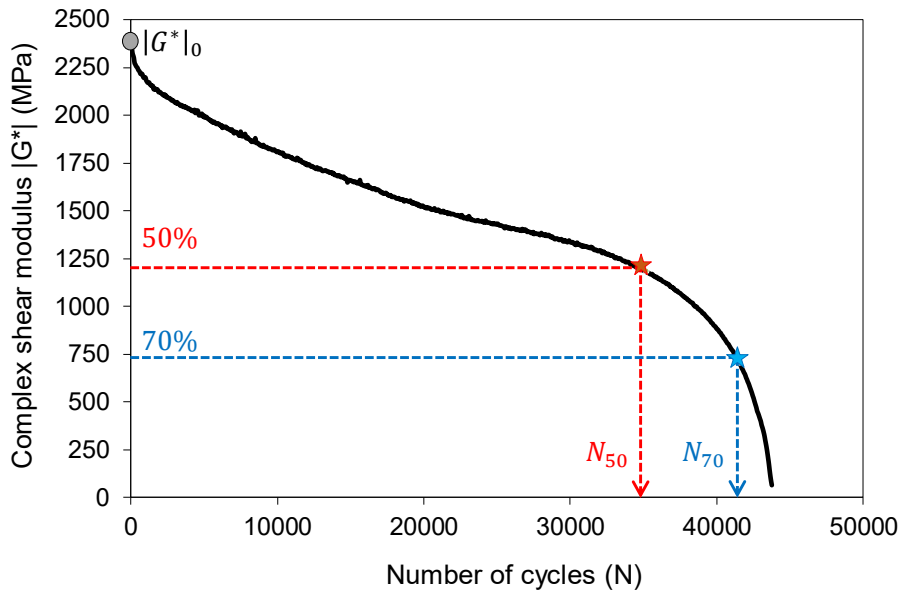

Figure 10.15. Definition of failure using the material modulus approach.

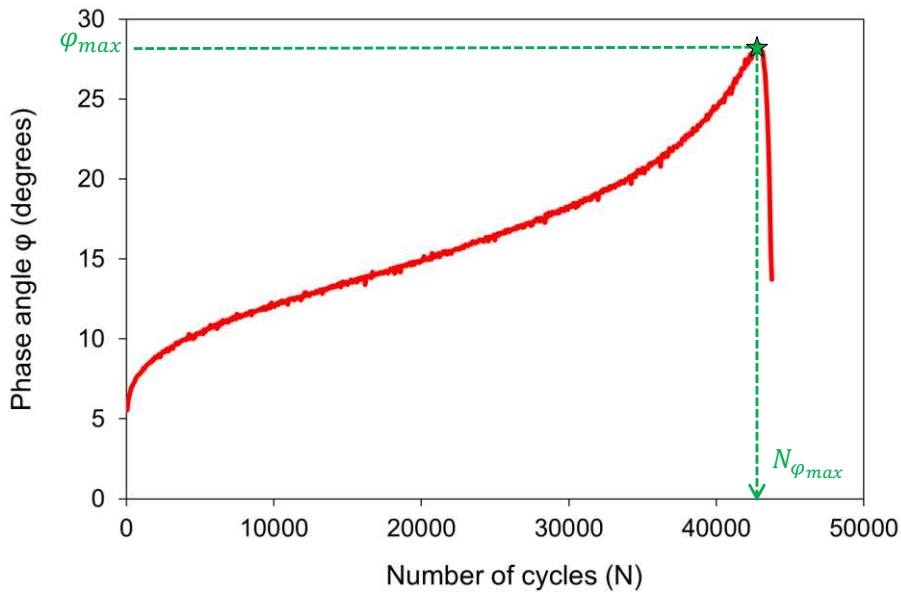

Figure 10.16. Definition of failure using Reese's approach.

10.4 Result and discussion

It is worth underling that a physical failure occurred exactly at the interface for all the tested specimens, also the two layers of the reinforced specimens were not still held together after the end of the test (Figure 10.17).

Figure 10.17. Failure mechanism of reinforced specimens in a shear-torque fatigue test.

The damage of the specimen is analysed using the evolution of the phase angle and the normalised norm of complex shear modulus. The latter is given by the following equation:

$$|G^*|_n = \frac{|G^*|_N}{|G^*|_0} \tag{10.6}$$

where $|G^*|_N$ is the norm of the complex shear modulus calculated at any given number of loading cycles (N), and $|G^*|_0$ is the initial norm of the complex shear modulus. The norm of the complex shear modulus evaluated at the 50th cycle is assumed as the $|G^*|_0$, in fact, at this stage of the test, the double-layered specimen is still not damaged and therefore it can be considered in its initial value.

The results of specimen FG_7 tested with an amplitude torque T_0 = 55 Nm at 10 Hz and 10 °C are presented herein as a typical example. In Figure 10.18, the norm of the complex shear modulus, as well as the phase angle, are presented according to the number of cycles. It is interesting to observe from Figure 10.18 that the complex shear modulus $|G^*|$ decreases with the number of cycles. Hence, there is a progressive weakening of the material during the cyclic test that involves decreasing in the material stiffness. The typical three phases of a fatigue test are observed from this curve (Babadopulos et al., 2019; Di Benedetto et al., 2004; Nguyen et al., 2012). Whereas, the phase angle φ increases during the cyclic test and drops suddenly approaching the end of the test. According to Reese (1997), the maximum point of the phase angle defines the point at which the location of the damage begins.

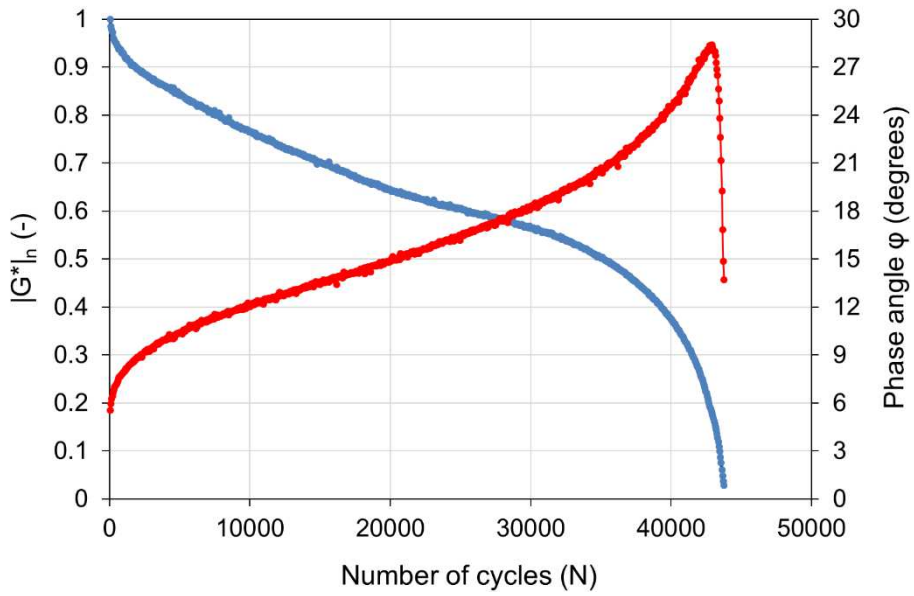

Figure 10.18. Evolution of normalised norm of complex shear modulus $|G^*|_n$ and phase angle φ of specimen FG_7 during shear-torque fatigue test at 10 Hz and 10 °C.

Figure 10.19 through Figure10.22 present the interlayer shear fatigue curves of the tested interface types in a log-log plane. A power-law model, expressed in Eq. (10.7), was used to obtain this relationship between the amplitude of the applied shear stress amplitude ($\tau_{max,0}$) and the number of cycles to failure (N_f).

$$\tau_{max,0} = a \cdot {N_f}^{-b} \tag{10.7}$$

where parameters a and b are regression coefficients.

In each plot, interlayer shear fatigue curves obtained using the classical fatigue criterion (N_{50}) were compared to those established by considering more appropriate failure criteria (N_{70} and $N_{\varphi max}$). The corresponding regression coefficients for the power-law model a and b are also presented in Table 10.4, as well as the coefficient of determination (R^2). Three tested specimens were omitted from the results (Figures 10.19 and 10.21) because they demonstrated outlier behaviour. As shown from these figures, applying the failure criteria N_{70} and $N_{\varphi max}$, the interlayer shear fatigue curves obtained are similar. However, a not clearly different tendency appears using N_{50} failure criterion, except for UN and FG interface type (at 20 °C) (Figures 10.19 and 10.21).

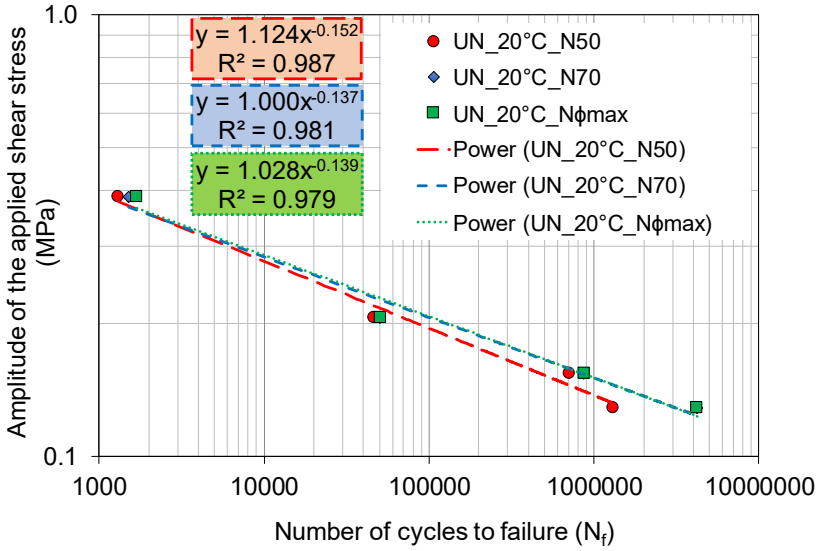

Figure 10.19. Interlayer shear fatigue curves for UN interface type at 20 °C.

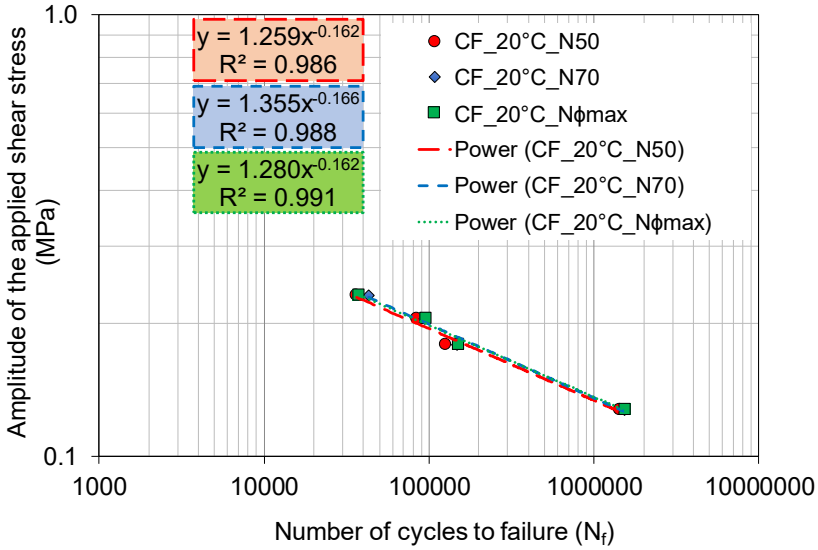

Figure 10.20. Interlayer shear fatigue curves for CF interface type at 20 °C.

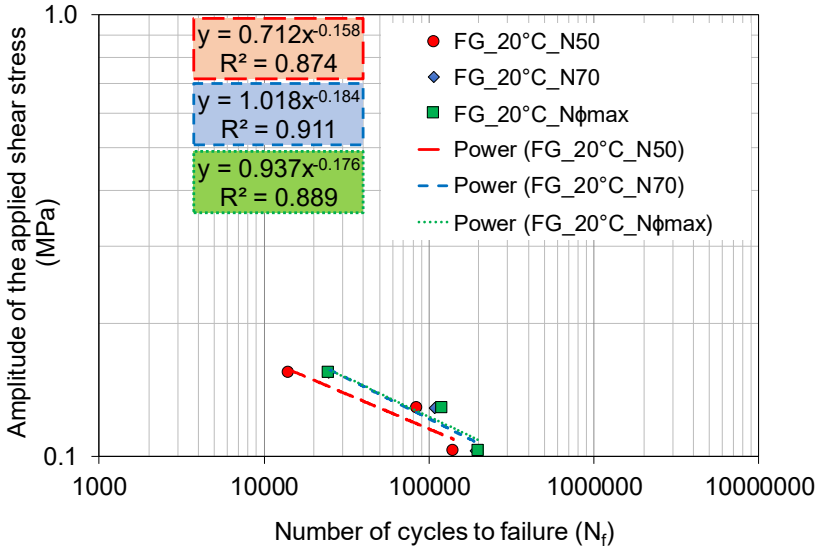

Figure 10.21. Interlayer shear fatigue curves for FG interface type at 20 °C.

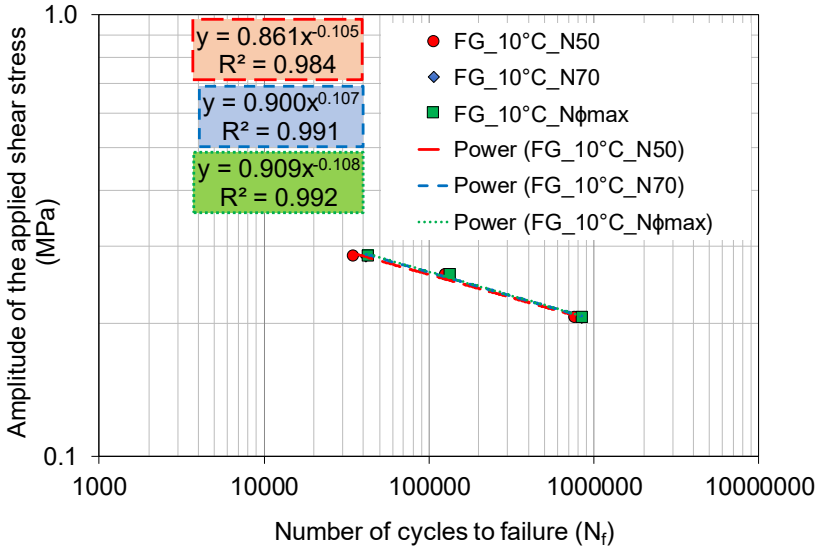

Figure 10.22. Interlayer shear fatigue curves for FG interface type at 10 °C.

Table 10.4. Parameters a and b for all interface types according to Eq. (10.7).

Interface type	Temperature (°C)	Failure criterion	a	b	R^2
UN	20	N_{50}	1.124	-0.152	0.987
		N_{70}	1.000	-0.137	0.981
		$N_{\varphi max}$	1.028	-0.139	0.979
CF	20	N_{50}	1.259	-0.162	0.986
		N_{70}	1.355	-0.166	0.988
		$N_{\varphi max}$	1.280	-0.162	0.991
FG	20	N_{50}	0.712	-0.158	0.874
		N_{70}	1.018	-0.184	0.911
		$N_{\varphi max}$	0.937	-0.176	0.889
FG	10	N_{50}	0.861	-0.105	0.984
		N_{70}	0.900	-0.107	0.991
		$N_{\varphi max}$	0.909	-0.108	0.992

Although comparing the failure criteria adopted, a clear difference in results cannot be observed, in Figures 10.19 and 10.21, the traditional failure criterion (N_{50}) can probably lead to a misleading ranking since it is incapable of quantifying the damage mechanisms that occur within the interlayer. Whereas, maximum phase angle ($N_{\varphi max}$) and the 70% failure criterion (N_{70}) are able to better correlate the number of cycles to failure with the damage process at the interlayer because they are related to a change in the inner behaviour of the specimen. For example, once the specimen becomes severely damaged at the interlayer, the strain response curve in a stress-controlled test varies significantly from an actual sinusoidal function and this distortion is responsible for the drop in phase angle. Thus, considering the weakness of the traditional approach, these results illustrate that the maximum phase angle and the 70% failure criterion can offer an accurate shear fatigue life prediction and provide similar results. Thus, they should be taken as the target failure point that the developed criterion needs to predict. However, to define the failure curve many specimens must be tested at different torque levels. Furthermore, the disadvantage is that it takes a couple of weeks of testing to get information since some specimens will fail after a million cycles. Comparing the coefficient of determination (R^2) of the FG interface type in Table 10.4, it is possible to note that the lower R^2 is obtained at the testing temperature of 20 °C indicating that the specimen-to-specimen interlayer shear variability increases at higher temperatures.

Comparing to the fatigue curves obtained previously at 20 °C with different materials and test devices, in this case, the curve slopes are greater and are close to b = -0.15 and very good correlations (R^2) are found.

To define a possible ranking between the different interface types (UN, FG and CF) and investigate the influence of testing temperature on the FG interface type, interlayer shear fatigue curves were represented in Figure 10.23 according to 70% complex shear modulus reduction criterion (N_{70}). Since the AC mixture, as well as the compaction method, of the tested specimens, is the same and assuming also that the quality of the tack coat applied at the interface is the same for the specimens, it can be asserted that the resistance to shear fatigue damage is a function only of the interface type. Figure 10.23 shows that a certain input shear stress level can lead to a completely different number of cycles to failure for the two reinforced interfaces. For example, with τ_0 = 0.15 MPa (i.e., T_0 = 30 Nm) as the input level, the interface FG has less than 25000 cycles to failure at 20 °C but the other CF reinforced interface has more than 300000 cycles to failure, always at 20 °C. Hence, the CF interface type requires an increase in stress level to achieve the same number of cycles to failure of the FG interface. Figure 10.23 shows that UN and CF interfaces provide very similar results in term of interlayer shear fatigue life, even if it seems that UN interface guarantees, in general, slightly higher performance at lower shear stress level with respect to CF interface. Starting from these results, it is expected that the CF geogrid is able to perform well in the field since the debonding effect highlighted by cyclic shear-torque loading is not so evident.

On the contrary, FG geogrid provides the lowest performance with respect to the other two interface types. Figure 10.23 also shows that in order to obtain a significant number of loading cycles, the amplitude of the applied shear stress in the FG-reinforced specimens are considerably lower than the relative amplitude of the applied shear stress in the unreinforced specimens (UN). This observation indicates that the unreinforced interfaces perform better under cyclic shear loading than the FG reinforced interfaces. This is probably due to the presence of the polyester knitted veil of the FG geogrid, which probably hindered the achievement of an optimal bonding and interlocking between the two bituminous layers in contact.

As far as the testing temperature is concerned, the FG interface type at a lower temperature (i.e., 10 °C) provides higher shear fatigue performance compared to those at 20 °C (Figure 10.23). This is in accordance with previous investigations, carried out with various experimental equipment in static modality (Canestrari et al., 2018), where an improvement of interlayer resistance was measured at low temperatures. Therefore, it might be assumed that as the temperature decreases, since the asphalt concrete is a thermo-dependent material, the interlayer becomes more brittle and more loading cycles of the same stress intensity are needed to cause the failure of the specimen.

Finally, the results confirm that the ability of geogrid-reinforced asphalt systems to improve pavement performance without generating debonding effect depends on the selection of the appropriate reinforcement product. Besides, the fatigue approach adopted appears to be sensitive to the interface evaluated and the variation of the testing parameters. Hence, shear-torque fatigue tests provide useful guidance for the selection of the appropriate geosynthetic to utilise. However, because there are no guidelines for cyclic torque test yet,

the lack of an appropriate torque-level determination guideline generates currently difficulties in selecting the torque-level range to run. Thus, a practical method is needed to determine torque levels to run the cyclic torque test efficiently. However, as shown herein, the problem is that different material and/or type of interface experience different levels of sensitivity to changes in stress level.

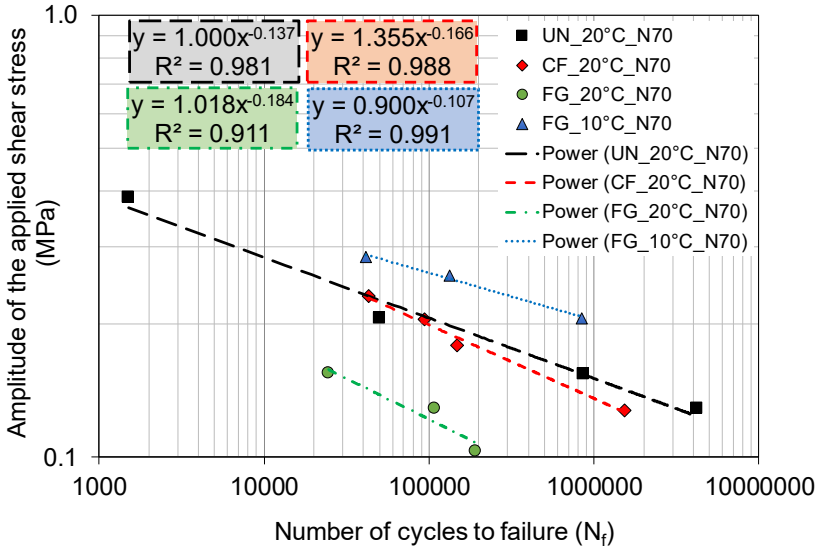

Figure 10.23. Interlayer shear fatigue curves for all interface types.

10.5 Conclusions

This additional experimental study aimed at evaluating the effect of geogrid reinforcement on the shear fatigue behaviour of bituminous pavements. To this end, a full-scale test field was constructed with 3 different interfaces: unreinforced (UN), reinforced with a carbon fibre geogrid (CF) and reinforced with a glass fibre geogrid (FG). The experimental program involved shear-torque fatigue tests in a stress-controlled mode performed at 20 °C and 10 Hz. Additional testing temperature of 10 °C was used for the FG interface type. Failure criteria based on the monitoring of the complex shear modulus decrease until 50% and 70% of its initial value along with phase angle failure criterion were used to investigate the shear fatigue behaviour. Based on the experimental results, the following main conclusions can be drawn:

- Results clearly rank the studied materials showing that the reinforced interface with carbon fibre geogrid (CF) provides similar shear fatigue behaviour with respect to the unreinforced interface (UN). On the contrary, a significant reduction of shear fatigue behaviour is evident with the glass fibre geogrid (FG).

- As far as the temperature effect is concerned, it was observed that shear fatigue resistance increases with decreasing temperature for the FG interface type. Further research is needed to investigate the influence of temperature also for CF interface type.
- These findings demonstrated that a correct choice of the most suitable geogrid could reduce the debonding effect that inevitably occurs introducing a reinforcement system within asphalt pavement.
- Good correlations were found between maximum phase angle and 70% stiffness reduction failure criteria. The results indicate that even though these fatigue failure criteria are not developed originally to be used with reinforced double-layered specimens, they can still be useful in ranking the different reinforced interfaces and seems capable of predicting the actual interlayer shear fatigue life.
- Shear-torque fatigue tests have proved to be powerful tools for investigating the damage progress in reinforced double-layered asphalt concrete specimens. Considering the crucial importance to properly select and assess the reinforcement system to be inserted in bituminous pavements, this test method could provide useful information to the interlayer bonding condition and interlayer fatigue failure of reinforced systems under stresses and strains close to those experienced in-situ.

Summary of the overall experimental study

Chapter 11.

Concluding remarks

The laboratory characterisation of the behaviour of bituminous interlayers is a challenging issue because of the difficulty of establishing loading conditions that can simulate field behaviour. The development of dynamic interlayer bond testing devices could represent a significant improvement in the pavement research field since this innovative approach could simulate the field conditions more realistically because the traffic loads applied to the pavement are dynamic in nature. Dynamic bond testing offers a complex evaluation of interlayer bond properties and can characterise the bond level during the service life of the pavement. This PhD thesis was focused on the dynamic testing for the characterisation of bituminous interlayers. The experimental activities carried out in this PhD work can be divided into two main phases.

The first phase was entirely carried out at Università Politecnica delle Marche and regarded the design and construction of a new testing device named Cyclic-ASTRA as well as the development of a testing protocol for performing dynamic (cyclic) interlayer testing. At the meantime, experimental activities were carried out for organising the RILEM interlaboratory test on "Dynamic Interlayer Shear Testing", consisting in the preparation of the double-layered slab samples to be tested by the participating laboratories.

In the second phase, experimental activities were carried out in three different research laboratories (Università Politecnica delle Marche, North Carolina State University, and University of Limoges) principally within the framework of the RILEM interlaboratory test. Different dynamic (cyclic) interlayer testing devices were used, and different testing programs were adopted, to characterise a single interlayer system, with the aim of identifying appropriate testing protocols and meaningful parameters. In particular, dynamic bond tests were used to simulate the repetitive load of moving vehicles in order to measure the number of shear load cycles that is required to cause failure at the interface.

Dynamic bond tests carried out at the Università Politecnica delle Marche demonstrated that the new Cyclic-ASTRA equipment allows characterising the interlayer properties, in terms of stiffness and resistance to repeated loading (cumulative damage). In particular, the results of the Cyclic-ASTRA device are promising due to increased precision of the measurements, lower compliance of the testing equipment and possibility to allow dilatancy movements perpendicular to the interface, as well as the application of normal stress at the interface (also if it was not applied in this experimentation). The measured interlayer shear stiffness K decreases as the testing temperature is increased. However, to improve the Cyclic-ASTRA device and its testing procedure, further experimental investigations are needed. The developed equipment, after further improvements, can be considered for including in the EN European Standards as a typical test for assessing the

fatigue life of interlayer bonding and the time-temperature dependence of the interlayer stiffness properties.

The other two cyclic bond devices (Cyclic-MAST and shear-torque fatigue test) used during this experimentation also showed to be suitable for the evaluation of the fatigue shear properties.

Results acquired through the experimental activities showed that the presence of the interface constitutes a weakness zone, noticeably influencing the shear fatigue performance of the pavement structure. The measured interlayer shear stiffness K represents a useful parameter to characterise the interlayer shear behaviour of double-layered specimens. The cyclic shear fatigue tests are evaluated in the same way as conventional fatigue tests. Based on the test results at different displacement/stress amplitudes, the characteristic interlayer shear fatigue curves are identified (power function). The regression parameter b maintained very similar and comparable values (approximately b = -0.1). The determination coefficient R^2 of the resulting fatigue functions showed relatively good value (approximately R^2 = 0.8–0.9). Results showed that increased displacement/stress amplitude leads to decreased interlayer fatigue life. Moreover, the results obtained showed that the presence of the tack coat at the interface or the reduced testing temperature provides a significant increase in the resistance to repeated shear loading. The classical fatigue failure criterion (N_{50}) has proven not to properly identify the material behaviour at the interface for shear-torque fatigue tests. Since an appropriate evaluation of the fatigue properties of the bituminous interlayers is a quite difficult task, acoustic emissions (AE) technique can be used to better evaluate the fatigue behaviour of bituminous pavement interlayers. The real potential of the AE technique is that they provide the possibility to observe where and when the damage is localised inside the specimen. During the shear-torque fatigue test, acoustic emission allowed to check that failure events are close to the interface of the specimen in all the interface area and not necessarily firstly for high radius values (i.e., where shear stresses are higher). It confirms that asphalt concrete is a heterogeneous (or geocomposite) materials and failure appears at the interface.

Proposed cyclic interlayer bond tests can be used for fatigue evaluation of the bituminous interlayer and can successfully define the service life of the pavement sections in a realistic manner, but testing procedures need to be homogenised. In fact, it is important to choose an optimal testing protocol able to appropriately address performance properties. In this regard, it seems that stress-controlled mode is preferred compared to displacement-controlled mode regarding applications to surface layer interface as it should be closer to what occurs in-situ. Also, the choice of sinusoidal or haversine applied load has to be justified by the actual shear stress in the pavement layers. The testing temperature of 20 °C seems to be preferable compared to warmer or colder temperatures, also because is commonly adopted to the study of interlayer bonding using static bond tests. As regards the clamping mechanisms, it is preferable to glue the specimen to the testing device to avoid any movements of the specimen during the dynamic test that might influence testing results. Although it cannot be disguised that gluing samples can offer several problems.

Finally, the obtained findings strongly encourage the adoption of dynamic (cyclic) tests for characterisation of interlayers in bituminous pavements. The work described in this thesis certainly represents a useful contribution to the achievement of standardised procedures related to the laboratory characterisation of bituminous interlayers. However, further investigations are needed to improve test repeatability and to obtain a more exhaustive picture of the governing mechanical properties. For instance, interlayer shear stiffness calculated performing cyclic bond tests for small deformations at different levels of frequency and temperature can be used for interlayer bond performance prediction (e.g., master curve) and modelling purposes. Moreover, an in-depth analysis of the interlayer stress time history induced by traffic loading in road pavement, employing different software programs (i.e., ABAQUS, KENLAYER, FlexPAVE^{TM}), can improve the knowledge in this field. Thus, further scientific insights are recommended to lead to a better understanding of the dynamic behaviour of the interfaces also in order to improve the current practice of structural pavement design and the prediction of premature distresses.

Lists of 3-years PhD publications

Ferrotti G., Ragni D., Lu X., Canestrari F. (2017). Effect of warm mix asphalt chemical additives on the mechanical performance of asphalt binders. Materials and Structures, 50, 226.

Ragni D., Ferrotti G., Lu X., Canestrari F. (2018). Effect of temperature and chemical additives on the short-term ageing of polymer modified bitumen for WMA. Materials and Design, 160, 514–526.

Ragni D., Ferrotti G., Lu X., Canestrari F. (2019). Influence of chemical additives for warm mix asphalt on the short-term ageing of a plain bitumen. Road Materials and Pavement Design, 20 (sup1), S34–S48.

Ragni D., Graziani A., Canestrari F. (2019). Cyclic interlayer testing in bituminous pavements. Proceedings of the 7th International Conference "Bituminous Mixtures and Pavements", 12-14 June 2019, Thessaloniki, Greece, CRC Press.

Ragni D., Takarli M., Petit C., Graziani A., Canestrari F. (2020). Use of acoustic techniques to analyse interlayer shear-torque fatigue test in asphalt mixtures. International Journal of Fatigue, 131, 105356.

Ragni D., Montillo T., Marradi A., Canestrari F. (2020). Fast falling weight accelerated pavement testing and laboratory analysis of asphalt pavements reinforced with geocomposites. In: Pasetto M., Partl M., Tebaldi G. (eds) Proceedings of the 5th International Symposium on Asphalt Pavements & Environment (APE), ISAP APE 2019, Lecture Notes in Civil Engineering, vol 48, Springer, Cham.

Canestrari F., Attia T., Di Benedetto H., Graziani A., Jaskula P., Kim Y.R., Maliszewski M., Pais J., Petit C., Raab C., Ragni D., Rys D., Sangiorgi C., Sauzéat C., Zofka A. (2020). Interlaboratory test to characterize the cyclic behavior of bituminous interlayers: an overview of testing equipment and protocols. Accepted for RILEM International Symposium on Bituminous Materials (ISBM Lyon 2020), 8-10 June 2020, Lyon, France.

Ragni D., Ferrotti G., Petit C., Canestrari F. (2020). Analysis of shear-torque fatigue test for bituminous pavement interlayers. Submitted to Construction and Building Materials.

References

AASHTO T 331 (2013). American Association of State Highway and Transportation Officials – Standard method of test for bulk specific gravity (G_{mb}) and density of compacted hot mix asphalt (HMA) using automatic vacuum sealing method.

AASHTO TP 133-19 (2019). American Association of State Highway and Transportation Officials – Provisional standard method of test for determining the damage characteristic curve and failure criterion using small specimens in the asphalt mixture performance tester (AMPT) cyclic fatigue test.

Airey G.D., Collop A.C., Zoorob S. (2005). The influence of laboratory compaction methods on the performance of asphalt mixtures. Final Report, Engineering and Physical Science Research Council.

Airey G.D., Collop A.C. (2016). Mechanical and structural assessment of laboratory- and field-compacted asphalt mixtures. International Journal of Pavement Engineering, 17 (1), 50–63.

Akhtarhusein A.T., Rahman M.S., Moreshwar B.K., Xu Q.X. (2004). A mechanistic approach to evaluate contribution of prime and tack coat in composite asphalt pavements. Final Report, FHWA/NC/2004-05, North Carolina DOT, Department of Civil Engineering, North Carolina State University, 25 June 2004.

Al Hakim B., Cheung L.W., Armitage R.J. (2000). Use of FWD data for prediction of bonding between pavement layers. International Journal of Pavement Engineering, 1 (1), 49–59.

Al Hakim B.A. (2002). The importance of good bond between bituminous layers. Proceedings of the 9th International Conference on Asphalt Pavements, Copenhagen, Denmark.

Al Nageim H., Al Hakim B., Pountney D.C. (1996). Reflection of interface condition modelling error on backcalculated moduli and pavement remaining life. Proceedings of Eurasphalt and Eurobitume Congress, Strasbourg, France.

Al Nageim H., Al Hakim B. (1999). Bonding conditions between pavement layers and their influence on pavement layers moduli and remaining life. Proceedings of the 3rd European Symposium on Performance and durability of bituminous materials and hydraulic stabilised composites, Leeds, United Kingdom.

Ali B., Sadek M., Shahrour I. (2008). Elasto-viscoplastic finite element analysis of the long-term behavior of flexible pavements. Road Materials and Pavement Design, 9 (3), 463–479.

Al-Qadi I.L., Carpenter S.H., Leng Z., Trepanier J.S. (2008). Tack coat optimization for HMA overlays: laboratory testing. Final Report No. FHWA-ICT-08-023, Illinois Department of Transportation, Illinois Center of Transportation, ICT-R55, September.

Andrawes K., Butterfield R. (1973). The measurement of planar displacement of sand grains. Geotechnique, 23 (4), 571–576.

Ascher D., Wellner F. (2007). Untersuchungen zur wirksamkeit des haftverbundes und dessen auswirkungen auf die lebensdauer von asphaltbefestigungen [Investigation of the effectiveness of bonding and its influence on the service life of asphalt pavements]. Technical University of Dresden, Germany, Report No. 13589 BR/1, 100 p.

Attia T., Di Benedetto H., Sauzéat C., Pouget S. (2018). Experimental investigation of the mechanical behaviour of interfaces between pavement layers. Proceedings of GeoShanghai 2018 International Conference: Transportation Geotechnics and Pavement Engineering, edited by Xianming Shi, Zhen Liu, and Jenny Liu, 344–352, Singapore: Springer Singapore.

Augustin H. (1997). Design of tack coat. Proceedings of the 2nd world congress on emulsions, Bordeaux, France.

Austin R.A., Gilchrist A.J.T. (1996). Enhanced performance of asphalt pavements using geo-composites. Geotextiles and Geomembranes, 14, 175–186.

Babadopulos L.F.A.L., Orozco G., Sauzéat C., Di Benedetto H. (2019). Reversible phenomena and fatigue damage during cyclic loading and rest periods on bitumen. International Journal of Fatigue, 124, 303–314.

Behnia B., Buttlar W., Reis H. (2018). Evaluation of low-temperature cracking performance of asphalt pavements using acoustic emission: a review. Applied Science, 8, 306.

Bocci M., Grilli A., Santagata F.A., Virgili A. (2007). Influence of reinforcement geosynthetics on flexion behaviour of double-layer bituminous systems. Proceedings of the International Conference on Advanced Characterisation of Pavement and Soil Engineering Materials, Athens, Greece.

Bognacki C.J., Frisvold A., Bennert T. (2007). Investigation of asphalt pavement slippage failures on runway 4r-22l, Newark international airport. 2007 FAA Worldwide Airport Technology Transfer Conference: New Directions in Airport Technology, Atlantic City, New Jersey, USA.

Boudabbous M., Millien A., Petit C., Neji J. (2013). Energy approach for the fatigue of thermoviscoelastic materials: Application to asphalt materials in pavement surface layers. International Journal of Fatigue, 47, 308–318.

Bourchak M., Farrow I.R., Bond I.P., Rowland C.W., Menan F. (2007). Acoustic emission energy as a fatigue damage parameter for CFRP composites. International Journal of Fatigue, 29, 457–70.

British Board of Agreement (2004). Guidelines document for the assessment and certification of thin surfacing systems for highways. SG3/05/234, British Board of Agreement, Watford, UK.

Brown S.F., Brunton J.M. (1984). The influence of bonding between bituminous layers. Highways and Transportation, 31 (5), 16–17.

Brown S.F., Brunton J.M., Hughes D.A.B., Brodrick B.V. (1985). Polymer grid reinforcement of asphalt. Journal of the Association of Asphalt Paving Technologists, 54, 18–44.

Brown S.F., Thom N.H., Sanders P.J. (2001). A study of grid reinforced asphalt to combat reflection cracking. Journal of the Association of Asphalt Paving Technologists, 70, 543–569.

Brunner A.J., Howald M.T., Niemz P. (2006). Acoustic emission rate behavior of laminated wood specimens under tensile loading. Journal of Acoustic Emissions, 24, 104–10.

BS 594-2 (2002). British Standards – Hot rolled asphalt for roads and other paved areas – Part 2: Specification for transport, laying and compaction of hot rolled asphalt.

Buchanan M.S., Woods M.E. (2004). Field tack coat evaluator (ATACKer™). Report No. FHWA/MS-DOT-RD-04-168, Mississippi Department of Transportation, Jackson, MS, USA.

Butterfield R., Harkness R.M., Andrews K. (1970). A stereophotogrammetric method for measuring displacement fields. Geotechnique, 20 (3), 308–314.

Buttlar W.G. (2014). Digital image correlation techniques to investigate strain fields and cracking phenomena in asphalt materials. Material and Structure, 47 (8), 1373–1390.

Button J.W., Lytton R.L. (2007). Guidelines for using geosynthetics with hot-mix asphalt overlays to reduce reflective cracking. Transportation Research Board 86th Annual Meeting, Washington D.C., USA.

Caltabiano M., Brunton J. (1991). Reflection cracking in asphalt overlays (with discussion). Journal of the Association of Asphalt Paving Technologists, 60.

Canestrari F., Santagata E. (2005). Temperature effects on the shear behaviour of tack coat emulsions used in flexible pavements. International Journal of Pavement Engineering, 6 (1), 39–46.

Canestrari F., Ferrotti G., Partl N.M., Santagata E. (2005). Advanced testing and characterization of interlayer shear resistance. Transportation Research Record: Journal of the Transportation Research Board, 1929, 69–78.

Canestrari F., Grilli A., Santagata F.A., Virgili A. (2006). Interlayer shear effect of geosynthetic reinforcements. Proceedings of the 10th International Conference on Asphalt Pavements, Québec City, Canada.

Canestrari F., Pasquini E., Belogi L. (2012). Optimization of geocomposite for double layer bituminous system. In: Scarpas A., Kringos N., Al-Qadi I., A. L. (eds) 7th RILEM International Conference on Cracking in Pavements, RILEM Bookseries, 4, 1229–1239, Springer, Dordrecht.

Canestrari F., Ferrotti G., Lu X., Millien A., Partl M.N., Petit C., Phelipot-Mardelé A., Piber, H, Raab C. (2013). Mechanical testing of interlayer bonding in asphalt pavements. In: Partl M. et al. (eds) Advances in Interlaboratory Testing and Evaluation of Bituminous Materials, RILEM State-of-the-Art Reports, 9, 303–360, Springer, Dordrecht.

Canestrari F., Belogi L., Ferrotti G., Graziani A. (2015). Shear and flexural characterization of grid-reinforced asphalt pavements and relation with field distress evolution. Materials and Structures, 48 (4), 959–975.

Canestrari F., D'Andrea A., Ferrotti G., Graziani A., Partl M.N., Petit C., Raab C., Sangiorgi C. (2018). In: Partl M., Porot L., Di Benedetto H., Canestrari F., Marsac P., Tebaldi G. (eds) Testing and Characterization of Sustainable Innovative Bituminous Materials and Systems, RILEM State-of-the-Art Reports, 24, 127–202, Springer, Cham.

Carr A.G. (2001). The behaviour of layered pavement structures: the dynamic shear box. Project Report of School of Civil Engineering, NCPE, Nottingham, UK.

Chang F.-L., Yaacob H., Hainin M.R., Rashid A.S.A. (2014). Compilation of pavement interface bond strength devices for bond strength quantification. Jurnal Teknologi, 71 (3), 15–22.

Chehab G., Kim Y.R., Schapery R.A., Witczack M., Bonaquist R. (2002). Time-temperature superposition principle for asphalt concrete mixtures with growing damage in tension state. Journal of the Association of Asphalt Paving Technologists, 71, 559–593.

Chehab G., Seo Y., Kim Y.R. (2007). Viscoelastoplastic damage characterization of asphalt-aggregate mixtures using digital image correlation. International Journal Geomechanics, 7 (2), 111–118.

Chen Z, Gabbitas B, Hunt D. (2006). Monitoring the fracture of wood in torsion using acoustic emission. Journal of Material Science, 41 (12), 3645–3655.

Chen J.S., Huang C.C. (2010). Effect of surface characteristics on bonding properties of bituminous tack coat. Transportation Research Record: Journal of the Transportation Research Board, 2180 (1), 142–149.

Cho S.H., Karshenas A., Tayebali A.A., Guddati M.N., Kim Y.R. (2017a). A mechanistic approach to evaluate the potential of the debonding distress in asphalt pavements. International Journal of Pavement Engineering, 18 (12), 1098–1110.

Cho S.H., Safavizadeh S.A., Kim Y.R. (2017b). Verification of the applicability of the time–temperature superposition principle to interface shear stiffness and strength of GlasGrid-reinforced asphalt mixtures. Road Materials and Pavement Design, 18 (4), 766–784.

Chun S., Kim K., Greene J., Choubane B. (2015). Evaluation of interlayer bonding condition on structural response characteristics of asphalt pavement using finite element analysis and full-scale field tests. Construction and Building Materials, 96, 307–318.

Chupin O., Chabot A., Piau J.-M., Duhamel D. (2010). Influence of sliding interfaces on the response of a layered viscoelastic medium under a moving load. International Journal of Solids and Structures, 47, 3435–3446.

Collop A.C., Thom N.H. (2002). The importance of bond between pavement layers. Final Summary Report to EPSRC, NCPE, Nottingham.

Collop A.C., Sutanto M.H., Airey G.D., Elliott R.C. (2011). Development of an automatic torque test to measure the shear bond strength between asphalt. Construction and Building Materials, 25, 623–629.

D'Andrea A., Tozzo C., Boschetto A., Bottini L. (2013). Interface roughness parameters and shear strength. Modern Applied Science, 7, 10.

D'Andrea A., Tozzo C. (2016). Dynamic tests on bituminous layers interface. Materials and Structures, 49, 917–928.

Destrée A., Visscher J.D., Piérard N., Vanelstraete A. (2016). Field study to investigate the impact of conditions of application of tack coats on the interlayer bond strength. In: Canestrari F., Partl M. (eds) 8th RILEM International Symposium on Testing and Characterization of Sustainable and Innovative Bituminous Materials, RILEM Bookseries, 11, 347–358, Springer, Dordrecht.

Deysarkar I., Tandon V. (2005). Field evaluation of tack coat quality measurement equipments. International Journal of Pavement Engineering, 4 (1-2), 25–37.

Diakhaté M., Phelipot-Mardelé A., Millien A., Petit C. (2006). Shear fatigue behaviour of tack coats in pavements. Road Materials and Pavement Design, 7 (2), 201–22.

Diakhaté M., Millien A., Petit C., Phelipot-Mardelé A., Pouteau B. (2011). Experimental investigation of tack coat fatigue performance: towards an improved lifetime assessment of pavement structure interfaces. Construction and Building Materials, 25, 1123–1133.

Diakhaté M., Larcher N., Takarli M., Angellier N., Petit C. (2012). Acoustic techniques for fatigue cracking mechanisms characterization in hot mix asphalt (HMA). In: Scarpas A.,

Kringos N., Al-Qadi I.A.L (eds) 7th RILEM International Conference on Cracking in Pavements, RILEM bookseries, 4, Springer, Dordrecht.

Di Benedetto H., Ashayer S., Chaverot P. (1996). Fatigue damage for bituminous mixtures: a pertinent approach. Journal of the Association of Asphalt Paving Technologists, 65, 142–58.

Di Benedetto H., de La Roche C., Baaj H., Pronk A., Lundström R. (2004). Fatigue of bituminous mixtures. Materials and Structures, 37, 202–216.

Di Benedetto H., Nguyen Q.T., Sauzéat C. (2011). Nonlinearity, heating, fatigue and thixotropy during cyclic loading of asphalt mixtures. Road Materials and Pavement Design, 12 (1), 129–58.

Di Benedetto H., Gabet T., Grenfell J., Perraton D., Sauzéat C., Bodin D. (2013). Mechanical testing of bituminous mixtures. In: Partl M. et al. (eds) Advances in Interlaboratory Testing and Evaluation of Bituminous Materials, RILEM state-of-the-art reports, 9, 143–256, Springer, Dordrecht.

Donovan E.P., Al-Qadi I.L., Loulizi A. (2000). Optimization of tack coat application rate for geocomposite membrane on bridge decks. Transportation Research Record: Journal of the Transportation Research Board, 1740, 143–150.

Dubois V., de La Roche C., Burban O. (2010). Influence of the compaction process on the air void homogeneity of asphalt mixtures samples. Construction and Building Materials, 24, 885–897.

Elseifi M.A., Al-Qadi I.L., Yoo P.J. (2006). Viscoelastic modeling and field validation of flexible pavements. Journal of Engineering Mechanics, 132 (2), 172–178.

EN 1097-6 (2013). European standards for tests for mechanical and physical properties of aggregates – Part 6: Determination of particle density and water absorption.

EN 12591 (2009). European standards for bitumen and bituminous binders – Specifications for paving grade bitumens.

EN 12595 (2015). European standards for bitumen and bituminous binders – Determination of kinematic viscosity.

EN 12607-1 (2014). European standards for bitumen and bituminous binders – Determination of the resistance to hardening under the influence of heat and air – Part 1: RTFOT method.

EN 12697-5 (2010). European standards for bituminous mixtures – Test methods for hot mix asphalt – Part 6: Determination of maximum density.

EN 12697-6 (2012). European standards for bituminous mixtures – Test methods for hot mix asphalt – Part 6: Determination of bulk density of bituminous specimens.

EN 12697-8 (2003). European standards for bituminous mixtures – Test methods for hot mix asphalt – Determination of void characteristics of bituminous specimens.

EN 12697-33 (2007). European standards for bituminous mixtures – Test methods for hot mix asphalt – Part 33: specimen prepared by roller compactor.

EN 13108-1 (2016). European standards for bituminous mixtures – material specifications – Part 1: asphalt concrete.

EN 13398 (2010). European standards for bitumen and bituminous binders – Determination of the elastic recovery of modified bitumen.

EN 1426 (2015). European standards for bitumen and bituminous binders – Determination of needle penetration.

EN 1427 (2015). European standards for bitumen and bituminous binders – Determination of the softening point – Ring and Ball method.

Ferrotti G., Canestrari F., Virgili A., Grilli A. (2011). A strategic laboratory approach for the performance investigation of geogrids in flexible pavements. Construction and Building Materials, 25 (5), 2343–2348.

Ferrotti G., Canestrari F., Pasquini E., Virgili A. (2012). Experimental evaluation of the influence of surface coating on fiberglass geogrid performance in asphalt pavements. Geotextiles and Geomembranes, 34, 11–18.

Francken L. (2005). Prevention of cracks in pavements. Road Materials and Pavement Design, 6 (3), 407–425.

Gibson J.J. (1950). The perception of the visual world. Houghton Mifflin, Boston.

Graziani A., Pasquini E., Ferrotti G., Virgili A., Canestrari F. (2014). Structural response of grid-reinforced bituminous pavements. Materials and Structures, 47, 1391–1408.

Grosse C.U., Ohtsu M. (2008). Acoustic emission testing. Springer, Berlin, Heidelberg.

Hachiya Y., Sato K. (1997). Effect of tack coat on bonding characteristics at interface between asphalt concrete layers. Proceedings of the 8th International Conference on Asphalt Pavements, Seattle, Washington, USA.

Hasiba K. (2012). Development of a testing approach for tack coat application rate at pavement layer interfaces. Radiology, 237 (1), 57–66.

Hesp S., Terlouw T., Vonk W. (2000). Low temperature performance of SBS-modified asphalt mixes. Journal of the Association of Asphalt Paving Technologists, 69, 540–73.

Horak E., Emery S., Maina J., Walker B. (2009). Mechanistic modelling of potential interlayer slip at base and sub-base level. Proceedings of the 8th International Conference on

the Bearing Capacity of Roads, Railways and Airfields, 29 June - 2 July 2009, 543–550, Urbana-Champaign, USA.

Hristov B., Wellner F., Canon Falla G. (2016). Experimental and numerically supported determination of the interlayer bond shear stiffness. Proceedings of the 4th Chinese-European Workshop on Functional Pavement Design (4th CEW 2016), 29 June - 1 July 2016, Delft, The Netherlands.

Hristov B. (2018). Master function for analytical determination of the interlayer bond shear stiffness and fatigue functions for asphalt pavements. MATEC Web of Conferences, 251, 01001.

Hu X., Walubita L.F. (2011). Effects of layer interfacial bonding conditions on the mechanistic responses in asphalt pavements. Journal of Transportation Engineering, 137 (1), 28–36.

Hu X., Faruk A.N.M., Zhang J., Souliman M.I., Walubita L.F. (2017). Effects of tire inclination (turning traffic) and dynamic loading on the pavement stress-strain responses using 3-D finite element modeling. International Journal of Pavement Research and Technology, 10, 304–314.

Hunter E.A., Airey G.D., Collop A.C. (2004). Aggregate orientation and segregation in laboratory-compacted asphalt samples. Transport research record: Journal of Transport Research Board, 1891, 8–15.

Isailović I., Cannone Falchetto A., Wistuba M. (2017). Fatigue investigation on asphalt mixture layers' interface. Road Materials and Pavement Design, 18 (sup4), 514–34.

Ishikawa T., Sekine E., Miura S. (2011). Cyclic deformation of granular material subjected to moving-wheel loads. Canadian Geotechnical Journal, 48, 691–703.

Italian Standard UNI/TS 11214 (2014). Proprietà meccaniche delle pavimentazioni stradali ed aeroportuali – Caratterizzazione prestazionale a taglio delle interfacce – Metodo di prova ASTRA.

Jaskula P. (2014). Influence of compaction effectiveness on interlayer bonding of asphalt layers. Proceedings of the 9th International Conference "Environmental Engineering", 22–23 May 2014, Vilnius, Lithuania.

Jaskula P., Rys D. (2017). Effect of interlayer bonding quality of asphalt layers on pavement performance. IOP Conference Series: Materials Science and Engineering, 236.

Jayawickrama P.W., Lytton R.L. (1978). Methodology for predicting asphalt concrete overlay life against reflection cracking. Proceedings of the 6th International Conference on Structural Design of Asphalt Pavements, 1, 921–924, Ann Arbor: Cushing-Malloy Inc.

Kennedy C.K. (1978). The Development of slip-planes in rolled asphalt surfacings. TRRL (Transport and Road Research Laboratory) Laboratory Report (LR) n° 813.

Khosla N.P., Goetz W.H. (1979). Tensile characteristics of bituminous mixtures as affected by modified binders. Joint Highway Research Project, Purdue University and the Indiana State Highway Commission, West Lafayette, Indiana, USA.

Khweir K., Fordyce D. (2003). Influence of layer bonding on the prediction of pavement life. Proceedings of the Institution of Civil Engineers, 73–83.

Kim K.W., Doh Y.S., Lim S. (1999). Mode I reflection cracking resistance of strengthened asphalt concretes. Construction and Buildings, 13 (5), 243–245.

Kim Y.R., Wen H. (2002). Fracture energy from indirect tension test. Journal of the Association of Asphalt Paving Technologists, 71, 779–793.

Kim H., Arriagada M., Raab C., Partl M.N. (2011). Numerical and experimental analysis for the interlayer behavior of double-layered asphalt pavement specimens. Journal of Materials in Civil Engineering, 23 (1).

Kruntcheva M.R., Collop A.C., Thom N.H. (2001). Shear box test: finite element modelling. Project Report PGR01-05, NCPE, Nottingham, UK.

Kruntcheva M.R., Collop A.C., Thom N.H. (2005). Effect of bond condition on flexible pavement performance. Journal of Transportation Engineering (ASCE).

Kruntcheva M.R., Collop A.C., Thom N.H. (2006). Properties of asphalt concrete layer interfaces. Journal of Materials in Civil Engineering, 18 (3), 467–471.

Ktari R., Fouchal F., Millien A., Petit C. (2016a). Damage modeling of asphaltic pavement rough interfaces under tensile and shear loading. In: Chabot A., Buttlar W., Dave E., Petit C., Tebaldi G. (eds) 8th RILEM International Conference on Mechanisms of Cracking and Debonding in Pavements, RILEM Bookseries, 13, Springer, Dordrecht.

Ktari R., Millien A., Fouchal F., Pop I.-O., Petit C. (2016b). Pavement interface damage behavior in tension monotonic loading. Construction and Building Materials, 106, 430–442.

Ktari R., Fouchal F., Millien A., Petit C. (2017). Surface roughness: a key parameter in pavement interface design. European Journal of Environmental and Civil Engineering, 21 (sup1), 27–42.

Lamy F., Takarli M., Angellier N., Dubois F., Pop O. (2015). Acoustic emission technique for fracture analysis in wood materials. International Journal of Fracture, 192 (1), 57–70.

Landis E.N. (1999). Micro-macro fracture relationships and acoustic emissions in concrete. Construction and Building Materials, 13, 65–72.

Leng Z., Al-Qadi I.L., Ozer H., Carpenter S. (2008a). Tack coat application rate optimization and environmental effect on HMA overlay-PCC pavement bonding. Proceedings of the International ISAP Symposium on Asphalt Pavements and Environment,18-20 August 2008, 825–835, Zurich, Switzerland.

Leng Z., Ozer H., Al-Qadi I.L., Carpenter S. (2008b). Interface bonding between hot-mix asphalt and various portland cement concrete surfaces: laboratory assessment. Transport Research Record: Journal of Transport Research Board, 205 (1), 46–53.

Leng Z., Al-Qadi I.L., Carpenter S.H., Ozer H. (2009). Interface bonding between hot-mix asphalt and various portland cement concrete surfaces: assessment of accelerated pavement testing and measurement of interface strain. Transport Research Record: Journal of Transport Research Board, 2127 (1), 20–28.

Leutner R. (1979). Untersuchung des schichtenverbundes beim bituminosen oberbau. Bitumen, 41 (3), 84–91.

Li X., Marasteanu M. (2010). The fracture process zone in asphalt mixture at low temperature. Engineering Fracture Mechanics, 77 (7), 1175–1190.

Li H., Yu B. (2014). Fatigue performance and prediction model of multilayer deck pavement with different tack coat materials. Journal of Materials in Civil Engineering, 26 (5), 872–877.

Li S., Liu X., Liu Z. (2014). Interlaminar shear fatigue and damage characteristics of asphalt layer for asphalt overlay on rigid pavement. Construction and Building Materials, 68, 341–347.

Li M., Wang H., Xu G., Xie P. (2017). Finite element modeling and parametric analysis of viscoelastic and nonlinear pavement responses under dynamic FWD loading. Construction and Building Materials, 141, 23–35.

Liao J., Sargand S. (2010). Viscoelastic FE modeling and verification of a U.S. 30 perpetual pavement test section. Road Materials and Pavement Design, 11 (4), 993–1008.

Liu L., Hao P. (2011). ABAQUS program-based numerical analysis on U-shaped cracking of asphalt pavement. Proceedings of the International Conference on Remote Sensing, Environment and Transportation Engineering, 24-26 June 2011, Nanjing, China.

Maji A.K., Shah S.P. (1988). Process zone and acoustic emission in concrete. Experimental Mechanics, 28 (1), 27–33.

Masad E., Muhunthan B., Shashidhar N., Harman T. (1999). Quantifying laboratory compaction effects on the internal structure of asphalt concrete. Transport Research Record: Journal of Transport Research Board,1681, 179–85.

Mirò Recasens R., Pérez Jiménez F., Borras Gonzalez J.M. (2003). Evaluation of the effect of tack coats. LCB shear test. Proceedings of the 6th International RILEM Symposium PTEBM'03, 14-16 April 2003, Zurich, Switzerland.

Mirò Recasens R., Martinez A., Pérez Jiménez F. (2005). Assessing heat-adhesive emulsions for tack coats. Proceedings of the Institution of Civil Engineers (ICE), 45–51.

Mohammad L.N., Zhong W., Raqib M.A. (2005). Investigation of the behavior of asphalt tack interface layer. FHWA/LA.04/394. Louisiana Transportation Research Center, Baton Rouge, LA, USA.

Mohammad L.N., Saadeh S., Qi Y., Button J., Scherocman J. (2008). Worldwide state of practice on the use of tack coats: a survey. Journal of the Association of Asphalt Paving Technologists, 1–34.

Mohammad L.N., Bae A., Elseifi M.A., Button J., Scherocman J. (2009). Interface shear strength characteristics of emulsified tack coats. Journal of the Association of Asphalt Paving Technologists, 78, 249–278.

Mohammad L.N., Hassan M., Patel N. (2011). Effects of shear bond characteristics of tack coats on pavement performance at the interface. Transport Research Record: Journal of Transport Research Board, 2209 (1), 1–8.

Nejad F.M., Asadi S., Fallah S., Vadood M. (2016). Statistical-experimental study of geosynthetics performance on reflection cracking phenomenon. Geotextiles and Geomembranes, 44, 178–187.

Nesvijski E., Marasteanu M. (2006). Spectral analysis of acoustic emission of cold cracking asphalt. E-Journal of Nondestructive Testing, 11, 10.

NF EN 13285 (2010). French Standards – Unbound mixtures – Specification.

Nguyen Q.T., Di Benedetto H., Sauzéat C. (2012). Determination of thermal properties of asphalt mixtures as another output from cyclic tension-compression test. Road Materials and Pavement Design, 13 (1), 85–103.

Nicholas J.H. (1979). Final report of the working party on the slippage of rolled asphalt wearing course. Transport and Road Research Laboratory Supplementary Report, 493.

Partl M.N., Raab C. (1999). Shear adhesion between top layers of fresh asphalt pavements in Switzerland. Proceedings of the 7th Conference on Asphalt Pavements for Southern Africa, CAPSA '99, 5.130–5.137, Victory Falls, Zimbabwe.

Pasetto M., Pasquini E., Giacomello G., Baliello A. (2019). Innovative composite materials as reinforcing interlayer systems for asphalt pavements: an experimental study. Road Materials and Pavement Design, 20 (sup2), 1–15.

Pasquini E., Bocci M., Ferrotti G., Canestrari F. (2013). Laboratory characterisation and field validation of geogrid-reinforced asphalt pavements. Road Materials and Pavement Design, 14 (1), 17–35.

Pasquini E., Bocci M., Canestrari F. (2014). Laboratory characterisation of optimised geocomposites for asphalt pavement reinforcement. Geosynthetics International, 21 (1), 24–36.

Peattie K.R. (1979). The incidence and investigation of slippage failures. Proceedings of the Conference "the Performance of Rolled Asphalt Road Surfacings", 3–15, ICE, London, UK.

Petit C., Diakhaté M., Millien A., Phelipot-Mardelé A., Pouteau B. (2009). Pavement design for curved road sections: fatigue performance of interfaces and longitudinal topdown cracking in multilayered pavements. Road Materials and Pavement Design, 10 (3), 609–624.

Petit C., Chabot A., Destrée A., Raab C. (2018a). Recommendation of RILEM TC 241-MCD on interface debonding testing in pavements. Materials and Structures, 51 (4), 96.

Petit C., Allou F., Millien A., Fakhari Terhani F., Dopeux J. (2018b). Hot mix asphalt cyclic torque tests for viscoelastic bulk shear behaviour. Proceedings of 21st International Conference on Asphalt Pavements, ISAP, Fortaleza, Brazil.

Petit C., Lesueur D., Millien A., Leguernevel G., Dopeux J., Picoux B., Allou F., Terhani F. (2019). Des géosynthétiques intelligents pour renforcer et suivre les déformations de chaussées bitumineuses. 12èmes Rencontres Géosynthétiques, 11–13 March 2019, Nancy, France.

Powrie W., Yang L.A., Clayton C.R.I. (2007). Stress changes in the ground below ballasted railway track during train passage. Proceedings of the Institution of Mechanical Engineers, Part F: Journal of Rail and Rapid Transit, 221 (2), 247–262.

Prashanth M.H., Singh P., Kishen J.M.C. (2019). Role of longitudinal reinforcement on the behavior of under reinforced concrete beams subjected to fatigue loading. International Journal of Fatigue, 125, 271–90.

prEN 12697-48 (2013). European pre-standard for bituminous mixtures – Test methods – Part 48: Interlayer Bonding.

Prieto J. N., Gallego J., Perez I. (2007). Application of the wheel reflective cracking test for assessing geosynthetics in anti-reflection pavement cracking systems. Geosynthetics International, 14 (5), 287–297.

Raab C., Partl M.N. (2004). Interlayer shear performance: experience with different pavement structures. Proceedings of the 3rd Eurasphalt and Eurobitume Congress, May 2004, 1, 535–545, Vienna, Austria.

Raab C., Partl M.N. (2009). Interlayer bonding of binder, base and subbase layers of asphalt pavements: long-term performance. Construction and Building Materials, 23, 2926–2931.

Raab C., Partl M.N., Abd El Halim A.O. (2009). Evaluation of interlayer shear bond devices for asphalt pavements. The Baltic Journal of Road and Bridge Engineering, 4 (4), 186–195.

Raab C., Partl M.N., Abd El Halim A.O. (2010). Effect of gap width on interlayer shear bond results. International Journal of Pavement Research and Technology, 3 (2), 79–85.

Raab C., Abd El Halim A.O., Partl M.N. (2012). Interlayer bond testing using a model material. Construction and Building Materials, 26 (1), 190–199.

Raab C., Partl M.N., Fourquet E., Abd El Halim A.O. (2017). Static and cyclic evaluation of interlayer bonding. Proceedings of the 10th International Conference on the Bearing Capacity of Roads, Railways and Airfields, Athens, Greece.

Rabiot D., Morizur M. (1996). Polymer-modified bitumen emulsions an advantage for the various road applications. Proceedings of the Eurasphalt and Eurobitume Congress, Strasbourg, France.

Rahman A., Ai C., Xin C., Gao X., Lu Y. (2017). State-of-the-art review of interface bond testing devices for pavement layers: toward the standardization procedure. Journal of Adhesion Science and Technology, 31 (2), 109–126.

Ragni D., Montillo T., Marradi A., Canestrari F. (2020). Fast falling weight accelerated pavement testing and laboratory analysis of asphalt pavements reinforced with geocomposites. In: Pasetto M., Partl M., Tebaldi G. (eds) Proceedings of the 5th International Symposium on Asphalt Pavements & Environment (APE), ISAP APE 2019, Lecture Notes in Civil Engineering, 48, Springer, Cham.

Recasens R.M., Martínez A., Jiménez F.P. (2005). Assessing heat-adhesive emulsions for tack coats. Proceedings of the Institution of Civil Engineers - Transport, 158 (1), 45–51.

Recasens R.M., Martínez A., Jiménez F.P. (2006). Evaluation of effect of heat-adhesive emulsions for tack coats with shear test: from the road research laboratory of Barcelona. Transportation Research Record: Journal of the Transportation Research Board, 1970 (1), 64–70.

Reese R. (1997). Properties of aged asphalt binder related to asphalt concrete fatigue life. Journal of the Association of Asphalt Paving Technologists, 66, 604–632.

Romain J. (1968). Stresses, deformations and deflections in four-course elastic systems. Rapport De Recherche No. 147/JER/1968, 147.

Romanoschi S.A., Metcalf J.B. (2001). Effect of interface condition and horizontal wheel loads on the life of flexible pavement structures. Transportation Research Record: Journal of the Transportation Research Board, 1778, 123–131.

Romanoschi S.A., Metcalf J.B. (2002). The characterization of pavement layer interfaces. Proceedings of the 9th International Conference on Asphalt Pavements, Copenhagen, Denmark.

Romanoschi S.A., Metcalf J.B. (2003). Errors in pavement layer moduli backcalculation due to improper modeling of layer interface condition. Proceedings of the 82nd TRB Annual Meeting, Washington D.C., USA.

Safavizadeh A., Kim Y.R. (2014). Mode II fatigue and reflective cracking performance of glasgrid-reinforced asphalt concrete under repeated loading. Proceedings of the 12th ISAP Conference on Asphalt Pavements, 1893–1902, Raleigh, NC, USA.

Safavizadeh S.A., Kim Y.R. (2017). DIC technique to investigate crack propagation in grid-reinforced asphalt specimens. Journal of Materials in Civil Engineering, 29 (6).

Santagata F.A., Partl M.N., Ferrotti G., Canestrari F., Flisch A. (2008). Layer characteristics affecting interlayer shear resistance in flexible pavements. Journal of the Association of Asphalt Paving Technologists, 77, 221–256.

Santagata F.A., Ferrotti G., Partl M.N., Canestrari F. (2009). Statistical investigation of two different interlayer shear test methods. Materials and Structures, 42 (6), 705–714.

Saride S., Kumar V.V. (2017). Influence of geosynthetic-interlayers on the performance of asphalt overlays on pre-cracked pavements. Geotextiles and Geomembranes, 45, 184–196.

Seo Y., Kim Y.R. (2008). Using acoustic emission to monitor fatigue damage and healing in asphalt concrete. KSCE Journal of Civil Engineering, 12 (4), 237–243.

Shah S.G., Ray S., Kishen J.M.C. (2014). Fatigue crack propagation at concrete–concrete biomaterial interfaces. International Journal of Fatigue, 63, 118–126.

Shahin M.Y., Kirchner K., Blackmon E.W., Tomita H. (1986). Effect of layer slippage on performance of asphalt concrete pavements. Transport Research Record: Journal of Transport Research Board, 1095, 79–85.

Shahin M.Y., Kirchner K., Blackmon E. (1987). Analysis of asphalt concrete layer slippage and its effect on pavement performance and rehabilitation design. Proceedings of 6th International Conference Structural Design of Asphalt Pavements, 1, 958–964.

Shen S., Lu Z. (2011). Energy based laboratory fatigue failure criteria for asphalt materials. Journal of Testing Evaluation, 39 (3), 846–852.

Sholar G.A. (2004). Preliminary investigation of a test method to evaluate bond strength of bituminous tack coats. Journal of the Association of Asphalt Paving Technologists, 73, 771–801.

Shukla S.K., Yin J.-H. (2004). Functions and installation of paving geosynthetics. Proceedings of the 3rd Asian Regional Conference on Geosynthetics, Seoul, Korea.

Sobhan K., Tandon V. (2008). Mitigating reflection cracking in asphalt overlay using geo-synthetic reinforcements. Road Materials and Pavement Design, 9 (3), 367–387.

Song W., Shu X., Huang B., Woods M. (2016). Laboratory investigation of interlayer shear fatigue performance between open-graded friction course and underlying layer. Construction and Building Materials, 115, 381–389.

Struthers S.L., Richardson J. (2002). Use of engineered bitumen emulsions as bond coats. Proceedings of the 3rd World Congress on Emulsions, Lyon, France.

Su K., Sun L., Hachiya Y., Maekawa R. (2008). Analysis of shear stress in asphalt pavements under actual measured tire-pavement contact pressure. Proceedings of the 6th International Conference on Road and Airfield Pavement Technology (6th ICPT 2008), 20-23 July 2008, Sapporo, Japan.

Sudarsanan N., Karpurapu R., Amrithalingam V. (2015). Critical review on the bond strength of geosynthetic interlayer systems in asphalt overlays. Japanese Geotechnical Society Special Publication, 2 (67), 2296–2301.

Sudyka J., Krysiński L., Zofka A., Pszczoła M., Jaskuła P. (2018). High frequency impulse ground penetrating radar application in assessment of interlayer connections. MATEC Web of Conferences, 163.

Szydlo A., Malicki K. (2016). Analysis of the correlation between the static and fatigue test results of the interlayer bondings of asphalt layers. Archives of Civil Engineering, 62 (1), 83–98.

Tang L.S., Chen H.K., Sang H.T., Zhang S.Y., Zhang J.Y. (2015). Determination of traffic-load-influenced depths in clayey subsoil based on the shakedown concept. Soil Dynamics and Earthquake Engineering, 77, 182–191.

Tashman L., Nam K., Papagiannakis T., Willoughby K., Pierce L., Baker T. (2008). Evaluation of construction practices that influence the bond strength at the interface between pavement layers. Journal of Performance of Constructed Facilities, 22 (3), 154–161.

Tayebali A.A., Rahman M.S., Kulkarni M.B., Xu Q. (2004). A mechanistic approach to evaluate contribution of prime and tack coat in composite asphalt pavements. FHWA/NC/2004-05, North Carolina Department of Transportation, Raleigh, NC, USA.

Tozzo C., D'Andrea A., Cozzani D., Meo A. (2014a). Fatigue investigation of the interface shear performance in asphalt pavement. Modern Applied Science, 8 (2).

Tozzo C., Fiore N., D'Andrea A. (2014b). Dynamic shear tests for the evaluation of the effect of the normal load on the interface fatigue resistance. Construction and Building Materials, 61, 200–205.

Tschegg E.K., Kroyer G., Tang D., Stanzl-Tschegg S.E., Litzka J. (1995). Investigation of bonding between asphalt layers on road construction. Journal of Transportation Engineering, 121 (4), 309–317.

Uijting B.G.J., Jenner C.G., Gilchrist A.J.T. (2002). Evaluation of 20 years experience with asphalt reinforcement using geogrids. Proceedings of the 3rd International conference in bituminous mixtures and Pavements, Thessaloniki, Greece.

Unnthorsson R., Runarsson T.P., Jonsson M.T. (2008). Acoustic emission based fatigue failure criterion for CFRP. International Journal of Fatigue, 30, 11–20.

Uzan J., Livneh M., Eshed Y. (1978). Investigation of adhesion properties between asphaltic concrete layers. Journal of the Association of Asphalt Paving Technologists, 47, 495–521.

Vanelstraete A., De Visscher J. (2004). Long term performance on site of interface systems. Proceedings of the 5th International RILEM Conference on Reflective Cracking in Pavements, Limoges, France.

Walsh I.D., Williams J.T. (2001). HAPAS certificates for procurement of thin surfacing. Highways and Transportation, 48 (7–8), 12–14.

Wang H., Al-Qadi I.L. (2009). Combined effect of moving wheel loading and three-dimensional contact stresses on perpetual pavement responses. Transportation Research Record: Journal of the Transportation Research Board, 2095 (1), 53–61.

Wang H., Al-Qadi I.L. (2010). Near-surface pavement failure under multiaxial stress state in thick asphalt pavement. Transportation Research Record: Journal of the Transportation Research Board, 2154, 91–99.

Wang H., Xu G., Wang Z., Bennert T. (2018). Flexible pavement interface bonding: theoretical analysis and shear-strength measurement. Journal of Testing and Evaluation, 46 (1), 99–107.

Wellner F., Hristov B. (2015). Numerically supported experimental determination of the behavior of the interlayer bond in asphalt pavement. Transportation Research Record: Journal of the Transportation Research Board, 2506, 116–125.

West R.C., Zhang J., Moore J. (2005). Evaluation of bond strength between pavement layers. NCAT Report 05-08, National Center for Asphalt Technology, Auburn University, Auburn, Alabama.

White G. (2016). Shear stresses in an asphalt surface under various aircraft braking conditions. International Journal of Pavement Research and Technology, 9, 89–101.

Willis J.R., Timm D.H. (2006). Forensic investigation of a rich-bottom pavement. NCAT Report 06-04, National Center for Asphalt Technology, Auburn, AL, USA.

Wu T., Cai Y., Guo L., Ling D., Wang J. (2017). Influence of shear stress level on cyclic deformation behaviour of intact Wenzhou soft clay under traffic loading. Engineering Geology, 228, 61–70.

You L., Yan K., Hu Y., Ma Y. (2018). Impact of interlayer on the anisotropic multi-layered medium overlaying viscoelastic layer under axisymmetric loading. Applied Mathematical Modelling, 61, 726–743.

Zamora-Barraza D., Calzada-Peréz M., Castro-Fresno D., Vega-Zamanillo A. (2010). New procedure for measuring adherence between a geosynthetic material and a bituminous mixture. Geotextiles and Geomembranes, 28, 483–489.

Zamora-Barraza D., Calzada-Peréz M., Castro-Fresno D., Vega-Zamanillo A. (2011). Evaluation of anti-reflective cracking systems using geosynthetics in the interlayer zone. Geotextiles and Geomembranes, 29, 130–136.

Zhou F., Scullion T. (2003). Upgraded overlay tester and its application to characterize reflection cracking resistance of asphalt mixtures. Report 0-4467-1, Project 0-4467, Project Title: Developing an upgraded overlay tester system to characterize the reflection cracking resistance of asphalt concrete, Texas Transportation Institute, USA.

Zofka A., Bernier A., Josen R., Maliszewski M. (2014). Advanced shear tester for solid and layered samples. Proceedings of 2014 International Society for Asphalt Pavements (ISAP) Conference, Raleigh, USA.

Zofka A., Maliszewski M., Bernier A., Josen R., Vaitkus A., Kleizienė R. (2015). Advanced shear tester for evaluation of asphalt concrete under constant normal stiffness conditions. Road Materials and Pavement Design, 16, 187–210.

Zornberg J.G. (2017). Functions and applications of geosynthetics in roadways. Procedia Engineering, 189, 298 – 306.

Zou X., Gong H., Tang B., Xiao D., Zhao D. (2013). Effects of shear stress on pavement cracking and interface debonding: case study in Arkansas. Transport Research Record: Journal of Transport Research Board, 17.